

ICRC2017

35th International Cosmic Ray Conference
The Astroparticle Physics Conference



The Pierre Auger Observatory: Contributions to the 35th International Cosmic Ray Conference (ICRC 2017)

The Pierre Auger Collaboration



PIERRE
AUGER
OBSERVATORY

A. Aab⁷⁷, P. Abreu⁶⁹, M. Aglietta^{50,49}, I.F.M. Albuquerque¹⁸, I. Allekotte¹, A. Almela^{8,11}, J. Alvarez Castillo⁶⁵, J. Alvarez-Muñiz⁷⁶, G.A. Anastasi^{41,43}, L. Anchordoqui⁸³, B. Andrada⁸, S. Andringa⁶⁹, C. Aramo⁴⁷, N. Arsene⁷¹, H. Asorey^{1,27}, P. Assis⁶⁹, J. Aublin³², G. Avila^{9,10}, A.M. Badescu⁷², A. Balaceanu⁷⁰, F. Barbato⁵⁷, R.J. Barreira Luz⁶⁹, K.H. Becker³⁴, J.A. Bellido¹², C. Berat³³, M.E. Bertaina^{59,49}, X. Bertou¹, P.L. Biermann^b, J. Biteau³¹, S.G. Blaess¹², A. Blanco⁶⁹, J. Blazek²⁹, C. Bleve^{53,45}, M. Boháčová²⁹, D. Boncioli^{43,8}, C. Bonifazi²⁴, N. Borodai⁶⁶, A.M. Botti^{8,36}, J. Brack^f, I. Brancus⁷⁰, T. Bretz³⁸, A. Bridgeman³⁵, F.L. Briechle³⁸, P. Buchholz⁴⁰, A. Bueno⁷⁵, S. Buitink⁷⁷, M. Buscemi^{55,44}, K.S. Caballero-Mora⁶³, B. Caccianiga⁴⁶, L. Caccianiga⁵⁶, A. Cancio^{11,8}, F. Canfora⁷⁷, L. Caramete⁷¹, R. Caruso^{55,44}, A. Castellina^{50,49}, F. Catalani¹⁶, G. Cataldi⁴⁵, L. Cazon⁶⁹, A.G. Chavez⁶⁴, J.A. Chinellato¹⁹, J. Chudoba²⁹, R.W. Clay¹², A. Cobos⁸, R. Colalillo^{57,47}, A. Coleman⁸⁷, L. Collica⁴⁹, M.R. Coluccia^{53,45}, R. Conceição⁶⁹, G. Consolati⁴⁶, G. Consolati^{46,51}, F. Contreras^{9,10}, M.J. Cooper¹², S. Coutu⁸⁷, C.E. Covault⁸¹, J. Cronin⁸⁸, S. D'Amico^{52,45}, B. Daniel¹⁹, S. Dasso^{5,3}, K. Daumiller³⁶, B.R. Dawson¹², R.M. de Almeida²⁶, S.J. de Jong^{77,79}, G. De Mauro⁷⁷, J.R.T. de Mello Neto^{24,25}, I. De Mitri^{53,45}, J. de Oliveira²⁶, V. de Souza¹⁷, J. Debatin³⁵, O. Deligny³¹, M.L. Díaz Castro¹⁹, F. Diogo⁶⁹, C. Dobrigkeit¹⁹, J.C. D'Olivo⁶⁵, Q. Dorosti⁴⁰, R.C. dos Anjos²³, M.T. Dova⁴, A. Dundovic³⁹, J. Ebr²⁹, R. Engel³⁶, M. Erdmann³⁸, M. Erfani⁴⁰, C.O. Escobar^e, J. Espadanal⁶⁹, A. Etchegoyen^{8,11}, H. Falcke^{77,80,79}, J. Farmer⁸⁸, G. Farrar⁸⁵, A.C. Fauth¹⁹, N. Fazzini^e, F. Fenu^{59,49}, B. Fick⁸⁴, J.M. Figueira⁸, A. Filipčić^{74,73}, M.M. Freire⁶, T. Fujii⁸⁸, A. Fuster^{8,11}, R. Gaïor³², B. García⁷, F. Gaté^d, H. Gemmeke³⁷, A. Gherghel-Lascu⁷⁰, P.L. Ghia³¹, U. Giaccari²⁴, M. Giammarchi⁴⁶, M. Giller⁶⁷, D. Głás⁶⁸, C. Glaser³⁸, G. Golup¹, M. Gómez Berisso¹, P.F. Gómez Vitale^{9,10}, N. González^{8,36}, A. Gorgi^{50,49}, A.F. Grillo⁴³, T.D. Grubb¹², F. Guarino^{57,47}, G.P. Guedes²⁰, R. Halliday⁸¹, M.R. Hampel⁸, P. Hansen⁴, D. Harari¹, T.A. Harrison¹², A. Haungs³⁶, T. Hebbeker³⁸, D. Heck³⁶, P. Heimann⁴⁰, A.E. Herve³⁵, G.C. Hill¹², C. Hojvat^e, E. Holt^{36,8}, P. Homola⁶⁶, J.R. Hörandel^{77,79}, P. Horvath³⁰, M. Hrabovský³⁰, T. Huege³⁶, J. Hulsman^{8,36}, A. Insolia^{55,44}, P.G. Isar⁷¹, I. Jandt³⁴, J.A. Johnsen⁸², M. Josebachuili⁸, J. Jurysek²⁹, A. Kääpä³⁴, O. Kambeitz³⁵, K.H. Kampert³⁴, B. Keilhauer³⁶, N. Kemmerich¹⁸, E. Kemp¹⁹, J. Kemp³⁸, R.M. Kieckhafer⁸⁴, H.O. Klages³⁶, M. Kleifges³⁷, J. Kleinfeller⁹, R. Krause³⁸, N. Krohm³⁴, D. Kuempel³⁴, G. Kukec Mezek⁷³, N. Kunka³⁷, A. Kuotb Awad³⁵, B.L. Lago¹⁵, D. LaHurd⁸¹, R.G. Lang¹⁷, M. Lauscher³⁸, R. Legumina⁶⁷, M.A. Leigui de Oliveira²², A. Letessier-Selvon³², I. Lhenry-Yvon³¹, K. Link³⁵, D. Lo Presti⁵⁵, L. Lopes⁶⁹, R. López⁶⁰, A. López Casado⁷⁶, R. Lorek⁸¹, Q. Luce³¹, A. Lucero^{8,11}, M. Malacari⁸⁸, M. Mallamaci^{56,46}, D. Mandat²⁹, P. Mantsch^e, A.G. Mariazzi⁴, I.C. Mariş¹³, G. Marsella^{53,45}, D. Martello^{53,45}, H. Martinez⁶¹, O. Martínez Bravo⁶⁰, J.J. Masías Meza³, H.J. Mathes³⁶, S. Mathys³⁴, G. Matthiae^{58,48}, E. Mayotte³⁴

P.O. Mazur^e, C. Medina⁸², G. Medina-Tanco⁶⁵, D. Melo⁸, A. Menshikov³⁷, K.-D. Merenda⁸², S. Michal³⁰, M.I. Micheletti⁶, L. Middendorf³⁸, L. Miramonti^{56,46}, B. Mitrica⁷⁰, D. Mockler³⁵, S. Mollerach¹, F. Montanet³³, C. Morello^{50,49}, G. Morlino^{41,43}, M. Mostafá⁸⁷, A.L. Müller^{8,36}, G. Müller³⁸, M.A. Muller^{19,21}, S. Müller^{35,8}, R. Mussa⁴⁹, I. Naranjo¹, L. Nellen⁶⁵, P.H. Nguyen¹², M. Niculescu-Oglinzanu⁷⁰, M. Niechciol⁴⁰, L. Niemietz³⁴, T. Niggemann³⁸, D. Nitz⁸⁴, D. Nosek²⁸, V. Novotny²⁸, L. Nožka³⁰, L.A. Núñez²⁷, L. Ochilo⁴⁰, F. Oikonomou⁸⁷, A. Olinto⁸⁸, M. Palatka²⁹, J. Pallotta², P. Papenbreer³⁴, G. Parente⁷⁶, A. Parra⁶⁰, T. Paul⁸³, M. Pech²⁹, F. Pedreira⁷⁶, J. Pękala⁶⁶, R. Pelayo⁶², J. Peña-Rodríguez²⁷, L. A. S. Pereira¹⁹, M. Perlin⁸, L. Perrone^{53,45}, C. Peters³⁸, S. Petrera^{41,43}, J. Phuntsok⁸⁷, R. Piegaiá³, T. Pierog³⁶, M. Pimenta⁶⁹, V. Pirronello^{55,44}, M. Platino⁸, M. Plum³⁸, J. Poh⁸⁸, C. Porowski⁶⁶, R.R. Prado¹⁷, P. Privitera⁸⁸, M. Prouza²⁹, E.J. Quel², S. Querschfeld³⁴, S. Quinn⁸¹, R. Ramos-Pollán²⁷, J. Rautenberg³⁴, D. Ravignani⁸, J. Ridky²⁹, F. Riehn⁶⁹, M. Risse⁴⁰, P. Ristori², V. Rizi^{54,43}, W. Rodrigues de Carvalho¹⁸, G. Rodriguez Fernandez^{58,48}, J. Rodriguez Rojo⁹, M.J. Roncoroni⁸, M. Roth³⁶, E. Roulet¹, A.C. Rovero⁵, P. Ruehl⁴⁰, S.J. Saffi¹², A. Saftoiu⁷⁰, F. Salamida^{54,43}, H. Salazar⁶⁰, A. Saleh⁷³, G. Salina⁴⁸, F. Sánchez⁸, P. Sanchez-Lucas⁷⁵, E.M. Santos¹⁸, E. Santos⁸, F. Sarazin⁸², R. Sarmento⁶⁹, C. Sarmiento-Cano⁸, R. Sato⁹, M. Schauer³⁴, V. Scherini⁴⁵, H. Schieler³⁶, M. Schimp³⁴, D. Schmidt^{36,8}, O. Scholten^{78,c}, P. Schovánek²⁹, F.G. Schröder³⁶, S. Schröder³⁴, A. Schulz³⁵, J. Schumacher³⁸, S.J. Sciutto⁴, A. Segreto^{42,44}, R.C. Shellard¹⁴, G. Sigl³⁹, G. Silli^{8,36}, R. Šmída³⁶, G.R. Snow⁸⁹, P. Sommers⁸⁷, S. Sonntag⁴⁰, J. F. Soriano⁸³, R. Squartini⁹, D. Stanca⁷⁰, S. Stanić⁷³, J. Stasielak⁶⁶, P. Stassi³³, M. Stolpovskiy³³, F. Strafella^{53,45}, A. Streich³⁵, F. Suarez^{8,11}, M. Suarez Durán²⁷, T. Sudholz¹², T. Suomijärvi³¹, A.D. Supanitsky⁵, J. Šupík³⁰, J. Swain⁸⁶, Z. Szadkowski⁶⁸, A. Taboada³⁶, O.A. Tabora¹, V.M. Theodoro¹⁹, C. Timmermans^{79,77}, C.J. Todero Peixoto¹⁶, L. Tomankova³⁶, B. Tomé⁶⁹, G. Torralba Elipse⁷⁶, P. Travnicek²⁹, M. Trini⁷³, R. Ulrich³⁶, M. Unger³⁶, M. Urban³⁸, J.F. Valdés Galicia⁶⁵, I. Valiño⁷⁶, L. Valore^{57,47}, G. van Aar⁷⁷, P. van Bodegom¹², A.M. van den Berg⁷⁸, A. van Vliet⁷⁷, E. Varela⁶⁰, B. Vargas Cárdenas⁶⁵, R.A. Vázquez⁷⁶, D. Veberič³⁶, C. Ventura²⁵, I.D. Vergara Quispe⁴, V. Verzi⁴⁸, J. Vicha²⁹, L. Villaseñor⁶⁴, S. Vorobiov⁷³, H. Wahlberg⁴, O. Wainberg^{8,11}, D. Walz³⁸, A.A. Watson^a, M. Weber³⁷, A. Weindl³⁶, M. Wiedeński⁶⁸, L. Wiencke⁸², H. Wilczyński⁶⁶, T. Winchen³⁴, M. Wirtz³⁸, D. Wittkowski³⁴, B. Wundheiler⁸, L. Yang⁷³, A. Yushkov⁸, E. Zas⁷⁶, D. Zavrtnik^{73,74}, M. Zavrtnik^{74,73}, A. Zepeda⁶¹, B. Zimmermann³⁷, M. Ziolkowski⁴⁰, Z. Zong³¹, F. Zuccarello^{55,44}

— • —

- ¹ Centro Atómico Bariloche and Instituto Balseiro (CNEA-UNCuyo-CONICET), San Carlos de Bariloche, Argentina
- ² Centro de Investigaciones en Láseres y Aplicaciones, CITEDEF and CONICET, Villa Martelli, Argentina
- ³ Departamento de Física and Departamento de Ciencias de la Atmósfera y los Océanos, FCEyN, Universidad de Buenos Aires and CONICET, Buenos Aires, Argentina
- ⁴ IFLP, Universidad Nacional de La Plata and CONICET, La Plata, Argentina
- ⁵ Instituto de Astronomía y Física del Espacio (IAFE, CONICET-UBA), Buenos Aires, Argentina
- ⁶ Instituto de Física de Rosario (IFIR) – CONICET/U.N.R. and Facultad de Ciencias Bioquímicas y Farmacéuticas U.N.R., Rosario, Argentina
- ⁷ Instituto de Tecnologías en Detección y Astropartículas (CNEA, CONICET, UNSAM), and Universidad Tecnológica Nacional – Facultad Regional Mendoza (CONICET/CNEA), Mendoza, Argentina
- ⁸ Instituto de Tecnologías en Detección y Astropartículas (CNEA, CONICET, UNSAM), Buenos Aires, Argentina
- ⁹ Observatorio Pierre Auger, Malargüe, Argentina
- ¹⁰ Observatorio Pierre Auger and Comisión Nacional de Energía Atómica, Malargüe, Argentina
- ¹¹ Universidad Tecnológica Nacional – Facultad Regional Buenos Aires, Buenos Aires, Argentina
- ¹² University of Adelaide, Adelaide, S.A., Australia
- ¹³ Université Libre de Bruxelles (ULB), Brussels, Belgium

- 14 Centro Brasileiro de Pesquisas Físicas, Rio de Janeiro, RJ, Brazil
- 15 Centro Federal de Educação Tecnológica Celso Suckow da Fonseca, Nova Friburgo, Brazil
- 16 Universidade de São Paulo, Escola de Engenharia de Lorena, Lorena, SP, Brazil
- 17 Universidade de São Paulo, Instituto de Física de São Carlos, São Carlos, SP, Brazil
- 18 Universidade de São Paulo, Instituto de Física, São Paulo, SP, Brazil
- 19 Universidade Estadual de Campinas, IFGW, Campinas, SP, Brazil
- 20 Universidade Estadual de Feira de Santana, Feira de Santana, Brazil
- 21 Universidade Federal de Pelotas, Pelotas, RS, Brazil
- 22 Universidade Federal do ABC, Santo André, SP, Brazil
- 23 Universidade Federal do Paraná, Setor Palotina, Palotina, Brazil
- 24 Universidade Federal do Rio de Janeiro, Instituto de Física, Rio de Janeiro, RJ, Brazil
- 25 Universidade Federal do Rio de Janeiro (UFRJ), Observatório do Valongo, Rio de Janeiro, RJ, Brazil
- 26 Universidade Federal Fluminense, EEIMVR, Volta Redonda, RJ, Brazil
- 27 Universidad Industrial de Santander, Bucaramanga, Colombia
- 28 Charles University, Faculty of Mathematics and Physics, Institute of Particle and Nuclear Physics, Prague, Czech Republic
- 29 Institute of Physics of the Czech Academy of Sciences, Prague, Czech Republic
- 30 Palacky University, RCPTM, Olomouc, Czech Republic
- 31 Institut de Physique Nucléaire d'Orsay (IPNO), Université Paris-Sud, Univ. Paris/Saclay, CNRS-IN2P3, Orsay, France
- 32 Laboratoire de Physique Nucléaire et de Hautes Energies (LPNHE), Universités Paris 6 et Paris 7, CNRS-IN2P3, Paris, France
- 33 Laboratoire de Physique Subatomique et de Cosmologie (LPSC), Université Grenoble-Alpes, CNRS/IN2P3, Grenoble, France
- 34 Bergische Universität Wuppertal, Department of Physics, Wuppertal, Germany
- 35 Karlsruhe Institute of Technology, Institut für Experimentelle Kernphysik (IEKP), Karlsruhe, Germany
- 36 Karlsruhe Institute of Technology, Institut für Kernphysik, Karlsruhe, Germany
- 37 Karlsruhe Institute of Technology, Institut für Prozessdatenverarbeitung und Elektronik, Karlsruhe, Germany
- 38 RWTH Aachen University, III. Physikalisches Institut A, Aachen, Germany
- 39 Universität Hamburg, II. Institut für Theoretische Physik, Hamburg, Germany
- 40 Universität Siegen, Fachbereich 7 Physik – Experimentelle Teilchenphysik, Siegen, Germany
- 41 Gran Sasso Science Institute (INFN), L'Aquila, Italy
- 42 INFN – Istituto di Astrofisica Spaziale e Fisica Cosmica di Palermo, Palermo, Italy
- 43 INFN Laboratori Nazionali del Gran Sasso, Assergi (L'Aquila), Italy
- 44 INFN, Sezione di Catania, Catania, Italy
- 45 INFN, Sezione di Lecce, Lecce, Italy
- 46 INFN, Sezione di Milano, Milano, Italy
- 47 INFN, Sezione di Napoli, Napoli, Italy
- 48 INFN, Sezione di Roma "Tor Vergata", Roma, Italy
- 49 INFN, Sezione di Torino, Torino, Italy
- 50 Osservatorio Astrofisico di Torino (INAF), Torino, Italy
- 51 Politecnico di Milano, Dipartimento di Scienze e Tecnologie Aerospaziali, Milano, Italy
- 52 Università del Salento, Dipartimento di Ingegneria, Lecce, Italy
- 53 Università del Salento, Dipartimento di Matematica e Fisica "E. De Giorgi", Lecce, Italy
- 54 Università dell'Aquila, Dipartimento di Scienze Fisiche e Chimiche, L'Aquila, Italy
- 55 Università di Catania, Dipartimento di Fisica e Astronomia, Catania, Italy
- 56 Università di Milano, Dipartimento di Fisica, Milano, Italy
- 57 Università di Napoli "Federico II", Dipartimento di Fisica "Ettore Pancini", Napoli, Italy
- 58 Università di Roma "Tor Vergata", Dipartimento di Fisica, Roma, Italy
- 59 Università Torino, Dipartimento di Fisica, Torino, Italy
- 60 Benemérita Universidad Autónoma de Puebla, Puebla, México

- ⁶¹ Centro de Investigación y de Estudios Avanzados del IPN (CINVESTAV), México, D.F., México
- ⁶² Unidad Profesional Interdisciplinaria en Ingeniería y Tecnologías Avanzadas del Instituto Politécnico Nacional (UPIITA-IPN), México, D.F., México
- ⁶³ Universidad Autónoma de Chiapas, Tuxtla Gutiérrez, Chiapas, México
- ⁶⁴ Universidad Michoacana de San Nicolás de Hidalgo, Morelia, Michoacán, México
- ⁶⁵ Universidad Nacional Autónoma de México, México, D.F., México
- ⁶⁶ Institute of Nuclear Physics PAN, Krakow, Poland
- ⁶⁷ University of Łódź, Faculty of Astrophysics, Łódź, Poland
- ⁶⁸ University of Łódź, Faculty of High-Energy Astrophysics, Łódź, Poland
- ⁶⁹ Laboratório de Instrumentação e Física Experimental de Partículas – LIP and Instituto Superior Técnico – IST, Universidade de Lisboa – UL, Lisboa, Portugal
- ⁷⁰ “Horia Hulubei” National Institute for Physics and Nuclear Engineering, Bucharest-Magurele, Romania
- ⁷¹ Institute of Space Science, Bucharest-Magurele, Romania
- ⁷² University Politehnica of Bucharest, Bucharest, Romania
- ⁷³ Center for Astrophysics and Cosmology (CAC), University of Nova Gorica, Nova Gorica, Slovenia
- ⁷⁴ Experimental Particle Physics Department, J. Stefan Institute, Ljubljana, Slovenia
- ⁷⁵ Universidad de Granada and C.A.F.P.E., Granada, Spain
- ⁷⁶ Universidad de Santiago de Compostela, Santiago de Compostela, Spain
- ⁷⁷ IMAPP, Radboud University Nijmegen, Nijmegen, The Netherlands
- ⁷⁸ KVI – Center for Advanced Radiation Technology, University of Groningen, Groningen, The Netherlands
- ⁷⁹ Nationaal Instituut voor Kernfysica en Hoge Energie Fysica (NIKHEF), Science Park, Amsterdam, The Netherlands
- ⁸⁰ Stichting Astronomisch Onderzoek in Nederland (ASTRON), Dwingeloo, The Netherlands
- ⁸¹ Case Western Reserve University, Cleveland, OH, USA
- ⁸² Colorado School of Mines, Golden, CO, USA
- ⁸³ Department of Physics and Astronomy, Lehman College, City University of New York, Bronx, NY, USA
- ⁸⁴ Michigan Technological University, Houghton, MI, USA
- ⁸⁵ New York University, New York, NY, USA
- ⁸⁶ Northeastern University, Boston, MA, USA
- ⁸⁷ Pennsylvania State University, University Park, PA, USA
- ⁸⁸ University of Chicago, Enrico Fermi Institute, Chicago, IL, USA
- ⁸⁹ University of Nebraska, Lincoln, NE, USA

^a School of Physics and Astronomy, University of Leeds, Leeds, United Kingdom

^b Max-Planck-Institut für Radioastronomie, Bonn, Germany

^c also at Vrije Universiteit Brussels, Brussels, Belgium

^d SUBATECH, École des Mines de Nantes, CNRS-IN2P3, Université de Nantes, France

^e Fermi National Accelerator Laboratory, USA

^f Colorado State University, Fort Collins, CO

^g now at Deutsches Elektronen-Synchrotron (DESY), Zeuthen, Germany

Acknowledgments

The successful installation, commissioning, and operation of the Pierre Auger Observatory would not have been possible without the strong commitment and effort from the technical and administrative staff in Malargüe. We are very grateful to the following agencies and organizations for financial support:

Argentina – Comisión Nacional de Energía Atómica; Agencia Nacional de Promoción Científica y Tecnológica (ANPCyT); Consejo Nacional de Investigaciones Científicas y Técnicas (CONICET); Gobierno de la Provincia de Mendoza; Municipalidad de Malargüe; NDM Holdings and Valle Las Leñas; in gratitude for their continuing cooperation over land access; Australia – the Australian Research Council; Brazil – Conselho Nacional de Desenvolvimento Científico e Tecnológico (CNPq); Financiadora de Estudos e Projetos (FINEP); Fundação de Amparo à Pesquisa do Estado de Rio de Janeiro (FAPERJ); São Paulo Research Foundation (FAPESP) Grants No. 2010/07359-6 and No. 1999/05404-3; Ministério de Ciência e Tecnologia (MCT); Czech Republic – Grant No. MSMT CR LG15014, LO1305, LM2015038 and CZ.02.1.01/0.0/0.0/16_013/0001402; France – Centre de Calcul IN2P3/CNRS; Centre National de la Recherche Scientifique (CNRS); Conseil Régional Ile-de-France; Département Physique Nucléaire et Corpusculaire (PNC-IN2P3/CNRS); Département Sciences de l’Univers (SDU-INSU/CNRS); Institut Lagrange de Paris (ILP) Grant No. LABEX ANR-10-LABX-63 within the Investissements d’Avenir Programme Grant No. ANR-11-IDEX-0004-02; Germany – Bundesministerium für Bildung und Forschung (BMBF); Deutsche Forschungsgemeinschaft (DFG); Finanzministerium Baden-Württemberg; Helmholtz Alliance for Astroparticle Physics (HAP); Helmholtz-Gemeinschaft Deutscher Forschungszentren (HGF); Ministerium für Innovation, Wissenschaft und Forschung des Landes Nordrhein-Westfalen; Ministerium für Wissenschaft, Forschung und Kunst des Landes Baden-Württemberg; Italy – Istituto Nazionale di Fisica Nucleare (INFN); Istituto Nazionale di Astrofisica (INAF); Ministero dell’Istruzione, dell’Università e della Ricerca (MIUR); CETEMPS Center of Excellence; Ministero degli Affari Esteri (MAE); Mexico – Consejo Nacional de Ciencia y Tecnología (CONACYT) No. 167733; Universidad Nacional Autónoma de México (UNAM); PAPIIT DGAPA-UNAM; The Netherlands – Ministerie van Onderwijs, Cultuur en Wetenschap; Nederlandse Organisatie voor Wetenschappelijk Onderzoek (NWO); Stichting voor Fundamenteel Onderzoek der Materie (FOM); Poland – National Centre for Research and Development, Grants No. ERA-NET-ASPERA/01/11 and No. ERA-NET-ASPERA/02/11; National Science Centre, Grants No. 2013/08/M/ST9/00322, No. 2013/08/M/ST9/00728 and No. HARMONIA 5–2013/10/M/ST9/00062, UMO-2016/22/M/ST9/00198; Portugal – Portuguese national funds and FEDER funds within Programa Operacional Factores de Competitividade through Fundação para a Ciência e a Tecnologia (COMPETE); Romania – Romanian Authority for Scientific Research ANCS; CNDI-UEFISCDI partnership projects Grants No. 20/2012 and No. 194/2012 and PN 16 42 01 02; Slovenia – Slovenian Research Agency; Spain – Comunidad de Madrid; Fondo Europeo de Desarrollo Regional (FEDER) funds; Ministerio de Economía y Competitividad; Xunta de Galicia; European Community 7th Framework Program Grant No. FP7-PEOPLE-2012-IEF-328826; USA – Department of Energy, Contracts No. DE-AC02-07CH11359, No. DE-FR02-04ER41300, No. DE-FG02-99ER41107 and No. DE-SC0011689; National Science Foundation, Grant No. 0450696; The Grainger Foundation; Marie Curie-IRSES/EPLANET; European Particle Physics Latin American Network; European Union 7th Framework Program, Grant No. PIRSES-2009-GA-246806; European Union’s Horizon 2020 research and innovation programme (Grant No. 646623); and UNESCO.

Contributions

1	Energy Spectrum	8
1.1	Francesco Fenu: <i>The cosmic ray energy spectrum measured using the Pierre Auger Observatory</i>	9
1.2	Raphael Krause: <i>A new method to determine the energy scale for high-energy cosmic rays using radio measurements at the Pierre Auger Observatory</i>	17
2	Arrival Directions and Anisotropies	25
2.1	Oscar Taborda: <i>Dipolar anisotropy of cosmic rays above 8 EeV</i>	26
2.2	Ugo Giaccari: <i>Arrival directions of the highest-energy cosmic rays detected by the Pierre Auger Observatory</i>	31
3	Nuclear mass composition, photons, and neutrinos	39
3.1	Jose Bellido: <i>Depth of maximum of air-shower profiles at the Pierre Auger Observatory: Measurements above $10^{17.2}$ eV and Composition Implications</i>	40
3.2	Patricia Sanchez-Lucas: <i>$\langle X_{max} \rangle$ measurements and tests of hadronic models using the surface detector of the Pierre Auger Observatory</i>	48
3.3	Marcus Niechciol: <i>Diffuse and targeted searches for ultra-high-energy photons using the hybrid detector of the Pierre Auger Observatory</i>	56
3.4	Enrique Zas: <i>Searches for neutrino fluxes in the EeV regime with the Pierre Auger Observatory</i>	64
4	Hadronic Interactions and Shower Physics	72
4.1	Manuela Mallamaci: <i>Measurements of the depth of maximum muon production and of its fluctuations in extensive air showers above 1.5×10^{19} eV at the Pierre Auger Observatory</i>	73
4.2	Ariel Bridgeman: <i>Shower universality reconstruction of data from the Pierre Auger Observatory and validations with hadronic interaction models</i>	81
4.3	Alan Coleman: <i>The influence of weather effects on the reconstruction of extensive air showers at the Pierre Auger Observatory</i>	89
4.4	Juan Manuel Figueira: <i>An improved reconstruction method for the AMIGA detectors</i>	97
4.5	Ewa M. Holt: <i>Recent Results of the Auger Engineering Radio Array (AERA)</i>	105
4.6	Romain Gaïor: <i>Studies of the microwave emission of extensive air showers with GIGAS and MIDAS at the Pierre Auger Observatory</i>	113

5	Cosmology and Geophysics	121
5.1	Denise Boncioli: <i>Probing Lorentz symmetry with the Pierre Auger Observatory</i>	122
5.2	David Wittkowski: <i>Reconstructed properties of the sources of UHECR and their dependence on the extragalactic magnetic field</i>	130
5.3	Roberta Colalillo: <i>Peculiar lightning-related events observed by the surface detector of the Pierre Auger Observatory</i>	138
6	Detectors and AugerPrime Upgrade	146
6.1	Daniele Martello: <i>The Pierre Auger Observatory Upgrade</i>	147
6.2	Tiina Suomijärvi: <i>New electronics for the surface detectors of the Pierre Auger Observatory</i>	155
6.3	Antonella Castellina: <i>The dynamic range of the AugerPrime Surface Detector: technical solution and physics reach</i>	161
6.4	Radomír Šmída: <i>Scintillator detectors of AugerPrime</i>	169
6.5	Zizhao Zong: <i>First results from the AugerPrime engineering array</i>	177
6.6	David Schmidt: <i>AugerPrime implementation in the <u>Offline</u> simulation and reconstruction framework</i>	185
6.7	Max Malacari: <i>Improvements to aerosol attenuation measurements at the Pierre Auger Observatory</i>	193
6.8	Jiri Blazek: <i>The FRAM Telescope at the Pierre Auger Observatory</i>	201
7	Outreach	209
7.1	Charles Timmermans: <i>Education and public outreach of the Pierre Auger Observatory</i> . .	210

1

Energy Spectrum





The cosmic ray energy spectrum measured using the Pierre Auger Observatory

Francesco Fenu^{*ab} for the Pierre Auger Collaboration^c

^a*Università degli studi di Torino, Via Pietro Giuria 1, 10152 Torino, Italy*

^b*INFN Torino, Via Pietro Giuria 1, 10152 Torino, Italy*

^c*Observatorio Pierre Auger, Av. San Martín Norte 304, 5613 Malargüe, Argentina*

E-mail: auger_spokespersons@fnal.gov

Full author list: http://www.auger.org/archive/authors_icrc_2017.html

We present an update of the cosmic ray energy spectrum measured from 3×10^{17} eV to over 10^{20} eV at the Pierre Auger Observatory. This energy range is covered by combining data from the surface detector (subdividing the events into a vertical and a horizontal data set), from a denser array of stations and from hybrid events simultaneously recorded by the surface and the fluorescence detectors. Data collected to date, with a total exposure exceeding $67,000 \text{ km}^2 \text{ sr yr}$, rely on the energy scale provided by the fluorescence detector. The spectral features, and the impact of systematic uncertainties on their significance, are discussed in detail.

*35th International Cosmic Ray Conference — ICRC2017
10–20 July, 2017
Bexco, Busan, Korea*

*Speaker.

1. Introduction

The Pierre Auger Observatory [1] is the largest cosmic ray Observatory built so far. It is located in the Argentinian pampa near Malargüe, Mendoza province and has been in operation since 2004. The cosmic rays are studied by combining the measurements of a Surface Detector (SD) and a Fluorescence Detector (FD). The SD consists of 1600 Water Cherenkov Detectors (WCDs) on a 1500 m triangular grid (SD 1500), covering an area of $\sim 3000 \text{ km}^2$, and of additional 61 detectors covering 23.5 km^2 on a 750 m grid (SD 750). The SD 1500 is fully efficient at $3 \times 10^{18} \text{ eV}$ while the SD 750 from $3 \times 10^{17} \text{ eV}$ onwards. The atmosphere above the array is monitored by the 27 telescopes of the FD located in five buildings along the perimeter of the site. 24 telescopes have a field of view of $30^\circ \times 30^\circ$ in azimuth and elevation, with a minimum elevation of 1.51° above the horizon. Three additional telescopes, the High Elevation Auger Telescopes, can cover an elevation up to 60° to detect the low energy showers in coincidence with the SD 750. The FD measurements provide an almost calorimetric estimate of the shower energy but are limited by the atmospheric conditions while the SD measurements are made nearly 100% of the time. The main advantage of a hybrid system that combines the FD and SD measurements is the good control of the systematic uncertainties in the energy scale. It is possible to calibrate the SD signal by exploiting the events where a simultaneous measurement of SD signal and FD energy is made, thus largely avoiding the use of Monte Carlo to reconstruct the energy.

In this contribution we present the energy spectrum measured at the Pierre Auger Observatory using an exposure exceeding $67,000 \text{ km}^2 \text{ sr yr}$ accumulated since January 2004 until December 2016. The measurements benefit from an improved reconstruction of the FD and SD events which will be described in detail.

2. Improvements in the event reconstruction

An accurate reconstruction of the FD events is complex, since it requires the knowledge of parameters like the fluorescence yield, the atmospheric conditions, the absolute calibration of the telescopes and many others. The entire procedure allows us to reconstruct the longitudinal profile of the energy deposit (dE/dX) of the air shower in the atmosphere. Finally, from $E_{\text{cal}} = \int (dE/dX) dX$, which represents the energy deposited by the shower in atmosphere, the total energy is obtained by adding the so-called invisible energy, which is the energy carried into the ground by high energy muons and neutrinos. The analysis used to obtain the Auger energy scale and the estimate of its systematic uncertainties has been presented in [2]. Since this work, we have refined the reconstruction of the FD events obtaining an improved determination of the shower energies.

The reconstruction technique of the central laser facility of the Observatory, used to obtain the hourly measurements of the vertical aerosol optical depth, has improved, and now accounts for the shape of the aerosol scattering phase function and for the multiple scattering in the atmosphere. The two improvements cause an increase in the aerosol optical depth and consequently the shower energy increases of about 1% to 3% [3].

We have also improved the calibration of the FD telescopes. In the previous estimation, the optical efficiency, which is the relative FD response at various wavelengths, was the same for all telescopes. Now, after a dedicated campaign of measurements, we use the optical efficiency

appropriate to each telescope which allows us to correctly take into account the different materials of which the mirrors are made [4]. We furthermore improved the estimation of the photomultiplier calibration constants used for the first years of data taking, during the construction phase of the Observatory. The shower energy is only marginally affected by all the improvements in the detector modelling with an average increase of 1%.

Another improvement concerns the reconstruction of the longitudinal profiles of the showers. The measured dE/dX is fitted using a Gaisser-Hillas (GH) function, but when only part of the energy deposited is detected, the extrapolation of the GH profile beyond the range of the measurements can introduce significant uncertainties in the determination of the electromagnetic shower energy. This happens in the showers of low energy ($<10^{18}$ eV), for which only the flux of photons coming from the atmospheric depths around the profile maximum is bright enough to dominate over the night sky background. This problem has been solved by introducing a Gaussian constraint on the ratio $k = E_{\text{cal}}/(dE/dX)_{\text{max}}$ in the likelihood minimization procedure to fit the dE/dX profile, where $(dE/dX)_{\text{max}}$ is the energy deposited close to the maximum. The value of the constraint has been parameterised as a function of E_{cal} using an average of the QGSJetII-04 [5], EPOS-LHC [6], Sibyll2.3 [7] predictions with a mixed proton and iron composition and has been set to $k = (332.6 + 13.67 \log_{10} E_{\text{cal}}) \text{ g/cm}^2$. The uncertainty σ_k is calculated as the standard deviation of k , taking into account the different models used and the different composition simulated, and amounts to 29 g/cm^2 . Both the parameter k and σ_k are used in the likelihood function to constrain the GH fit. The new constraint improves the reconstruction of the low energy events, while its effect becomes negligible at energies $>10^{18}$ eV. A more precise determination of the shower axis and a better pixel selection is also performed leading to a decrease in the shower energy by less than 1%.

The estimation of the invisible energy (E_{inv}) has been also improved. Our previous estimate was derived from events detected simultaneously by the FD and SD detectors (hybrid events) with zenith angles below 60° [8]. In this work, E_{inv} is estimated from the SD events with zenith angles between 60° and 80° and with energies above 4×10^{18} eV [9]. The advantage of using these showers is that the electromagnetic component is largely absorbed by the atmosphere and the signal in the SD detectors is dominated by muons. The estimator of the muon content in the shower R_μ [10] is well correlated with E_{inv} through a power law function $E_{\text{inv}} = CR_\mu^\delta$. The coefficients C and δ have been determined using the QGSJetII-04 interaction model with a mixed composition of protons and iron nuclei ($C = 0.71 \times 10^{18}$ eV and $\delta = 0.96$) and then used to estimate E_{inv} from

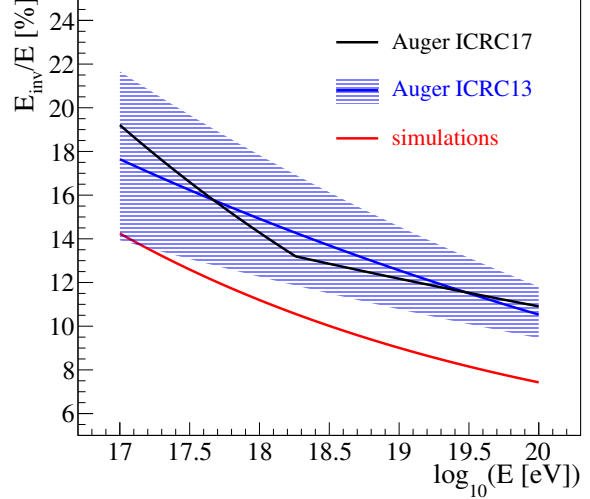


Figure 1: Ratio of the invisible energy to the total shower energy as a function of energy. The new Auger estimation (ICRC17) is compared with the previous parameterisation (ICRC13) [8] (the shaded band represents its systematic uncertainty) and with the one obtained by simulations.

the measurements of R_μ . In this way, most of the systematic uncertainties in E_{inv} related to the predictions of the muon size are avoided. To extend the invisible energy evaluation to events below 60° , E_{inv} is parameterised as a function of E_{cal} based on an analysis of the hybrid events. This parameterisation is valid only above 4×10^{18} eV where the R_μ measurements are performed. The extrapolation to lower energies is obtained taking into account the evolution with energy of the mean mass composition measured at the Auger Observatory [11]. This is done using model-based functions with parameters that have been fixed to match the measurements at higher energies, finally obtaining

$$E_{\text{inv}} = f_\theta a \left(\frac{E_{\text{cal}}}{10^{18} \text{ eV}} \right)^b \times 10^{18} \text{ eV} \quad ; E_{\text{cal}} \geq E_{\text{cal}}^A$$

$$E_{\text{inv}} = f_\theta a \left(\frac{E_{\text{cal}}^A}{10^{18} \text{ eV}} \right)^b \left(\frac{E_{\text{cal}}}{E_{\text{cal}}^A} \right)^{b_{\text{extr}}} \times 10^{18} \text{ eV} \quad ; E_{\text{cal}} < E_{\text{cal}}^A$$

where $a = 0.1633$, $b = 0.9463$, $b_{\text{extr}} = 0.8475$. $E_{\text{cal}}^A = 1.67 \times 10^{18}$ eV is the energy at which the measurements made at the Observatory show a break in the elongation rate of the slant depth of the shower maximum (X_{max}) and $f_\theta = 0.957$ is a factor that allows us to get an unbiased E_{inv} estimation for the majority of the events with zenith angles $\theta < 60^\circ$, given that the invisible energy tends to be larger for showers at larger zenith angles. The new E_{inv} estimation is shown in Fig. 1. It is fully consistent with our previous measurements, the only difference being the slope. The change arises from the improved sensitivity to the evolution of the mass composition with energy. The difference between our estimate and the one obtained using Monte Carlo (shown in Fig. 1 by the red line) is a consequence of the well-known deficit of muons in the simulations, demonstrated in various analyses of the Auger data [12, 13].

With the improved reconstruction presented in this paper, the cumulative energy shift of the FD energies is slightly energy dependent (larger at higher energies) and below 4%. The total uncertainty of 14% in the energy scale and the uncertainties estimated for each sector of the reconstruction [2] are not significantly affected by the improvements in the FD reconstruction discussed above.

3. The energy spectrum from SD 1500 events under 60 degrees

The energy estimator of the SD events with zenith angles below 60° is based on the lateral distribution of secondary particles on ground at an optimal distance from the shower core. For the SD 1500, the optimal distance is determined empirically and is 1000 m. The seasonal and diurnal variations in the atmospheric parameters affect the distribution of the charged particles on ground and therefore the energy estimators. Such effects are corrected by modelling the dependence of the signal on the atmospheric parameters [14]. The presence of the geomagnetic field is accounted for [15].

Because of the attenuation of the shower when crossing the atmosphere, $S(1000)$ decreases with zenith angle for a given energy. Assuming an isotropic flux of cosmic rays, this dependence can be removed by using the Constant Intensity Cut method [16] converting $S(1000)$ to the equivalent signal at median zenith angle of 38° (S_{38}).

The correlation between the SD energy estimator S_{38} and the calorimetric energy E_{FD} , measured by the FD, can be well described by a simple power law function $E_{FD} = A(S_{38})^B$ [17]. The parameters A and B are obtained through a fit on a sub-sample of high quality hybrid events in the energy range of full efficiency of the SD.

The events are selected if the detector with the highest signal is enclosed in an hexagon of 6 active stations and the exposure is obtained geometrically [18]. A first estimate of the flux (the raw flux) is then obtained.

Finite energy resolution and the consequent bin migration, are accounted for using a forward folding procedure. The result is an energy dependent factor $C(E)$, which is the correction to be applied to the raw flux $J_{\text{unfolded}} = C(E)J_{\text{raw}}$. The correction to the flux by this procedure is of the order of 8% at 3×10^{18} eV, 1% at 10^{19} eV and 10% at 10^{20} eV.

The SD 1500 vertical spectrum shown here includes data from January 2004 to December 2016, with a total exposure of $51,588 \text{ km}^2 \text{ sr yr}$ (roughly 20% higher than [19]). Several quality cuts are required: space–time coincidence of at least 3 neighboring triggering stations, containment of the events into an active hexagon and successful reconstruction of the lateral distribution of the events. Events detected in periods with problems in communication systems or in the vicinity of lightnings are excluded.

A total of 183,332 events with zenith angles below 60° and energies above 3×10^{18} eV is selected. The spectrum is shown in Fig. 2 where we clearly see the ankle around 5×10^{18} eV and a steepening at the highest energies.

The events collected in the SD 1500 vertical spectrum cover a wide range of declinations from -90° to 25° (more than 70% of the sky). This, along with the large cumulated exposure, can be exploited to investigate possible dependences of the spectrum on the declination. Data have been divided in two declination bands, $(-90^\circ, -15.7^\circ)$ (south) and $(-15.7^\circ, 25^\circ)$ (north) and the spectrum has been evaluated for each sample. This choice also allows us to compare the spectrum measured by the Pierre Auger Observatory with the one by Telescope Array in the common declination band [20].

We show in Fig. 3 (left) the spectrum divided in declination bands together with the overall one; the residuals with respect to the overall spectrum are plotted in the right panel.

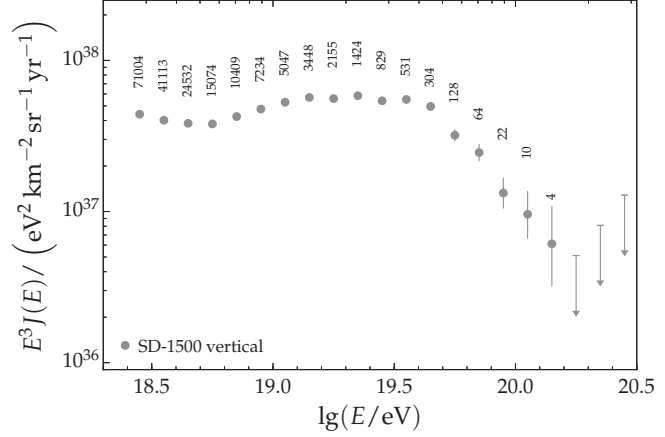


Figure 2: The unfolded spectrum for the SD 1500 vertical sample. The number of events is shown for each bin. The error bars represent statistical uncertainties. The upper limits correspond to the 84% C.L.

4. Other measurements of the energy spectrum

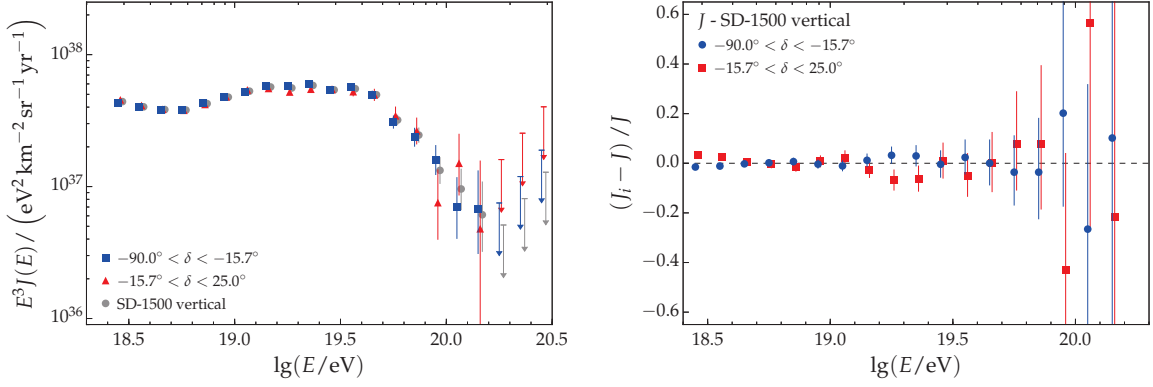


Figure 3: Left panel: The spectrum in declination bands (blue and red points), compared to the overall one (in gray). Right panel: the residual of the spectra in the various declination bands with respect to the overall spectrum.

Different data samples (see Tab. 1 for their parameters) can be used from the Pierre Auger Observatory to derive the energy spectrum. Similar approaches are used to obtain each of the spectra but there are minor differences. The SD 750 energy estimator is the signal measured at 450 m from the core, $S(450)$, corrected to a reference zenith angle of 35° , S_{35} . The SD 1500 events with zenith angles above 60° are reconstructed with an estimation of the relative muon content N_{19} with respect to a simulated proton shower with energy 10^{19} eV [10]. Finally, the hybrid sample is built from events detected by the FD simultaneously with at least one detector of the SD 1500. The hybrid exposure is calculated using a detailed Monte Carlo simulation [21].

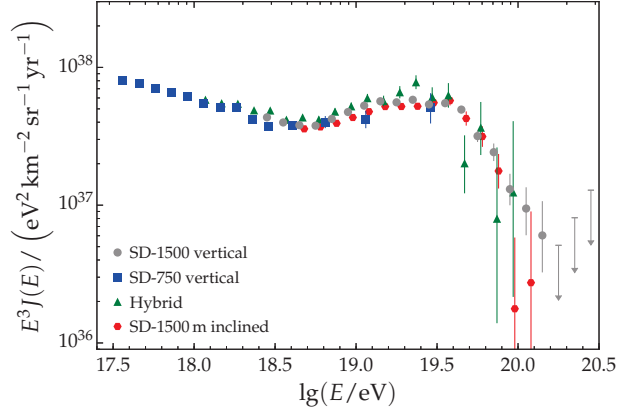


Figure 4: The energy spectra obtained with SD 1500 vertical, inclined, hybrid and SD 750 events are shown here. The systematic uncertainty on the energy scale, common to all of them, is 14%

The SD 1500 spectra obtained with events below and above 60° , the SD 750 and the hybrid spectra are shown together in Fig. 4.

All the spectra agree within the systematic uncertainties, which are dominated by the energy scale one (14%). The systematic uncertainties on the flux are between 5 and 10% and are responsible for the difference in normalization between the spectra visible in Fig.4.

A combined spectrum is obtained by means a maximum likelihood fit. The likelihood function is defined in such a way as to fit all the four data sets globally. The flux normalizations are used as additional constraints to obtain the flux scaling factors that match them: $(-0.8 \pm 0.2)\%$ for the SD 1500 vertical, $(-1 \pm 4)\%$ for the SD 750, $(5.4 \pm 0.7)\%$ for the SD 1500 horizontal and $(-6 \pm 2)\%$ for the hybrid.

	SD 1500 <60°	SD 1500 >60°	SD 750	Hybrid
Data taking period	Jan. 2004 – Dec. 2016	Jan. 2004 – Dec. 2016	Aug. 2008 – Dec. 2016	Jan. 2007 – Dec. 2015
Exposure [km ² sr yr]	51,588	15,121	228	1946 at 10 ¹⁹ eV
Number of events	183,332	19,602	87,402	11,680
Zenith angle range [°]	0 to 60	60 to 80	0 to 55	0 to 60
Energy threshold [eV]	3 × 10 ¹⁸	4 × 10 ¹⁸	3 × 10 ¹⁷	10 ¹⁸
Calibration parameters				
Number of events	2661	312	1276	
A [eV]	$(1.78 \pm 0.03) \times 10^{17}$	$(5.45 \pm 0.08) \times 10^{18}$	$(1.4 \pm 0.04) \times 10^{16}$	
B	1.042 ± 0.005	1.030 ± 0.018	1.000 ± 0.008	
Energy resolution [%]	15	17	13	

Table 1: The parameters of the data samples presented here together with the calibration parameters.

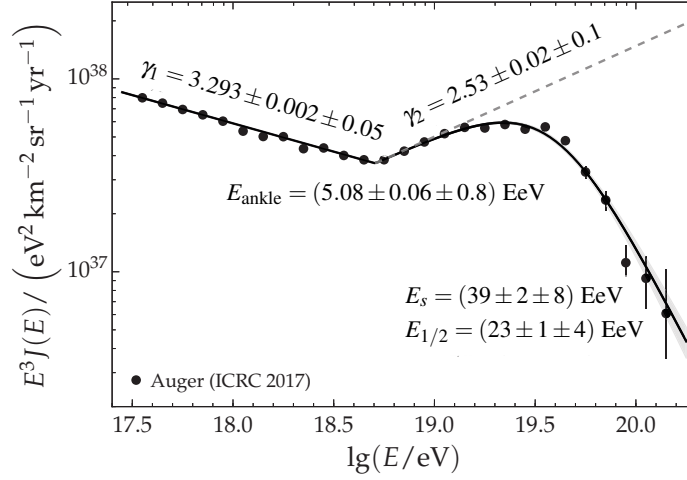


Figure 5: The combined spectrum and the fitting function with the fitting parameters.

To obtain the spectral parameters, the combined spectrum is fitted with the function

$$J_{\text{unf}}(E) = \begin{cases} J_0 \left(\frac{E}{E_{\text{ankle}}} \right)^{-\gamma_1} & ; E \leq E_{\text{ankle}} \\ J_0 \left(\frac{E}{E_{\text{ankle}}} \right)^{-\gamma_2} \left[1 + \left(\frac{E_{\text{ankle}}}{E_s} \right)^{\Delta\gamma} \right] \left[1 + \left(\frac{E}{E_s} \right)^{\Delta\gamma} \right]^{-1} & ; E > E_{\text{ankle}} \end{cases} \quad (4.1)$$

The spectrum, the fit and the optimized parameters are plotted in Fig. 5. An ankle is found at $E_{\text{ankle}} = (5.08 \pm 0.06(\text{stat.}) \pm 0.8(\text{syst.})) \times 10^{18}$ eV, while the suppression is at $E_s = (3.9 \pm 0.2(\text{stat.}) \pm 0.8(\text{syst.})) \times 10^{19}$ eV. The energy $E_{1/2}$ at which the integral spectrum drops by a factor of two below what would be the expected with no steepening is $E_{1/2} = (2.26 \pm 0.08(\text{stat.}) \pm 0.4(\text{syst.})) \times 10^{19}$ eV. The spectral indexes are: $\gamma_1 = 3.293 \pm 0.002(\text{stat.}) \pm 0.05(\text{syst.})$, $\gamma_2 = 2.53 \pm 0.02(\text{stat.}) \pm 0.1(\text{syst.})$ while $\Delta\gamma = 2.5 \pm 0.1(\text{stat.}) \pm 0.4(\text{syst.})$.

5. Summary

We have presented an update of the energy spectrum above 3×10^{17} eV as obtained using the Pierre Auger Observatory. An improved FD reconstruction caused an increase in the FD energy of less than 4%, while the systematic uncertainties previously estimated by the Auger Collaboration

are confirmed. The SD 1500 vertical spectrum has been obtained with unprecedented precision based on an exposure of more than $51,000 \text{ km}^2 \text{ sr yr}$. A study of the declination dependence of the spectrum showed no significant north–south asymmetry.

The combined spectrum from four different data sets has been derived using data collected by the Pierre Auger Observatory over more than 10 years (cumulating $67,000 \text{ km}^2 \text{ sr yr}$ of exposure). The measured cosmic ray flux is well described by a broken power law plus a smooth suppression at the highest energies. The dominant systematic uncertainty stems from the overall uncertainty in the energy scale of 14%. The obtained spectral parameters are in good agreement with those previously shown [19].

References

- [1] The Pierre Auger Collaboration, *Nucl. Instrum. Meth. A* 798 (2015) 172.
- [2] V. Verzi for the Pierre Auger Collaboration, *Proc. 33th ICRC 2013*, Rio de Janeiro, Brazil [arXiv:1307.5059].
- [3] M. Malacari for the Pierre Auger Collaboration, *Proc. 35th ICRC 2017*, this conference.
- [4] B. Gookin, [doctoral thesis](#), Colorado State University (2015).
- [5] S. Ostapchenko, *Phys. Rev. D* 83 (2011) 014018.
- [6] T. Pierog, *Phys. Rev. C* 92 (2015) 034906.
- [7] F. Riehn, *Proc. 34th ICRC 2015*, The Hague, The Netherlands [arXiv:1510.00568].
- [8] M. Tueros for the Pierre Auger Collaboration, *Proc. 33th ICRC 2013*, Rio de Janeiro, Brazil [arXiv:1307.5059].
- [9] A. Mariuzzi for the Pierre Auger Collaboration, *Proc. Conference on Ultrahigh Energy Cosmic Rays*, Kyoto, Japan (2016), in press.
- [10] The Pierre Auger Collaboration, *JCAP* 08 (2014) 019.
- [11] A. Porcelli for the Pierre Auger Collaboration, *Proc. 34th ICRC 2015*, The Hague, The Netherlands, PoS(ICRC2015)420.
- [12] The Pierre Auger Collaboration, *Phys. Rev. D* 91, 032003 (2015).
- [13] The Pierre Auger Collaboration, *Phys. Rev. Lett.* 117 (2016) 192001.
- [14] The Pierre Auger Collaboration, *JINST* 12 (2017) P02006.
- [15] The Pierre Auger Collaboration, *JCAP11* (2011) 022.
- [16] J. Hersil *et al.*, *Phys. Rev. Lett.* 6 (1961) 22.
- [17] R. Pesce for the Pierre Auger Collaboration, *Proc. 32nd ICRC 2011*, Beijing, China, DOI:10.7529/ICRC2011/V02/1160.
- [18] The Pierre Auger Collaboration, *Nucl. Instrum. Meth. A* 613 (2010) 29.
- [19] I. Valiño for the Pierre Auger Collaboration, *Proc. 34th ICRC 2015*, The Hague, The Netherlands, PoS(ICRC2015)271.
- [20] D. Ivanov for the Pierre Auger and Telescope Array collaborations, *Proc. 35th ICRC 2017*, this conference.
- [21] The Pierre Auger Collaboration, *Astropart. Phys.* 34 (2011) 368.



A new method to determine the energy scale for high-energy cosmic rays using radio measurements at the Pierre Auger Observatory

Raphael Krause^{*a} for the Pierre Auger Collaboration^b

^a*III. Physikalisches Institut A, RWTH Aachen University, Aachen, Germany*

^b*Observatorio Pierre Auger, Av. San Martín Norte 304, 5613 Malargüe, Argentina*

E-mail: auger_spokespersons@fnal.gov

Full author list: http://www.auger.org/archive/authors_icrc_2017.html

Coherent radio signals in the MHz range are emitted from extensive air showers initiated by high-energy cosmic rays. Observing this emission enables precise measurement of the energy of the primary particle. Compared with those made with the well-established fluorescence technique, radio measurements are less dependent on atmospheric conditions, and thus offer the potential of energy determination with reduced systematic uncertainties. Combining these accurate measurements with absolute predictions of the radio signal by first-principle calculations based on classical electrodynamics then allows a determination of the cosmic-ray energy scale.

This approach is discussed in the context of the Auger Engineering Radio Array (AERA), sited at the Pierre Auger Observatory. More than 150 autonomous radio stations, covering about 17 km², are used to record radio emission in the 30 to 80 MHz band from showers produced by primary particles with energies of about 10¹⁸ eV.

The systematic uncertainties of the measurement using AERA are presented. The calibration of the antenna is identified as the dominant uncertainty. The antenna response was measured in a recent calibration campaign using a flying drone. To this end, an octocopter was used to place a calibrated source at any position above the array. The campaign results in an antenna calibration accuracy of about 10%.

*35th International Cosmic Ray Conference — ICRC2017
10–20 July, 2017
Bexco, Busan, Korea*

^{*}Speaker.

1. Introduction

Ultrahigh-energy cosmic rays (UHECRs) interact with the Earth's atmosphere and produce large numbers of secondary particles. Well-established detection techniques are stochastic measurements of the remaining secondary particles at ground level and direct detection of fluorescence light emitted from air molecules excited by the particle cascade. Both techniques provide information about the primary cosmic ray, e.g., the cosmic-ray energy. The primary cosmic-ray energy is an important observable for most analyses, as is the systematic uncertainty of the energy measurement. At the Pierre Auger Observatory [1] the fluorescence technique is used for the absolute energy calibration. 27 telescopes are used to reconstruct the primary cosmic-ray energy with a systematic uncertainty at the absolute scale of 14.3% [2]. Such measurements depend sensitively on atmospheric conditions, which requires extensive atmospheric monitoring efforts [1].

In recent years, measurement of radio emission from air showers in the megahertz (MHz) regime has become a complementary detection technique [5, 6]. The radio technique combines the reconstruction of the longitudinal and lateral shower profiles with a duty cycle close to 100% which allows for precise and accurate measurements, e.g., of the cosmic-ray energy. In the following, a new method to determine the cosmic-ray energy scale using the AERA detector [3, 4] is presented and its systematic uncertainties are discussed [7, 8, 9].

2. Radio Emission from Extensive Air Showers

The radio emission comes from accelerated charges in the Earth's atmosphere. Two mechanisms contribute to coherent radio emission from air showers, namely the geomagnetic effect and the time-varying negative charge excess in the shower front. The geomagnetic emission is induced by acceleration of charged particles in the Earth's magnetic field forming a signal polarized according to the Lorentz force [10]. The charge excess is due to the knock-out of electrons from air molecules and annihilation of positrons in the shower front forming a radially polarized signal [11]. The radio emission from air showers can be calculated from first principles using classical electrodynamics [12, 13, 14]. The emission originates purely from the well-understood electromagnetic part of the air shower. The contribution of muons deflected in the Earth's magnetic field is negligible due to their large mass. Thus, the theoretical aspect of radio measurements is on solid grounds [5].

3. The Auger Engineering Radio Array

The Auger Engineering Radio Array is located within the northwest corner of the Pierre Auger Observatory. More than 150 autonomous radio stations, deployed on a regular grid with different spacings, cover about 17 km² and are used to record radio emission in the 30 to 80 MHz band from showers produced by primary particles with energies of over 10¹⁷ eV. Each radio station consists of two perpendicularly oriented antennas which are aligned to magnetic north and east with a precision better than 1°. The read-out system of the radio station is located in an electronics box underneath the radio antenna. Together with a GPS antenna, a solar panel and a battery, the stations are autonomously operated 24 h each day. Two different kinds of antenna types are used at

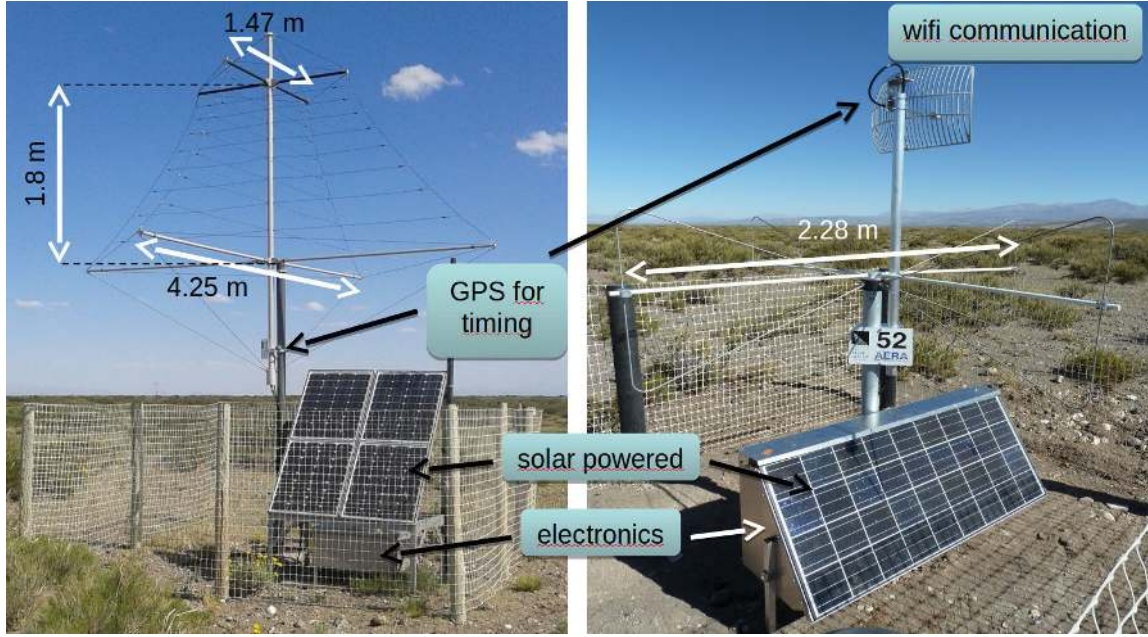


Figure 1: Photos of the LPDA (left) and butterfly (right) radio stations.

AERA: the log-periodic dipole antenna (LPDA) and the butterfly antenna [15]. Both station types are shown in Fig. 1. The following analysis is concentrated on the inner 24 radio stations with the smallest grid spacing of 144 m. These radio stations are equipped with LPDAs.

4. Calibration of the LPDA Radio Station

The relation between voltage U measured with each radio antenna and the incoming electric field \vec{E} is described by the vector effective length (VEL). The VEL is a complex quantity for the antenna sensitivity and group delay for different incoming directions and frequencies. In Fourier space the following relation holds:

$$U(\theta, \phi, f) = \vec{H}(\theta, \phi, f) \cdot \vec{E}(\theta, \phi, f) \quad (4.1)$$

where \vec{H} denotes the VEL depending on the arrival direction, described by spherical coordinates θ and ϕ , and the frequency f . The VEL \vec{H} is oriented in the plane perpendicular to the arrival direction of the signal and can be expressed as a superposition of a horizontal component H_ϕ and a component H_θ oriented perpendicular to H_ϕ which is called meridional component,

$$\vec{H} = H_\phi \vec{e}_\phi + H_\theta \vec{e}_\theta. \quad (4.2)$$

The VEL of the LPDA is determined by transmitting a defined signal from a calibrated signal source from different arrival directions and measuring the LPDA response. A signal with power P_t from a signal generator is injected to a calibrated transmitting antenna with known antenna characteristics G_t . Both are mounted underneath a GPS-controlled flying drone, a so-called octocopter. The signal P_r received at the LPDA is measured using a spectrum analyzer. To be unaffected by near-field effects, the calibration has to be done in the far-field region which is fulfilled to a reasonable

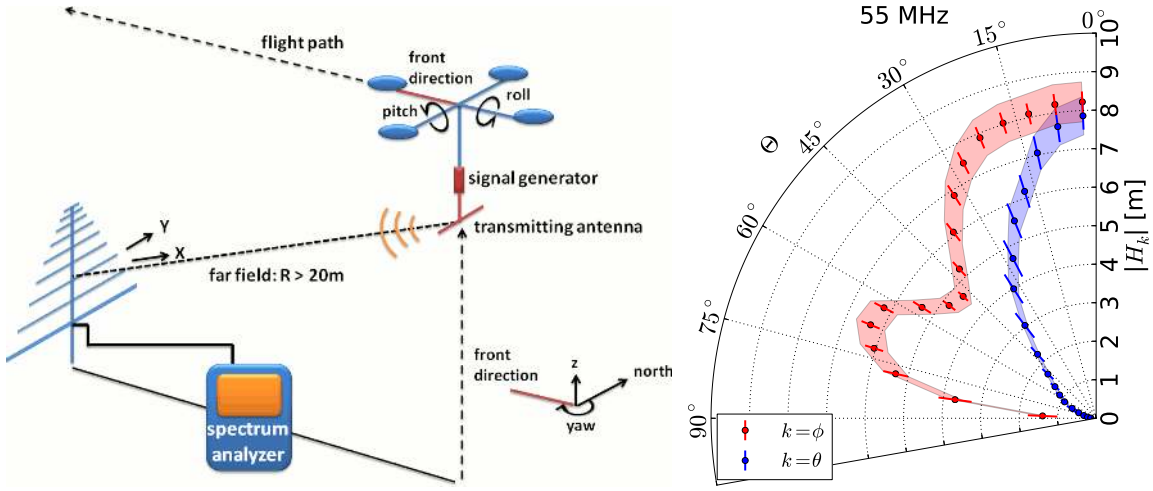


Figure 2: (left) LPDA calibration setup using an octocopter. The orientation of the octocopter is described by the yaw (twist of front measured from north in the mathematically negative direction) and the tilt by the pitch and the roll angles [16]. (right) Magnitude of horizontal and meridional LPDA VEL magnitudes (dots) and the flight-dependent uncertainties (error bars) as a function of the zenith angle in 5° bins at 55 MHz. The colored bands describe the corresponding constant systematic uncertainties [16].

approximation at a distance of $R > 2\lambda = 20$ m for the LPDA frequency range of 30 to 80 MHz. The full calibration setup is shown on the left side of Fig. 2.

The VEL magnitude is then expressed by

$$|H_k(\Phi, \Theta, f)| = \sqrt{\frac{4\pi Z_R}{Z_0}} R \sqrt{\frac{P_{T,k}(\Phi, \Theta, f)}{P_t(f) G_t(f)}}. \quad (4.3)$$

Here, f is the signal frequency, $Z_R = 50\Omega$ is the readout impedance, $Z_0 \approx 120\pi\Omega$ is the impedance of free space, the index $k = \phi$ or θ indicates the polarization depending on the orientation of the transmitting antenna [16], and Φ and Θ denote the azimuth and zenith angle of the arrival direction. On the right side of Fig. 2 the measured horizontal and meridional VEL magnitudes of the LPDA at 55 MHz are shown. The median overall uncertainty including statistical and systematic uncertainties is 7.4% for $|H_\phi|$ and 10.3% for $|H_\theta|$, respectively [16]. The uncertainty of the VEL magnitudes has a direct impact on the uncertainty of the cosmic-ray energy reconstruction. The energy deposit per area of the cosmic-ray radio pulse is called energy fluence. On the left side of Fig. 3 the systematic uncertainty of the square root of the energy fluence is shown which arises by propagating the uncertainties from the calibration to the electric-field reconstruction. On the right side the uncertainty is histogrammed. For zenith angles smaller than 60° (80°), the systematic uncertainty of the square root of the energy fluence is $8.8^{+2.1}_{-1.3}\%$ ($9.6^{+5.3}_{-1.9}\%$) in the median [16]. The square root of the energy fluence is shown because the energy fluence scales quadratically with the electric-field amplitude and the cosmic-ray energy (refer to the next section). Hence, the uncertainty of the square root of the energy fluence is the relevant uncertainty in most analyses.

5. Reconstruction of the Cosmic-Ray Energy

The cosmic-ray energy is reconstructed in the following way: from the measured voltage traces

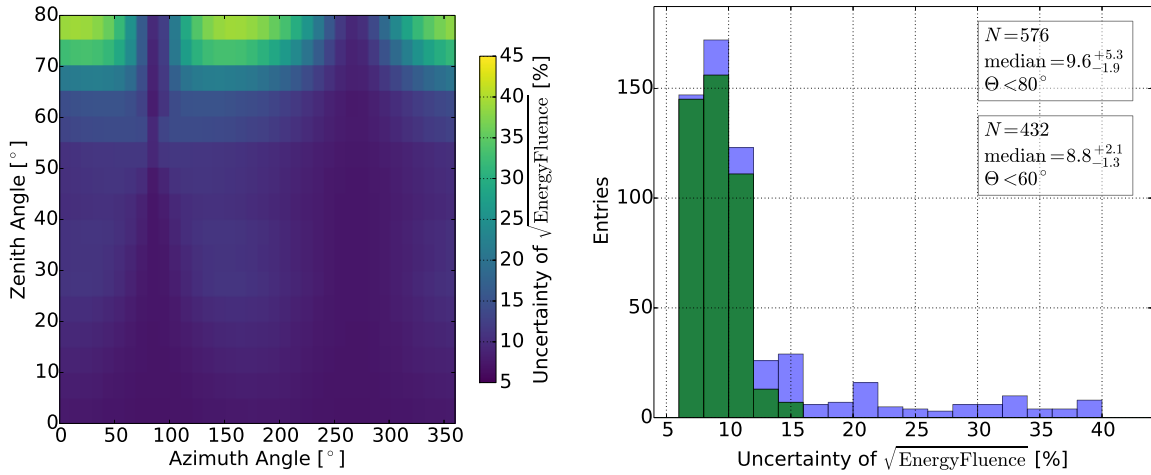


Figure 3: (left) Systematic uncertainty of the square root of the energy fluence for all arrival directions taking into account a signal polarization due to the dominant geomagnetic emission process. (right) Histogram of the systematic uncertainty of the square root of the energy fluence of signals with zenith angles smaller than 80° (blue) and of signals with zenith angles smaller than 60° (green) [16].

the incoming electric field is reconstructed using the antenna VEL. The energy fluence is calculated by a time integral of the Poynting vector of the reconstructed electric field in each station. A two-dimensional lateral distribution function (LDF) [17] is fitted, taking into account asymmetries resulting from the two emission processes. The LDF shape is best understood within the shower plane with one axis perpendicular to the shower direction \vec{v} and the Earth's magnetic field \vec{B} : $\vec{v} \times \vec{B}$, and the perpendicular axis: $\vec{v} \times (\vec{v} \times \vec{B})$. On the left side of Fig. 4, the energy fluence distribution of a measured cosmic ray and the corresponding LDF fit are presented. The radiation energy, which is the total amount of energy transferred from the primary cosmic ray into radio emission, is then obtained by integrating the LDF fit over the area. Then, the radiation energy is corrected for the geometric dependence of the geomagnetic emission by dividing by $\sin^2(\alpha)$ where α is the angle between \vec{v} and \vec{B} . On the right side of Fig. 4, the corrected radiation energies of 126 air showers are shown, measured with the LPDA radio stations at AERA and cross-calibrated with the well-understood data of the Pierre Auger Observatory. The observed radiation energy scales quadratically with the cosmic-ray energy. From the scatter around the calibration curve, the cosmic-ray energy resolution of AERA is determined to be 22%, improving to 17% for events with at least five stations with signal, which is of the same order of magnitude as the energy resolution of the Auger surface detector [2].

6. Independent Energy Scale Using AERA

In the previous section the measured radiation energy is calibrated using the information of the baseline detectors of the Pierre Auger Observatory. Instead, the energy calibration can be done by using the theoretical prediction of the radiation energy. The idea is illustrated on the left side of Fig. 5. The procedure to determine the radiation energy is divided into an experimental part, as explained in the previous section, and a theoretical part. The radio emission comes from accelerated charges in the Earth's atmosphere and originates from the well-understood electromagnetic part of

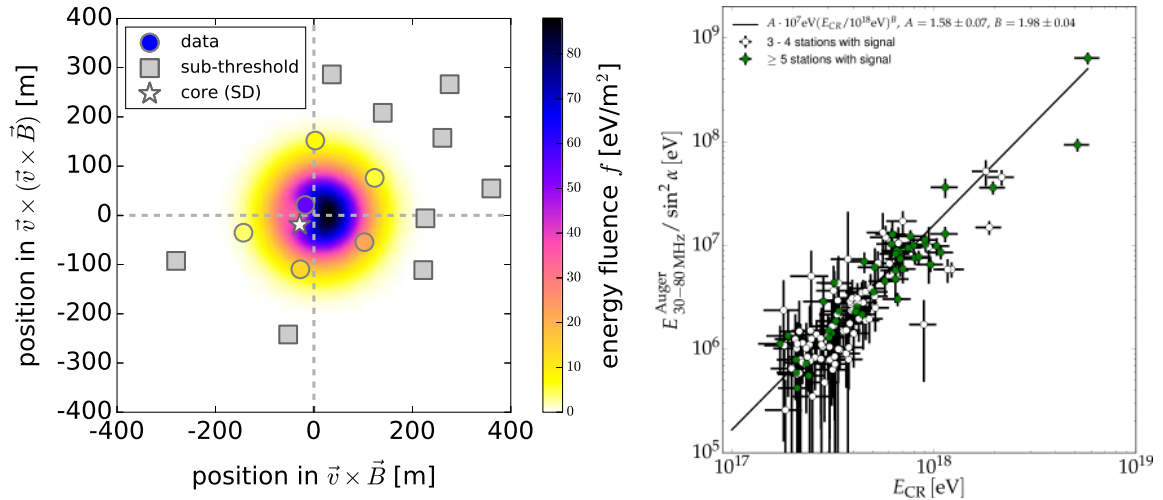


Figure 4: (left) Energy fluence for an extensive air shower with an energy of 4.4×10^{17} eV and a zenith angle of 25° measured with AERA (colored circles). The center indicates the shower core reconstructed with the radio data. The colored background indicates the two-dimensional LDF fit. The white star marks the shower core reconstructed using the surface detector data of the Pierre Auger Observatory [7, 8]. (right) The corrected radiation energy in relation to the cosmic-ray energy measured with the baseline detectors of the Pierre Auger Observatory. Events with 3 and 4 stations with signal are marked as white circles and in case of more than 5 stations with signal are marked as green circles [7, 8].

the air shower. As soon as the radio emission stops at the end of the air-shower development, the radiation energy stays constant because the Earth’s atmosphere is essentially transparent for radio waves in the VHF band. Thus, measurement and theoretical prediction of the radiation energy are directly comparable. For a detailed discussion about the theoretical part refer to [14]. In the following, the CoREAS simulation code [13] is used to simulate air showers and their radio emission. CoREAS is a microscopic simulation code, where the radiation of each single particle is calculated by first principles of classical electrodynamics, and then superposed to the full radio emission. As the emission originates from the electromagnetic part of the air shower, the radiation energy correlates best with the energy of the electromagnetic cascade. In addition to the geometric dependence of the geomagnetic emission process, a second dependence on the air density at the shower maximum was identified and parametrized. This corrected radiation energy is presented as a function of the energy in the electromagnetic cascade on the right side of Fig. 5. A quadratic relation with a scatter of less than 3% is observed [14].

To obtain the cosmic-ray energy from the electromagnetic shower energy, the invisible energy needs to be taken into account, e.g., neutrinos and high-energy muons do not contribute to the radiation energy. This can be done using a parametrization that was obtained from measurements [18].

In the following, the currently estimated systematic uncertainties with respect to the cosmic-ray energy are briefly discussed [9]. The uncertainty from the antenna calibration of the radio detector is identified as the dominant uncertainty of the cosmic-ray energy measurement with AERA.

Experimental uncertainties The experimental uncertainties involve the systematic uncertainties of the radio detector, the analog signal chain from the radio antenna to the digitizer and the fitted

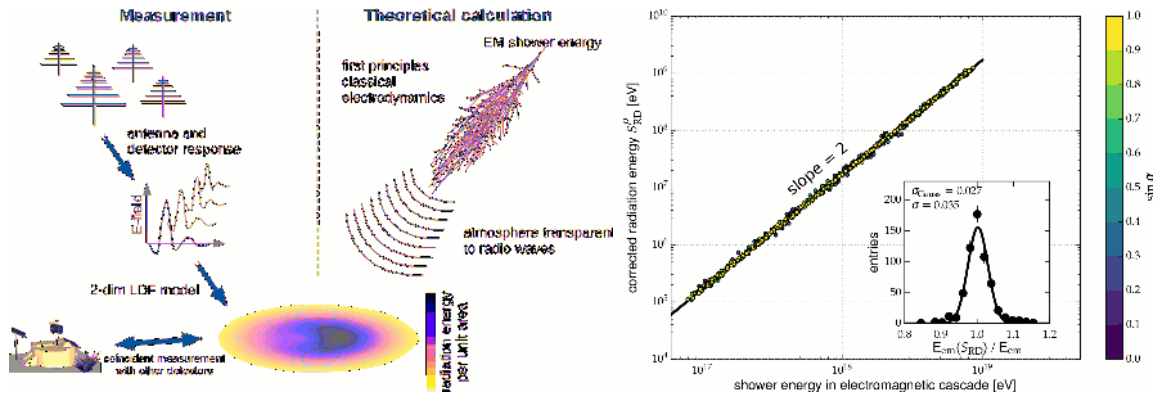


Figure 5: (left) Idea of the determination of the energy scale from first-principles calculations using radio measurements [9]. (right) The corrected radiation energy estimator vs. the energy in the electromagnetic cascade from CoREAS simulations. Adapted from [14].

LDF model. With a recent calibration campaign the systematic uncertainty was lowered to about 10% as described in section 4. For more details refer to [16]. The analog signal chain is measured with a systematic uncertainty below 1%. The systematic uncertainty of the LDF model contributes about 2.5% [8].

Uncertainties of the relation between radiation energy and electromagnetic shower energy

The calculation of the radio emission is purely based on classical electrodynamics. Therefore, it has no free parameters and thus no systematic uncertainty. Nevertheless, the modeling of the electromagnetic air-shower component and approximations made in the simulation code result in further uncertainties. The influence of all known approximations have been checked and are small compared to the experimental uncertainties [9]. Additional theoretical uncertainties cannot be excluded but the form of the measured radio pulse and the measured signal distribution on ground are in good agreement with the CoREAS simulation, e.g., refer to [19]. Thus, uncertainties of the relation between radiation energy and electromagnetic shower energy are expected to be small compared to the experimental uncertainties.

Environmental uncertainties Changing atmospheric conditions, i.e., changing density profiles and varying refractivity, result in a scatter of about 1% during the course of the year which is taken as estimated uncertainty [9]. Furthermore, changing ground conditions, e.g., ground permittivity and ground conductivity, change the reflectivity of the ground and thereby directly impact the radio detector directional sensitivity. An LPDA simulation study reveals an average change of the antenna response pattern of 1% for different realistic ground conditions at the AERA site [16].

Invisible energy correction The systematic uncertainty of the parametrization to obtain the cosmic-ray energy from the electromagnetic shower energy was determined to be 3% at 10^{18} eV [18].

7. Conclusion

The Auger Engineering Radio Array is the largest cosmic-ray radio detector worldwide and enables the measurement of the radio emission of extensive air showers. This provides information,

e.g., about the cosmic-ray energy. Well-calibrated radio stations enable both precise and accurate measurements of the radio signal. In a recent calibration campaign, the magnitude of the horizontal and meridional VEL of the LPDA radio stations has been measured. The systematic uncertainty of the LPDA VEL propagates to a systematic uncertainty of 8.8% of the square root of the energy fluence. The radiation energies of 126 air showers have been measured and compared with the cosmic-ray energies measured with the baseline detectors of the Pierre Auger Observatory. A quadratic relation between radiation energy and cosmic-ray energy is found. AERA obtains a cosmic-ray energy resolution of 17% for events with more than 5 radio stations with signal.

Furthermore, a new method to independently determine the cosmic-ray energy scale using radio is presented combining radio measurements of the radiation energy with theoretical calculations from first principles using classical electrodynamics. The systematic uncertainties of the cosmic-ray energy scale using AERA are briefly discussed. The uncertainty due to the antenna calibration is identified as the dominant one. Finally, the systematic uncertainty of the cosmic-ray energy scale using AERA is expected to be at the same level as the systematic uncertainty of the cosmic-ray energy scale using the fluorescence detector of the Pierre Auger Observatory.

References

- [1] A. Aab *et al.* (Pierre Auger Collaboration), Nucl. Instrum. Meth. A **798** (2015) 172–213.
- [2] V. Verzi *for the Pierre Auger Collaboration*, Proc. 33rd ICRC, Rio de Janeiro, Brazil (2013) 928.
- [3] J. Schulz *for the Pierre Auger Collaboration*, Proc. 34th ICRC, The Hague, The Netherlands (2015) PoS (ICRC2015) 615.
- [4] E. Holt *for the Pierre Auger Collaboration*, Proc. 35th ICRC, Busan, South Korea (2017).
- [5] T. Huege, Phys. Rep. **620** (2016) 1–52.
- [6] F.G. Schröder, Prog. Part. Nucl. Phys. **93** (2017) 1–68.
- [7] A. Aab *et al.* (Pierre Auger Collaboration), Phys. Rev. Lett. **116** (2016) 241101.
- [8] A. Aab *et al.* (Pierre Auger Collaboration), Phys. Rev. D **93** (2016) 122005.
- [9] C. Glaser, PhD thesis, RWTH Aachen University (2017).
- [10] F.D. Kahn and I. Lerche, Proc. R. Soc. Lon. Ser.-A **289** (1966) 206–213.
- [11] G. Askaryan, Soviet Phys. JETP Lett. (USSR) **14** (1962) 441.
- [12] J. Alvarez-Muñiz, W.R. Carvalho, and E. Zas, Astropart. Phys. **35** (2012) 325–341.
- [13] T. Huege, M. Ludwig, and C.W. James, Proc. AIP Conf. **1535** (2013) 128–132.
- [14] C. Glaser, M. Erdmann, J.R. Hörandel, T. Huege, and J. Schulz, JCAP **09** (2016) 024.
- [15] P. Abreu *et al.* (Pierre Auger Collaboration), JINST **7** (2012) P10011.
- [16] A. Aab *et al.* (Pierre Auger Collaboration), submitted to JINST (2017).
- [17] A. Nelles *et al.*, Astropart. Phys. **60** (2015) 13–24.
- [18] M.J. Tueros *for the Pierre Auger Collaboration*, Proc. 33rd ICRC, Rio de Janeiro, Brazil (2013) 705.
- [19] S. Buitink *et al.*, Nature **531** (2016) 70–73.

2

Arrival Directions and Anisotropies





Dipolar anisotropy of cosmic rays above 8 EeV

Oscar Taborda^{*a} for the Pierre Auger Collaboration^b

^a*Centro Atómico Bariloche and Instituto Balseiro (CNEA-UNCuyo-CONICET), San Carlos de Bariloche, Argentina*

^b*Observatorio Pierre Auger, Av. San Martín Norte 304, 5613 Malargüe, Argentina*

E-mail: auger_spokespersons@fnal.gov

Full author list: http://www.auger.org/archive/authors_icrc_2017.html

We report on the search of large-scale anisotropies in the flux of cosmic rays with energies above 4 EeV observed using data recorded at the Pierre Auger Observatory with more than 12 years of operation. We consider events with zenith angles up to 80° , so that 85% of the sky is observed, and for energies in excess of 4 EeV, for which the Observatory is fully efficient. Analyses of the first harmonic in the right ascension and azimuth distributions are sensitive to a dipolar component perpendicular and parallel to the Earth's rotation axis, respectively. These studies are performed in the two energy bins $4 \text{ EeV} < E < 8 \text{ EeV}$ and $E \geq 8 \text{ EeV}$.

*35th International Cosmic Ray Conference — ICRC2017
12–20 July, 2017
Bexco, Busan, Korea*

^{*}Speaker.

1. Introduction

The origin and nature of the ultra-high energy cosmic rays is still one of the important open problems in physics and astrophysics. Besides the measurement of the cosmic ray spectrum, whose features may indicate the transitions between different propagation regimes or source populations, and the determination of the identity of the particles to know which kind of nuclei contribute to the fluxes, also the analysis of the arrival direction distribution provides a crucial handle for these studies. In particular, the identification of the cosmic ray sources should help to understand how these particles, which have the highest energies observed in nature, are produced and how they do propagate up to us.

The Pierre Auger Observatory [1] is located in Malargüe, Argentina, at a latitude of -35.2° . It is operated as a hybrid system consisting of an array of 1600 water-Cherenkov detectors spanning an area of about 3000 km^2 on a triangular grid with 1.5 km spacing. A smaller denser sub-array covers about 1% of the area, but it is not used in this analysis. It also has four buildings with 27 telescopes overlooking the array to observe the fluorescence light emitted by the nitrogen molecules in the air that were excited by a shower of particles that crossed the atmosphere. The surface detectors sample the lateral profile of the showers at ground level while the fluorescence telescopes measure its longitudinal profile in the atmosphere.

The Auger Observatory has reported studies of the large-scale distribution of arrival directions in right ascension [2, 3] and in both declination and right ascension [4, 5], from the analysis of events with zenith angles smaller than 60° . These analyses provided hints of a change in the phase of the first harmonic in right ascension taking place at few EeV energies. Results including also events with zenith angles between 60° and 80° , and hence increasing the sky coverage from 71% to 85%, showed indications at the 4σ level of a non-vanishing amplitude in the first harmonic in right ascension for events with energies above 8 EeV [6]. Here we present an update of these studies which includes ~ 2.6 additional years of data with respect to [6] and also consider a less restrictive trigger selection of events, leading to an increase in statistics of 62%.

2. Data set

In this work we consider the data recorded at the Pierre Auger Observatory from 1st January 2004 to 31st August 2016, excluding periods of instability in the data acquisition process. The collected exposure is about $76,800 \text{ km}^2 \text{ sr yr}$. The events are reconstructed by fitting the signals and arrival times associated with the secondary particles of the air showers reaching the water-Cherenkov detectors of the surface array. The events with zenith angles $\theta \leq 60^\circ$, referred to as vertical events, have a different reconstruction and separate calibration from those having $60^\circ < \theta < 80^\circ$, referred to as inclined events. We focus on events with energies in excess of 4 EeV, for which the array is fully efficient for zenith angles $\theta < 80^\circ$. This allows us to get rid of all systematic modulations related to trigger inefficiencies and permits the inclusion of the inclined events which are reliably reconstructed above this energy.

The estimation of the energy in the vertical sample is based on the shower size at 1000 m from the shower core. The steepness of the energy spectrum of cosmic rays implies that even small variations in this energy estimator as a function of the angular coordinates or of time, can

induce significant systematic modulations in the counting rate of events above a given signal. The variations of the atmospheric conditions are one of the sources of these distortions. In particular, the air density affects the lateral profile of the electromagnetic component of the showers while the pressure determines the depth along the longitudinal profile at which the shower is observed at ground. The bias in the modulation of the first harmonic arising from the weather conditions could be up to $\pm 1.7\%$ in solar frequency, although it is smaller in sidereal frequency because it is averaged after many years of observation. These effects are taken into account by correcting the energy estimator [7]. Another effect that influences the shower size at 1000 m is the deflection of the shower particles in the geomagnetic field. This breaks the circular symmetry of the shower around its axis and leads to a spurious azimuthal modulation of about $\sim 0.7\%$, that is corrected following [8].

For inclined showers the muonic component is dominant as the electromagnetic one is attenuated because the amount of atmosphere traversed by a shower is higher for larger zenith angles. This leads to a negligible dependence on the atmospheric effects while the effects induced by the geomagnetic field are already taken into account at the reconstruction stage of these events [9].

We consider here the energy bins $4\text{EeV} < E < 8\text{EeV}$ and $E \geq 8\text{EeV}$, which are included in preceding anisotropy searches [2–6]. The median energies in these bins are 5.0 EeV and 11.5 EeV.

Previous large-scale anisotropy studies [2,4,6], some of which extended also to lower energies, considered only events passing a strict trigger condition in which the station with the highest signal is surrounded by six detectors in operation at the time of detection. This quality cut is mandatory when working with lower energy events to guarantee a reliable reconstruction of its energy and arrival direction. Nevertheless, in the present study we consider showers with energies above 4 EeV. A fraction of 99.2% of these showers triggered four or more detectors (this fraction is 99.9% above 8 EeV), allowing also the use of events with only five of its closest neighbour detectors working at the time of the event.

To assess the reliability of showers passing the relaxed cuts we re-analysed a set of events fulfilling the tight trigger condition after removing one of its six neighbouring stations. The reconstructed directions differ on average by 0.4° for $4\text{EeV} < E < 8\text{EeV}$ and 0.3° for $E \geq 8\text{EeV}$, while for the energy reconstruction the differences are on average 0.3% and 0.2%, respectively. The dispersion in the energy assignments obtained with the two reconstructions is about 8% in the lower energy bin and $\sim 5\%$ above 8 EeV. This is well below the statistical uncertainties in the energy determination, which is better than 16% above 4 EeV and 12% above 10 EeV. The systematic uncertainty on the absolute energy scale is 14% [10].

Relaxing the trigger condition increases the total number of events by 18.7%, in agreement with what would be expected from the associated increase in exposure of 18.5%.

3. Analysis method

A standard approach to study the distribution at large angular scales of the arrival directions of cosmic rays is to perform a classical harmonic analysis [11] generalized by introducing weights. The weights take into account possible small modulations in the coverage of the array arising from the variations in its operating size as a function of time and for the effects of a net tilt of the array surface [6]. We performed two harmonic analyses over the distributions in right ascension, α , and

azimuth, ϕ , which are sensitive to the component of a dipole orthogonal and parallel to the Earth's rotation axis, respectively. An advantage of this combined harmonic analysis is allowing us to join the vertical and inclined samples considered here without introducing a spurious large-scale modulation which could arise from differences in the energy calibration of the two samples.

The two Fourier amplitudes of the harmonic modulation are

$$\alpha^x = \frac{2}{\mathcal{N}} \sum_{i=1}^N w_i \cos x_i, \quad b^x = \frac{2}{\mathcal{N}} \sum_{i=1}^N w_i \sin x_i, \quad (3.1)$$

with $x = \alpha$ or ϕ . The sums run over the number N of events in the considered energy ranges and α_i (ϕ_i) is the right ascension (azimuth) of the i -th event. The weights are given by $w_i = [\Delta N_{\text{cell}}(\alpha_0^i)(1 + 0.003 \tan \theta_i \cos(\phi_i + \phi_{\text{tilt}}))]^{-1}$ where the first factor $\Delta N_{\text{cell}}(\alpha_0^i)$ is the relative variation of the total number of active cells at the sidereal time α_0^i of the i th-event. The number of active cells is the number of active detectors having at least five of their six neighbours working. The second factor accounts for a small average in the tilt of the array of about 0.2° towards $\phi_{\text{tilt}} = -30^\circ$. The normalization factor is $\mathcal{N} = \sum_{i=1}^N w_i$.

3.1 Harmonic analysis in right ascension

From the coefficients in eq. (3.1) we determine, for $x = \alpha$, the corresponding amplitude and phase of the first harmonic in right ascension as

$$r^\alpha = \sqrt{(a^\alpha)^2 + (b^\alpha)^2}, \quad \tan \varphi^\alpha = \frac{b^\alpha}{a^\alpha}. \quad (3.2)$$

The statistical uncertainties for the Rayleigh coefficients are given by $\sqrt{2/\mathcal{N}}$, while the 68% confidence interval of the marginalized probability distribution of the amplitude and phase is calculated. The probability that an amplitude larger than the one observed could arise from fluctuations in an isotropic distribution (p -value) is given by $P(\geq r^\alpha) = \exp(-\mathcal{N}(r^\alpha)^2/4)$.

3.2 Reconstruction of the dipole

The combination of first harmonic analyses in right ascension and azimuth distributions allows the reconstruction of the three components of a dipole. The right ascension distribution, introduced in the previous section, is sensitive to a dipolar component along the equatorial plane. In turn, the distribution in the azimuth angle, particularly the b^ϕ coefficient, reflects the presence of a North-South dipole.

The amplitude of the dipole component in the equatorial plane d_\perp , that along the rotation axis of the Earth d_z and the right ascension and declination of the dipole's direction (α_d, δ_d), assuming that the dipolar pattern dominates and hence neglecting higher multipoles, can be estimated as

$$\begin{aligned} d_\perp &\simeq \frac{r^\alpha}{\langle \cos \delta \rangle}, \\ d_z &\simeq \frac{b^\phi}{\cos \ell_{\text{obs}} \langle \sin \theta \rangle}, \\ \alpha_d &= \varphi^\alpha, \\ \delta_d &= \arctan \left(\frac{d_z}{d_\perp} \right), \end{aligned} \quad (3.3)$$

where $\langle \cos \delta \rangle = 0.78$ is the average cosine of the declinations of the events, $\langle \sin \theta \rangle = 0.65$ the average sine of the zenith of the events and $\ell_{\text{obs}} \simeq -35.2^\circ$ the average latitude of the Observatory.

4. Discussion and conclusions

Results and discussion will be presented at the conference.

References

- [1] The Pierre Auger Collaboration, *Nucl. Instrum. Meth. A* **798** (2015) 172.
- [2] The Pierre Auger Collaboration, *Astropart. Phys.* **34** (2011) 627.
- [3] I. Sidelnik, for The Pierre Auger Collaboration, in proceedings of *33rd Int. Cosmic Ray Conf.*, Rio de Janeiro, Brasil (2013).
- [4] The Pierre Auger Collaboration, *Astrophys. J. Lett.* **762** (2013) L13; The Pierre Auger Collaboration, *Astrophys. J. Supplement* **203** (2012) 34.
- [5] R.M. de Almeida, for The Pierre Auger Collaboration, in Proceedings of *33rd Int. Cosmic Ray Conf.*, Rio de Janeiro, Brasil (2013).
- [6] The Pierre Auger Collaboration, *Astrophys. J.* **802** (2015) 111.
- [7] The Pierre Auger Collaboration, *JINST* **12** (2017) P02006.
- [8] The Pierre Auger Collaboration, *JCAP* **11** (2011) 022.
- [9] The Pierre Auger Collaboration, *JCAP* **08** (2014) 019.
- [10] V. Verzi, for The Pierre Auger Collaboration, in Proceedings of *33rd Int. Cosmic Ray Conf.*, Rio de Janeiro, Brasil (2013).
- [11] J. Linsley, *Phys. Rev. Lett.* **16** (1975) 748.



Arrival directions of the highest-energy cosmic rays detected by the Pierre Auger Observatory

Ugo Giaccari^{*a} for the Pierre Auger Collaboration^b

^a*Instituto de Física, Universidade Federal do Rio de Janeiro, Brazil*

now at Centro Brasileiro de Pesquisas Físicas, Rio de Janeiro, Brazil

^b*Observatorio Pierre Auger, Av. San Martín Norte 304, 5613 Malargüe, Argentina*

E-mail: auger_spokespersons@fnal.gov

Full author list: http://www.auger.org/archive/authors_icrc_2017.html

We present the analysis of the arrival direction distribution of the highest-energy cosmic rays detected at the Pierre Auger Observatory. The data collected to date, with a total exposure of approximately $90,000 \text{ km}^2 \text{ sr yr}$, allow us a precise characterisation of the patterns in the arrival direction distribution.

An update of the two largest departures from isotropy already reported is discussed here. The region of the sky close to the direction of Centaurus A is analyzed and the correlation with the positions of the most luminous AGNs detected by *Swift*-BAT is investigated.

We also examine the correlation of our highest energy events with two populations of extragalactic sources of gamma rays, namely star-forming galaxies and AGNs motivated by the observations of the *Fermi*-LAT satellite. In this new search, a likelihood analysis is adopted which gives weights to the individual sources in proportion to their fluxes. The same flux-weighted search for an angular correlation with the extragalactic sources listed in the *Swift*-BAT catalog is also performed.

The significances of the excesses around Centaurus A and the most luminous AGNs detected by *Swift*-BAT have increased and reached to the 3σ level approximately. An excess at 2.7σ level is found for the gamma-ray AGNs while for the star-forming galaxies there is a 4σ deviation from isotropy for energies greater than 39 EeV at an intermediate angular scale of 13° .

35th International Cosmic Ray Conference — ICRC2017

10–20 July, 2017

Bexco, Busan, Korea

^{*}Speaker.

1. Introduction

The identification of the astrophysical objects able to accelerate ultra high-energy cosmic rays (UHECRs) is a longstanding question in astrophysics. Patterns in the arrival direction distribution of UHECRs over the celestial sphere could provide significant clues for clarifying the origin of these particles.

Cosmic rays with energies above the steepening of the energy spectrum at $\sim 4 \times 10^{19}$ eV [1], give us information about UHECR sources within the local Universe up to ~ 200 to 300 Mpc. Particles in this energy range reach us from very few hundred Mpc due to the energy losses in the interactions with the cosmic microwave and infrared backgrounds. With the isotropic distant sources removed at energies above the aforementioned steepening in the spectrum, it is feasible to detect anisotropies in the arrival direction distribution reflecting the inhomogeneities in the distribution of the local sources.

This paper deals with the study of the arrival directions of the highest-energy cosmic rays detected at the Pierre Auger Observatory. Despite the tiny flux of particles in this energy range, the huge collecting area of the Observatory together with its ability to detect air showers up to 80° in zenith offer the possibility to study the arrival direction distribution of the UHECRs with unprecedented statistics.

At the Pierre Auger Observatory, data collected through 31 March 2014 have been subjected to different searches for anisotropies for different energy thresholds between 40 and 80 EeV and within different angular windows, between 1° and 30° [2]. Searches for intrinsic anisotropies have been performed, as well as cross-correlations with the directions of candidate UHECR accelerators. Out of all the performed searches the two largest deviations from isotropy, both with post-trial probability $\sim 1.4 \times 10^{-2}$, have been found for an energy threshold of 58 EeV when looking into the region of the sky within 15° from the location of Centaurus A (Cen A) and when considering the cross-correlation with the most luminous active galactic nuclei (AGNs) detected in X-ray from the *Swift*-BAT mission [3].

In this report we first update these two searches with respect to that already reported using the conventional correlation methods [2]. We also discuss the correlation of our highest energy events with two populations of extragalactic sources of gamma rays: AGNs and star-forming galaxies motivated by the observations of the *Fermi*-LAT satellite.

With these two classes of astrophysical objects we search not only for angular correlations with the directions of the objects on the sky but also with their flux through appropriate weights. The same analysis technique, for an angular and flux correlation, is also discussed for the extragalactic objects listed in the *Swift*-BAT catalog.

All the searches presented here are *a posteriori* explorations. Numerous studies have been performed in the past with Auger data within and outside the collaboration. This makes difficult to evaluate a proper penalty factor for all the previous searches.

2. The Observatory and the datasets

The Pierre Auger Observatory [4] is the world's largest cosmic ray observatory at energies above 10^{17} eV. It is located in the Province of Mendoza, Argentina. The site is placed at an average

latitude of $\sim 35.2^\circ$ S and a mean altitude of ~ 1400 m above the sea level. The Observatory is a hybrid detector combining the information from a large surface detector array (SD) and a fluorescence detector (FD). The SD, spread over an area of 3000 km^2 , is composed of a baseline array of 1600 water-Cherenkov detectors separated by 1500 m in a triangular grid, and a smaller nested array of 49 additional detectors spaced by 750 m covering an area of 24 km^2 . The FD consists of 27 telescopes at five peripheral buildings viewing the atmosphere over the array. The combination of the two detection techniques provides a unique handle for precision energy calibration and the understanding of reconstruction uncertainties of energy of the cosmic rays. The FD operates only on clear, moonless nights, so its duty cycle is about 15%. On the other hand, the SD has a duty cycle close to 100%. The unique characteristics of the SD, the huge collecting area, the sensitivity to detect showers up to 80° and the long data collection period, provide the accumulation of a large body of data for anisotropy studies.

In this analysis we consider showers observed with the SD between the 1 January 2004 and the 30 April 2017 with zenith angle $\theta \leq 80^\circ$ and reconstructed energy $E \geq 40 \text{ EeV}$. The event reconstruction procedure depends on the zenith angle of the air shower. Events with zenith angle $\theta \leq 60^\circ$ are labeled as *vertical*, while those with $60^\circ < \theta < 80^\circ$ are labeled as *inclined* ones. A detailed description of the data selection criteria can be found in [2]. The angular uncertainty is better than 1° above 10 EeV [5] and the final energy estimation uses the cross-calibration with the FD providing a quasi-calorimetric measurement. The statistical uncertainty in the energy determination is better than 12% [6] above 10 EeV and the systematic uncertainty in the absolute energy scale is 14% [7]. In this energy range the SD is fully efficient, the total exposure amounts to 71,070 and $18,650 \text{ km}^2 \text{ sr yr}$ for the vertical and inclined samples respectively. The directional exposure relies on geometrical considerations and can be expressed analytically. Unfolding factor corrections as derived in the framework of the energy spectrum studies [8] are included in the exposures of vertical and inclined events, to account for the different migration effects due to the different energy resolutions of each data stream.

3. Update of the correlation studies with Centaurus A and with the most luminous AGNs of the *Swift*-BAT catalog

Among all the searches performed so far [2] the two most important deviations from isotropy have been found looking in the direction of Cen A and when considering the most luminous AGNs of the *Swift*-BAT catalog. In this section we update these two analyses. The search for excess around Cen A is performed counting the number of observed (n_{obs}) and expected (n_{exp}) events from an isotropic flux within circles of radius ψ centered around this AGN position above a given energy threshold E_{th} . Then we computed the cumulative binomial probability P to measure n_{obs} or more events given n_{exp} . For quantifying the cross-correlation between our highest energy events and the most luminous AGNs of the *Swift*-BAT catalog we use the standard two-point correlation function. We count the number of pairs between the event directions and the positions of the astrophysical objects having an angular separation less than a given angle ψ . We search for excesses of pairs above the isotropic expectation by calculating the fractions of isotropic simulations, f , having an equal or higher number of pairs than the data.

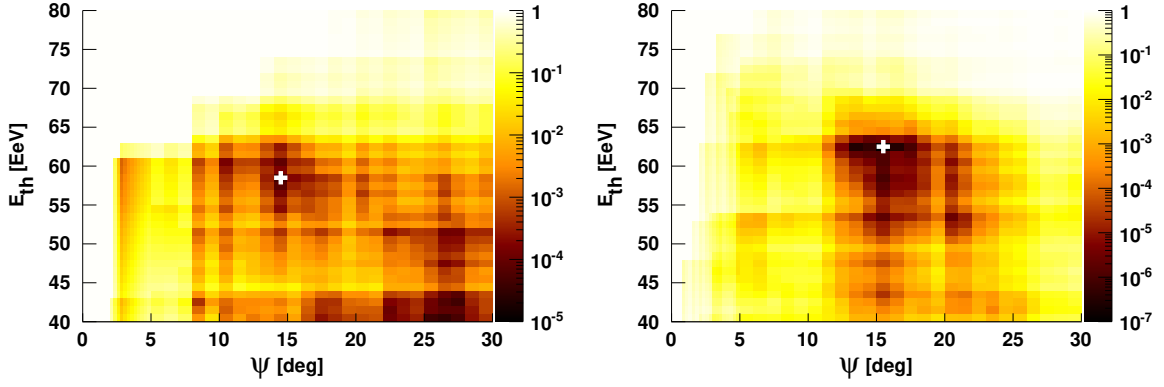


Figure 1: *Left:* Correlation of events with Cen A as a function of the angular distance ψ and the energy threshold E_{th} . *Right:* Scan in (E_{th}, ψ) for the cross-correlation of events with the most luminous AGNs of the *Swift*-BAT catalog within 130 Mpc and brighter than 10^{44} erg/s.

In both analyses we search for the most relevant excess in different energy thresholds E_{th} , ranging from 40 up to 80 EeV in steps of 1 EeV, and in the angular scale ψ between 1° and 30° in steps of 0.25° up to 5° and of 1° for larger angles. The total data set for these two analyses is the combination of 650 vertical events and 170 inclined ones above 40 EeV.

For the correlations with the AGNs of the *Swift*-BAT catalog we select only the brightest sources by applying a cut in intrinsic luminosity. This is motivated by the expectation that the maximum energy achievable by the cosmic rays may be related to the intrinsic electromagnetic bolometric luminosity of the objects. In this case, we test the assumption that only sources intrinsically brighter than some given luminosity can accelerate cosmic rays above an energy threshold E_{th} . The scan in luminosity ranges from $L = 10^{42}$ erg/s up to 10^{44} erg/s considering three logarithmic steps per decade. We also impose a cut in the maximum AGN distance D , that can vary from 10 Mpc up to 190 Mpc in steps of 20 Mpc.

The left panel of Fig. 1 shows the correlation with Cen A. The white cross indicates the minimum value of the cumulative binomial probability, $P = 1.1 \times 10^{-5}$ located at $E_{\text{th}} = 58$ EeV and $\psi = 15^\circ$. For these parameters there are 19 observed events in the data (out a total of 203) while ~ 6.0 are expected on average from an isotropic flux. The significance of this excess can be obtained by penalising for the same scan in energy and angular scale. Performing such procedure we obtain a statistical significance of $\sim 3.1\sigma$.

The most relevant excess, corresponding to the minimum value of f , for the AGNs of the *Swift*-BAT catalog is obtained for $D = 130$ Mpc and $L = 10^{44}$ erg/s. For these two parameters the right panel of Fig. 1 shows the results of the scan in angle and energy threshold. The minimum value $f_{\text{min}} = 10^{-7}$ corresponds to $E_{\text{th}} = 62$ EeV and $\psi = 16^\circ$, where 57 pairs are observed in data and 26.4 are expected in average from isotropy. The significance after considering the same scan anywhere in the parameter space $(D, L, E_{\text{th}}, \psi)$ is $\sim 3.2\sigma$.

4. Cross-correlation studies in relation to other catalogs

In this section we examine the correlation of our highest energy events with two classes of astrophysical UHECR accelerators. Analyses such as that in [9] show that gamma ray emitters

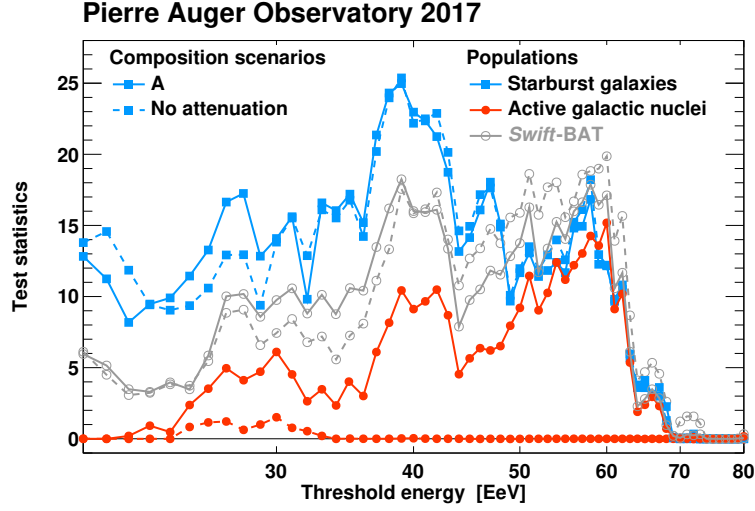


Figure 2: Test statistic as a function of the threshold energy for starburst galaxies (blue lines), gamma-ray AGNs (red lines) and *Swift*-BAT AGNs (gray lines). The continuous lines indicate the TS values obtained accounting for attenuation as in scenario A (see text) while the dotted lines refer to the values without any attenuation.

could meet the requirements to accelerate UHECRs. Among the nearby astrophysical objects that satisfy these conditions there are AGNs as well as star-forming galaxies even though only a handful of them have been detected in the gamma-ray band. We select active and star-forming galaxies motivated by the observations made by *Fermi*-LAT. Active galaxies are extracted from the 2FHL Catalog [10], which includes 360 gamma-ray sources detected above 50 GeV. Selecting only radio-loud AGNs within a 250 Mpc radius results in a list of 17 bright nearby candidates, whose integral gamma-ray fluxes between 50 GeV and 2 TeV are used as a proxy for the UHECR flux. For star-forming objects, we supplement the informations from *Fermi*-LAT with observations in the radio band, where more in-depth surveys of this population of sources have been carried out. Only a handful of star-forming galaxies have been detected in the gamma-ray band, but their gamma-ray luminosity has been shown to nearly linearly scale with their continuum radio flux [11]. We use their continuum emission at 1.4 GHz as a proxy for the UHECR flux [12]. Among the 63 objects within 250 Mpc that have been searched for gamma-ray emission [11], we select only the 23 brightest nearby objects with a radio flux larger than 0.3 Jy, noting though *a posteriori* that this criterion does not affect the results presented in Section 4.1. The selection procedure results in two nearly equal-size flux-limited samples: the active galaxies and the star-forming or starburst galaxies.

4.1 Maximum-likelihood technique

In Section 3 we investigated the correlation with the brightest AGNs of the *Swift*-BAT catalog under the assumption that all the selected sources contribute equally to the UHECR flux. Motivated by the expectation that brighter objects contribute more to the flux, we perform here correlation analyses by weighting the contribution of each astrophysical object to their relative flux.

Given a model of candidate sources, a probability map of the arrival distribution of cosmic rays can be obtained in the form of a smoothed density map and compared to the observed distribution

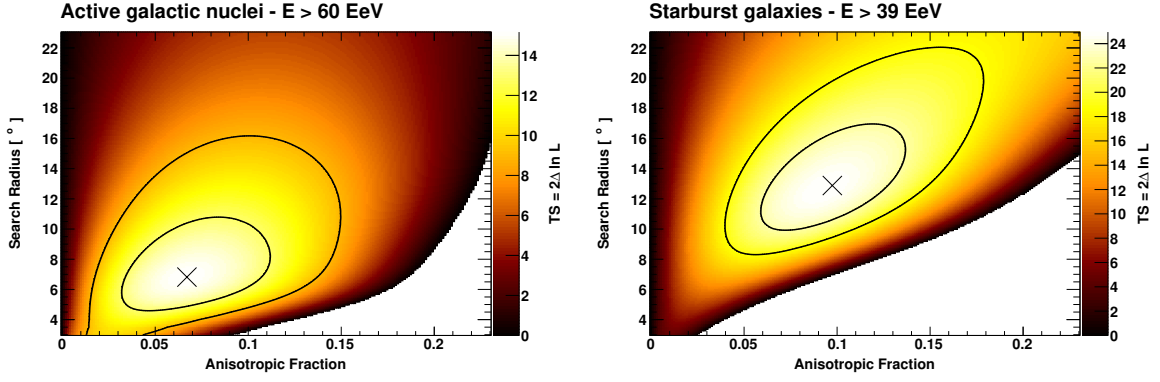


Figure 3: Test statistic as a function of the smoothing angle and anisotropic fraction for the best fit energy for the AGNs (left panel) and for the starburst galaxies (right panel). The solid lines indicate the 1 and 2 σ confidence contours.

of events using an appropriate test statistic (TS). The smoothed maps are constructed by weighting the objects by their relative flux, we use the gamma-ray and the radio flux for the AGNs and the starburst galaxies respectively. The contribution of each individual object is modeled with a Fisher-Von Mises distribution characterized by an angular width. This smearing angle, acting as an effective search radius, takes into account the unknown deflections of the UHECRs in the magnetic fields and constitutes the first free parameter in the analysis.

The contribution of each object is weighted also for its distance to take into account the propagation effects in the intergalactic medium. The attenuation factor used in this analysis corresponds to the mass composition scenario at sources that best reproduce the energy spectrum and the average nuclear composition measured by the Pierre Auger Observatory [13]. An isotropically distributed fraction of events is also added to the probability maps for modelling the diffuse component in the UHECR flux. This component could account for the events highly deflected by the magnetic fields (due to high electric charge and/or strong fields). The anisotropic fraction, the counterpart of the isotropic fraction, is the second free parameter in the analysis. A value of the anisotropic fraction significantly different from zero indicates that the contribution from astrophysical sources deviates strongly from a purely diffuse flux. Such maps are multiplied by the exposure, and then normalised to the total number of UHECR events.

The model predictions are compared to the data using the maximum likelihood ratio method. The likelihood function (\mathcal{L}) as defined in [14] is given by the product over the events of the probability map. The likelihood of the *null hypothesis* \mathcal{L}_0 (isotropy) is the likelihood obtained as the product over the events of the directional exposure function in the arrival directions. The likelihood ratio constitutes the test statistic (TS) used in this search analysis, $TS = 2 \ln \mathcal{L} / \mathcal{L}_0$. According to the Wilks's theorem [15] the realizations from isotropic skies should lead to a TS that follows a χ^2 distribution with two degrees of freedom, an expectation found to be in good agreement with simulations of isotropy.

We maximize the test statistic TS as a function of two free parameters for each source population in different energy threshold E_{th} in steps of 1 EeV from 20 up to 80 EeV. In this case we scan in energy down to 20 EeV because the largest departure from isotropy has been found close to 40 EeV for one population of gamma-ray emitters. Above 20 EeV the total data set is the combination of

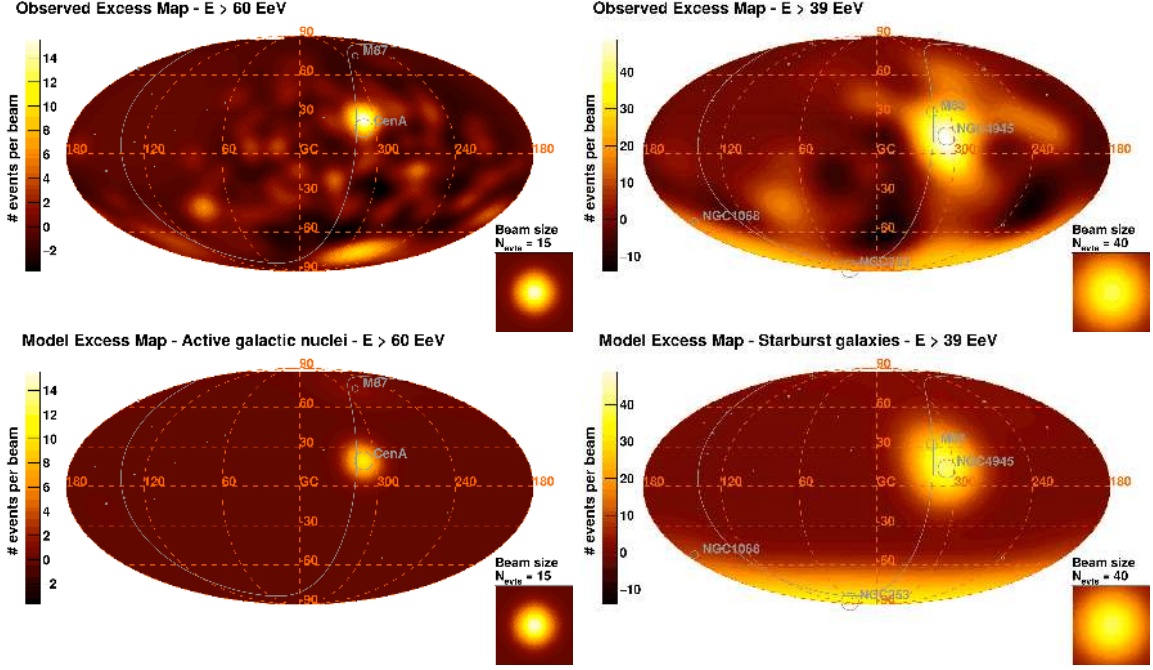


Figure 4: Observed (top) and model (bottom) excess maps obtained with the best-fit parameters for the gamma-ray AGNs (left) and for the starburst galaxies (right) in galactic coordinates.

4,396 vertical events and 1,118 inclined ones.

In Fig. 2 there is the maximum value of the TS in each energy threshold for the two selected populations of gamma-ray sources. The maximum value of the test statistic for the gamma-ray AGNs, $TS = 15.2$, is obtained for $E_{th} = 60$ EeV, while for the star-forming galaxies the maximum value $TS = 24.9$ is reached at $E_{th} = 39$ EeV. The same search is performed without considering any attenuation model due to the UHECR propagation. The energy losses due to the propagation have a negligible effect for the starburst galaxies, because the brightest objects are located 3 Mpc to 20 Mpc away. The gamma-ray AGNs are more distant objects and the impact of the selected attenuation factor is more important.

In Fig. 2 we also show the same weighted search for the AGNs of the *Swift*-BAT catalog within 250 Mpc with flux greater than 13.4×10^{-12} erg/s/cm² in the X-ray band from 14 to 195 keV. In this case the maximum value of the test statistic $TS = 19.9$ is found for $E_{th} = 60$ EeV and no attenuation.

The behaviour of test statistic, for the energy threshold that maximize the likelihood ratio, is shown in Fig. 3 as a function of the two fit parameters. The smearing angle and the anisotropic fraction corresponding to the best-fit parameters are 13° and 10% for the starburst-galaxies and 7° and 7% for the gamma-ray AGNs.

The significance of the maximum value of the TS can be obtained by simulating a large number of isotropic samples and by counting the fraction of random sets leading, under the scan in energy, to a greater value of the TS than the data. We found an excess at 2.7σ level for the gamma-ray AGNs, while for the starburst galaxies there is a deviation from isotropy at 4σ level. The maximum TS value for the gamma-ray AGN is located at 60 EeV, we see in the observed and model maps shown in Fig. 4 that the major contribution come from events in the region of the sky close to Cen A.

Events from this region contribute also to the maximum deviation from isotropy observed in the *Swift*-BAT AGNs found at ~ 60 EeV obtained in Section 3 and shown also in Fig. 4. The events that contribute most to the starburst model are those arriving from directions close to Cen A and South Galactic pole, nearby the locations of the brightest starburst galaxies (NGC 4945, NGC 1068 NGC 253 and M83).

5. Discussions and conclusion

In this work we have examined with *a posteriori* explorations the patterns of the arrival direction distribution of the highest energy cosmic rays detected by the Pierre Auger Observatory.

We have updated the two largest departures from isotropy above 40 EeV previously reported around the direction towards Centaurus A and the most luminous AGNs of the *Swift*-BAT catalog. The significance with an enlarged dataset has increased to the $\sim 3\sigma$ level for both searches. The most important excess around Centaurus A is found for cosmic rays with energies greater than 58 EeV in an angular window of 15° . Around 16° from the directions of the AGNs of the *Swift*-BAT catalog brighter than 10^{44} erg/s and within 130 Mpc we find an excess for energies greater than 62 EeV.

We also examine the correlation of our highest energy events with two nearby populations of extragalactic gamma rays sources, namely star-forming galaxies and AGNs motivated by the observations of the *Fermi*-LAT satellite. A 2.7σ excess has been found in the directions of the active galaxies, while with the starburst galaxies there is a 4σ deviation from isotropy at intermediate angular scale.

References

- [1] The Pierre Auger Collaboration, *Phys. Rev. Lett.* **101** (2008) 061101.
- [2] The Pierre Auger Collaboration, *Astrophys. J.* **804** (2015) 15.
- [3] W.H. Baumgartner *et al.*, *Astrophys. J. Suppl.* **207** (2013) 19.
- [4] The Pierre Auger Collaboration, *Nucl. Instrum. Meth. A* **798** (2015) 172.
- [5] C. Bonifazi, for The Pierre Auger Collaboration, *Nucl. Phys. B Proc. Suppl.* **190** (2009) 20.
- [6] R. Pesce, for the Pierre Auger Collaboration, *Proc. 32nd ICRC (2011)*, [arXiv:1107.4809].
- [7] V. Verzi, for the Pierre Auger Collaboration, *Proc. 33rd ICRC (2013)*, [arXiv:1307.5059].
- [8] F. Fenu, for the Pierre Auger Collaboration, *Proc. 35nd ICRC (2017)*, [CRI267].
- [9] C.D. Dermer and S. Razzaque, *Astrophys. J.* **724** (2010) 1366.
- [10] M. Ackermann *et al.*, *Astrophys. J.* **222** (2016) 5.
- [11] M. Ackermann *et al.*, *Astrophys. J.* **755** (2012) 164.
- [12] Y. Gao and P.M. Solomon, *Astrophys. J. Suppl. Ser.* **152** (2004) 63.
- [13] The Pierre Auger Collaboration, *JCAP* **04** (2017) 038.
- [14] The Pierre Auger Collaboration, *Astropart. Phys.* **34** (2010) 34.
- [15] S.S. Wilks, *Ann. Math. Statist.* **9** (1938) 60.

3

Nuclear mass composition, photons, and neutrinos



PIERRE
AUGER
OBSERVATORY



Depth of maximum of air-shower profiles at the Pierre Auger Observatory: Measurements above $10^{17.2}$ eV and Composition Implications

Jose Bellido^{*a} for the Pierre Auger Collaboration^b

^a*The University of Adelaide, School of Physical Sciences, South Australia, 5005, Australia*

^b*Observatory Pierre Auger, Av. San Martín Norte 304, 5613 Malargüe, Argentina*

E-mail: auger_spokespersons@fnal.gov

Full author list: http://www.auger.org/archive/authors_icrc_2017.html

We present distributions of shower depth of maximum (X_{\max}) and their interpretation in terms of the cosmic ray mass composition. The measurements of X_{\max} are based on data from the fluorescence telescopes of the Pierre Auger Observatory. Due to the extension of the field of view with the High Elevation Auger Telescopes, a lower energy threshold of $10^{17.2}$ eV can be reached. At the highest energies we have increased the available statistics by including three more years of data in the analysis compared to our previous publications. We present estimates of the first two moments of the X_{\max} distribution and of the composition fractions over a large energy range, from $10^{17.2}$ eV to about $10^{19.6}$ eV. The composition fractions are estimated by fitting the X_{\max} distributions with four elemental groups represented by p, He, N and Fe and using post-LHC hadronic models.

35th International Cosmic Ray Conference — ICRC2017

10- 20 July, 2017

Bexco, Busan, Korea

**Speaker.*

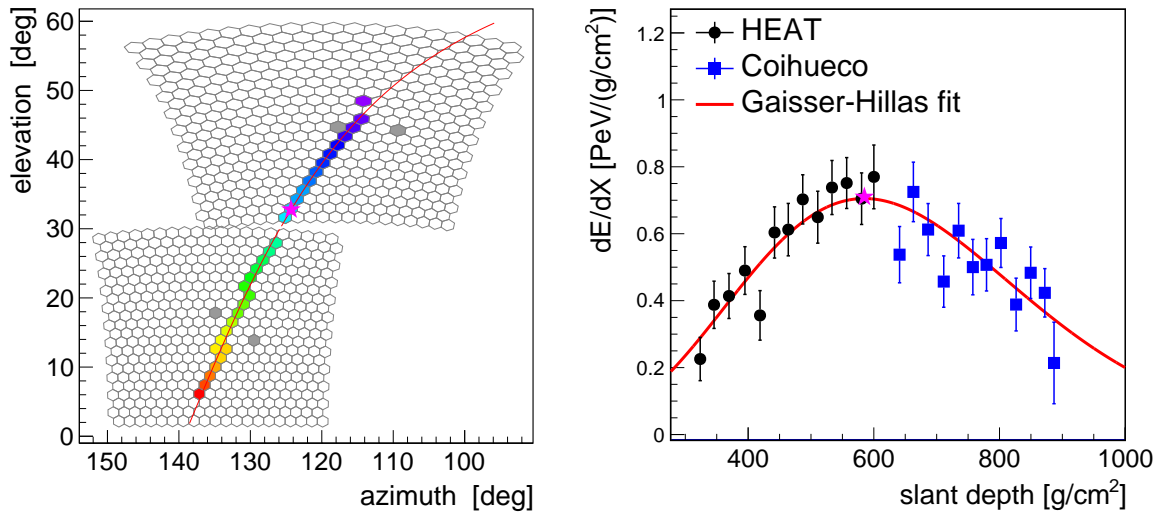


Figure 1: Example of a HeCo event with an energy of $(4.7 \pm 0.2) \times 10^{17}$ eV. Left: the camera view with the timing of the pixel pulses color-coded (early = blue, late = red). Right: the measured longitudinal profile (black circles — HEAT, blue squares — Coihueco) with the Gaisser-Hillas fit (red line). The magenta star in both panels indicates the X_{\max} position.

1. Introduction

Knowledge of the composition of cosmic rays in the energy range of 0.1 to 1 EeV is the key to identifying a possible transition from galactic to extra-galactic sources and for understanding the nature of features in the energy spectrum, such as the “ankle” (at ~ 4 EeV) and the flux suppression (the differential flux falls to one-half of the value of the power-law extrapolation at 4×10^{19} eV [1]).

The atmospheric depth at which the energy deposited by the Extensive Air Shower (EAS) reaches its maximum, X_{\max} , is one of the most robust observables for studying the mass composition. Experimentally, the longitudinal profile of the shower development can be measured using fluorescence light emitted by molecules of atmospheric nitrogen excited by EAS particles. At the Pierre Auger Observatory, which has taken data continuously since 01.2004, such measurements are performed using the fluorescence detector (FD) consisting of 24 telescopes placed at 4 locations and, since 06.2010, using the High Elevation Auger Telescopes (HEAT). The HEAT telescopes have expanded the field of view (FoV) of the Coihueco site (CO) from $2^\circ \div 30^\circ$ up to $2^\circ \div 60^\circ$ in elevation, which allows one to observe nearby low energy showers ($E < 10^{17.8}$ eV). In the following, we refer to the HEAT/CO system as HeCo.

In Fig. 1 an example of a low energy event in the enlarged FoV is shown: the track on the camera (left) and the longitudinal profile with the Gaisser-Hillas fit (right).

In this paper, over five years of calibrated HEAT data, from 1 June 2010 to 31 December 2015, are used to extend the previous measurement of the X_{\max} distributions [2] from $10^{17.8}$ eV down to $10^{17.2}$ eV. In addition, at the highest energies we have increased the available statistics by including data from three more years in the analysis compared to [2].

In estimating the unbiased X_{\max} distributions and their corresponding first two moments, we have followed an identical procedure to that in a previous publication [2]. Most of the systematic uncertainties estimated in [2] for the standard fluorescence detectors (Standard-FD) are also valid

for the HEAT/Coihueco (HeCo) X_{\max} analysis. So for further details of the X_{\max} analysis and of most of the systematic studies we refer the reader to [2].

The determination of the primary composition is performed by comparing the measured X_{\max} distributions of EAS with expectations according to high energy hadronic interaction models [3]. The first two moments of the X_{\max} distribution ($\langle X_{\max} \rangle$ and $\sigma(X_{\max})$) are related to the first two moments of the distribution of the logarithm of masses of primary particles ($\ln A$ and $\sigma(\ln A)$) [4],

$$\langle X_{\max} \rangle = \langle X_{\max} \rangle_p + f_E \langle \ln A \rangle \quad (1.1)$$

$$\sigma^2(X_{\max}) = \langle \sigma_{\text{sh}}^2 \rangle + f_E^2 \sigma^2(\ln A). \quad (1.2)$$

$\langle X_{\max} \rangle_p$ and $\langle \sigma_{\text{sh}}^2 \rangle$ are the mean X_{\max} for protons and the composition-averaged shower-to-shower fluctuations, and f_E is a parameter depending on details of hadronic interactions, properly parametrized from the interaction models for energies $\geq 10^{17}$ eV.

2. Data analysis

The analysis presented in this paper is based on two statistically independent datasets. These are the data collected by the Standard-FD telescopes (during the period from 1 December 2004 to 31 December 2015), and the data collected with HeCo (during the period from 1 June 2010 to 31 December 2015). The events with energies below $10^{18.1}$ eV recorded by CO telescopes during periods where HEAT telescopes were in operation are considered in the HeCo dataset (even if they do not include any HEAT telescope). Otherwise, they are considered in the Standard-FD telescope dataset. So, the Standard-FD dataset contains events with energies above $10^{17.8}$ eV and the HeCo dataset contains events with energies between $10^{17.2}$ eV and $10^{18.1}$ eV.

HEAT can be operated in upward and downward modes. The downward mode is when the telescopes are oriented such that their elevation angle extends up to 30° . The upward mode is when they cover an elevation angle ranging from 30° to 60° (this is the HEAT standard operation mode). The HEAT downward mode is used for systematic cross checks, because it allows one to observe the same showers in coincidence with telescopes from the Coihueco site.

There have been some updates in the energy and X_{\max} scale. These changes arose from improvements in the reconstruction of the shower profile (mainly affecting lower energy events) and improvements in the estimate of the vertical atmospheric optical depth [5].

2.1 Data selection

The analysis is based on hybrid events, i.e. on events with geometries reconstructed using information on arrival times of both light in the cameras of FD telescopes and of the shower front at ground as measured by the surface station closest to the shower axis. We selected data recorded during stable running conditions and good atmospheric conditions [2]. In addition to these selection criteria a set of fiducial FoV cuts are applied to reduce to a minimum the detector effects in the sampled X_{\max} distributions (as explained in Section 2.2).

2.2 FoV selection criteria

A shower is reconstructed accurately only if its X_{\max} is within the detector FoV. Shallow or deep events are more likely to have their X_{\max} values outside the FoV and be excluded from the

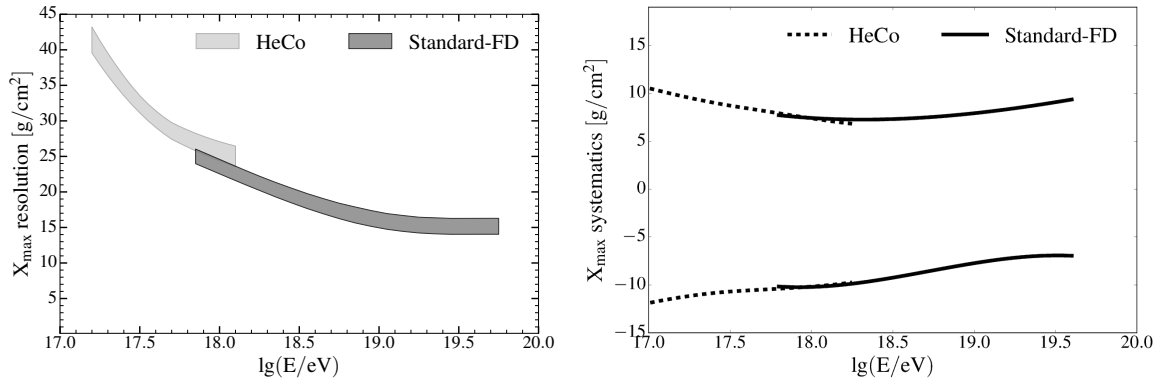


Figure 2: Left: X_{\max} resolution as a function of energy for the HeCo and the Standard-FD datasets. Right: Systematic uncertainties in the X_{\max} scale as a function of energy.

analysis. In general, at lower energies where the showers are closer to the telescopes, the limited FoV biases the sample towards lighter composition (i.e. towards deeper X_{\max} values).

For data satisfying the selection criteria explained in Section 2.1, a fiducial FoV is derived. This fiducial range is characterized by the lower X_{low} and upper X_{up} boundaries. These parameters define the slant depth range where X_{\max} of each event would be reconstructed with a resolution better than $40 \text{ g}/\text{cm}^2$. To have higher quality events, the X_{\max} value must fall inside these boundaries. Furthermore, if the values of X_{low} and X_{up} are not within certain limits (i.e. X_{low} and X_{up} should enclose the bulk of the X_{\max} distribution), the event is also excluded. The processes to calculate the X_{low} and X_{up} parameters, and the limits on them, are explained in detail in [2].

2.3 Estimating the X_{\max} moments

After the application of all selection criteria, the moments of the X_{\max} distribution are estimated as described in [2]. Small energy and X_{\max} reconstruction biases are estimated through simulations and corrected for. The observed width of the distribution is corrected by subtracting the detector resolution (Fig. 2, left) in quadrature to obtain $\sigma(X_{\max})$. The X_{\max} resolution worsens at lower energies because the average length of the observed profiles (in g/cm^2) decreases at lower energies. The step between the HeCo and the Standard-FD resolution is because the X_{\max} reconstruction of events involving HEAT and Coihueco telescopes is very sensitive to small differences in the energy calibration of the HEAT and Coihueco telescopes. Inter-telescope calibration fluctuations with time have widened the sampled X_{\max} distributions. We correct for this detector effect by increasing the detector resolution for HeCo. The $\langle X_{\max} \rangle$ fluctuations as a function of time are evaluated to determine how much the resolution should be increased.

The systematic uncertainty in the X_{\max} scale is displayed in Fig. 2 (right). At low energies it is dominated by uncertainties in the analysis procedure, while at high energies atmospheric uncertainties also contribute.

2.4 Results and Interpretation

We present the results of the HeCo and the Standard-FD X_{\max} distributions in energy bins of $\Delta \lg(E/\text{eV}) = 0.1$ extending from $10^{17.2}$ eV to $10^{18.1}$ eV for HeCo and above $10^{17.8}$ eV for the

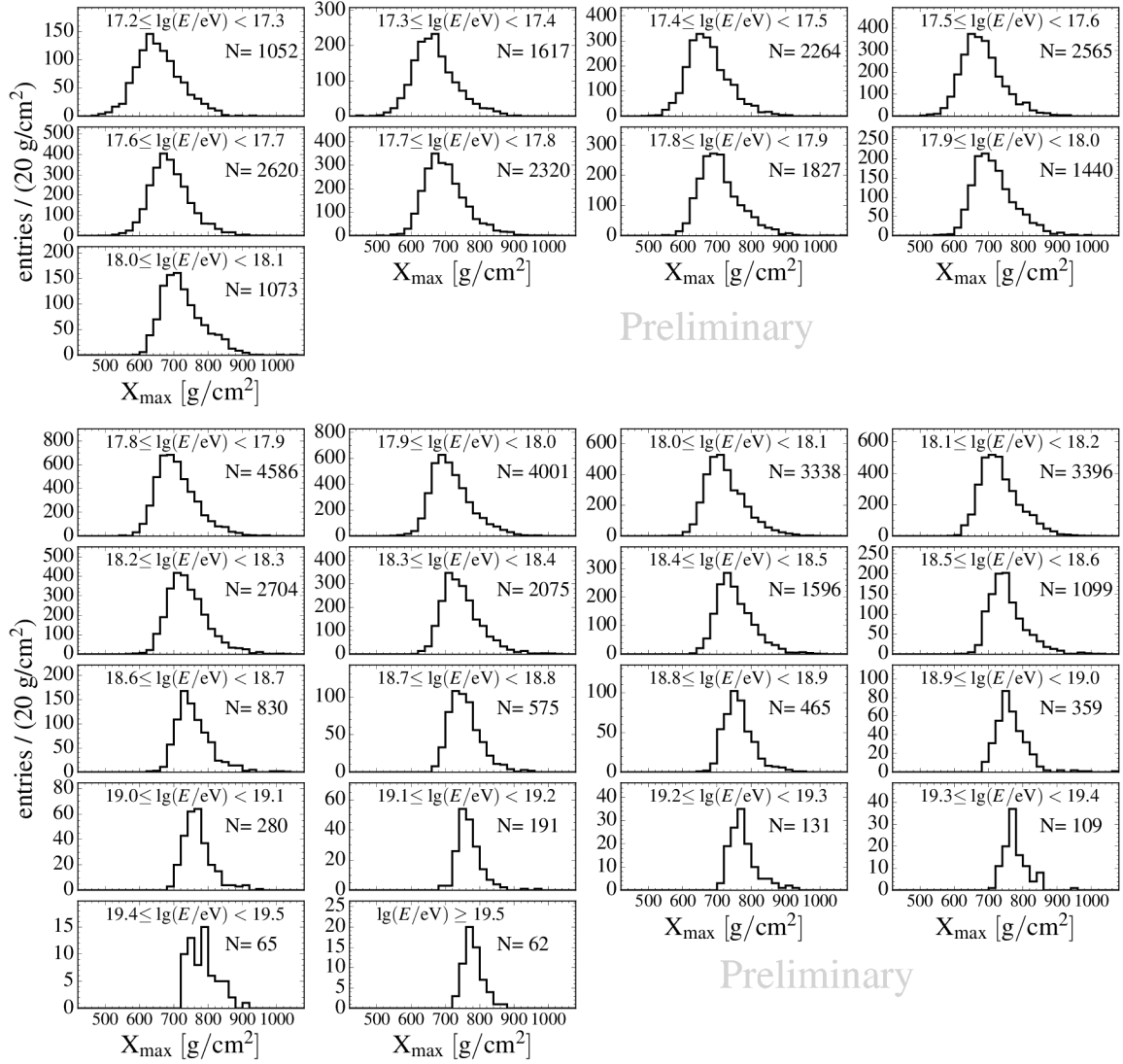


Figure 3: X_{\max} distributions for different energy intervals from the HeCo (top) and Standard-FD (bottom) datasets. The number of events in each energy bin is indicated.

Standard-FD telescopes. The X_{\max} distributions after applying quality and fiducial selection cuts are shown in Fig. 3. These distributions still include effects of the detector resolution and the detector acceptance. The total number of events that passed all cuts (quality and FoV cuts) is 16778 and 25688 for HeCo and Standard-FD respectively.

The $\langle X_{\max} \rangle$ difference between HeCo and the Standard-FD datasets is on average $\sim 2.3 \text{ g/cm}^2$ for overlapping energy bins. This small offset is within the uncorrelated systematics of the two analyses. Consequently, for the combination of the datasets the HeCo $\langle X_{\max} \rangle$ is shifted accordingly and the resulting $\langle X_{\max} \rangle$ and $\sigma(X_{\max})$ as a function of energy are shown in Fig. 4. These X_{\max} moments are in good agreement with those in our previous publications [6, 2] and they can be compared directly with expectations from hadronic models. This is because we have removed all detector effects, such as the detector resolution and the non homogeneous X_{\max} acceptance within

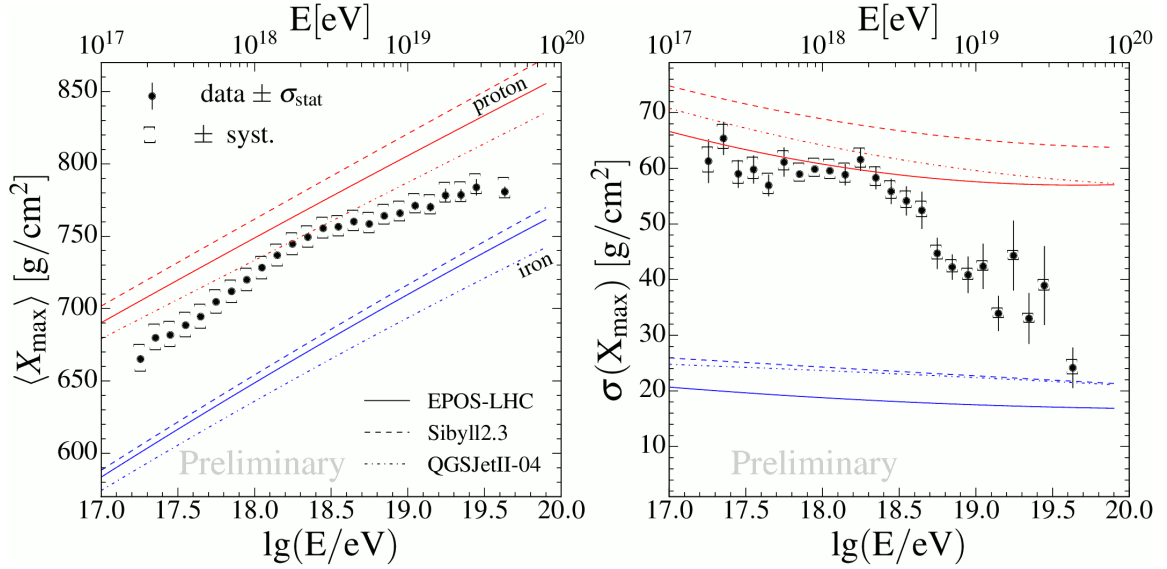


Figure 4: The mean (left) and the standard deviation (right) of the measured X_{\max} distributions as a function of energy compared to air-shower simulations for proton and iron primaries.

the tails of the X_{\max} distributions.

Between $10^{17.2}$ and $10^{18.33}$ eV the observed elongation rate (rate of change of $\langle X_{\max} \rangle$) is (79 ± 1) g/cm²/decade (Fig. 4, left). This value, being larger than that expected for a constant mass composition (~ 60 g/cm²/decade), indicates that the mean primary mass is becoming lighter with increasing energy. At $10^{18.33 \pm 0.02}$ eV the elongation rate becomes significantly smaller ((26 ± 2) g/cm²/decade) indicating that the composition is becoming heavier with increasing energy. The fluctuations of X_{\max} (Fig. 4, right) decrease above $10^{18.3}$ eV, also indicating a composition becoming heavier with increasing energy.

The mean value of $\ln A$, $\langle \ln A \rangle$, and its variance, $\sigma^2(\ln A)$, determined from Eqs. (1.1) and (1.2), are shown in Fig. 5. For the parameters $\langle X_{\max} \rangle_p$, f_E and $\langle \sigma_{\text{sh}}^2 \rangle$, the EPOS-LHC [7], QGSJetII-04 [8] and Sibyll2.3 [9] hadronic interaction models are used. The unphysical negative values obtained for $\sigma^2(\ln A)$ result from the corresponding hadronic model predicting $\sigma(X_{\max})$ values (for pure compositions) that are larger than the observed ones. An average value of $\sigma^2(\ln A) \simeq 1.2$ to 2.6 has been estimated in [10] using the correlation between X_{\max} and S_{1000} (the signal recorded at 1000 m). This range for $\sigma^2(\ln A)$ is valid for the three hadronic models and for the energy range $\lg(E/\text{eV}) = 18.5$ to 19.0. The average $\sigma^2(\ln A)$ from Fig. 5, for the same energy range, is (0.8 ± 0.4) for EPOS-LHC, (-0.7 ± 0.4) for QGSJetII-04, (0.6 ± 0.4) for Sibyll2.3. The QGSJetII-04 and Sibyll2.3 models failed to provide consistent interpretation, and EPOS-LHC is marginally consistent.

For the three models, similar trends with energy for $\langle \ln A \rangle$ and $\sigma^2(\ln A)$ are observed. The primary mass is decreasing with energy reaching minimum values at $10^{18.33 \pm 0.02}$ eV, and then it starts to increase again towards higher energies. The spread of the masses is almost constant until $\approx 10^{18.3}$ eV after which it starts to decrease. Together with the behavior of $\langle \ln A \rangle$, this is an indication that the relative fraction of protons becomes smaller for energies above $\approx 10^{18.3}$ eV.

The expected X_{\max} distributions for p, He, N and Fe have been parametrized [11] using a

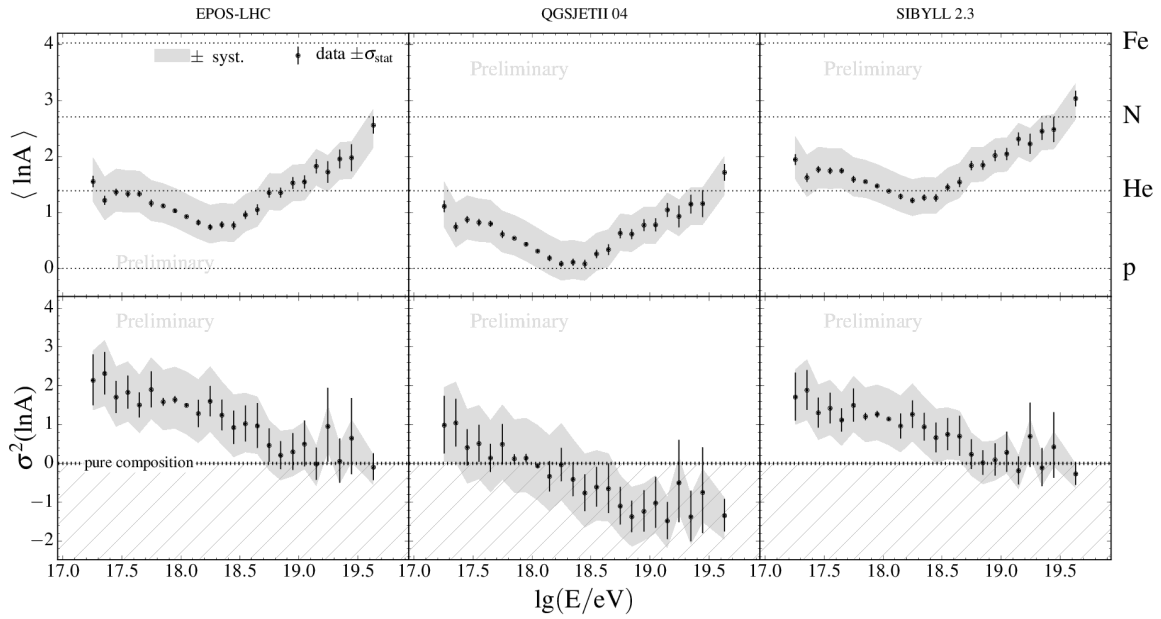


Figure 5: The mean (top) and the variance (bottom) of $\ln A$ estimated from data with EPOS-LHC (left), QGSJetII-04 (middle) and Sibyll2.3 (right) hadronic interaction models.

gaussian convolution with an exponential function according to the hadronic models (EPOS-LHC, QGSJetII-04 and Sibyll2.3) using CONEX [12]. These parametrization have been used to fit for the fraction of p, He, N and Fe in each energy bin. The corresponding detector resolution and acceptance (for each energy bin) have been considered in the fits. Fig. 6 shows the fit fractions as a function of energy for the three different models. The panel at the bottom indicates the goodness of the fits (p -values). The trend of the He and N fractions as a function of energy has a strong dependence on the particular hadronic model used. However, the three hadronic models agree when estimating a null Fe abundance between $10^{18.3}$ eV and $10^{19.4}$ eV.

This interpretation of the cosmic ray composition as a function of energy relies on the validity of the hadronic interaction models. The p -values estimated in Fig. 6 provide an indication on how well the models managed to reproduced the observed X_{\max} distributions with the fractions fit. For good fits, the p -values should be randomly distributed between 0 and 1, and should not be too small. A large fraction of the p -values shown in Fig. 6 (bottom panel) are below the 0.1 line, but we only expect 10% of p -values to be below this line. There is a total of 24 energy bins, so we expect in average 2.4 p -values below the 0.1 line, but we observe 8 (for EPOS-LHC), 11 (for Sibyll2.3), and 17 (for QGSJetII-04). The large fraction of small p -values indicates that the models were not able to find combinations of fractions to reproduce the details of the observed X_{\max} distribution.

References

- [1] P.L. Ghia, *Highlights from the Pierre Auger Observatory*, PoS(ICRC2015)034, 2016.
- [2] A. Aab et al., *Depth of maximum of air-shower profiles at the Pierre Auger Observatory. I. Measurements at energies above $10^{17.8}$ eV*, Phys. Rev. D **90** (2014) 122005.

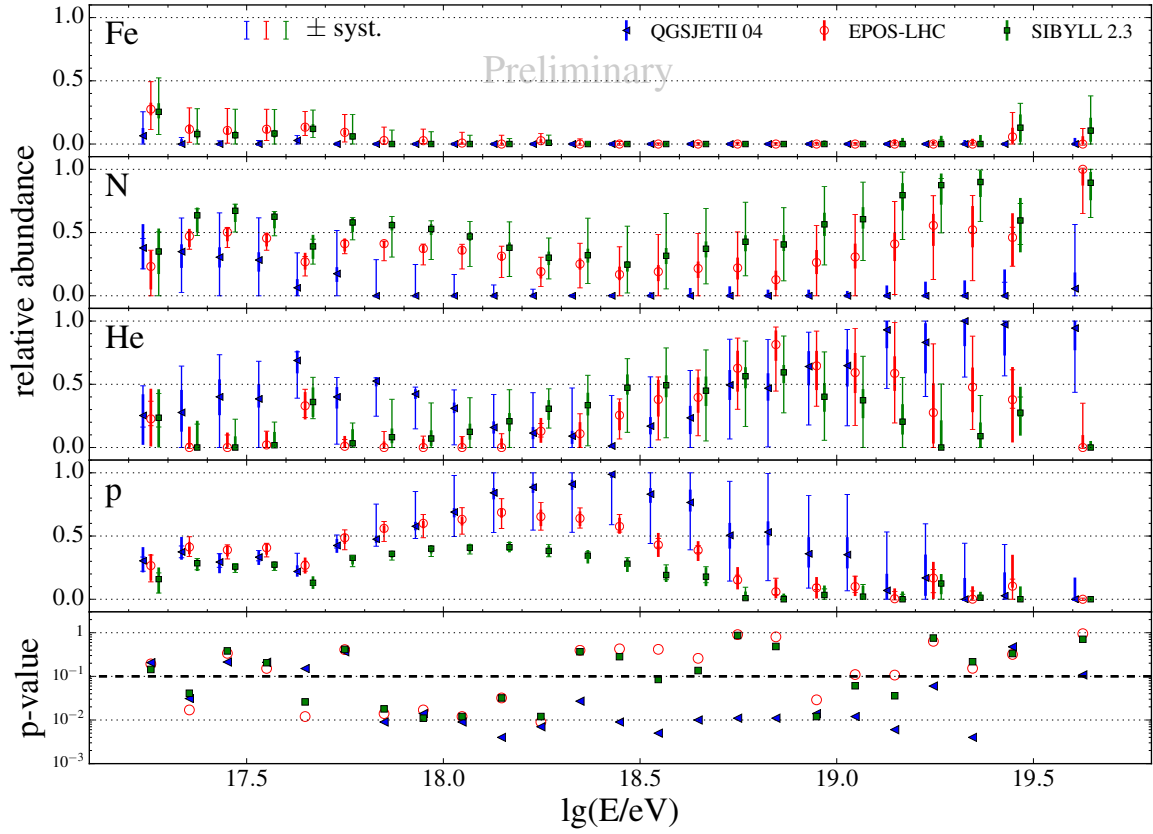


Figure 6: Mass fraction fits obtained using parametrizations of the expected X_{\max} distributions using the HeCo and the Standard-FD X_{\max} data. The error bars indicate the statistics (smaller cap) and the systematic uncertainties (larger cap). The bottom panel indicates the goodness of the fits (p -values).

- [3] A. Aab *et al.*, *Depth of maximum of air-shower profiles at the Pierre Auger Observatory. II. Composition implications*, *Phys. Rev. D* **90** (2014) 122006.
- [4] P. Abreu *et al.*, *Interpretation of the Depths of Maximum of Extensive Air Showers Measured by the Pierre Auger Observatory*, *JCAP* **1302** (2013) 026.
- [5] M. Malacari *et al.* [Pierre Auger Collaboration]. Proc. 35th ICRC (2017), this conference.
- [6] J. Abraham *et al.*, *Measurement of the Depth of Maximum of Extensive Air Showers above 10^{18} eV*, *Phys. Rev. Lett.* **104** (2010) 091101.
- [7] T. Pierog and K. Werner *Phys. Rev. Lett.* **101** (2008) 171101.
- [8] S. Ostapchenko *Phys. Rev. D* **83** (2011) 014018.
- [9] F. Riehn, R. Engel, A. Fedynitch, T.K. Gaisser, and T. Stanev, *A new version of the event generator Sibyll*, *PoS (ICRC2015) 558* (2016).
- [10] A. Aab *et al.*, *Evidence for a mixed mass composition at the "ankle" in the cosmic-ray spectrum*, *Phys. Lett. B* **762** (2016) 288.
- [11] S. Blaess, J. Bellido, and B. Dawson, *PoS (ICRC2017) 490* (2017).
- [12] T. Bergmann *et al.*, *Astropart. Phys.* **26** (2007) 420.



$\langle X_{\max} \rangle$ measurements and tests of hadronic models using the surface detector of the Pierre Auger Observatory

Patricia Sanchez-Lucas^{*a} for the Pierre Auger Collaboration^b

^aUniversity of Granada and CAFPE, Granada, Spain

^bObservatory Pierre Auger, Av. San Martín Norte 304, 5613 Malargüe, Argentina

E-mail: auger_spokespersons@fnal.gov

Full author list: http://www.auger.org/archive/authors_icrc_2017.html

The time structure of the signals from air showers, recorded with the water-Cherenkov detectors of the Pierre Auger Observatory, contains information that can be related to the mass composition of primary cosmic rays and to hadronic multi-particle production. We can study both because the recorded signals contain a mix of the muonic and electromagnetic components. Using information from the time structure, we define observables that enable a comparison of observations with predictions from hadronic models. We have found that the interpretation obtained from a comparison of our data to these predictions is inconsistent with the interpretation obtained by comparing fluorescence measurements and model predictions, over a greater energy range, and with higher precision, than in previous studies. Information about mass composition is obtained by calibrating the observables based on time structure with fluorescence measurements. Following this approach, we infer the depth of shower maximum, X_{\max} , from 0.3 EeV to over 100 EeV. In particular, above 30 EeV, our sample is nearly fourteen times larger than currently available from fluorescence measurements. With this novel approach we find good agreement with previous studies and, with our larger sample, we have extended the measurement of $\langle X_{\max} \rangle$ to greater energies than hitherto.

*35th International Cosmic Ray Conference — ICRC2017
10–20 July, 2017
Bexco, Busan, Korea*

*Speaker.

1. Introduction

The measurement of the mass composition is one of the most important questions related to uncovering the origin of ultra-high-energy cosmic rays (UHECRs) but the study of the mass spectrum is especially difficult for two reasons. On the one hand, to interpret the data one must use assumptions about the hadronic models at centre-of-mass energy around $\sqrt{s} \sim 300$ TeV, well beyond what is accessible in particle accelerators. On the other hand, the observable X_{\max} is based on fluorescence measurements, restricted to clear moonless nights, with the consequent reduction of statistics.

To overcome the limitations imposed by the small number of events accumulated with the fluorescence technique, use can be made of data recorded with the 1660 water-Cherenkov detectors of the Pierre Auger Observatory [1] which are operational nearly 100% of the time. Nevertheless, most of the observables obtained from these detectors cannot be used to make inferences about the mass composition because they are related to the hadronic component of the extensive air showers (EASs) and thus the comparison with models results in unreliable predictions. In this paper, we describe a new method for extracting information about the development of air showers from the time profiles of the signals in the water-Cherenkov detectors.

2. The Risetime and the Delta method

For the study described below, we characterise the signal at each detector by the risetime, $t_{1/2}$, defined as time taken by the total signal to increase from 10% to 50% of its final level. It is a function of distance, zenith angle and energy. $t_{1/2}$ is sensitive to the state of the development of the shower and so directly related to mass of the primary particle. In inclined showers, $t_{1/2}$ shows an asymmetry around the azimuthal angle in the shower plane, ζ , which strongly depends on the zenith angle [2]. For the present study, this asymmetry is corrected for, by referencing each risetime to $\zeta = 90^\circ$.

The uncertainty in a measurement of $t_{1/2}$ is found empirically from the data using pairs of detectors that are 11 m apart and also detectors that are at similar distances from the shower core. The uncertainty in a risetime measurement, $\sigma_{1/2}$, is given by

$$\sigma_{1/2} = \frac{\sqrt{\pi}}{2} \langle |t_{1/2}^1 - t_{1/2}^2| \rangle \quad (2.1)$$

where the superscripts define each detector. $\sigma_{1/2}$ is parameterized as a function of total signal, distance and zenith angle. Full details of the methods used and of the results are given in [3].

When a large number of risetimes is recorded in an event it is desirable to characterise the whole event with a single parameter. To do this, we have determined, for the two arrays of the Observatory, independent relationships that describe the risetimes as a function of distance and zenith angle in a narrow energy range. We call these functions *benchmarks*. Risetimes at particular stations are compared with the relevant times from the benchmark, $t_{1/2}^{\text{bench}}$, in units of the accuracy with which they are determined, leading to a new parameter called Δ_i . This approach, *the Delta method*, is illustrated in Fig. 1. Each shower is then characterised for the average value of the Δ_i s, Δ_s , for the selected stations, N .

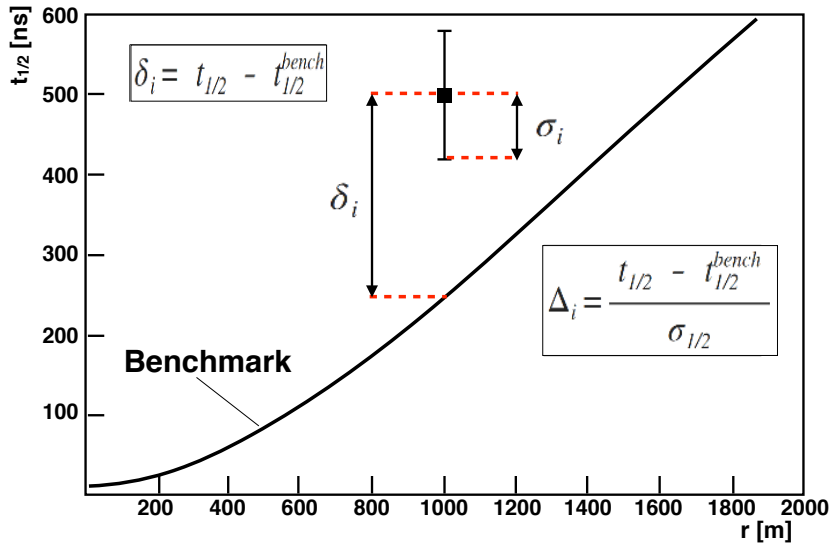


Figure 1: Schematic concept of the Delta method.

3. Data Selection

We have used data collected with the two arrays of the Pierre Auger Observatory. For the 1500 m array (750 m array) data from January 2004 (January 2008) to December 2014 with energies above 3 EeV (0.3 EeV) are selected. A cut in zenith angle, $\sec \theta < 1.45$ ($\sec \theta < 1.30$) is imposed to avoid short risetimes close to the electronics resolution. The events are required to satisfy the standard trigger levels and at least three selected detectors are required for an event to be included in the data sample. For these detectors, the low-gain trace must not be saturated. The recorded signal must be larger than 5 VEM (3 VEM)¹ and the stations must lie between 300 m and 1400 m (800 m). For the highest energies this upper limit on distances has been extended to 2000 m. After application of these cuts a total of 27553 events for the 750 m array and 54022 for the 1500 m array remain. Further details of the selection are described in [3].

4. Benchmark Determination

The determination of the benchmarks is fundamental to the success of the technique. Essentially the same procedure has been adopted for both arrays. For each station two time traces are recorded on high-gain and low-gain channels. $t_{1/2}$ is always calculated from the trace of the high-gain channel unless there is saturation in this channel, in which case we are forced to recover the trace from the low-gain channel. If there is saturation in the low-gain channel $t_{1/2}$ cannot be measured.

Benchmark are obtained for the high-gain and low-gain traces independently. The energy bins chosen for the benchmarks of the 750 and 1500 m arrays are $17.7 < \lg(E/\text{eV}) < 17.8$ and

¹ 1 VEM is the signal produced by a vertical and central through-going muon.

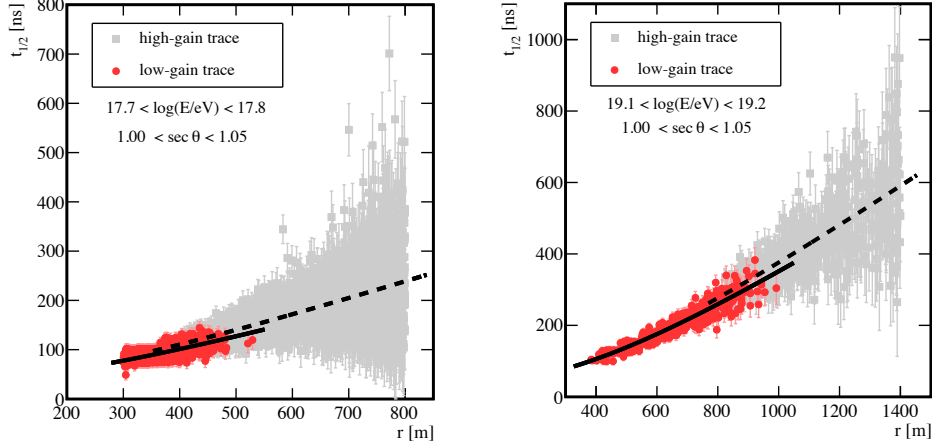


Figure 2: Example of benchmark fits for the 750 m array (left panel) and the 1500 m array (right panel). The solid (dashed) line corresponds to the fit done to the risetimes from the low-gain (high-gain) traces.

$19.1 < \lg(E/eV) < 19.2$ respectively. A fit is first made to the data from the low-gain channels using the relation

$$t_{1/2}^{\text{low-gain}} = C + \sqrt{A(\theta)^2 + B(\theta)r^2} - A(\theta) \quad (4.1)$$

where A and B are free parameters and $C = 40$ ns. Having used low-gain traces to evaluate A and B , the risetimes from the high-gain traces are now fitted with the function

$$t_{1/2}^{\text{high-gain}} = C + N(\theta) \left(\sqrt{A(\theta)^2 + B(\theta)r^2} - A(\theta) \right) \quad (4.2)$$

in which there is only one free parameter, $N(\theta)$, describing the shift between the measurements in the two channels. Examples of these fits in a particular $\sec \theta$ bin are shown in Fig. 2 for both arrays.

Fits were made for A , B and N in 6 and 9 intervals of $\sec \theta$ of width 0.5 for the 750 m and 1500 m array in their respective $\sec \theta$ ranges. Fuller details can be found in [3].

5. Δ_s as a function of energy and comparison with model predictions

Once the benchmarks have been determined we can describe the observed variation of $\langle \Delta_s \rangle$, the mean of Δ_s for a set of events, as a function of energy. The variation of $\langle \Delta_s \rangle$ with energy for the two arrays is shown in Fig. 3. Note that at the benchmark energies, $\langle \Delta_s \rangle = 0$, as expected by definition. The overall systematic uncertainties in $\langle \Delta_s \rangle$ is 0.07 and 0.11 for the 750 m and 1500 m array, respectively [3].

We can use $\langle \Delta_s \rangle$ to test the validity of hadronic models. In previous works [2][4][5][6] strong evidence has been found showing that the models do not adequately describe the data and that the problem is related to the description of the muonic component in the showers. As muons dominate the early part of the shower front, $t_{1/2}$ is particularly useful for studying this effect further. For the comparison with the models, simulations with QGSJetII-04 [7] and EPOS-LHC [8] for proton and

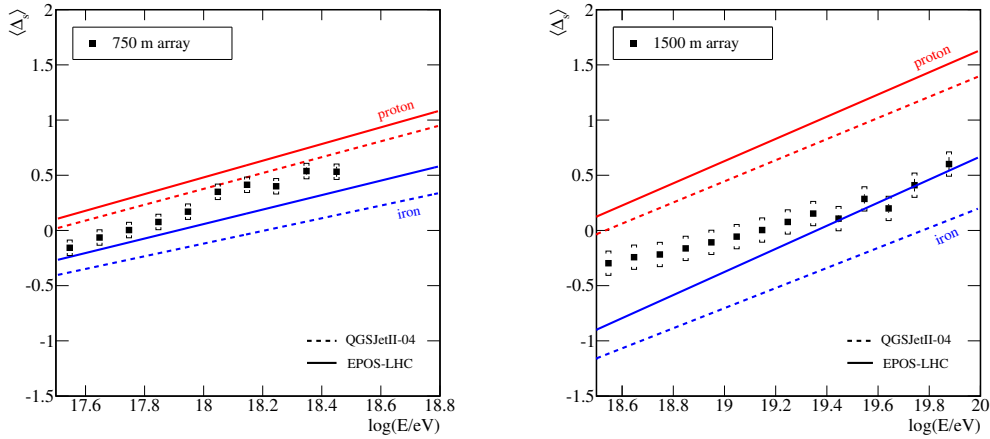


Figure 3: $\langle \Delta_s \rangle$ as a function of energy for the two surface arrays. Brackets correspond to the systematic uncertainties. Data are compared to the predictions obtained from simulations.

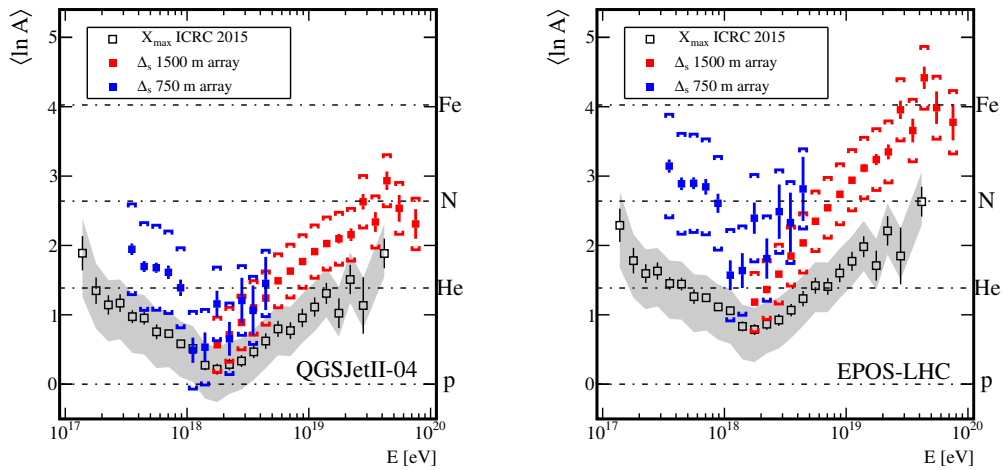


Figure 4: $\langle \ln A \rangle$ as a function of energy for the Delta Method and for X_{\max} measurements done with the FD. QGSJetII-04 and EPOS-LHC have been used as the reference hadronic models.

iron primaries with zenith angles $\theta < 45^\circ$ and $17.5 < \lg(E/eV) < 20.0$ have been produced. For consistency, in making the comparisons, only the benchmarks determined from the data are used. The values of $\langle \Delta_s \rangle$ obtained for the different primaries and models are also shown in Fig. 3. These can be transformed to a prediction of the composition of the UHECRs in terms of $\langle \ln A \rangle$ (Fig. 4) where the results are compared with the Auger measurements of X_{\max} made with the FD [9]. While the absolute values of $\langle \ln A \rangle$ for the Delta method and the FD X_{\max} differ from each other, the trend with the energy is very similar. The difference probably arises because the electromagnetic cascade dominates the FD measurements whereas Δ_s is a parameter describing a mixture of the muonic and the electromagnetic components. The inconsistency between data and models is observed over a greater energy range than hitherto.

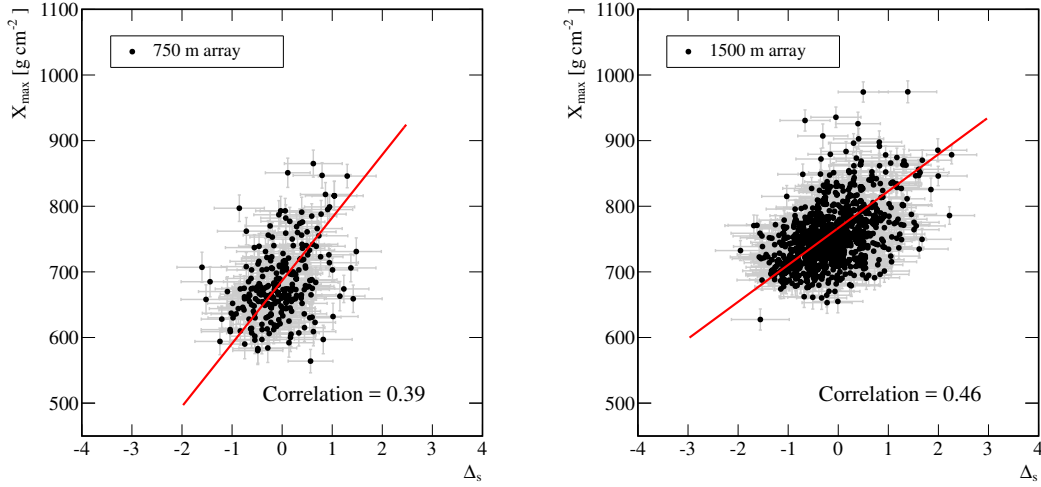


Figure 5: (Left) Correlation of X_{\max} and Δ_s for the 252 events from the 750 m array. (Right) Correlation of X_{\max} and Δ_s for the 885 events of the 1500 m array.

6. Correlation of Δ_s with X_{\max}

We now address the correlation of Δ_s with X_{\max} . We would not expect a 1:1 correlation between these parameters because X_{\max} is dominated by the electromagnetic component whereas Δ_s is dependent on a muon/electromagnetic mix. The X_{\max} and Δ_s for the events selected for the calibration are shown in Fig. 5. These events have been taken from the FD data set discussed in [9]. There are 252 and 885 events for the 750 m and 1500 m arrays respectively available for calibration. The selected samples of events are unbiased.

For the calibration of the two data set we fit functions of the form

$$X_{\max} = a + b\Delta_s + c \lg(E/\text{eV}) \quad (6.1)$$

The maximum likelihood method was used to make the fits which give the following values for the parameters a , b and c for the 1500 m (750 m) array: $a = 699 \pm 12(636 \pm 20) \text{ g/cm}^2$, $b = 56 \pm 3(96 \pm 10) \text{ g/cm}^2$ and $c = 3.6 \pm 0.7(2.9 \pm 1.2) \text{ g/cm}^2$.

The values of X_{\max} found from this analysis are shown as a function of energy in Fig. 6. From Fig. 7 one can see that they agree well with the measurements made with the fluorescence detectors [9]. The comparison with hadronic models allows the average depth of shower maxima to be expressed in terms of $\langle \ln A \rangle$. The evolution of $\langle \ln A \rangle$ as a function of energy is shown in Fig. 8. In the energy range where the FD and the SD measurements overlap, the agreement is good. The SD measurements confirm, with a larger data set that extends to higher energies, what has been observed with the FD: the primary flux is predominantly composed of light particles at around 2 EeV with the average mass increasing up to 40 EeV. Above this energy the last two energy bins might suggest that the increase of the primary mass is stopping for the highest energies. However we still need to further reduce statistical and systematic uncertainties to be able to draw strong conclusions.

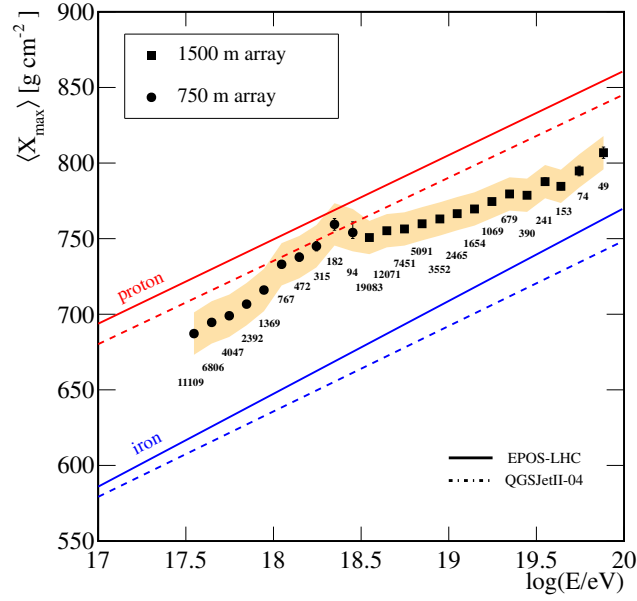


Figure 6: $\langle X_{max} \rangle$ obtained independently with the data from the 750 and 1500 m arrays as a function of energy. The shaded area indicates the systematic uncertainty. Data are compared to the behaviour of protons and iron nuclei predicted for two different models.

References

- [1] Pierre Auger Collaboration, Nucl. Instrum. Meth. A 798 (2015) 172; arXiv:1502.01323.
- [2] Pierre Auger Collaboration, Phys. Rev. D 93 (2016) 072006; arXiv:1604.00978.
- [3] Pierre Auger Collaboration, submitted to Phys. Rev. D.
- [4] Pierre Auger Collaboration, Phys. Rev. D 90 (2014) 012012; Addendum: Phys. Rev. D 90 (2014) 039904; Erratum: Phys. Rev. D 92 (2015) 019903; arXiv:1407.5919.
- [5] Pierre Auger Collaboration, Phys. Rev. D 91 (2015) 032003; Erratum: Phys. Rev. D 91 (2015) 059901; arXiv:1408.1421.
- [6] Pierre Auger Collaboration, Phys. Rev. Lett. 117 (2016) 192001; arXiv:1610.08509.
- [7] S. Ostapchenko, Phys. Rev. D 83 (2011) 014018; arXiv:1010.1869.
- [8] T. Pierog, I. Karpenko, J.M. Katzy, E. Yatsenko, and K. Werner, Phys. Rev. C 92 (2015) 034906; arXiv:1306.0121.
- [9] A. Porcelli, for the Pierre Auger Collaboration, PoS ICRC2015 (2016) 420.

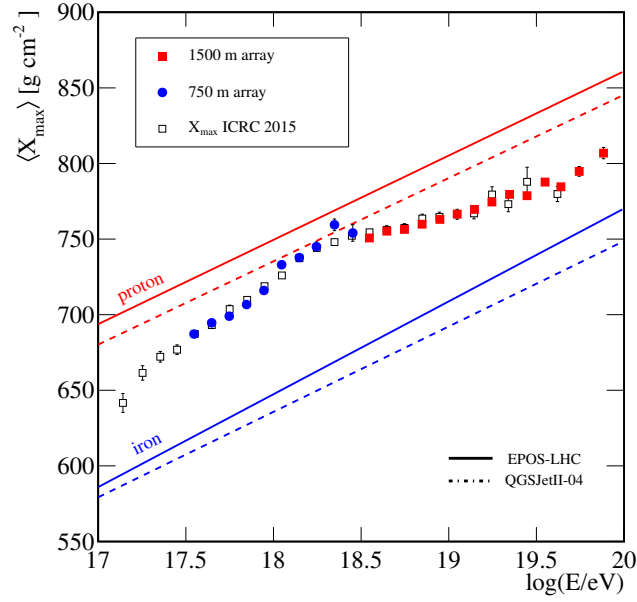


Figure 7: Comparison of $\langle X_{max} \rangle$ measured using the fluorescence and surface detectors. The systematic uncertainties have been removed for a clearer view.

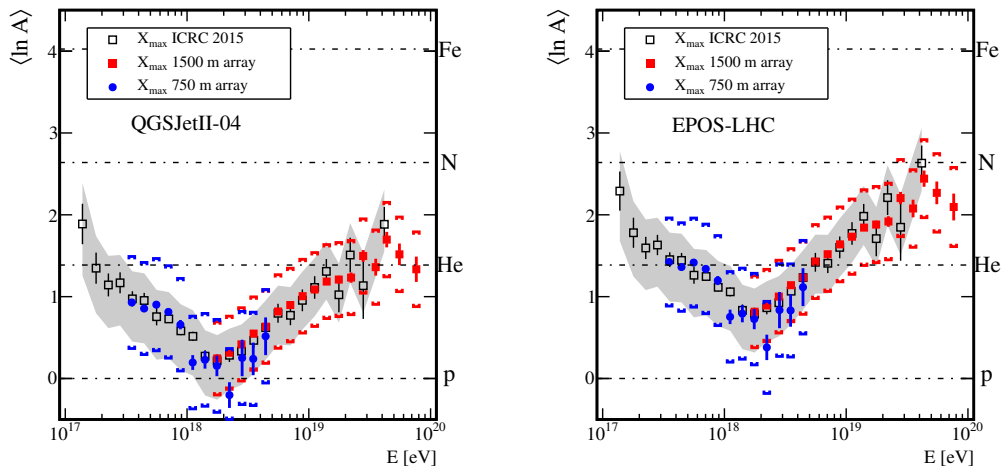


Figure 8: $\langle \ln A \rangle$ as a function of energy. QGSJetII-04 and EPOS-LHC have been used as the reference hadronic models. The results of the Delta method are compared with those based on X_{max} measurements done with the FD [9]. Brackets corresponds to the systematic uncertainties.



Diffuse and targeted searches for ultra-high-energy photons using the hybrid detector of the Pierre Auger Observatory

Marcus Niechciol^{*a} for the Pierre Auger Collaboration^b

^a*Department Physik, Universität Siegen, 57068 Siegen, Germany*

^b*Observatorio Pierre Auger, Av. San Martín Norte 304, 5613 Malargüe, Argentina*

E-mail: auger_spokespersons@fnal.gov

Full author list: http://www.auger.org/archive/authors_icrc_2017.html

Two hybrid analyses using air shower events recorded by both the Surface Detector Array (SD) and the Fluorescence Detector (FD) of the Pierre Auger Observatory are presented. In the first analysis, a search for a diffuse flux of photons with energies above 10^{18} eV = 1 EeV is performed. An unprecedented separation power between photon and hadron primaries is achieved through combining observables from both the FD and the SD. The upper limits on the photon flux determined in this analysis are the most stringent limits to date at these energies, reaching the expected flux of cosmogenic photons in some astrophysical scenarios and placing severe constraints on non-standard models for the production of UHE cosmic rays.

In the second analysis, a targeted search for EeV photon point sources is performed using several classes of galactic and extragalactic candidate objects. No significant excess of photon-like air shower events is found for any of the source candidates. The photon flux limits for selected source candidates constrain theoretical models for EeV proton production at non-transient Galactic and nearby extragalactic sources, and in particular at the Galactic center region.

*35th International Cosmic Ray Conference — ICRC2017
10–20 July, 2017
Bexco, Busan, Korea*

^{*}Speaker.

1. Introduction

Photons are the main messenger particles for exploring the Universe. They are observed in a broad energy range, spanning from the radio regime, through the visible light up to the X-ray and gamma-ray regimes. The maximum photon energy that has been observed so far is in the order of 100 TeV, detected using ground-based air Cherenkov telescopes [1]. At ultra-high energies, in the EeV regime, only charged cosmic rays have been detected so far. However, the nature and origin of these ultra-high-energy (UHE) cosmic rays is not yet known. A discovery of UHE photons could help to answer fundamental questions about UHE cosmic rays. For example, UHE photons are tracers of the Greisen-Zatsepin-Kuzmin (GZK) process, i.e. the interaction of UHE protons with photons from the cosmic microwave background (CMB). In these interactions, neutral pions are produced, which subsequently decay into pairs of UHE photons. If these predicted GZK photons were observed, it would be an indicator for the GZK process being the reason for the observed suppression in the energy spectrum of UHE cosmic rays [2].

Due to their small incoming flux (less than one particle per square kilometer per year), UHE cosmic particles impinging on the Earth can only be detected indirectly by measuring the extensive air showers they initiate when entering the Earth's atmosphere. For the identification of primary photons in the recorded air shower data, the differences between air showers initiated by primary photons and those induced by primary hadrons are of great importance [3]. On average, air showers initiated by UHE photons develop deeper in the atmosphere than showers of the same primary energy induced by hadrons, due to the typically smaller multiplicity of electromagnetic interactions. This can be expressed through the observable X_{\max} , which describes the atmospheric depth of the shower maximum. Another key difference is the lower average number of muons in photon-induced air showers compared to air showers initiated by hadrons, a consequence of the smaller cross section for photo-nuclear interactions compared to the cross sections for electromagnetic interactions.

The Pierre Auger Observatory [4], located near Malargüe, Argentina, offers an unprecedented exposure for UHE cosmic particles. A key feature of the Pierre Auger Observatory is the hybrid concept, combining a Surface Detector Array (SD) with a Fluorescence Detector (FD). The SD consists of 1660 water-Cherenkov detectors arranged on a triangular grid with a spacing of 1.5 km, covering a total area of more than 3000 km². The SD is overlooked by 27 fluorescence telescopes, located at four sites at the border of the array. The SD samples the lateral shower profile at ground level, i.e. the distribution of particles as a function of the distance from the shower axis, with a duty cycle of $\sim 100\%$, while the FD records the longitudinal shower development in the atmosphere above the SD. The FD can only be operated in clear, moonless nights, reducing the duty cycle to $\sim 13\%$. Combining measurements from both detector systems in hybrid events yields data of superior quality, which are exploited in the two analyses presented in the following sections. In the first analysis, a search for a diffuse flux of photons with energies above 10^{18} eV is performed [5], while the second analysis is a targeted search for point sources of EeV photons [6].

2. Search for a diffuse flux of photons

The main observable for the search for photons with hybrid data is X_{\max} , since it can be directly measured with the FD. To make full use of the information available in hybrid events, X_{\max} is com-

plemented with observables related to the SD measurement of the air shower. The lateral shower profile, can be described by a Lateral Distribution Function (LDF). In general, photon-induced air showers have a steeper LDF and consequently a smaller footprint on ground (and thus a smaller number of triggered SD stations N_{stat}) compared to those initiated by hadrons. The differences in the LDF between the different primary particle types can be exploited with the observable S_b [7]:

$$S_b = \sum_i^{N_{\text{stat}}} S_i \left(\frac{r_i}{r_0} \right)^b, \quad (2.1)$$

where S_i and r_i are the signal, measured in units of Vertical Equivalent Muon (VEM), and the distance from the shower axis of the i -th station, $r_0 = 1000\text{m}$ is a reference distance and b is a constant [5].

The photon/hadron discrimination has been studied using detailed MC simulations of the air showers and the detector response with primary energies between 10^{17} and 10^{20} eV and zenith angles between 0 and 65° . In Fig. 1, the correlation between the three discriminating observables X_{max} , S_b and N_{stat} is shown exemplarily for the energy range between 10^{18} and 10^{19} eV. To fully extract the separation power of the discriminating observables, a multivariate analysis (MVA) is performed. Different algorithms and combinations of input observables have been tested (see Fig. 2, left). A boosted decision tree (BDT) combining X_{max} , S_b and N_{stat} has been found to give the best performance in separating photon-induced air shower events from the background of hadron-induced events. To take into account the energy and zenith angle dependences of the three observables, also energy and zenith angle are included in the BDT. Overall, the background contamination at a photon selection efficiency of 50% is 0.14% under the worst-case assumption of a pure proton background. The impact of different assumptions on the background contamination has been studied, e.g. by changing the hadronic interaction model (the background contamination changes from 0.14% to 0.21%) or by using a mixture of 50% proton and 50% iron as background (the background contamination decreases to 0.04%). To identify photons, a candidate cut is defined at the median of the BDT response distribution for primary photons. This way, the signal efficiency remains constant independently of any assumptions on the composition and the hadronic interactions.

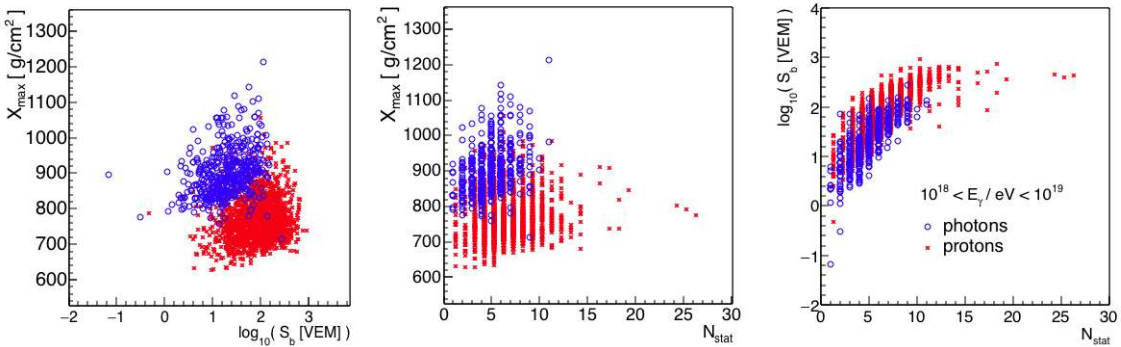


Figure 1: Correlation between the discriminating observables used in the MVA for the energy range $10^{18} < E_\gamma < 10^{19}$ eV [5]: the simulated photon sample is shown as blue circles, while the proton sample is denoted by red stars.

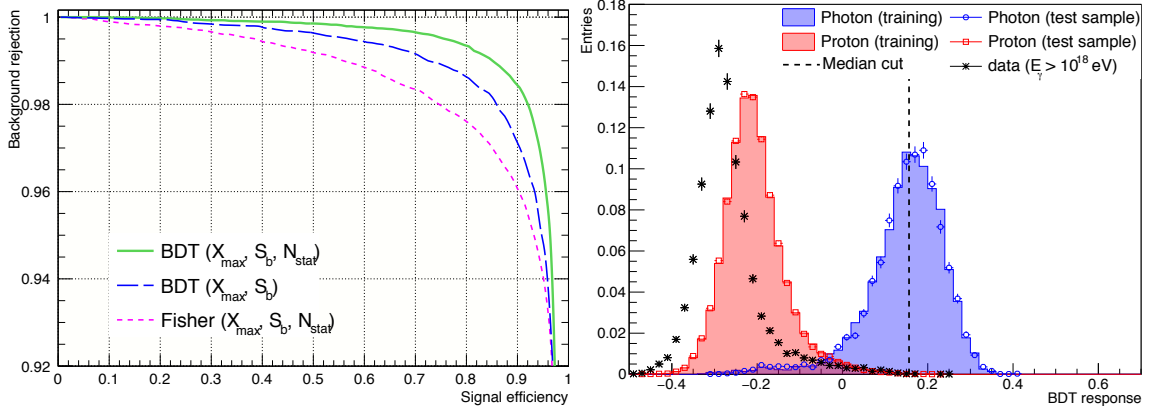


Figure 2: Left: background rejection efficiency as a function of the signal efficiency for different MVA algorithms; right: distribution of the BDT response for the signal sample (photon simulations, blue), background sample (proton simulations, red) and data (black); the photon candidate cut at the median of the photon distribution is indicated by the dashed line [5].

The analysis is then applied to hybrid data collected between January 2005 and December 2013. Selection criteria are applied to ensure a good geometry and profile reconstruction and a reliable determination of the discriminating observables. After the event selection, 8178 events remain for the analysis with energies above 10^{18} eV. The reference energy used here is the photon energy E_γ , i.e. the calorimetric energy determined from the longitudinal profile with a missing energy correction of 1% suitable for photon-induced air showers applied. The BDT response is given in Fig. 2, right, for the data and the simulated photon and proton samples for comparison. The discrepancy between the data and the proton simulations is in agreement with current experimental indications of a change to a heavier composition in the EeV range [8] and the muon deficit observed in simulations with respect to Auger data [9]. Three events pass the photon candidate cut, with 11.4 (3.3) expected for a pure-photon (mixed) background.

Since the number of selected photon candidates is compatible with the background expectation, upper limits (UL) on the integral photon flux at 95% confidence level (C.L.) are derived as:

$$\Phi_{\text{UL}}^{0.95}(E_\gamma > E_0) = \frac{N_\gamma^{0.95}(E_\gamma > E_0)}{\mathcal{E}_\gamma(E_\gamma > E_0 | E_\gamma^{-\Gamma})}, \quad (2.2)$$

where $N_\gamma^{0.95}$ is the Feldman-Cousins upper limit at 95% C.L. on the number of photon candidates assuming zero background events and \mathcal{E}_γ is the integrated exposure, derived from MC simulations, above the energy threshold E_0 , under the assumption of a power law spectrum $E^{-\Gamma}$ with $\Gamma = 2$. Upper limits to the integral photon flux are set to 0.027, 0.009, 0.008, 0.008, 0.007 $\text{km}^{-2} \text{sr}^{-1} \text{yr}^{-1}$ for energy thresholds of 1, 2, 3, 5 and 10 EeV. The three candidate events all have energies close to 1 EeV, so the observed number is zero for all but the first energy threshold. The upper limit for $E_0 = 1$ EeV has been derived under the conservative choice that the three candidate events are indeed induced by photons, as if there were no expected background. This makes the limits more robust against hadronic interaction and mass composition assumptions. Rescaling the photon flux limits by the measured all-particle spectrum [10] results in photon fraction limits of 0.1%, 0.15%, 0.33% 0.85% and 2.7% for the same energy thresholds.

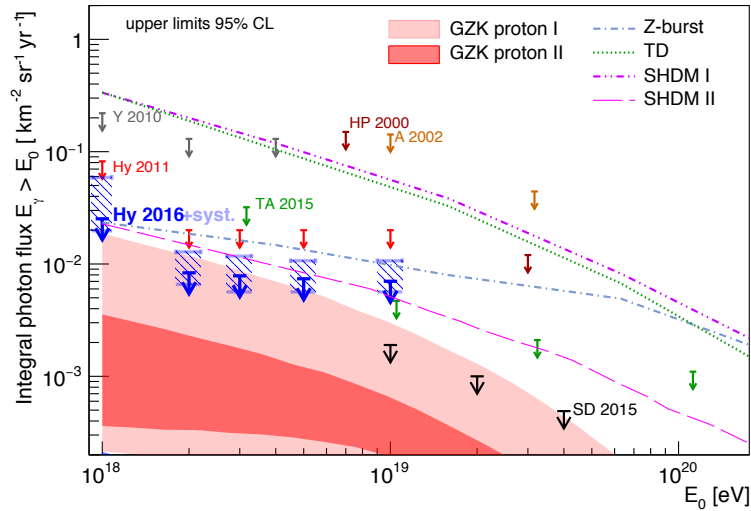


Figure 3: Upper limits on the integral photon flux derived in the analysis presented here (blue arrows, Hy 2016) [5]. The limits obtained when the detector systematic uncertainties are taken into account are indicated by the light-blue dashed boxes around the blue arrows. Also shown are the limits previously published by the Pierre Auger Observatory (Hy 2011 and SD 2015) and other experiments (Telescope Array, Yakutsk, AGASA, Haverah Park). The shaded regions and the lines give the predictions for photon fluxes from GZK-based models and several top-down models (Z-burst, topological defects, super-heavy dark matter). For a full list of references, see [5].

The upper limits derived in the analysis presented here are shown in Fig. 3 in comparison to previous results and predictions from several theoretical models. The new results lower the upper limits on the photon fraction by up to a factor 4 compared to previously published limits (Hybrid 2011 in Fig. 3), due to the larger dataset used in this analysis and the improvements in the background rejection. The robustness of the results has been tested against several sources of systematic uncertainties, for example uncertainties on the energy scale, or uncertainties in the determination of the discriminating observables. The impact of the systematic uncertainties on the upper limits are indicated in Fig. 3. The current upper limits impose tight constraints on current top-down scenarios proposed to explain the origin of UHE cosmic rays. The achieved sensitivity allows testing photon fractions of about 0.1% and exploring the region of photon fluxes predicted in some astrophysical scenarios (indicated by the shaded areas in Fig. 3).

3. Targeted search for point sources of photons

In the analysis described in the previous section, the search for UHE photons has been performed without using the reconstructed arrival direction of the recorded air shower events. Since photons, unlike charged cosmic rays, are not deflected by galactic and extragalactic magnetic fields, they point back to their production site. Since the production mechanisms for UHE photons are closely tied to UHE cosmic rays, a search for point sources of UHE photons could also help to pinpoint the sources of UHE cosmic rays. In the data, a photon point source would be detectable through an excess of photon-like events from a certain direction in the observed sky. Previously, the Pierre Auger Collaboration published a blind search for photon point sources [11]. No evidence

for an excess of photon-like events has been found for any direction in the sky. The targeted search discussed in the following section complements the blind search by restricting the analysis to pre-defined target classes to reduce the statistical penalty of many trials. Since the attenuation length of photons in the energy range considered here ($10^{17.3}$ to $10^{18.5}$ eV) varies between 90 and 900 kpc [6], these target classes contain mostly galactic sources such as, e.g., millisecond pulsars, γ -ray pulsars, and low-mass and high-mass X-ray binaries as well as the Galactic center. In addition, two nearby extragalactic target sets are included: three powerful γ -ray emitters in the Large Magellanic Cloud and the core region of Centaurus A. The different target classes are listed in Tab. 1. A more detailed description can be found in [6]. The analysis uses hybrid events from the same data period as in the search for a diffuse flux of photons (January 2005 to December 2013), but in a different energy range ($10^{17.3}$ to $10^{18.5}$ eV) to take advantage of the higher statistics at lower energies. In total, 308,676 well-reconstructed events enter the analysis. The average angular resolution of this data set is 0.7° .

To reduce the contamination of hadronic background events, photon-like air showers are selected using a BDT trained with MC simulations of photon- and proton-induced air shower events. The main input observables of the BDT are X_{\max} and S_b , similar to the search for a diffuse flux of photons described in the preceding section. These two observables are complemented by additional observables [6]: the reduced χ^2 of the fit of a Greisen function to the recorded longitudinal profile, the normalized energy derived from the Greisen function, and the ratio of the early-arriving to the late-arriving signal in the surface detector with the highest signal. Photon-like events are then selected through a cut in the BDT response β . This cut is optimized for each target direction by taking into account the expected number of background events, which has been derived using the scrambling technique [12]. Averaged over all target directions, the photon selection cut is expected to retain 81.4% of primary photons with a background rejection of 95.2%. To determine how many events arrive from a given target direction in the data sample, a top-hat counting region

Class	N	\mathcal{P}	\mathcal{P}_w	p	p^*	$f_{\text{UL}}^{0.95}$ [$\text{km}^{-2} \text{yr}^{-1}$]
msec PSRs	67	0.14	0.57	0.010	0.476	0.043
γ -ray PSRs	75	0.98	0.97	0.007	0.431	0.045
LMXB	87	0.74	0.13	0.014	0.718	0.046
HMXB	48	0.84	0.33	0.040	0.856	0.036
H.E.S.S. PWN	17	0.90	0.92	0.104	0.845	0.038
H.E.S.S. other	16	0.52	0.12	0.042	0.493	0.040
H.E.S.S. UNID	20	0.45	0.79	0.014	0.251	0.045
Microquasars	13	0.48	0.29	0.037	0.391	0.045
Magnetars	16	0.89	0.30	0.115	0.858	0.031
Gal. Center	1	0.59	0.59	0.471	0.471	0.024
LMC	3	0.62	0.52	0.463	0.845	0.030
Cen A	1	0.31	0.31	0.221	0.221	0.031

Table 1: Combined unweighted probabilities \mathcal{P} and weighted Probabilities \mathcal{P}_w for the 12 target sets [6]. In addition, selected information on the most significant target from each target set is given: the unpenalized (p) and penalized (p^*) p -values and the upper limit on the photon flux at 95% C.L.. More details on the most significant targets, e.g. the galactic coordinates and upper limits on the energy flux from this target, can be found in [6].

of 1° is used. After applying the photon selection cut, the total number of events from all target directions is 474.

A p -value p_i is assigned to each candidate source i of a target set, taking into account the observed number of events from this target direction as well as the expected number of background events. The p -values of all targets in a set are combined with and without statistical weights w_i . The weight assigned to each target is proportional to both the measured electromagnetic flux from the source (taken from astrophysical catalogs) and the directional exposure for photons, derived from simulations. The combined weighted probability \mathcal{P}_w is the fraction of isotropic simulations yielding a weighted product $\prod_i p_{i,\text{iso}}^{w_i}$ that is not greater than the measured weighted product $\prod_i p_i^{w_i}$:

$$\mathcal{P}_w = \text{Prob} \left(\prod_i p_{i,\text{iso}}^{w_i} \leq \prod_i p_i^{w_i} \right), \quad (3.1)$$

where $p_{i,\text{iso}}$ denotes the p -value of target i in an isotropic simulation. The combined unweighted probability \mathcal{P} is given by the same formula with $w_i = 1$ for all targets. The results of the analysis for each of the 12 target sets are shown in Tab. 1, along with information about the target with the smallest p -value in each set. In addition, the penalized p -values $p^* = 1 - (1 - p)^N$ are given, which is the chance probability that one or more of the N targets in the set have a p -value less than p under the assumption of a uniform probability distribution. No combined p -value (weighted and unweighted) nor any individual p -value for a target has a statistical significance as great as 3σ . No target class therefore reveals compelling evidence for photon-emitting sources in the EeV range. There is also no evidence for one outstanding target in any target set.

Upper limits on the photon flux from the targets with the smallest p -values in the sets are calculated according to

$$f_{\text{UL}}^{0.95} = \frac{n_{\text{Zech}}^{0.95}}{\varepsilon \times n_{\text{inc}}}, \quad (3.2)$$

where $n_{\text{Zech}}^{0.95}$ is the upper limit, at 95% C.L., on the number of photons obtained using Zech's method [13], ε is the directional exposure to photons and n_{inc} is the expected signal fraction within the search window. The resulting upper limits for the individual targets are listed in Tab. 1 as well.

Of particular interest is the limit on the Galactic center. The H.E.S.S. collaboration recently reported evidence for the acceleration of PeV protons in this region [14]. Fig. 4 shows the spectrum measured by H.E.S.S. in the TeV range, along with an extrapolation of this spectrum to EeV energies. This extrapolation also takes into account interactions with, for example, the CMB. The flux limit derived in the analysis presented here can severely constrain the allowed parameter space for such an extrapolation. Furthermore, assuming a power law with an exponential cutoff, an upper limit on the cutoff energy of 2EeV can be placed. The corresponding spectrum is also shown in Fig. 4.

4. Summary

So far, the extensive searches for UHE photons at the Pierre Auger Observatory have not yielded an unambiguous detection of photons at these energies. The upper limits on the diffuse flux of photons presented here are the most stringent limits to date, severely constraining top-down models for the origin of UHE cosmic rays. The targeted search for photon point sources likewise

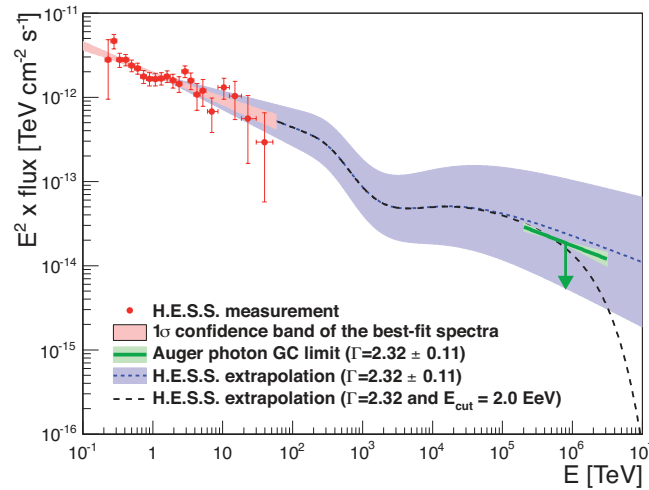


Figure 4: Photon flux as a function of energy from the Galactic center region [6]. The flux measured by H.E.S.S. in the TeV range [14] is shown in red, as well as the extrapolation to the EeV range (blue dashed line). The upper limit on the flux derived in the analysis presented here is given in green. A spectrum with an exponential cutoff at 2 EeV is shown as the black dashed line.

yielded no evidence for EeV photon emitters in any of the studied source classes. However, the connection to measurements from the TeV range enables new multi-messenger studies, for example in studies of the Galactic center.

References

- [1] F. Aharonian, et al., *Astron. Astrophys.* 464 (2007) 235.
- [2] The Pierre Auger Collaboration, *Phys. Rev. Lett.* 101 (2008) 061101.
- [3] M. Risse and P. Homola, *Mod. Phys. Lett. A* 22 (2007) 749.
- [4] The Pierre Auger Collaboration, *Nucl. Instr. Meth. Phys. Res. A* 798 (2015) 172.
- [5] The Pierre Auger Collaboration, *J. Cosmol. Astropart. Phys.* 04 (2017) 009.
- [6] The Pierre Auger Collaboration, *Astrophys. J.* 837 (2017) L25.
- [7] G. Ros, et al., *Astropart. Phys.* 35 (2011) 140.
- [8] The Pierre Auger Collaboration, *Phys. Rev. D* 90 (2014) 122005.
- [9] The Pierre Auger Collaboration, *Phys. Rev. D* 91 (2015) 032003.
- [10] I. Valiño for the Pierre Auger Collaboration, *PoS(ICRC2015)* 271.
- [11] The Pierre Auger Collaboration, *Astrophys. J.* 789 (2014) 160.
- [12] G. L. Cassiday, et al., *Nucl. Phys. Proc. Suppl.* 14A (1990) 291.
- [13] G. Zech, *Nucl. Instr. Meth. Phys. Res. A* 277 (1989) 608.
- [14] The H.E.S.S. Collaboration, *Nature* 531 (2016) 476.



Searches for neutrino fluxes in the EeV regime with the Pierre Auger Observatory

Enrique Zas^{*a} for the Pierre Auger Collaboration^b

^a*Depto. Física de Partículas & Instituto Galego de Física de Altas Enerxías, Universidade de Santiago de Compostela, 15782 Santiago de Compostela, Spain*

^b*Observatorio Pierre Auger, Av. San Martín Norte 304, 5613 Malargüe, Argentina*

E-mail: auger_spokespersons@fnal.gov

Full author list: http://www.auger.org/archive/authors_icrc_2017.html

The Pierre Auger Observatory has been used to search for neutrinos of energy exceeding 100 PeV by looking for inclined showers that develop deep in the atmosphere. Neutrinos of any flavor interacting deep in the atmosphere and triggering the Auger surface detector can be identified provided their zenith angles exceed 60° . Also tau neutrinos that enter the Earth's crust with a zenith angle close to 90° can interact and produce a tau that decays in the atmosphere inducing an “upward-going” shower that triggers the surface detector. The sensitivity obtained summing up these channels is shown to be comparable to other neutrino detectors in operation, and to constrain several models of cosmic-ray and neutrino production in the EeV region. The declination field of view for neutrino searches in these two channels spans from about -80° to 60° in equatorial coordinates. The Observatory has also been used for searches for neutrinos from point-like sources in the sky. We finally report on the results of the search for neutrino fluxes in coincidence with the gravitational wave events GW150914, GW151226 and GW170104 recently discovered with Advanced LIGO, and on their implications for the total energy emitted in EeV neutrinos by black hole merger events.

*35th International Cosmic Ray Conference — ICRC217
10–20 July, 2017
Bexco, Busan, Korea*

^{*}Speaker.

1. Introduction

Neutrinos of $\sim 10^{18}$ eV (1 EeV) are expected from interactions of Ultra-High Energy Cosmic Rays (UHECR) in the sources or during propagation through the Universe. Having no charge they point to their production sites even when they are shielded by large amounts of matter. Their energy spectrum is related to cosmic ray composition at the highest energies which is largely unknown [1]. As extraterrestrial neutrinos of several PeV have already been detected [2], extending the spectrum measurement to the EeV region is most natural to effectively constrain the production mechanisms of UHECR. Their detection would allow neutrino interactions to be probed at energies many orders of magnitude above those searched in accelerators and information about flavor ratios will further constrain the production mechanisms and may even signal new physics.

The Pierre Auger Observatory consists of a 3000 km² array of water-Cherenkov detectors (SD) in a hexagonal grid of 1.5 km spacing to detect the particle front of air showers and a Fluorescence Detector (FD) that monitors the fluorescence emission of Nitrogen over this surface. It is located in Mendoza, Argentina, at an average latitude of 35.5° S and at a mean atmospheric depth (altitude) of 875 g/cm² (1400 m) [3]. It has been running and taking data since its construction started in 2004. The SD can be used to detect down-going EeV neutrino interactions in the atmosphere [4] (DG) and Earth-skimming [5] (ES) tau neutrinos. The interaction of nearly horizontal ES tau neutrinos in the Earth produces a tau lepton that can exit to the atmosphere and decay producing an air shower. This channel is most sensitive between ~ 0.1 and 25 EeV where cosmological neutrinos (due to cosmic rays interactions with the Cosmic Microwave Background) are expected.

2. Searching for UHE neutrinos at the Pierre Auger Observatory

Atmospheric showers produced by inclined neutrinos (both ES and DG) that develop deep in the atmosphere can be distinguished from showers due to cosmic rays that interact in the upper layers. The signal of the SD stations is digitized in 25 ns time bins allowing a detailed measurement of the time profile of the shower front. In contrast, the electromagnetic component of inclined cosmic ray showers gets absorbed and only the muon component reaches ground level. These showers, that are regularly detected and reconstructed [6], consist of ~ 20 to 200 GeV energy muons that travel nearly parallel to the shower axis and undergo few interactions. As a result they accumulate small time delays and deposit the energy in a short time, while deep neutrino showers produce signals with a much broader time spread. This provides the basis for neutrino identification [4]. As the zenith angle rises it becomes easier to separate the neutrino candidates because the total slant depth of the atmosphere increases making the differences more patent.

The searches for ES and DG events require independent procedures for event selection, neutrino identification and exposure calculation. Extensive simulations of neutrino events are made varying the energy, zenith and azimuth angles, depth of interaction and impact parameter of the neutrino and, in the ES case, the tau lepton decay altitude. The response of the SD is also simulated with standard software. The search strategy involves a pre-selection of inclined events followed by a selection of neutrino candidates based on a single optimized variable. A cut value is decided a priori comparing the distributions of this variable for simulated neutrino events to that of a selected background of cosmic ray showers, taken from a small fraction of the data. Simulated neutrino

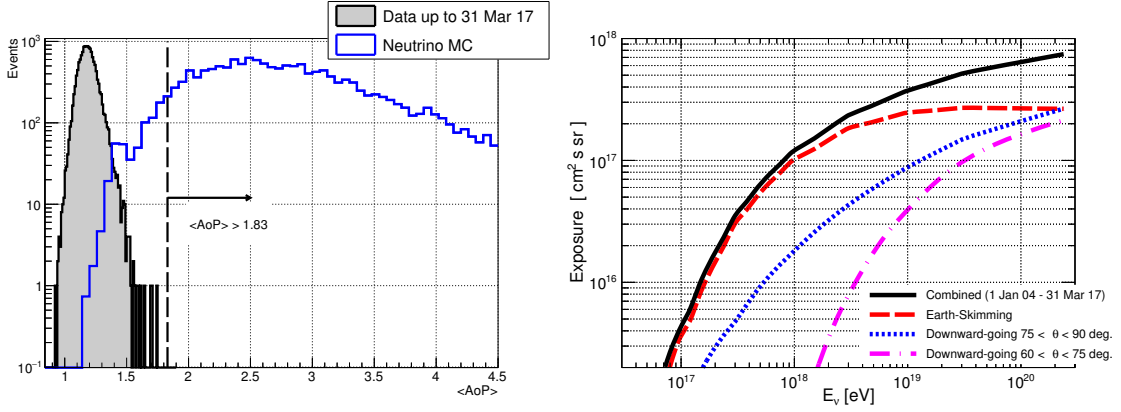


Figure 1: Left: Distributions of $\langle \text{AoP} \rangle$ after ES selection. The shaded histogram is the data up to 31 Mar 2017 (excluding the data used to select the cut) and the empty blue histogram are simulated ES ν_τ events. The vertical line represents the cut on $\langle \text{AoP} \rangle > 1.83$ to search for candidates.

Right: Total exposure (solid) as a function of neutrino energy and contributions of the ES (dashes), DGH (dots) and DGL (dot dashes) searches at Earth assuming equal fluxes for all neutrino flavors.

events and background are treated with the same selection and identification procedures. The efficiency of the neutrino search, needed to calculate the exposure, is obtained as the ratio of neutrino candidates to the total number of simulated neutrinos as a function of the relevant variables.

For optimization purposes inclined data are searched in three different zenith angle ranges. (1) Earth skimming tau neutrinos (ES) can be detected only with zenith angles between 90° and 95° . The ES selection requires a minimum of three stations, a high eccentricity of the elliptic shape of the triggered area on the ground and an apparent speed of the trigger times between station pairs with an average value very close to c and a small spread. (2) The selection of DG neutrinos between 75° and 90° (DGH) is made for events with at least 4 stations using the same variables as the ES selection with less stringent cuts. In addition the zenith angle of a plane fit must exceed 75° . (3) To select DG neutrinos between 60° and 75° (DGL) the reconstructed zenith from a plane front fit is required to be in the 58.5° to 76.5° range to allow for reconstruction tolerances in the simulated neutrino events (see [7] for full details).

To separate neutrinos from cosmic ray showers, observables have been chosen related to the width of the signal trace, particularly the Area over Peak (AoP) of the digitized signal. For the ES selection the average AoP of the triggered stations ($\langle \text{AoP} \rangle$) is chosen as a discrimination variable [7]. For the DG cases a Fisher discriminant approach is used combining up to 10 variables using the AoP of 4 (4 or 5) early (central) stations in the DGH (DGL) selections [7]. The critical value of the discrimination variable (above which events are classified as potential neutrino candidates) is chosen in each case using the distribution of background events, obtained from a small fraction of the data, assumed to be overwhelmingly (if not totally) made up of cosmic ray showers. These distributions have an exponential tail which can be easily extrapolated to obtain the parameter value corresponding to a background rate of one event every 50 years for the full SD array. A further subdivision based on the zenith angle (number of triggered SD stations) is made in the DGL (DGH) selection to select the cut in the corresponding discriminant variable. The AoP distribution for ES events is shown in Fig. 1. No neutrino candidates have been found.

3. Exposure calculation and neutrino bounds

To obtain a bound on the diffuse flux, the integral of the interaction and detection probabilities over surface area, solid angle and time is calculated as a function of neutrino energy. This quantity is the effective exposure which, convolved with a given neutrino flux spectrum, gives the expected number of events.

For ES tau neutrinos the probability of the tau lepton exiting the Earth is calculated as a function of arrival direction and tau energy using a propagation code for the tau neutrinos in rock that accounts for neutral and charged current interactions and includes regeneration. This probability is convolved with two others, that of the tau decaying which is a standard exponential and that of triggering, selecting and identifying the neutrinos which is obtained from simulations. Both depend on the decay position of the tau lepton. The exposure is obtained integrating over area, arrival direction, time and distance to the decay. For the DG case the calculation just involves an integral over area, arrival direction, interaction depth and time of the probabilities for interaction and for the trigger, selection and identification. Different channels must be considered depending on neutrino flavor and interaction type because the energy transfers to the shower are different. Three calculations are required: neutral current interactions, charged current electron neutrino interactions and charged current tau neutrino interactions. Charged current interactions of muon neutrinos are treated identically to neutral currents of all flavor neutrinos concerning the energy transfer, since the atmospheric shower is induced by the nuclear fragments.

The data set that has been used for all searches presented here spans the period from 1 Jan 2004 to 31 March 2017. A small fraction of the data is excluded because it corresponds to unusual periods in which the array was unstable. This period includes the *un-blinding* of nearly four years of data compared to previous results [7]. To account for the changing of array configuration particularly throughout the construction phase, the time integral is performed sampling the effective probabilities over real array configurations chosen every three days. As the area over which the neutrino flux is simulated always exceeds that of the array, the procedure also accounts for edge effects and occasional missing stations. The results of the exposure calculations for the ES, DGH and DGL searches and the combined exposure assuming all neutrino flavors have the same weight are displayed in Fig. 1. The figure illustrates that the Earth-skimming neutrinos dominate the exposure in spite of the reduced solid angle to which the detector is sensitive.

3.1 Limits to diffuse fluxes of UHE neutrinos

In the Feldman-Cousins approach if no events are observed the 90% C.L. limit is set for a flux predicting 2.39 events. The limits for a diffuse isotropic flux of single flavor neutrinos are shown in Fig. 2 using a semi-Bayesian extension of this approach to account for the systematic uncertainties. Two types of bounds are calculated: An integral bound is obtained integrating a conventional kE^{-2} neutrino spectrum, giving $k < 5 \times 10^{-9} \text{ GeV cm}^{-2} \text{ s}^{-1}$. It is conventionally plotted from 0.1 to 25 EeV, corresponding to the range in which 90% of the events are expected. A differential bound is calculated integrating the neutrino flux over consecutive energy bins of 0.5 in $\log_{10} E_\nu$. It clearly indicates that the SD is particularly well suited for detecting cosmological neutrinos resulting from interactions of UHE protons with the Cosmic Microwave Background. The obtained limits are compared to those from current neutrino telescopes in the equal flavor scenario.

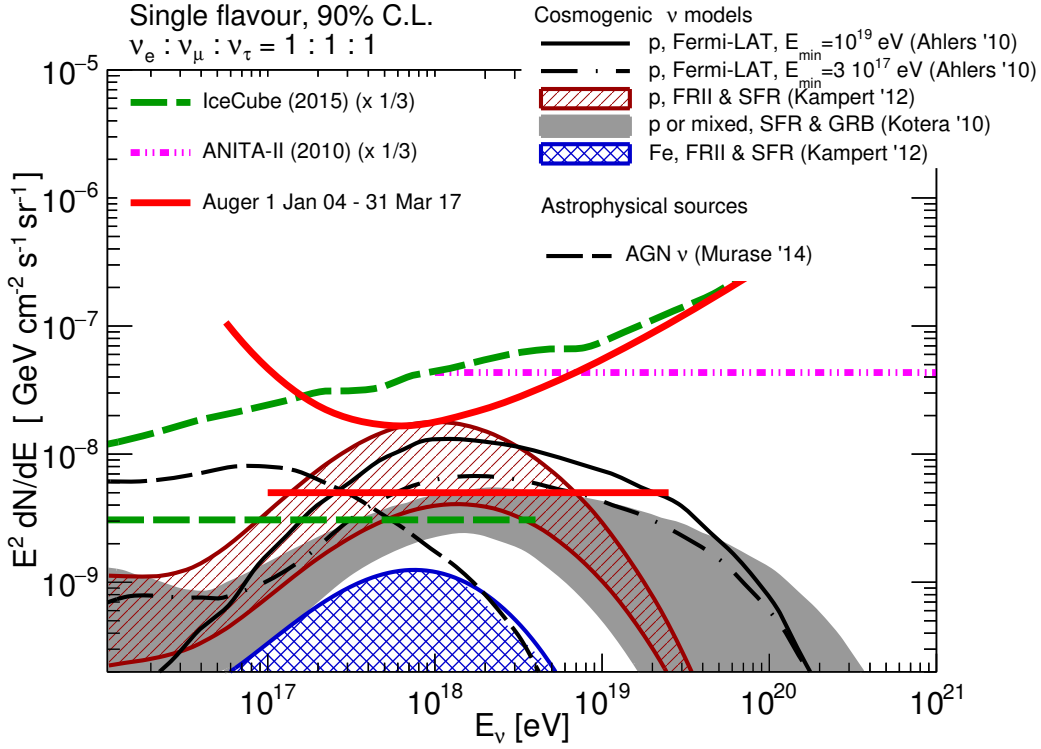


Figure 2: Integral upper limit (at 90% C.L.) for a diffuse neutrino flux of UHE $dN/dE_\nu = kE^{-2}$ given as a normalization, k , (straight red line), and differential upper limit (see text). Limits are quoted for a single flavor assuming equal flavor ratios. Similar limits from ANITAII [8] and IceCube [9] are displayed along with prediction for several neutrino models (cosmogenic [10, 11, 12], astrophysical [13].)

3.2 Limits to point-like sources of UHE neutrinos

The Earth-skimming channel is very effective at converting the tau neutrinos into exiting tau leptons when the arrival direction is very close to the horizontal. It can be shown that over 90% ($\sim 100\%$) of the ES exposure is obtained for zenith angles between 90° and 92.5° (95°). As a result the sky coverage provided by these interactions reaches declinations between -54.5° and 59.5° . The DG selections enhance the visible declination band towards the south all the way to -84.5° covering a large fraction of the sky. The exposure as a function of zenith can be converted to an average exposure for a given declination integrating in right ascension. It displays strong peaks for the ES selection close to two extreme declinations apparent in the obtained bounds.

The non-observation of neutrino candidates is cast into a bound on point sources which is calculated as a function of declination, δ , also assuming a flavor ratio of 1:1:1. The results are displayed in Fig. 3, for the first time combining the three searches and for data that have an increase of about seven years of full exposure over previous results [15].

3.3 Targeted searches for correlations with the GW events

The reported detection of gravitational wave events produced by binary Black Hole (BH) mergers by the Advanced Ligo Collaboration has triggered a targeted search for coincidence events that would complement these observations. BH mergers could accelerate cosmic rays to the high-

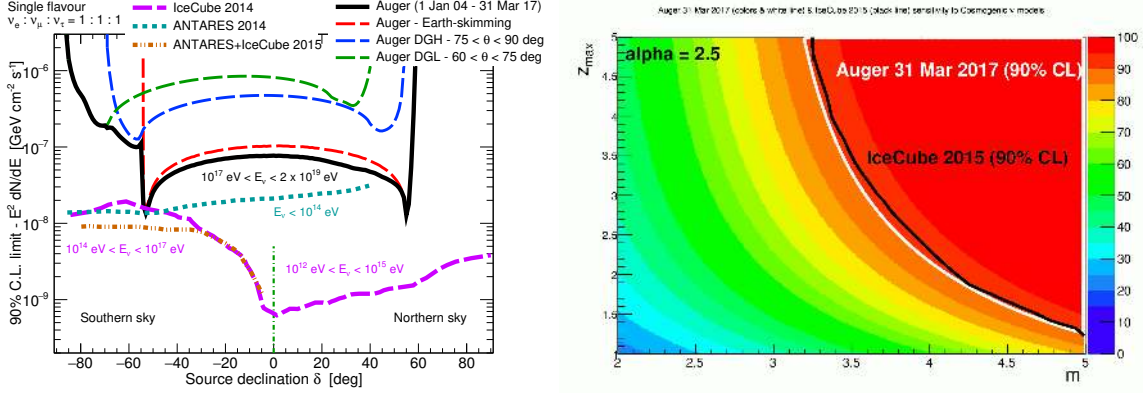


Figure 3: Left: Upper limits at 90% C.L. for k^{PS} as a function of the source declination for ES, DGH and DGL searches as labeled (assuming a single flavor point-like flux of UHE neutrinos $dN/dE_v = k^{\text{PS}} E_v^{-2}$). Also shown are the sensitivities for IceCube [16], ANTARES [17] and a combination of both [18]. Note the different energy ranges. Right: Constraints on parameter space for cosmological neutrinos in proton models (assuming a power-law $dN/dE \propto E^{-2.5}$) as a function of m (source evolution) and z_{max} (maximum redshift of the sources) following [22]. Colored areas represent different confidence levels of exclusion. The region above the black (white) line is excluded at 90% C.L. by IceCube [9] (Auger) data.

est energies and produce neutrinos provided there are magnetic fields and disk debris from the progenitor stars [19]. A search has been made for EeV events in the data collected with the Observatory and correlated in time and position with events GW150914, GW151226, GW170104 and the candidate event LVT151012. In each case two time windows have been considered to search for coincident neutrino events. One is of ± 500 s about detection time, motivated by an upper limit to the duration of the prompt phase of Gamma Ray Bursts (GRB) and the second one a single day after the event, motivated by an upper limit to the duration of GRB afterglows [20].

The directionality of the neutrino exposure makes the effectivity of the search quite dependent on the event position. Since this position is only known as a broad region of hundreds of square degrees, the results are given as a function of the event declination. The calculation of the exposure for each class of events is similar to that obtained for point source searches but the time integral is now limited to the preselected search window. It is only accounted for to the extent the source is visible in each one of the three zenith angle ranges considered.

Because of the zenith angle restrictions the visible part of the sky is limited at any instant as shown in Fig. 4 left. When we consider the short time-window, the 90% C.L. position of GW150914 has only a marginal overlap with the corresponding sky coverage of the Observatory for the DGH selection. A resulting bound could only be obtained if the position of the event was known to be in the overlapping region. The situation with GW151226, GW170104 and LVT151012 is different since there is a substantial overlap between the sky coverage with both with ES and DG searches and the reported positions, particularly for GW151226 (see Fig 4). No inclined background showers from cosmic rays were actually observed at all during the 1000 s-wide window around any of the GW events.

For the one-day period the instantaneous exposure is averaged over a sidereal day GW150914, GW170104 and LVT151012 have large overlap with the sky coverage of the Observatory and for

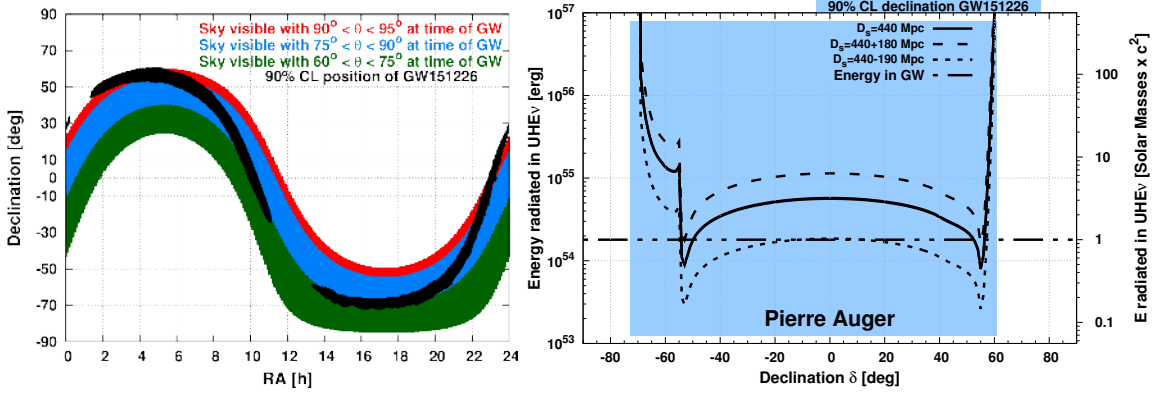


Figure 4: Left: Instantaneous sky coverage of the different selections as labeled at the time of the detection of GW151226. The black contour region corresponds to the 90 % C.L. region for the GW event location. Right: Constraints on the radiated energy in UHE neutrinos (per flavor) from the source of GW151226 as a function of δ [20]. Energies above the solid line are excluded at the 90% C.L.. The calculation is done for a distance $D_s = 410$ Mpc (dashed lines correspond to reported distances at the 90% C.L.). The dot-dashed horizontal line represents $E_{GW} \simeq 1.9 \times 10^{54}$ erg, the inferred energy radiated in gravitational waves for that event [21]. The shaded region indicates the 90% C.L. region for the GW event location.

GW151226 practically all the 90% C.L. declination band of the event is covered as illustrated by the shadowed band in Fig. 4. Inclined showers were observed within a day of the detected events but these were completely consistent with those expected from UHE cosmic rays.

A bound can be obtained assuming an E^{-2} spectrum. The 90% C.L. upper bound to the flux is obtained by fixing the normalization to expect 2.39 events. A bound can also be obtained on the total energy radiated in neutrinos using the luminosity distances quoted for the events, illustrated in Fig. 4 for GW151226. Bounds for GW150914 are better in relation to the GW energy radiated [20] while for GW170104 they are weaker because the event is located further away [21].

4. Summary and Discussion

The Auger Observatory is effective at searching for neutrinos of energies exceeding 0.1 EeV selecting inclined showers that have significant electromagnetic component. The search for neutrinos has given differential and integrated (assuming an E^{-2} spectrum) bounds to diffuse and point source fluxes using data from 1 Jan 2004 to 31 March 2017 and assuming equal flavor ratios. Precise statements about given models require folding the exposure with the model spectrum to obtain the expected number of events. Different models for cosmogenic neutrinos that attempt to explain the origin of cosmic rays are excluded at the 90% C.L., particularly those that assume proton primaries and attribute a strong evolution with redshift to the sources comparable to that of Fanaroff-Riley type II (FRII) galaxies [12, 11]. Some models that normalize the proton flux to the diffuse GeV gamma-ray flux measured by FERMI-LAT [10] are also excluded. A model that assumes protons with moderate evolution close to that of SFR [14] is disfavored while others [12, 11, 14] assuming heavier primaries would need a significant increase in exposure to become excluded. Some astrophysical models are also excluded at 90% C.L. for instance that assuming cosmic ray acceleration in radio-loud AGN [13].

It is possible to use a conservative analytical approximation of the cosmogenic neutrino flux so that exclusion plots can be made as functions of the most relevant parameters, namely m , the source evolution, z_{\max} , the maximum redshift to which the cosmic ray production is integrated, α , the spectral index, and E_{\max} , and the maximum energy of the cosmic ray flux [22, 23]. The corresponding plot for a spectral index of 2.5 and for $E_{\max} = 300$ EeV is shown in Fig. 3.

Finally new limits on steady point sources have also been obtained and a targeted search for correlations with the gravitational wave events from Black Hole mergers have yielded limits on a possible UHE neutrino emission and on its energy budget. These limits help to constrain all kinds of models as part of a multi-messenger approach.

References

- [1] D. Martello for the Pierre Auger Collaboration; these proceedings.
- [2] M.G. Aartsen *et al.*, *Phys. Rev. Lett.* **113**, 101101 (2014).
- [3] A. Aab *et al.*, *Nucl. Instrum. Meth. A* **789**, 172 (2015).
- [4] K.S. Capelle *et al.*, *Astropart. Phys.* **8**, 321 (1998).
- [5] X. Bertou *et al.*, *Astropart. Phys.* **17**, 183 (2002).
- [6] A. Aab *et al.*, *JCAP* **1408**, 019 (2014).
- [7] A. Aab *et al.* [Pierre Auger Collaboration], *Phys. Rev. D* **91**, 092008 (2015).
- [8] P.W. Gorham *et al.* [ANITA Collaboration], *Phys. Rev. D* **85**, 049901(E) (2012).
- [9] M.G. Aartsen *et al.* [IceCube Collaboration], *Phys. Rev. Lett.* **117**, 241101 (2016).
- [10] M. Ahlers *et al.*, *Astropart. Phys.* **34**, 106 (2010).
- [11] K.-H. Kampert and M. Unger, *Astropart. Phys.* **35**, 660 (2012).
- [12] D. Allard *et al.*, *JCAP* **10**, 013 (2010).
- [13] K. Murase, Y. Inoue, and C.D. Dermer, *Phys. Rev. D* **90**, 023007 (2014).
- [14] R. Aloisio, *et al.*, *JCAP* **1510**, 006 (2015).
- [15] P. Abreu *et al.*, *Astrophys. J.* **755**, L4 (2012).
- [16] M.G. Aarsten *et al.*, *Astrophys. J.* **796**, 109 (2014).
- [17] S. Adrian-Martinez *et al.* [ANTARES Collaboration], *Astrophys. J. Lett.* **786**, L5 (2014).
- [18] S. Adrian-Martinez *et al.*, *Astrophys. J.* **823**, 65 (2016).
- [19] K. Kotera and J. Silk; *Astrophys. J.* **823**, L29 (2016).
- [20] A. Aab *et al.*, [Pierre Auger Collaboration], *Phys. Rev. D* **94**, 122007 (2016).
- [21] B.P. Abbott *et al.*, [LIGO Scientific Collaboration and Virgo Collaboration], *Phys. Rev. Lett.* **116**, 061102 (2016); *ibid.* **116** 241103 (2016); *ibid.* **118** 221101 (2017).
- [22] S. Yoshida and A. Ishihara, *Phys. Rev. D* **85**, 063002 (2012).
- [23] M.G. Aartsen *et al.*, *Phys. Rev. Lett.* **117**, 241101 (2016).

4

Hadronic Interactions and Shower Physics





Measurements of the depth of maximum muon production and of its fluctuations in extensive air showers above 1.5×10^{19} eV at the Pierre Auger Observatory

Manuela Mallamaci^{*a} for the Pierre Auger Collaboration^b

^a*INFN, Sezione di Milano, Italy*

^b*Observatorio Pierre Auger, Av. San Martín Norte 304, 5613 Malargüe, Argentina*

E-mail: auger_spokespersons@fnal.gov

Full author list: http://www.auger.org/archive/authors_icrc_2017a.html

The surface detector array of the Pierre Auger Observatory measures the arrival time distribution of particles, providing indirect information on the longitudinal development of the muonic component of extensive air showers. In this work, the depth at which the muon production is maximum and the corresponding fluctuations are reconstructed for more than 2000 events above 1.5×10^{19} eV, in a wide range of zenith angles, between 45° and 65° . Both observables are exploited to gain insight about the most up-to-date hadronic interactions models, which are used in the simulation of extensive air showers. By constraining the models, these observables could allow one to obtain better information on high energy hadronic interactions, and therefore they could indirectly help for the mass composition study of ultra-high energy cosmic rays, one of the most intriguing issues of modern astrophysics.

*35th International Cosmic Ray Conference — ICRC2017
10–20 July, 2017
Bexco, Busan, Korea*

*Speaker.

1. Introduction

In recent decades, the advent of detectors reaching apertures as large as tens of thousands $\text{km}^2 \text{sr yr}$ have significantly improved our knowledge of the Ultra-High Energy Cosmic Rays (UHECRs). Among the most significant results, the extremely precise measurement of the UHECR flux at the Pierre Auger Observatory has to be mentioned [1]. Also our understanding of mass composition of UHECRs makes a considerable progress. In particular, the data taken by the Fluorescence Detector (FD) at the Pierre Auger Observatory have shown a trend from a light composition at the ankle of the spectrum to a heavier one for increasing energies [2, 3]. This conclusion is reinforced by exploiting Surface Detector (SD) data analyses [4] and by correlations among different observables measured by both FD and SD [5]. In this context, it has to be mentioned that the interpretation of the results depends crucially on the Monte Carlo simulation of Extensive Air Showers (EAS) and therefore on the accuracy of the modeling of hadron-air collisions at high energies. Even if a considerable progress has been done [6], the reliability of EAS simulations is the largest source of systematic uncertainty in the determination of the mass composition of UHECRs.

In this work, the SD has been exploited to reconstruct the so-called *Muon Production Depth* (MPD), i.e. the longitudinal profile of muons produced in EAS. The MPD turned out to be meaningful, being sensitive to the primary composition and in particular to the details of hadronic interactions. This is the reason why it is considered a potential tool for constraining the models used for the simulation of EAS [6, 7].

A first analysis of the MPD was performed in [8], considering events above 2×10^{19} eV, arriving with large zenith angles ($55^\circ \leq \theta \leq 65^\circ$) and considering stations far from the shower core ($r > 1700$ m), where the electromagnetic component is almost completely absorbed.

In the present work, a new method is used to reconstruct the MPD on a wider range of energies, arrival directions and distances from the shower core [9, 10]. It will be discussed in Sec. 2, focusing on the evaluation of X_{max}^μ , i.e. the atmospheric depth at which the muon production rate reaches a maximum in EAS, and on the corresponding fluctuations. The results on data will be presented in Sec. 3.

2. Reconstruction of the distribution of the muon production depths

The time structure of the muonic component of a shower can be exploited to obtain the distribution of muon production distances along the shower axis. This carries information about the nature of the primary UHECR and about the longitudinal development of the hadronic component of the EAS. The muonic longitudinal profile is reconstructed in terms of production depth X , i.e. the total amount of traversed matter in g/cm^2 . This quantity is easily related to the production height z , by taking into account the atmospheric density profile $\rho(z)$,

$$X(z) = \int_z^\infty \rho(z') dz'. \quad (2.1)$$

For each UHECR event, the set of depths X where muons are produced forms the MPD distribution. It has to be underlined that only muons surviving the passage through the atmosphere can be detected at ground. Therefore, the so-called *apparent* MPD profile will be measured. The maximum of this distribution is X_{max}^μ .

In this work, the MPD is reconstructed for EAS arriving with zenith angle $45^\circ \leq \theta \leq 65^\circ$, for energies larger than 1.5×10^{19} eV and considering all muons arriving at radial distances from the shower core $r > 1200$ m. Considering the above mentioned ranges and the realistic measurement conditions, the reconstruction of the MPD is a combination of different ingredients [9, 10], which are summarized below.

- The electromagnetic component must be removed in order to isolate the muonic signal in the FADC traces recorded by the SD stations. This step is mandatory, because of the significant contamination affecting especially events with low zenith angles. The background removal is implemented by means of a smoothing algorithm, based on the difference between the spiky structure of the muonic signals as compared to the smoother electromagnetic ones. In addition, a time cut on recorded traces allows one to get rid of the unavoidable background of high energy γ -rays ($E > 300$ MeV). These procedures are both applied on FADC traces recorded by the SD stations with $r > 1200$ m. This choice is related to the next point.
- Once the muonic signal is extracted, the production depth X must be evaluated. This is obtained by using a theoretical model developed in [11]. According to simple assumptions, the equation for the production height, z , is derived,

$$z = \frac{1}{2} \left(\frac{r^2}{ct_g} - ct_g \right) + \Delta - \langle z_\pi \rangle, \quad (2.2)$$

where t_g is the time delay of muons with respect to a shower front plane traveling at light speed, Δ is the distance from the shower front plane to the muon impact point at ground and $\langle z_\pi \rangle$ is the pion decay length. t_g , the *geometric delay*, is given by $t_g \simeq t - t_\epsilon$, where t is the total delay measured by the SD and t_ϵ is the *kinematic delay* due to the sub-luminal muon velocities. This quantity must be parametrized, as the SD does not measure particle energies. In this work, a parametrization based on the post-LHC hadronic interaction models, QGSJetII-04/EPOS-LHC, is used. It takes into account the dependence of t_ϵ on the zenith angle θ , on the radial distance r and on the muon production height z . At ground level, a limited range of core distances must be considered to keep the contribution of the kinematic delay low. A cut for $r < 1200$ m ensures $t_\epsilon < 0.2t_g$.

By simulating the reconstruction conditions, it has been found that the MPD profiles are distorted by detector effects, like the light propagation inside the detector and the electronics response. These effects smear the muon arrival times, causing an uncertainty which results in an uncertainty in X and therefore in a distortion of the reconstructed MPD distribution. This can be compensated on average by subtracting to each time bin a global time offset, $T_{\text{shift}} = 60$ ns. Its value is independent of energy and zenith angle and it is related to the decay time of the muon signal in the SD station [9, 10].

- For each event, the reconstructed MPD profile is fitted by means of the Universal Shower Profile (USP) function [12],

$$\frac{1}{N} \frac{dN}{dX} = \left[1 + \frac{R}{L} (X - X_{\text{max}}^\mu) \right]^{R-2} \exp \left(-\frac{X - X_{\text{max}}^\mu}{LR} \right), \quad (2.3)$$

where X is the slant depth defined by Eq. (2.1) and there are four parameters: N is the number of muons, X_{max}^μ is the point along the shower axis where the muon production reaches its maximum,

L represents the profile width and R quantifies the deformation of the profile with respect to a Gaussian distribution. The best set of parameters is obtained through a log-likelihood minimization of the USP function. Because of the discrete sampling (the SD stations are indeed separated by 1.5 km and have a finite collecting surface; in addition we select stations with $r > 1200$ m from the core), the number of muons is much lower than in the ideal case and this limits the efficiency of the estimation of X_{\max}^{μ} with a free parameter fit. The asymmetry parameter R is therefore fixed as a function of the zenith angle, on an event by event basis. Indeed it depends on the zenith angle, and also on the nature of the primary and the hadronic interaction model. For this reason, $R = f(\theta)$ has been determined with Monte Carlo on a mixed sample of proton/iron-induced showers, based on QGSJetII-04/EPOS-LHC. A second reconstruction based on a more flexible fit has been used to estimate the possible systematic uncertainty by such optimization.

- A set of selection cuts is used in order to have a sample of well-reconstructed events. First of all, only fully contained events are considered, by requiring that the SD station with the highest signal be surrounded by six closest and fully operational neighbors. In addition, at least 5 stations with signal larger than 3 VEM (Vertical Equivalent Muon) are required to contribute to the reconstruction. This avoids trigger fluctuations and minimizes the impact of accidental signals. Finally, a set of quality criteria is applied after the fit procedure. In particular, for converging fits, L is required to be between 130 and 415 g/cm², a range chosen as a three-sigma limit on its distribution for both data and Monte Carlo simulations. This allows one to discard events for which the MPD distribution is not well reconstructed in the first part or in the tail, leading to unphysical values for the parameter L . In addition, events with a relative uncertainty $(\delta X_{\max}^{\mu} \sqrt{\chi_*^2})/X_{\max}^{\mu} \geq \epsilon_{\max}$ are rejected, where δX_{\max}^{μ} and χ_*^2 are respectively the error on the parameter and the reduced χ^2 of the fit. ϵ_{\max} goes from 28% to 18%, depending on the energy, since the reconstruction improves with it, and its value is chosen as a three-sigma limit on the $(\delta X_{\max}^{\mu} \sqrt{\chi_*^2})/X_{\max}^{\mu}$ distribution, obtained on a mixed sample of proton/iron-induced showers. The overall selection efficiency, i.e. the number of events which pass the quality criteria, is larger than 90% (on both data and simulations) and the difference in efficiency between proton and iron simulated events is smaller than 5% at all energies, zenith angles, and for both hadronic interaction models.

Fig. 1 shows a typical simulated MPD histogram, after the reconstruction procedure here described. The USP fit is superimposed and the reconstructed maximum is indicated in the inset of the figure as $X_{\max}^{*\mu}$. The performances of the reconstruction have been evaluated on Monte Carlo by defining a *bias*, as the difference $X_{\max}^{*\mu} - X_{\max,MC}^{\mu}$, where $X_{\max}^{*\mu}$ is the MPD maximum reconstructed with all the ingredients listed above, and $X_{\max,MC}^{\mu}$ is instead obtained at the generation level (i.e. in the ideal condition in which X is a known quantity).

The bias and the corresponding resolution of the measurement are reported in Fig. 2 (respectively left and right panel) as a function of the primary energy, for a set of proton and iron-induced showers simulated with CORSIKA and QGSJetII-04/EPOS-LHC models [9, 10]. By looking at Fig. 2 (left), one can see how the reconstruction depends on the primary mass and hadronic model. This mass/model-dependent performance is due to a combination of factors, like the parametrization of the kinematical delay, the fitting procedure and detector effects like the time response of the SD stations. For what concerns the detector resolution, it improves with the energy and with the

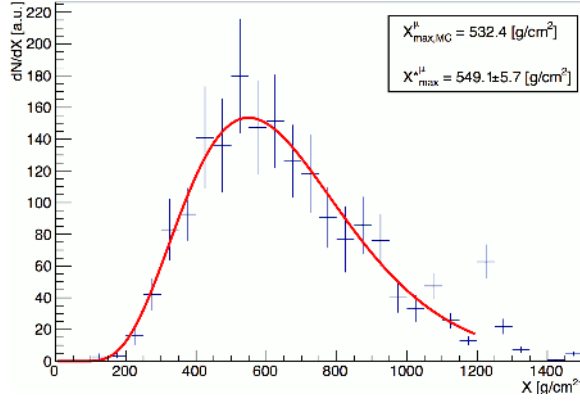


Figure 1: Example of a MPD distribution and USP fit (red line) for an iron-induced air shower simulated with CORSIKA and EPOS-LHC model, $\log_{10}(E/\text{eV}) = 19.65$, $\theta = 55^\circ$. The MPD is determined through complete shower simulation and reconstruction, using Auger Offline software and the procedure described in Sec. 2 (see text for the details). The inset shows the values for $X_{\text{max,MC}}^\mu$ and $X_{\text{max}}^{*\mu}$, which are respectively obtained at generation level and after the reconstruction chain.

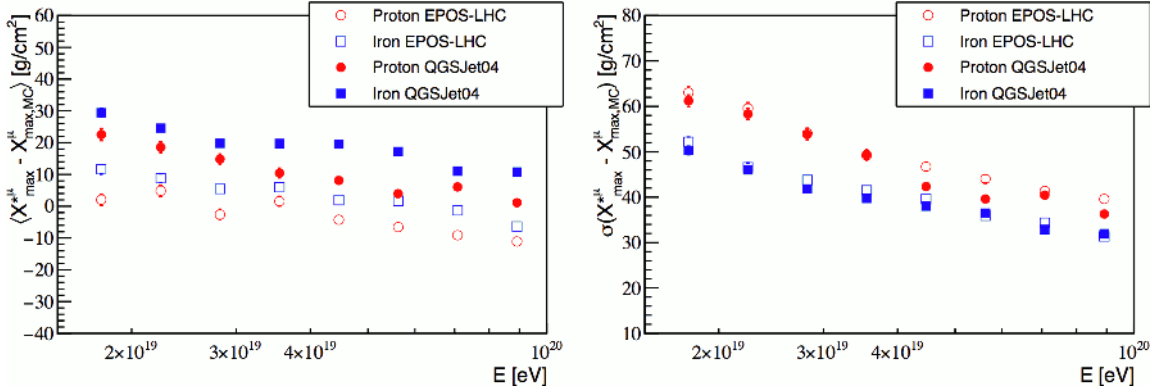


Figure 2: Average reconstruction bias of the MPD maximum (left) and resolution of the method (right) as a function of the primary energy, shown for the whole zenith angle range of this analysis [$45^\circ, 65^\circ$].

primary mass, as it depends especially on the number of muons at disposal for the reconstruction.

The dependence of the reconstruction on mass and hadronic models would be the largest source of systematic uncertainty: we call it *mass and model spread* and it amounts to $\pm 14 \text{ g/cm}^2$ (evaluated conservatively as the difference between the maximum and the minimum value of the bias). For this reason and given that the discriminating power of the MPD is not affected by the reconstruction (see expectations in Fig. 3), we choose to evaluate the MPD maximum folded with reconstruction effects, i.e. $X_{\text{max}}^{*\mu}$.

3. Results on data

All events recorded by the SD of the Pierre Auger Observatory between January 2004 and December 2016 have been used in this analysis. Considering the applicability ranges of this work and the selection criteria described in Sec. 2, the number of UHECR events here analyzed is 2227.

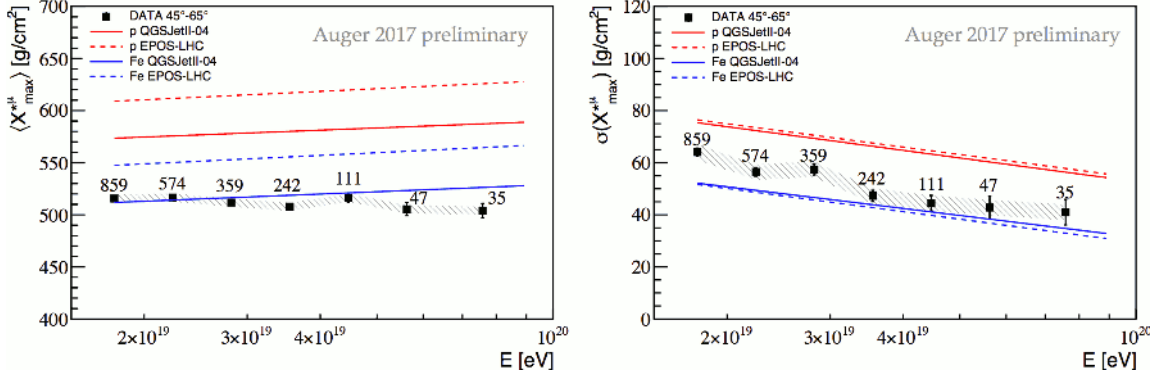


Figure 3: $\langle X_{\max}^{*\mu} \rangle$ (left) and the corresponding fluctuations (right) as a function of the primary energy. Data (black squares) are shown with statistical (black line) and systematic uncertainties (gray band) and compared to simulations (see text for the details).

Data have been studied as a function of the primary energy. A bin width $\Delta \log_{10}(E/\text{eV}) = 0.1$ is chosen for energies $\log_{10}(E/\text{eV})$ between 19.2 and 19.8. Not having enough statistics to keep the same binning, data are integrated in one bin for $\log_{10}(E/\text{eV})$ in the range [19.8, 20]. For each energy bin, the first two moments of the $X_{\max}^{*\mu}$ distribution are evaluated on data and are compared directly to the expectations obtained from Monte Carlo simulations after the reconstruction procedure (Sec. 2). We note that data and Monte Carlo are both equally biased by the reconstruction, so the relative distance to the reference lines does not vary in $X_{\max}^{*\mu}$ (see below conversion to the mean logarithmic mass $\langle \ln A \rangle$) and no systematics are associated to these effects. On the contrary, the physical X_{\max}^{μ} would display the mass and model spread as systematics, as discussed previously.

The overall systematic error on the first two moments of the $X_{\max}^{*\mu}$ distribution turns out to be around 4 g/cm^2 and 3 g/cm^2 respectively, and due to two sources: the small dependence of the selection efficiency of the quality cuts on the primary mass ($\simeq 1 \text{ g/cm}^2$) and the time variability of data. An additional systematic error of $\simeq 7.5 \text{ g/cm}^2$ can be associated with the event selection and procedure to fit the MPD profiles and needs to be taken into account in the determination of $\langle \ln A \rangle$ (see below).

The results on $\langle X_{\max}^{*\mu} \rangle$ are shown in Fig. 3 (left) by black squares, with their statistical (black line) and systematic uncertainties (gray band). For each energy bin, the number of events is indicated. From the comparison with the predictions, the inconsistency among models and data is evident. In the case of EPOS-LHC, data are at odds with predictions for all reasonable masses, in the whole energy range. Considering instead QGSJetII-04 and in particular iron expectations, a mild incompatibility arises at the highest energies. We have also checked that when converting $X_{\max}^{*\mu}$ to X_{\max}^{μ} by using the reconstruction bias (Fig. 2 left) averaged on mass/models, we obtain a good agreement with the results shown in Fig. 3 and with results presented in [8].

The inconsistencies outlined here make it difficult to draw firm conclusions on composition with our measurement of $\langle X_{\max}^{*\mu} \rangle$: we see that the predictions of $\langle X_{\max}^{*\mu} \rangle$ from the two hadronic models are significantly different in absolute value ($\sim 35 \text{ g/cm}^2$). However, we can note that the muonic elongation rate, i.e. the rate of change of $X_{\max}^{*\mu}$ with primary energy, is predicted to be about $\sim 25 \text{ g/cm}^2/\text{decade}$, independently of the primary mass and hadronic model, while on data we found $-16.9 \pm 7.2 \text{ g/cm}^2/\text{decade}$. We could thus interpret the elongation rate inferred from data

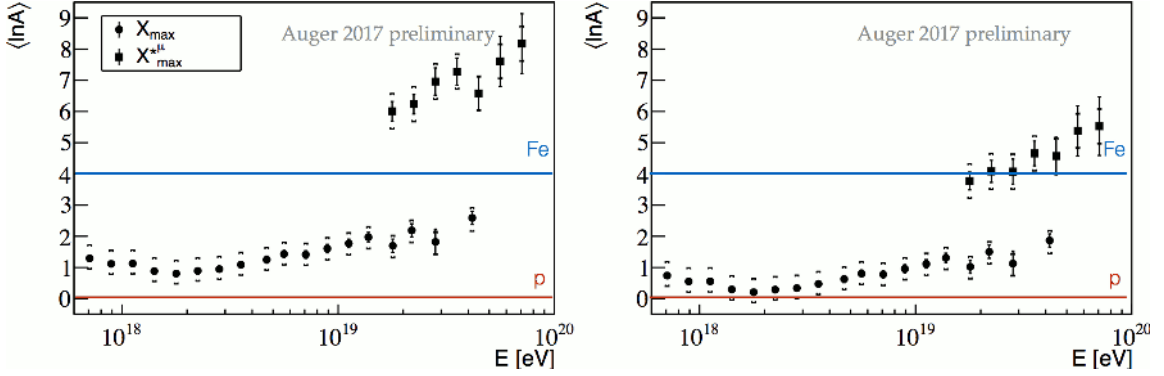


Figure 4: The evolution with energy of $\langle \ln A \rangle$ as obtained from the measured $X_{\max}^{*\mu}$ (squares). The results obtained for X_{\max} (dots) [2] are also shown. EPOS-LHC (left) and QGSJetII-04 (right) are used as reference models. Square brackets correspond to the systematic uncertainties.

at face value and conclude that our results appear to be in tension with a constant composition at the highest energies. Further work is however required to estimate more accurately the systematic uncertainty of the measured elongation rate.

An additional information comes from the second moment of the $X_{\max}^{*\mu}$ distribution. In particular, the observed fluctuations carry information about the physical fluctuations and therefore potentially about the primary mass. The results are shown in the right panel of Fig. 3. Note that in this case, the Monte Carlo predictions for different hadronic models agree with each other, making the second moment less hadronic model dependent. The energy dependence is due to the detector resolution, being $\sigma^2(X_{\max}^{*\mu}) = \sigma_{\text{phys}}^2 + \sigma_{\text{det}}^2$, where σ_{phys} and σ_{det} are respectively the physical fluctuations and the detector resolution (see right panel of Fig. 2). Comparing data and expectations, we see that they are compatible, but the systematic error does not allow one to draw a strong conclusion on the mass composition yet.

Finally, further information about the consistency of the hadronic interaction models can be obtained by converting $X_{\max}^{*\mu}$ to $\ln A$ (with A mass number), by using the following formula

$$\langle \ln A \rangle = \ln 56 \frac{\langle X_{\max}^{*\mu} \rangle_{\text{p}} - \langle X_{\max}^{*\mu} \rangle}{\langle X_{\max}^{*\mu} \rangle_{\text{p}} - \langle X_{\max}^{*\mu} \rangle_{\text{Fe}}} \quad (3.1)$$

where $\langle X_{\max}^{*\mu} \rangle_{\text{p}}$ and $\langle X_{\max}^{*\mu} \rangle_{\text{Fe}}$ are the average values for proton and iron-induced air showers respectively, obtained after the reconstruction. $\langle X_{\max}^{*\mu} \rangle$ is the average measured value for data. This comparison can be performed because the linear relation between $X_{\max}^{*\mu}$ and $\ln A$ has been checked and verified by means of a set of Monte Carlo simulations for different nuclei. To study the systematic uncertainties, a preliminary alternative fit procedure with a stronger event selection and with a looser constraint on the USP function has been performed. This different analysis changes $X_{\max}^{*\mu}$ on both data and model lines by about the same amount. The residual differences of the mass estimates when converted to $\langle \ln A \rangle$ are $\leq +0.5$. More studies on the uncorrelated systematics of the two methods need to be done in the future. Currently we conservatively add this difference in quadrature to the overall systematic uncertainties of $\langle \ln A \rangle$.

The results are shown in Fig. 4 together with $\langle \ln A \rangle$ from electromagnetic X_{\max} [2], for each model separately, EPOS-LHC (left) and QGSJetII-04 (right). Considering EPOS-LHC, values of

$\langle \ln A \rangle$ larger than 4 are obtained, while QGSJetII-04 provides values of $\langle \ln A \rangle$ compatible with heavy iron-like composition. This conclusion reflects that obtained for the muonic elongation rate (see Fig. 3 left) and for this analysis EPOS-LHC is disfavored. But using $\langle \ln A \rangle$ allows the comparison with different mass estimator such as X_{\max} . In that case the results are not compatible both for QGSJetII-04 ($\sim 3.3\sigma$), and for EPOS-LHC ($\sim 6\sigma$). Furthermore, it should be noted that QGSJetII-04 model, unlike EPOS-LHC, has problems to describe in a consistent way the first two moments of the $\ln A$ distribution obtained from the X_{\max} measurements, as discussed in [2]. Therefore, we conclude that neither of the models tuned to LHC data can satisfactorily describe at the same time both the electromagnetic and the muonic components of the showers. These are very important consistency checks for the models and from which some hadronic physics process could be excluded [7].

4. Conclusion

The arrival times of particles from EAS collected by the SD of the Pierre Auger Observatory have been exploited to measure the MPD for all events recorded in 13 years of data taking.

In this work, the first two moments of the $X_{\max}^{*\mu}$ distribution have been measured on extended intervals of zenith angle, energies and distances from the shower core. As a result, a large discrepancy between the EPOS-LHC hadronic interaction model and the MPD data has been found. Taking into account the mass estimated from FD measurements, the QGSJetII-04 model does not reproduce the data in a consistent way either. It is therefore difficult to make a mass composition estimation by using the MPD. However, the measurements here presented have the potential to help to understand the hadronic interactions to reduce the model systematics relevant for mass composition studies, see e.g. [13].

References

- [1] F. Fenu, for the Pierre Auger Collaboration, *Proc. 35th Int. Cosmic Ray Conf.*, PoS (ICRC2017) 486.
- [2] A. Aab *et al.* (Pierre Auger Collaboration), *Phys. Rev. D* 90 (2014) 122005.
- [3] A. Aab *et al.* (Pierre Auger Collaboration), *Phys. Rev. D* 90 (2014) 122006.
- [4] P. Sanchez-Lucas, for the Pierre Auger Collaboration, *Proc. 35th Int. Cosmic Ray Conf.*, PoS (ICRC2017) 495.
- [5] A. Aab *et al.* (Pierre Auger Collaboration), *Phys. Lett. B* 762 (2016) 288.
- [6] T. Pierog, *Proc. 35th Int. Cosmic Ray Conf.*, PoS (ICRC2017) 1100.
- [7] S. Ostapchenko and M. Bleicher, *Phys. Rev. D* 93 (2016) 051501.
- [8] A. Aab *et al.* (Pierre Auger Collaboration), *Phys. Rev. D* 90 (2014) 012012; Erratum *Phys. Rev. D* 90 (2014) 039904(E); Erratum *Phys. Rev. D* 92 (2015) 019903.
- [9] L. Collica, for the Pierre Auger Collaboration, *Eur. Phys. J. Plus* (2016) 131.
- [10] M. Mallamaci, *PhD Thesis*, Universita' degli Studi di Milano (2017).
- [11] L. Cazon, R. Conceição, M. Pimenta, and E. Santos, *Astropart. Phys.* 36 (2012) 211.
- [12] S. Andringa, L. Cazon, R. Conceição, M. Pimenta, *Astropart. Phys.* 35 (2012) 821.
- [13] S. Ostapchenko, *EPJ Web Conf.* 125 (2016) 03013.



Shower universality reconstruction of data from the Pierre Auger Observatory and validations with hadronic interaction models

Ariel Bridgeman^{*a} for the Pierre Auger Collaboration^b

^a*Institute for Nuclear Physics, Karlsruhe Institute of Technology (KIT), Karlsruhe, Germany*

^b*Observatorio Pierre Auger, Av. San Martín Norte 304, 5613 Malargüe, Argentina*

E-mail: auger_spokespersons@fnal.gov

Full author list: http://www.auger.org/archive/authors_icrc_2017.html

The determination of the mass composition of ultrahigh-energy cosmic rays remains one of the biggest challenges of astroparticle physics. We will show that the paradigm of shower universality can be applied to accurately reconstruct the properties of air showers, which includes information about the primary mass. The reconstruction is based solely on data from the surface detector of the Pierre Auger Observatory, which operates with a duty cycle of nearly 100 %. In contrast to purely empirical reconstruction methods, the foundation of the universality approach lies in physics models of the signal and arrival time distributions of secondary particles in air showers. In this contribution, results of the universality reconstruction are compared to their counterparts from the measurements of the Auger fluorescence detector. The focus of these comparisons is on the depth of the shower maximum, primary energy, and geometry. In addition, we extend these event-by-event comparisons to air shower simulations of various hadronic interaction models, primary masses, and energies. We will also present the performance of the method in estimating the muon content of air showers by comparing the true and reconstructed muon number for simulated showers.

*35th International Cosmic Ray Conference — ICRC2017
10–20 July, 2017
Bexco, Busan, Korea*

*Speaker.

1. Introduction

Determining the mass composition of ultrahigh-energy cosmic rays (UHECRs) at the highest energies remains one of the greatest challenges of experimental astroparticle physics. Together with the primary energy, knowledge of the primary mass is of critical importance to distinguish between different astrophysical scenarios and to find the sources of UHECRs. Via its accurate measurement of the depth of the shower maximum, the fluorescence detector (FD) of the Pierre Auger Observatory [1] has provided valuable insight into the mass composition of UHECRs [2]. However, the duty cycle of the FD is limited to around 13 %, as measurements are only possible on clear, moonless nights. While there is a wealth of data acquired with the extensive surface detector (SD) of Auger [3, 4] over the last 12 years, air showers of primaries with different masses create nearly indistinguishable signals in the water-Cherenkov detectors (WCDs).

In order to exploit the data from the SD for mass identification, a phenomenological method – known as shower universality – is used, which is based on the underlying physics of an extensive air shower. The average properties of the cascade of secondary particles depend mostly on the primary energy and the stage of shower development. As the shower-to-shower fluctuations are minimal compared to the overall shower development, a universal description of four uniquely-defined particle components may be employed. Using signal (Section 2.1) and time (Section 2.2) models, the universality approach allows us to reliably estimate the time-dependent signals of the different particle components in triggered surface detectors. This enables the reconstruction of macroscopic parameters – like the energy, the depth of the shower maximum, and the muonic content of an extensive air shower (Section 3). Comparisons between those results and measurements with the FD are discussed in this paper in Section 4.

2. Air shower universality

Our air shower models are based on the universal description of the time-dependent signals of four distinct groups of secondary particles: 1. muons (μ), 2. electromagnetic particles¹ from high-energy π^0 decays ($e\gamma$), 3. electromagnetic particles from muon decay or interactions ($e\gamma(\mu)$), and 4. electromagnetic particles from the decay of low-energy hadrons ($e\gamma(\text{had})$). The underlying universal behavior of the shower development has been previously studied ([5] and references therein). In particular, the development of the electromagnetic shower has been thoroughly explored [5–9]. To include showers of hadrons with $A > 1$ in the description, an additional parameter is needed to take into account the muon content and its development – the relative number of muons R_μ ² [10–12]. Each particle component except the main electromagnetic cascade is correlated to the overall muon scale. The stage of shower development is captured with ΔX – the integrated atmospheric overburden between the shower maximum X_{max} and the projected position of the station in the shower plane. As depicted in Fig. 1a, ΔX differs for stations at the same radial yet differing azimuthal location.

¹While all of the listed particles are electromagnetic, we use this nomenclature to refer only to electrons, positrons, and photons. This particular component corresponds with the main electromagnetic cascade.

²See Section 2.1 for more information.

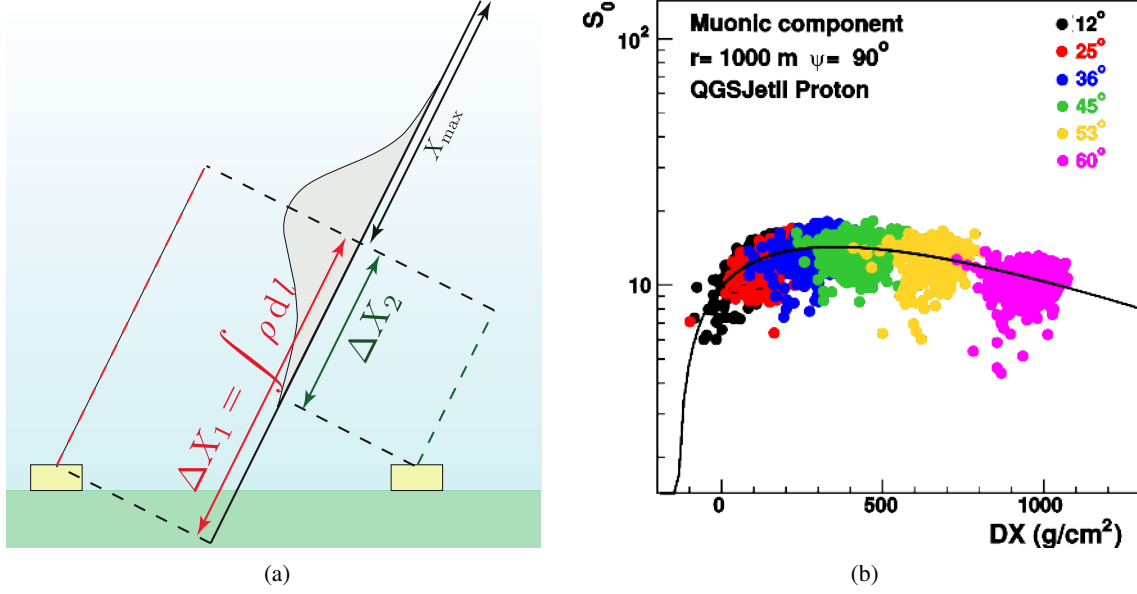


Figure 1: (a) The longitudinal development ΔX is the distance between a station and the X_{\max} . Stations at $\psi = 0$ and $\psi = 180^\circ$ illustrate the azimuthal dependence of the observed shower stage [12]. (b) Comparison of simulations with various zenith angles to the parameterization (solid line) [11] for the ΔX dependence of the measured signal S_0 in a WCD expected for the muonic component signal [13].

To derive the parameterizations for the signal and time models, a CORSIKA [14] shower library – consisting of proton and iron primaries simulated with QGSJET-II.03 and EPOS-1.99– was utilized [13]. Both models are derived from SD simulations which incorporate the hardware and calibration properties of the SD. As shown in this paper, the shower universality approach was extensively validated with new air shower simulations, i.e. QGSJET-II.04 [15] and EPOS-LHC [16], and successfully applied to hybrid data.

2.1 Signal model

For each particle component, the signal S in a WCD is calculated starting with the signal S_0 observed in an ideal 10 m^2 spherical detector. Afterwards, the asymmetries due to the detector geometry and particle production are parameterized. Employing both the parameterization of asymmetries and the ideal signal S_0 , the expected signal of a real detector is described as [13],

$$S_0(\Delta X, E) = S_{\max} \left(\frac{E}{10^{19} \text{ eV}} \right)^\gamma \left(\frac{\Delta X - \Delta X_0}{\Delta X_{\max} - \Delta X_0} \right)^{\frac{\Delta X_{\max} - \Delta X_0}{\lambda(E)}} \exp \left(\frac{\Delta X_{\max} - \Delta X}{\lambda(E)} \right), \quad (2.1)$$

with $\lambda(E) = \lambda_0 + f_\lambda \lg(E/10^{19} \text{ eV})$. For muons and muon decay products, the energy evolution f_λ vanishes. Results of the longitudinal parameterization $S_0(\Delta X)$ for the muonic component is shown in Fig. 1b.

For this comparison, signals from different primary energies are included, corrected for via $\lambda(E)$, and evaluated at a radial distance of 1000 m. The parameters of the longitudinal description – S_{\max} , ΔX_{\max} , γ , λ_0 , and f_λ – depend on the distance to the shower core, and subsequent parameterizations for these variables were found. In particular, $S_{\max}(r)$ is best described with a power-law

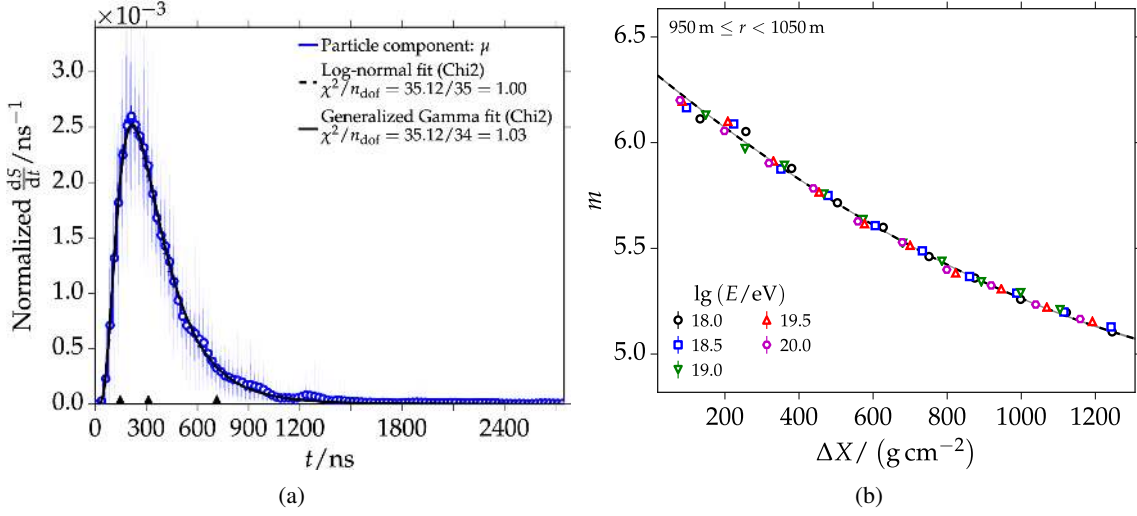


Figure 2: (a) Average time distributions of ground signals in air showers initiated by proton, carbon, and iron primaries with an energy of 10^{19} eV and a zenith angle of 0° . Shown are the average traces for specific distances to X_{\max} for the muonic particle component. The traces are normalized such that their integral is equal to one. (b) Model description of the ΔX dependence of the mean parameter m from Eq. (2.2) for muons [12].

lateral distribution function (LDF), which is independent of the mass composition and hadronic interaction model at 10^{19} eV. When coupled together, the parameterizations of the longitudinal and the lateral distributions of the ideal signal establish the model $S_0(\Delta X, r, E)$. The signal S in a real detector takes into account truncation asymmetries due to the presence of the ground and a non-spherical detector. For almost all regions of the parameter space, deviations in the description of S are smaller than 5% [13]. To derive R_μ , the signal model is used with the reference signal $S_{0,\mu}^{\text{ref}}$ from a QGSJET-II.03 proton shower with an energy of 10^{19} eV and local shower azimuth of $\psi = 90^\circ$.

2.2 Time model

The time-dependent signal in a WCD depends on the arrival time distribution of secondary particles and the detector response. Due to the various particle types and energies, an analytical expression of the detector response is hard to derive, and expensive detector simulations are necessary. To speed-up those simulations, the detector response was tabulated [11]. Then, independently for each particle component, we parametrize the arrival time distributions after the simulation of the detector response with Offline [17]. The procedure described here is an extension of what is described in [18].

First, traces are divided into bins with respect to distance to the core r , distance to shower maximum ΔX , primary energy E , zenith angle θ , and azimuth angle ψ . Within each $(r, \psi, \theta, E, \Delta X)$ bin, a weighted average of all traces is calculated, and fit with a chi-squared minimization. An example for the muonic particle component is depicted in Fig. 2a. The best fits were achieved with a log-normal or a generalized gamma distribution³.

³The generalized gamma distribution has three parameters, denoted as m , s , and ℓ . For $\ell = 0$, it reduces to a

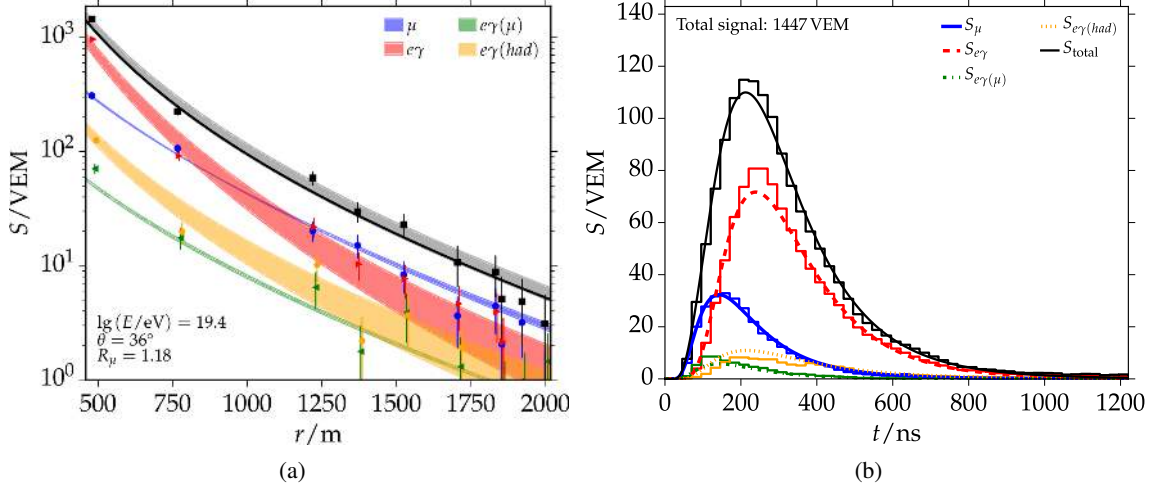


Figure 3: (a) Example LDFs in the universality reconstruction of a simulated event. The sum of component predictions is fit to the total signals (black). A comparison of the LDF components and their model predictions are given. (b) Results of the time fit of the hottest station. For comparison, the component traces (histograms) are plotted against the model predictions (smooth lines), which come from the fit of the total trace (black) [12].

Using the log-normal distribution, the evolution of the shape parameters mean m and width s is described with

$$f_{m,s}(\Delta X, \psi, \theta, E) = f_{\Delta X}(\Delta X) + f_{\text{geo}}(\theta, \psi, \Delta X) + f_{\lg E}(\lg E, \Delta X) \quad (2.2)$$

where

$$\begin{aligned} f_{\Delta X}(\Delta X) &= a_{\Delta X} + \Delta X_{\text{ref}}(b_{\Delta X} + \Delta X_{\text{ref}}(c_{\Delta X} + d_{\Delta X} \Delta X_{\text{ref}})), \\ f_{\text{geo}}(\theta, \psi, \Delta X) &= \sin \theta (a_{\text{geo}} \cos \psi + b_{\text{geo}} \Delta X_{\text{ref}}), \\ f_E(\lg E, \Delta X) &= \lg E_{\text{ref}}(a_{\lg E} + b_{\lg E} \Delta X_{\text{ref}}), \\ \Delta X_{\text{ref}} &= \Delta X / (750 \text{ g cm}^{-2}), \quad \text{and} \\ \lg E_{\text{ref}} &= \lg(E/\text{eV}) - 19. \end{aligned}$$

Depending on the particle component and parameter, the number of fit parameters is reduced. The model holds for a specific core distance range with width Δr . To fully capture dependencies on the core distance Eq. (2.2), is first fit in each of the available core distance bins, and then analytical expressions as a function of r are found. Results on the ΔX dependence of m for the muonic particle component is shown in Fig. 2b. The accuracy of the description of m is better than 1% for all particle components and dependencies. As there are more fluctuations in the spread s , deviations up to 5% occur for the muonic and the electromagnetic components. For the remaining particle components, most of the deviations are within 5%.

log-normal distribution with m and s – which are proportional to the mean and standard deviation.

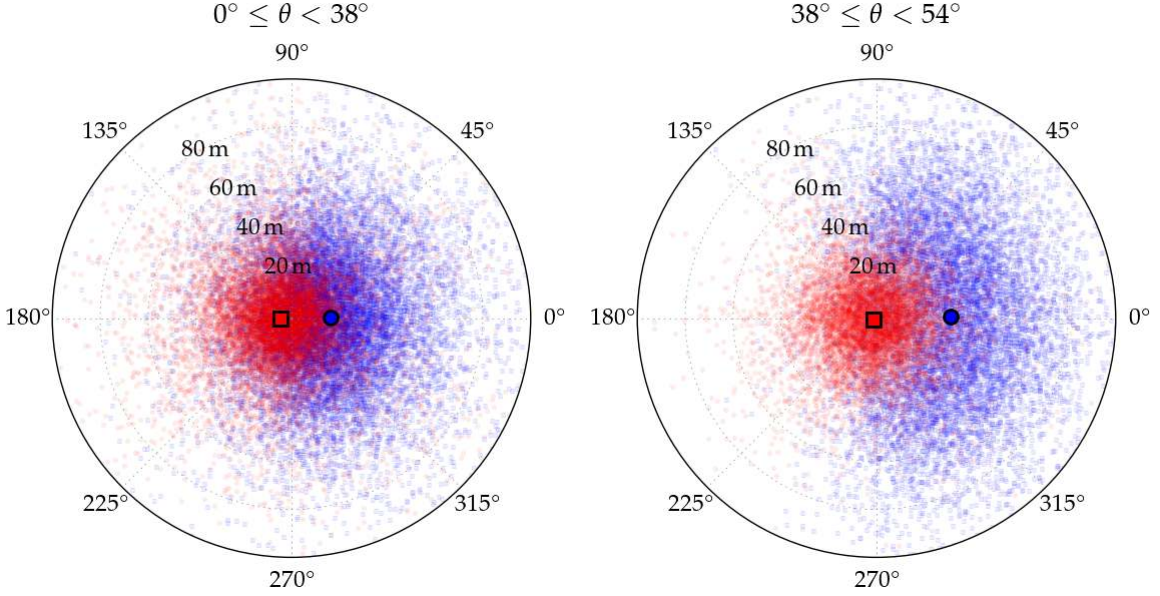


Figure 4: The universality reconstruction yields an—on average—unbiased core position (red) with respect to the MC core, whereas the core position of the SD reconstruction (blue) is systematically biased.

3. Reconstruction algorithm

The universality reconstruction employs the signal and time models to fit the measured particle traces and provide estimates of air shower properties. The reconstruction is composed of several aspects: a simultaneous fit of the distribution of time traces, the start times of triggered stations, and the lateral distribution of the total measured signals. A fit of time distributions is only attempted for stations with large enough signals (at least five time bins with a signal exceeding 0.7 VEM). The universality reconstruction is comprised of 9 parameters: the core position \bar{x} , the relative core time t_c , the shower arrival direction (θ, ϕ) , energy E , shower maximum X_{max} , and relative muon number R_μ . Depending on the reconstruction method employed, these parameters may be fixed or free during the minimization of the total log-likelihood. In Fig. 3, the lateral signal distributions and time distributions for each particle component resulting from the universality reconstruction of a proton event with $\lg(E/\text{eV}) = 19.4$ are depicted together with details about the simulated event. As universality utilizes the SD—whose energy is calibrated with the FD—the universality reconstruction fixes the energy to that found via the SD reconstruction [1] and then simultaneously fits the remaining 8 parameters.

4. Performance in simulations and with hybrid data

For the validation of the universality reconstruction, we study biases and resolutions of the reconstructed quantities. For this purpose, we used a CORSIKA shower library with more than 60 000 proton and iron simulations of QGSJET-II.04 and EPOS-LHC. Due to its explicit dependence on ΔX , the universality reconstruction naturally accounts for the asymmetric azimuthal dependence of the signal. As a consequence, as seen in Fig. 4, the universality reconstructed core is unbiased relative to the MC core. In Fig. 5a and Fig. 5b, an unbiased estimate of X_{max} and R_μ is observed

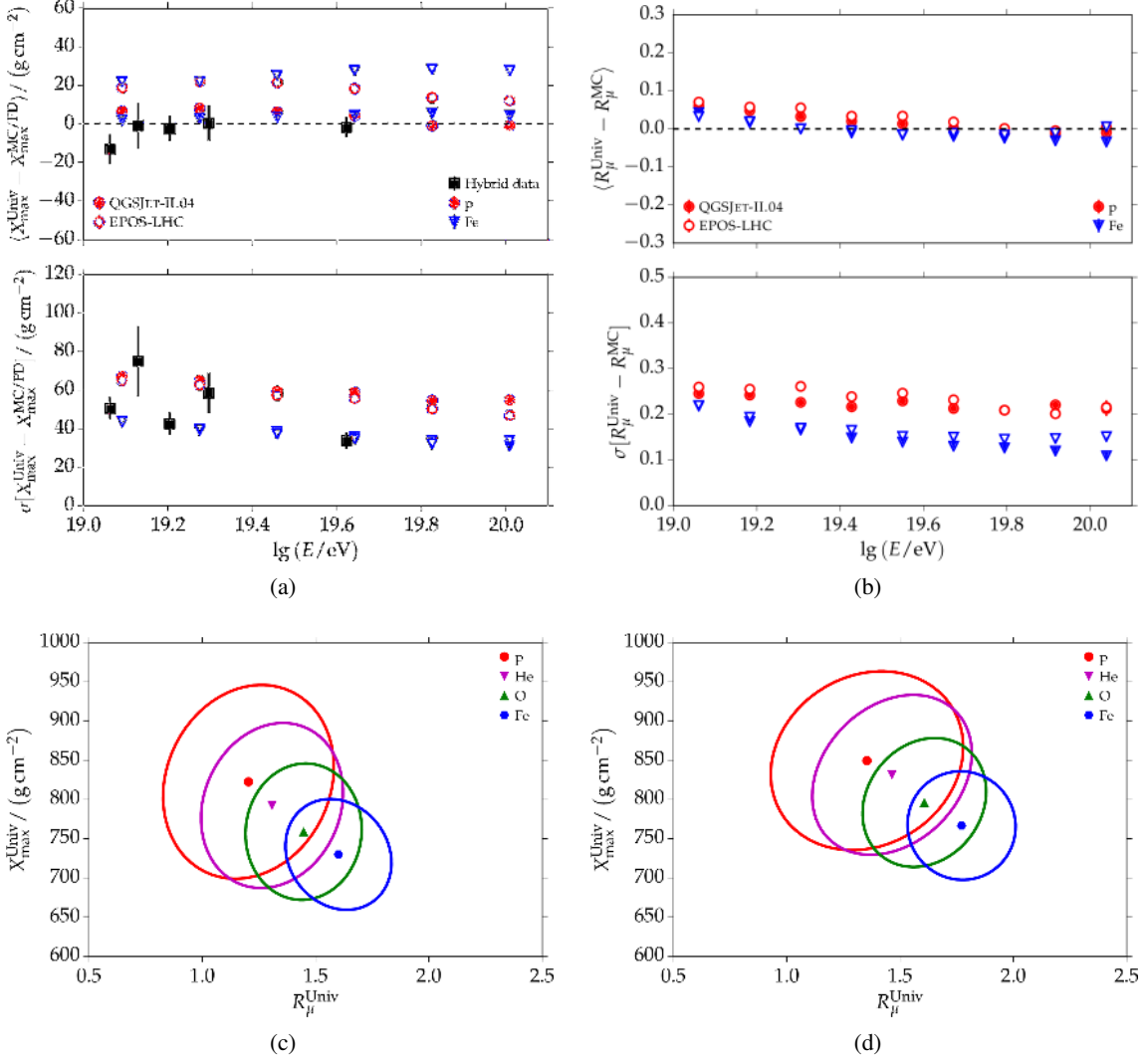


Figure 5: The bias and resolution plots for (a) X_{\max} and (b) R_{μ} for different primaries and hadronic interaction models. A comparison between the FD and universality reconstructed X_{\max} is also given. The correlation between R_{μ} and X_{\max} for different primaries of (c) QGSJET-II.04 and (d) EPOS-LHC. Shown are the 1σ contours of reconstructed quantities.

for QGSJET-II.04 proton and iron simulations. Hybrid data also exhibits an unbiased reconstruction. Due to small differences between the arrival time distributions of particles in QGSJET-II.04 and EPOS-LHC simulations, a bias is seen for EPOS-LHC simulations in Fig. 5a. The resolution of X_{\max} ranges from 80 to 30 g cm^{-2} at the highest energies. Due to their larger muon content, iron simulations are reconstructed with a smaller resolution, on average. The resolution of R_{μ} approaches 10% at the highest energies. The correlation between R_{μ} and X_{\max} is depicted in Fig. 5c and Fig. 5d. The bias in the reconstructed X_{\max} of EPOS-LHC causes slight differences in the shape of the correlations.

5. Conclusions

Shower universality is based on the intrinsic physics properties of extensive air showers. Air shower simulations with contemporary interaction models were used to extract models of the time-dependent signals in surface detectors for different particle components. We demonstrated that a reconstruction algorithm based on these assumptions and only SD information performs very well for both simulations and data. In particular, a direct comparison with FD measurements highlights an unbiased estimate of X_{\max} . This enables the reconstruction of mass-sensitive parameters with the full SD event statistics at the highest energies and with a competitive resolution. Together with the upgraded detectors of AugerPrime, the method will give access to event-by-event estimates of the primary mass at the highest energies.

References

- [1] Pierre Auger Collaboration, J. Abraham *et al.*, *Properties and performance of the prototype instrument for the Pierre Auger Observatory*, *Nucl. Instrum. Meth. A* **523** (2004), no. 1-2 50 – 95.
- [2] Pierre Auger Collaboration, A. Aab *et al.*, *Depth of Maximum of Air-Shower Profiles at the Pierre Auger Observatory: Composition Implications*, *Phys. Rev. D* (2014).
- [3] Pierre Auger Collaboration, A. Aab *et al.*, *The Pierre Auger Cosmic Ray Observatory*, *Nucl. Instrum. Meth. A* **798** (2015) 172 – 213.
- [4] Pierre Auger Collaboration, I. Allekotte *et al.*, *The Surface Detector System of the Pierre Auger Observatory*, *Nucl. Instrum. Meth. A* **586** (2008) 409–420.
- [5] P. Lipari, *The Concepts of 'Age' and 'Universality' in Cosmic Ray Showers*, *Phys. Rev. D* **79** (2008) 063001.
- [6] A. M. Hillas, *Angular and energy distributions of charged particles in electron photon cascades in air*, *J. Phys. G* **8** (1982) 1461–1473.
- [7] M. Giller, A. Kacperczyk, J. Malinowski, W. Tkaczyk, and G. Wieczorek, *Similarity of extensive air showers with respect to the shower age*, *J. Phys. G* **31** (2005) 947–958.
- [8] P. Lipari, *Universality of cosmic ray shower development*, *Nucl. Phys. Proc. Suppl.* **196** (2009) 309–318.
- [9] S. Lafebre, R. Engel, H. Falcke, J. Hörandel, T. Huege, J. Kuijpers, and R. Ulrich, *Universality of electron-positron distributions in extensive air showers*, *Astropart. Phys.* **31** (2009) 243–254.
- [10] F. Schmidt, M. Ave, L. Cazon, and A. S. Chou, *A Model-Independent Method of Determining Energy Scale and Muon Number in Cosmic Ray Surface Detectors*, *Astropart. Phys.* **29** (2008) 355–365.
- [11] M. Ave, R. Engel, J. Gonzalez, D. Heck, T. Pierog, and M. Roth, *Extensive air shower universality of ground particle distributions*, *Proc. of 31st Int. Cosmic Ray Conf., Beijing* (2011) #1025.
- [12] M. Roth, M. Ave, and A. Schulz, *A universal description of temporal and lateral distributions of ground particles in extensive air showers*, in *ICRC Proceedings 2015*, 2015.
- [13] M. Ave, R. Engel, M. Roth, and A. Schulz, *A generalized description of the signal size in extensive air shower detectors and its applications*, *Astropart. Phys.* **87** (2017) 23 – 39.
- [14] D. Heck, G. Schatz, T. Thouw, J. Knapp, and J. Capdevielle, *CORSIKA: A Monte Carlo code to simulate extensive air showers*, *Forschungszentrum Karlsruhe Report FZKA* (1998) 6019.
- [15] S. Ostapchenko, *Monte Carlo treatment of hadronic interactions in enhanced Pomeron scheme: QGSJET-II model*, *Phys. Rev. D* **83** (2011), no. 1.
- [16] T. Pierog and K. Werner, *EPOS Model and Ultra High Energy Cosmic Rays*, *Nucl. Phys. B Proc. Suppl.* **196** (2009) 102–105.
- [17] S. Argirò, S. Barroso, J. Gonzalez, L. Nellen, T. Paul, T. Porter, L. P. Jr., M. Roth, R. Ulrich, and D. Veberič, *The Offline software framework of the Pierre Auger Observatory*, *Nucl. Instrum. Meth. A* **580** (2007) 1485–1496.
- [18] M. Ave, M. Roth, and A. Schulz, *A generalized description of the time dependent signals in extensive air shower detectors and its applications*, *Astropart. Phys.* **88** (2017) 46 – 59.



The influence of weather effects on the reconstruction of extensive air showers at the Pierre Auger Observatory

Alan Coleman^{*a} for the Pierre Auger Collaboration^b

^a*Penn State Physics Department, State College, USA*

^b*Observatorio Pierre Auger, Av. San Martín Norte 304, 5613 Malargüe, Argentina*

E-mail: auger_spokespersons@fnal.gov

Full author list: http://www.auger.org/archive/authors_icrc_2017.html

The extensive air showers created by highly energetic cosmic rays are measured at the Pierre Auger Observatory. The development of these air showers in the dynamic medium of the Earth's atmosphere affects the reconstruction and ultimately the determination of the energy for the primary particle. We present an analysis using data from the two surface detector arrays (with 750 m and 1500 m spacing) which studies the modulation of the reconstructed energy estimator due to changes in atmospheric pressure and density. These dependencies on local weather are expected to affect the cosmic ray energy measurements by $\sim 0.5\%$ on average. While this is a rather small effect, not accounting for weather effects can introduce biases in event rates over a sidereal day and must be corrected to perform cleaner anisotropy analyses, in particular at large angular scales. Finally, a method by which these modulations can be corrected is detailed for the 750 m and 1500 m arrays.

*35th International Cosmic Ray Conference — ICRC2017
10–20 July, 2017
Bexco, Busan, Korea*

*Speaker.

1. Introduction

The development of cosmic ray air showers occurs in the dynamic medium of Earth's atmosphere. The atmospheric properties affect this development which can be seen via changes in the measured signal due to secondary particles on the ground. Due to the daily and yearly cycles in Earth's weather, the changes in atmospheric conditions can produce biases in the measured air shower signals. These effects must be corrected when attempting to measure cosmic ray anisotropy and determine the energy flux spectrum.

We present an update to a previous work [1] which developed a method by which the small changes in signal due to atmospheric fluctuations can be corrected. This method identifies biases in the measured signal as a function of air density, ρ , and pressure, P . This update includes seven more years of Pierre Auger data from the 1500 m surface detector (SD) as well as measurements using the smaller 750 m SD array. The method is also improved by including a timing delay in the model to account for the difference in atmospheric conditions in the last two radiation lengths above the detector.

The Pierre Auger Observatory and data sets used in this study are described in section 2. The method to develop the updated weather correction is detailed in section 3. Finally we explain how the atmospheric model will affect the SD reconstruction of air showers in section 4.

2. Observatory and data set

The Pierre Auger Observatory [2] is a hybrid cosmic ray detector located in the Mendoza province of Argentina. The Observatory, situated around 1400 m above the sea level, employs a fluorescence detector (FD) which overlooks two nested surface detector (SD) arrays. Together, the SD and FD are able to observe the fluorescence light given off by developing air showers as well as their particle signature on the ground.

Each SD consists of a hexagonal lattice of water Cherenkov detectors which measure the energy given off by secondary particles entering the water volume. Physically, the two SD arrays differ only in the lattice spacing, 1500 m (750 m), between stations (since many values for the two SD arrays will be presented in parallel, this notation will be used for the rest of the paper). The separation between stations defines the characteristics of cosmic rays that can be observed. See Table 1 for a comparison of the physics capabilities of the two SD arrays.

2.1 Energy measurements

Estimating the energy of an air shower using an SD begins with a measurement of the signal, S , deposited in the SD stations on the ground. The first-order energy estimator, $S(r_{\text{opt}})$, is found by fitting the lateral distribution of signal amplitudes from the shower axis. The value of $S(r_{\text{opt}})$ is given by the expected signal amplitude at an optimal distance, r_{opt} . This distance has been specifically chosen to minimize the impact of the empirically chosen lateral distribution model on the measurement of $S(r_{\text{opt}})$. For the 1500 m (750 m) array, r_{opt} is 1000 m (450 m).

A correction is then applied to remove zenith angle biases using a constant intensity cut (CIC) [3]. This correction has the geometric motivation that an increase in zenith angle leads to increase in average slant depth for showers at ground level. Thus, highly inclined showers reach the detector

	1500 m Array	750 m Array
Total Stations	1600	61
Lattice Cells	1380	42
Detector Area	3000 km ²	24 km ²
Fully Efficient Energy Threshold	3 EeV	0.3 EeV
Maximum Zenith Angle Considered	60°	55°
Signal Optimal Distance (r_{opt})	1000 m	450 m
Dataset Events	1, 146, 481	570, 123
Dataset Energy Threshold	1.0 EeV	0.1 EeV
Dataset Median Energy	1.5 EeV	0.15 EeV
Dates Used	01.01.2005 – 31.12.2015	01.01.2011 – 31.12.2015

Table 1: The Pierre Auger Observatory includes two SD arrays to measure cosmic ray air showers. The top section of the table lists differences in physical properties and physics capabilities of the two arrays. The bottom section details each array’s data set used in this work.

with more attenuation which produces a zenith angle dependent bias when considering events above a given $S(r_{\text{opt}})$. This bias is removed by scaling $S(r_{\text{opt}})$ to \hat{S} , the value that would have been measured for a shower arriving at a reference zenith angle of 38° (35°). See [3] for a more detailed explanation.

The corrected energy estimator, \hat{S} , is then converted to a shower energy using a calibration between the FD and the SD arrays. The FD has the benefit of almost calorimetrically measuring the electromagnetic energy of the shower. Thus, the calibration between \hat{S} and the shower energy is done by using the common set of high quality events that can be independently reconstructed by the FD and the SD arrays. For each respective SD array, \hat{S} and the shower energy, E , are related via a power law $E = A\hat{S}^B$ (see [3] for more information).

The FD calibration also highlights one of the motivations for a weather correction. As will be shown later in this section, the atmospheric density and pressure have daily cycles. The FD only records data at night and thus the events used in the calibration of the SD are inherently biased. The weather correction will unbiased the data before the FD calibration and will produce more accurate SD energy measurements.

2.2 The event set

The data set for this work was chosen to start when the construction of the respective SD array was approximately complete. Since construction of the 750 m array began much later than for the 1500 m array, the data periods cover different intervals of 10 (5) years.

To ensure a high quality measurement of the $S(r_{\text{opt}})$ values, the data set uses a fiducial cut which requires that the station with the largest signal has all six nearest neighbors active at the time of the event. This cut effectively demands that the shower core is contained within the array and that the lateral distribution of particles is well sampled. A further cut in zenith angle was applied to

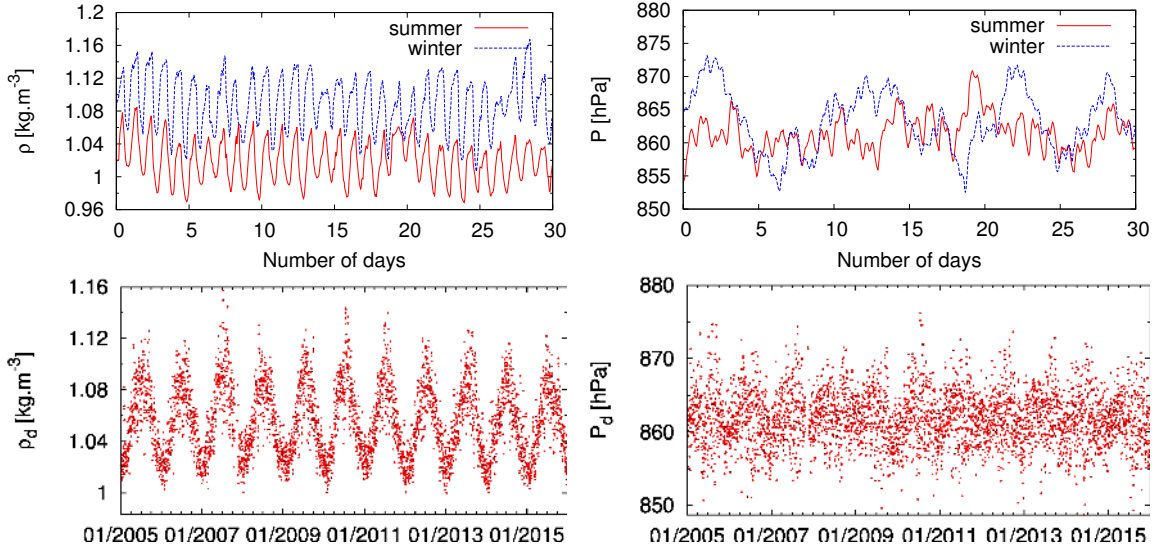


Figure 1: The weather data used in this study includes measurements of air density (left) and pressure (right). The top two plots show the hourly measurements over the course of one summer (solid red) and winter (dashed blue) month. Daily and yearly cycles can be seen most clearly in the density measurement with amplitudes of 3% and 6%, respectively. The air pressure does not have such strong yearly modulations though daily cycles are apparent.

the two arrays to ensure full efficiency, zenith angle $< 60^\circ$ (55°). Further, only data above 1 EeV (0.1 EeV) were used for this analysis. This event selection results in 1,146,481 (570,123) events.

2.3 Atmospheric Data Set

The atmospheric measurements for this work were recorded using the Observatory's weather monitoring stations. The primary atmospheric monitoring station used in this study is located roughly in the center of the 1500 m array near the central laser facility (CLF). The CLF weather station records measurements of the atmospheric temperature and pressure every 5 minutes. Occasionally, there are gaps in these measurements. When there are missing data for intervals between 10 minutes and 3 hours, the values are interpolated. For longer intervals, the atmospheric data from the weather stations at the FD sites are used¹ after correcting for the difference in altitude. The weather stations' measurements of temperature, T , and pressure, P , are used to calculate the air density, ρ , using the dry-air relation $\rho = (M/R)(P/T)$ where $M/R = 0.3484 \frac{\text{kg}}{\text{m}^3} \frac{\text{K}}{\text{hPa}}$.

The top plots in Figure 1 show measurements of density (left) and pressure (right). They include measurements taken every five minutes over the course of one summer (solid red) and winter (blue dashed) month. The bottom two plots show the density and pressure daily-averages over the course of the 10 years.

The strong yearly and daily modulations in density can be clearly seen with an amplitude of around 6% and 3%, respectively. Such modulations can also be seen in the pressure over the course of a year though the spread from day to day is not as large in amplitude. We also note that the fluctuations in pressure are much higher in winter months than they are in summer months.

¹FD weather measurements make up $\sim 7\%$ of the data set

3. Correcting for atmospheric conditions

We have shown in a previous work [1] that it is the atmospheric conditions in the last two radiation lengths above ground which most strongly correlate to changes in the measured signal. At these heights, up to one km above the detector, temperature fluctuations can be two to three times smaller than at the ground level. Thus, the ideal measurements to be used in a weather correction would be taken high over the SD array.

Instead of having to make measurements at these heights we note that there is an approximate 2 hour delay in the atmospheric conditions one km above the detector and at ground level. Thus, we propose a model which is based on the current pressure, P , the average density ± 12 hours of the event, ρ_d , and the density two hours previous ($\tilde{\rho}$)

$$S(r_{\text{opt}}) = S_0 [1 + \alpha_P(P - P_0) + \alpha_\rho(\rho_d - \rho_0) + \beta_\rho(\tilde{\rho} - \rho_d)]. \quad (3.1)$$

Here $S(r_{\text{opt}})$ is the measured reference signal (see section 2.1) and S_0 is the signal that would have been measured at the reference weather conditions, P_0 and ρ_0 . These values are defined to be the data set's yearly averages, $P_0 = 862$ hPa and $\rho_0 = 1.06$ kg m⁻³.

3.1 Cosmic ray arrival rate

The atmospheric conditions' impact on the arriving cosmic rays can be seen when considering the event rate above a given signal threshold, S_{cut} . Due to the modulation of measured signal by the changes in weather, some events will migrate above or below S_{cut} . Thus, the modulation can be found by looking at the event rate of observed air showers with $S(r_{\text{opt}}) > S_{\text{cut}}$ as a function of atmospheric conditions. The differential rate per unit area is given by

$$\frac{dR}{d\theta} = 2\pi \sin \theta \cos \theta \int_{S_{\text{cut}}}^{\infty} dS P_{\text{tr}}(S, \theta) \frac{d\Phi_{\text{CR}}}{dE_t} \frac{dE_t}{dS} \quad (3.2)$$

where P_{tr} is the function describing the trigger efficiency. The energy flux spectrum is described by a power law $d\Phi_{\text{CR}}/dE_t \propto E_t^{-\gamma}$ where E_t is the true cosmic ray energy. Using the FD calibration equation relating measured signal to this true energy, $E_t \simeq AS^B$, this can be rewritten to leading order in the weather corrections as

$$\frac{dR}{d\sin^2 \theta} \propto [1 + a_P(P - P_0) + a_\rho(\rho_d - \rho_0) + b_\rho(\tilde{\rho} - \rho_d)] \int_{S_{\text{cut}}}^{\infty} dS P_{\text{tr}}(S, \theta) S^{-B\gamma+B-1}. \quad (3.3)$$

Here the weather coefficients have the relation $a_P = B(\gamma - 1)\alpha_P$ (and equivalently for α_ρ and β_ρ). Using the FD calibration constant $B = 1.023 \pm 0.006$ and the measured spectral index of the cosmic ray flux $\gamma = 3.29$ [4], we simplify the relationship to $a_P \simeq 2.3\alpha_P$.

3.2 Determination of atmospheric coefficients

To find the value of the atmospheric constants $\{a_P, a_\rho, b_\rho\}$, the data was split into hourly time bins. Using equation (3.3) for the arrival rate, the expected number of counts in bin, i , can be written as

$$\mu_i = R_0 A_i [1 + a_P(P_i - P_0) + a_\rho(\rho_{d,i} - \rho_0) + b_\rho(\tilde{\rho}_i - \rho_d)] \quad (3.4)$$

Array	a_P [hPa ⁻¹]	a_ρ [kg ⁻¹ m ³]	b_ρ [kg ⁻¹ m ³]	χ^2/dof
1500 m	$(-3.2 \pm 0.3) \times 10^{-3}$	-1.72 ± 0.04	-0.53 ± 0.04	1.013
750 m	$(-4.9 \pm 0.4) \times 10^{-3}$	-1.07 ± 0.06	-0.37 ± 0.06	0.998

Table 2: This table gives the values of the weather correction variables corresponding to equation (3.4) for the 750 m and 1500 m arrays.

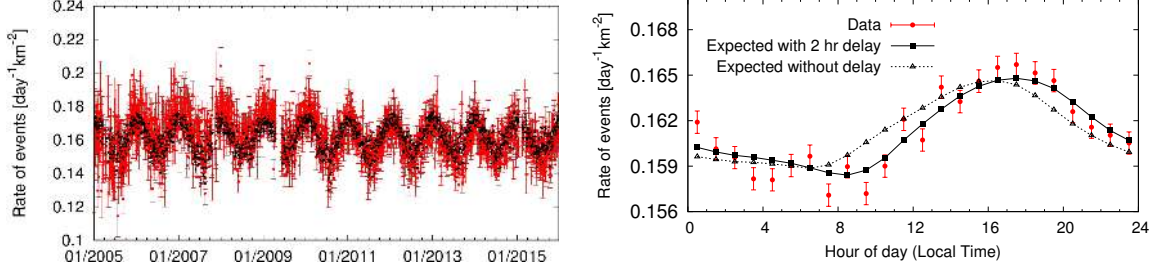


Figure 2: The measured and expected event rates for the 1500 m array are shown here. The left plot includes the measured (red) and expected (black) daily event rate over the 10 year data period. In the right plot, the event rates over the course of one day are shown. The measured rate (red) is shown along with the expected rate when using (black squares) and not using (grey triangles) the two hour delay in air density.

where R_0 is the global rate per area that would be observed at the reference atmospheric conditions and A_i is the combined area covered by active cells in the i -th time bin². The optimal atmospheric constants are thus the values that maximize the likelihood function

$$\mathcal{L} = \prod_i \frac{\mu_i^{n_i} e^{-\mu_i}}{n_i!} \quad (3.5)$$

where n_i is the actual number of observed events in bin i compared to the expected number μ_i given in equation (3.4).

3.3 Results for the SD Arrays

The fit of the atmospheric constants for the two arrays are given in Table 2. A chi-square test shows that the model fits the data well for both arrays. The number of degrees of freedom for the fits was 88,126 (39,258). As an example, the measured and expected event rates for the 1500 m array are shown in Figure 2 (the 750 m array results look similar).

The daily event rates (red) and the expected rates (black) spanning ten years are shown in the left plot. The right plot includes the average rates over the course of one day (red circles). The expected values have also been plotted when the two hour delay is both included (black squares) and neglected (empty triangles). The two hour delay seems to be justified both visually and via a reduced χ^2 goodness of fit test, changing from 4.2 to 1.9 when the air density is shifted by two hours.

²Each hexagonal cell contributes $\sqrt{3}/4 d^2$ where d is the lattice spacing.

Array	Coefficient	c_0	c_1	c_2
1500 m	a_p [hPa $^{-1}$]	$(2.1 \pm 0.9) \times 10^{-3}$	$(-2.6 \pm 0.6) \times 10^{-2}$	$(2.6 \pm 0.7) \times 10^{-2}$
	a_ρ [kg $^{-1}$ m 3]	-2.7 ± 0.1	1.5 ± 0.8	2.2 ± 1.0
	b_ρ [kg $^{-1}$ m 3]	-1.0 ± 0.1	1.2 ± 0.8	0.0 ± 1.1
750 m	a_p [hPa $^{-1}$]	$(-2.5 \pm 0.8) \times 10^{-3}$	$(-0.8 \pm 0.2) \times 10^{-2}$	-
	a_ρ [kg $^{-1}$ m 3]	-1.6 ± 0.1	1.8 ± 0.3	-
	b_ρ [kg $^{-1}$ m 3]	-0.4 ± 0.1	0.1 ± 0.3	-

Table 3: The weather corrections were carried out in different zenith angle bins. The resulting coefficients were then fit to a polynomial as described in equation (3.6). Since the 750 m array was split into only three zenith angle bins, it was fit to a line.

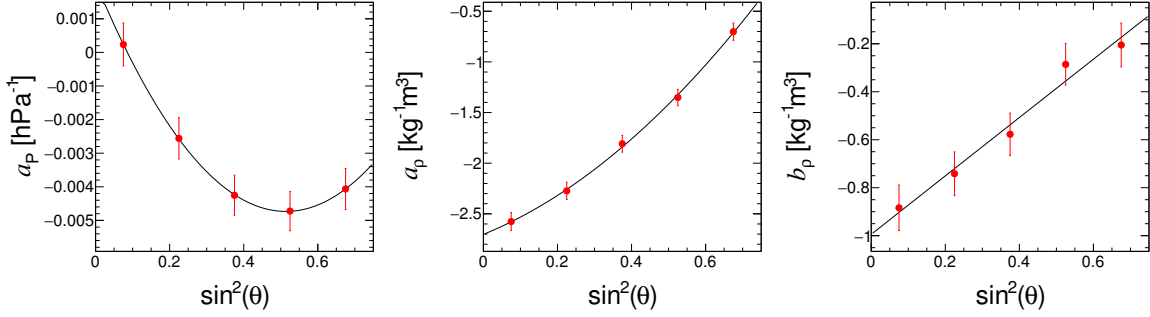


Figure 3: The weather correction was repeated in bins of equal $\sin^2 \theta$. The results below show the weather correction coefficients (see equation (3.1)) in red and the fitted curves whose values are given in Table 3.

3.4 Zenith angle dependency

To investigate the dependency on zenith angle, the data sets for the two arrays were separated into 5 (3) equal bins in $\sin^2 \theta$. The same procedure described above was carried out on the data in each of the bins independently. The resulting atmospheric coefficients were then fit to a polynomial

$$f(x) = c_0 + c_1x + c_2x^2, \text{ where } x = \sin^2 \theta. \quad (3.6)$$

Here $f(x)$ can represent any of the atmospheric parameters, $\{a_p, a_\rho, b_\rho\}$. Note that due to the limited number of zenith angle bins used for the 750 m array, the data were instead fit to a line ($c_2 = 0$). The results are summarized in Table 3 and shown in Figure 3 for the 1500 m array.

The density coefficients (controlled by a_ρ and b_ρ) are negative and decreasing in magnitude with zenith angle. During times of higher than average air density, the lateral spread of electromagnetic particles is reduced. The upward trend is consistent with the electromagnetic component being more attenuated at higher zenith angles, decreasing this effect when measured at the ground. The values of the pressure coefficient (a_p) are generally negative showing that increasing pressure leads to a smaller signal due to an increase in traversed matter when the air shower reaches the ground. Further, this attenuation will be even more pronounced for highly inclined showers which is demonstrated by the increasingly negative value of a_p .

4. The impact of atmospheric effects on energy measurements

Using the values obtained for $\{a_p, a_\rho, b_\rho\}$ in the previous section, the measured signals can be corrected by converting back to $\{\alpha_p, \alpha_\rho, \beta_\rho\}$ and inserting them into equation (3.1). After being corrected for weather effects, the signals then undergo the CIC correction. Since the CIC procedure also attempts to account for the attenuation of showers in air, this process must be tuned after applying weather corrections. However, since the weather correction converts the signal to a reference value chosen to be the global average, the impact on the CIC is small.

As detailed in section 2.1, the CIC corrected signals, \hat{S} , are then converted into an energy via a calibration with the FD calorimetric measurements, $E = A\hat{S}^B$. Here we expect some small changes to the calibration constants, due to the FD events only being recorded at night. To estimate the effects of the weather corrections on the FD calibration, we first note that b_ρ has the largest impact on the signals measured during the night compared to the daily average. This difference translates to approximately a 0.5% shift in the energy assignment and would be observed as a 0.5% change in the A calibration constant. However, this change is much smaller than the overall systematic uncertainties which are around 14%.

5. Conclusions

We have presented here an update of a weather correction for air showers which are measured at the ground level. The signal produced on the ground is modulated by changes in the atmospheric conditions. A model describing the impact of weather conditions on the measured shower signal was tuned for the 1500 m and 750 m SD arrays at the Pierre Auger Observatory. This model was an update to a previous work which includes a two hour offset in the air density which accounts for the difference in the atmospheric conditions in the last two radiation lengths above the detector. The model was also tuned for data in different zenith angle ranges. The weather correction is expected to shift the energy scale of the SD arrays by around 0.5% due to a bias in the energy calibration method.

References

- [1] J. Abraham *et al.* (The Pierre Auger Collaboration), *Atmospheric effects on extensive air showers observed with the surface detector of the Pierre Auger observatory*, *Astropart. Phys.* **32** (2009) 86 [arXiv:0906.5497].
- [2] A. Aab *et al.* (The Pierre Auger Collaboration), *The Pierre Auger Cosmic Ray Observatory*, *Nucl. Instrument. Meth. A* **798** (2015) 172 [astroph.HE/1502.01323]
- [3] J. Hersil *et al.*, *Observations of extensive air showers near the maximum of their longitudinal development*, *Phys. Rev. Lett.* **6** (1961) 22.
- [4] I. Valiño, for The Pierre Auger Collaboration, *The flux of ultra-high energy cosmic rays after ten years of operation of the Pierre Auger Observatory*, *Proc. 34th Int. Cosmic Ray Conf.* POS(ICRC2015) 271.



An improved reconstruction method for the AMIGA detectors

Juan Manuel Figueira^{*a} for the Pierre Auger Collaboration^b

^a*Instituto de Tecnologías en Detección y Astropartículas (CNEA, CONICET, UNSAM),
Centro Atómico Constituyentes, Comisión Nacional de Energía Atómica,
Av. General Paz 1499 (B1650KNA) San Martín, Buenos Aires, Argentina*

^b*Observatorio Pierre Auger, Av. San Martín Norte 304, 5613 Malargüe, Argentina*

E-mail: auger_spokespersons@fnal.gov

Full author list: http://www.auger.org/archive/authors_icrc_2017.html

The Auger Muon and Infill Ground Array (AMIGA) is a muon detector that is currently being built as part of AugerPrime, the upgrade of the Pierre Auger Observatory. It consists of 30 m² plastic scintillator counters buried 2.3 m underground and water-Cherenkov detectors at the surface, organized in a periodic 750 m triangular array, and deployed over an area of 23.5 km². Each counter is composed of three 10 m² modules segmented into 64 scintillator strips. Two positions of the engineering array were further equipped with "twin" detectors to assess reconstruction uncertainties. AMIGA allows for direct measurement of the muon content of air showers with primary energies above 10¹⁷ eV. In this work, the detector reconstruction strategy is revisited and the bias induced by particles traversing two adjacent strips, the so-called corner-clipping effect, is thoroughly analyzed. A bias correction based on end-to-end simulations of both the air showers and the detector response is presented. The improved reconstruction method was applied to experimental data acquired by the AMIGA engineering array, and preliminary results of the muon content estimator ρ_{450} (muon density 450 m from the shower axis) are presented.

*35th International Cosmic Ray Conference — ICRC2017
10–20 July, 2017
Bexco, Busan, Korea*

^{*}Speaker.

1. Introduction

The Pierre Auger Observatory [1] is a hybrid detector, composed of 27 air-fluorescence telescopes (the fluorescence detector, FD) that have a view of the atmosphere over an arrangement of 1660 water-Cherenkov particle detector stations spread over 3000 km² (the surface detector, SD). The SD stations are situated on a triangular grid with a spacing of 1500 m (mostly, with some closer together as described below), and the FD telescopes are located at four sites at the edge of the SD array pointing inwards.

The Observatory is embarking on its next phase, named AugerPrime. As one of the enhancements to the detection system, a dedicated detector to directly measure the muon content of air showers, AMIGA [1, 2, 3], is being built. AMIGA is a joint system of 61 water-Cherenkov stations and buried plastic scintillation counters arranged in a 750 m spacing array nested inside the 1500 m array, that extends over an area of 23.5 km². The 750 m array is fully efficient from 3×10^{17} eV onwards for air showers with zenith angles $\leq 55^\circ$ [4]. The buried scintillators (the underground muon detector, UMD) are the core of the detection system for the muonic component of air showers since the electromagnetic component is largely absorbed by the overburden. To effectively shield the UMD, scintillators are situated 2.3 m underground, which corresponds to ~ 540 g/cm² of vertical mass from the local soil and imposes a cutoff for vertical muons of about 1 GeV. The scintillator plane of each UMD station is highly segmented, composed of three 10 m² modules comprising sixty four 400 cm \times 4.1 cm \times 1.0 cm strips each or, in the case of the engineering array, composed of two 5 m² modules made up of sixty four 200 cm \times 4.1 cm \times 1.0 cm strips each and two 10 m² modules. The SD 750 m array was completed in September 2011 while the UMD engineering array, consisting of seven stations arranged in a hexagonal layout (vertices and center), has been operational since February 2015.

When a muon crosses a UMD scintillator strip a fraction of the produced light reaches a photomultiplier tube (PMT), which converts a bunch of photons into a current pulse. The pulse is amplified and inverted to produce the so-called analog trace, which is typically $\lesssim 30$ ns wide. Then a pulse amplitude discriminator produces a constant output if the input signal is higher than a programmable threshold voltage set at $\sim 30\%$ of the average single photoelectron amplitude. Finally, the pulse is sampled at 320 MHz by a field programmable gate array (FPGA). Samples can be either a logical “1” or “0” depending on whether the incoming signal was above or below the discrimination threshold. So, at the end every channel has a digital trace consisting of a binary string. UMD scintillator modules receive the trigger signal from their associated SD station. The lowest level trigger (T1) of the surface detectors is used. Once a T1 condition is fulfilled, its UMD companion freezes a 6.4 μ s data sample into a local buffer capable of storing 1024 triggers.

2. Main sources of counting biases

The main sources of counting biases in UMD modules with PMTs are: *i*) crosstalk, *ii*) muon pile-up, and *iii*) corner-clipping muons. Crosstalk and corner-clipping muons tend to an overcounting of the real number of muons impinging the counter while, on the other hand, muon pile-up leads to undercounting. Crosstalk and muon pile-up were already considered in the previous reconstruction counting strategy. We will present here a new reconstruction method that also takes

into account the corner-clipping effect. In the following subsections, the three sources of counting biases will be briefly explained.

Crosstalk Normally, in a multianode PMT (e.g., the Hamamatsu UBA H8804-200MOD [5], as used in the engineering array of the UMD), the photoelectrons emitted from the photocathode are accelerated and guided by a focusing mesh towards the first dynode of a pixel where secondary electrons are released; these electrons are multiplied by a factor of $\sim 10^6$ in a cascade process from the first to the last dynode of the same pixel, before finally reaching an anode connected to an output processing circuit. On occasion, the electronic crosstalk phenomenon may occur, which consists of a secondary electron leaking out from the cascade multiplication process of the original pixel into a dynode of an adjacent pixel and triggering another cascade multiplication process on it. In such a situation, the anode connected to the adjacent pixel would have an output current pulse similar to the one produced by a single photoelectron emitted from the photocathode. There is also a chance for the optical crosstalk phenomenon to occur, which happens when a photon (out of a group of them) arriving at the PMT from the fiber connected to a certain pixel strikes the photocathode near the focusing electrodes of a neighboring pixel, mainly due to the numerical aperture of the fiber or a small misalignment of the fiber with the pixel.

Pile-up Muon traces typically span $\lesssim 30$ ns and, due to exponential decay processes involved in the light emission of the scintillators and fibers, can have a complex time structure. Because of this, after the pulse discrimination, a digital muon trace may not comprise only a sequence of consecutive positive samples (“1s”), but could also have null samples (“0s”) in between. For this reason, to prevent the binary string produced by one muon to be counted as two or more, an inhibition time window, over which the searching process for a muon identification pattern is stopped, has to be applied starting from the first identified positive sample on the binary string. As a consequence of the amplitude discrimination, once this inhibition time window is triggered by a muon arriving at the scintillator strip, it is not possible to identify whether another muon arrives at the same strip over the same time interval spanned by the window. Therefore, the so-called muon pile-up effect, which can be defined as two or more muons arriving at the same detection strip over a time interval shorter than an inhibition time window, is hampering the muon counting, among other factors. Even though this phenomenon was taken into account in the design of the muon counter by choosing a high segmentation (64 scintillation strips per module), it can still be encountered in situations such as counters sufficiently close to the shower core or counters in high-energy events.

Corner clipping The arrangement of the scintillator strips in the UMD counters [2] is such that most of the muons impinging the detector will pass through only one strip, i.e., they will go from the top face to the base of a strip without crossing any other. Some muons, however, due to their directions and impact point, will cross a lateral face of a scintillator strip. This is the so-called corner-clipping effect. In this situation, since the strips are touching each other along their lateral faces, it is most likely that the muon will go across two strips. In such a case, the muon could be detected in both strips, only in one of them, or not at all, depending on whether the deposited energy on each strip is above or below the threshold required to be reconstructed. Additionally, while they are traveling along the surrounding area of the counter, muons will scatter knock-on electrons at very forward angles which may have enough energy to produce secondary ionization. In case they

are produced, it is most likely that they will be injected in the same strip as the muon, but it is also possible that some of them are injected into an adjacent strip, depositing enough energy to be detected and, therefore, contributing as another overcounting source. Figure 1 illustrates simulation results of the mean relative counting bias (i.e., the relative deviation of the measured value from the expected value) caused by corner-clipping as a function of the distance to the shower axis, averaged over azimuth angle. As expected for geometrical reasons, the bias increases with zenith angle due to the increased number of corner-clipping muons. For zenith angles of 0° and 45° , the mean overcounting becomes $\sim 5\%$ and $\sim 20\%$ respectively, and is almost independent of the distance to the shower axis or the primary energy.

3. The improved reconstruction method

The reconstruction begins with a searching process for a recognition pattern on the digital trace of every counter channel. This pattern, which was studied in Ref. [6], must discriminate between digital traces produced by muons and digital traces from single photoelectron-like pulses produced by crosstalk and, eventually, thermal fluctuations. Since single photoelectron pulses have a typical width of ~ 4 ns, and the digital sampling is performed every 3.125 ns, the possible digital traces that a single photoelectron can produce comprise null samples (000), an isolated positive sample (010) or two consecutive and isolated positive samples (0110). The used recognition pattern for muon detection demands, therefore, an extra sample between two positive samples, irrespective of whether it is positive or null. Thus, all the traces which contain at least the strings 101 or 111 will be considered as signals generated by at least one muon while those produced by single photoelectron-like pulses from crosstalk will not be taken into account. Once the recognition pattern of a muon is found in a counter channel, an inhibition time window is applied from the detection of the first positive sample in the digital trace. The length of the inhibition time window was also studied in Ref. [6] from the widths at the discrimination level of muon pulses measured in the laboratory, and it was found that it should be equal to or larger than 30 ns to prevent any double counting due to the pulse structure of a single muon, as explained above.

Once the 64 digital traces of a UMD module are examined over the $6.4 \mu\text{s}$ that the event acquisition lasts to find patterns generated by muons, the start times of the muon signals are determined as those corresponding to the first positive samples of the patterns. To perform the muon pile-up correction, the event is divided in time windows with the same duration as the inhibition time window. Subsequently, the number of channels with signal N_s is determined in each window. Then, as shown in Ref. [7], the bias due to muon pile-up can be corrected by means of the unbiased

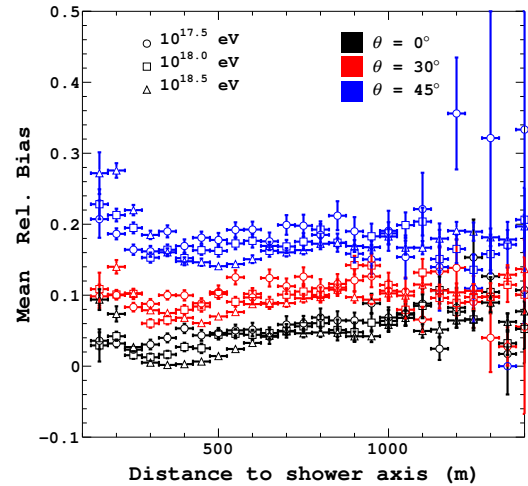


Figure 1: Simulations of the biases due to the corner-clipping effect vs. the distance to the shower axis for showers of different zenith angles and energies.

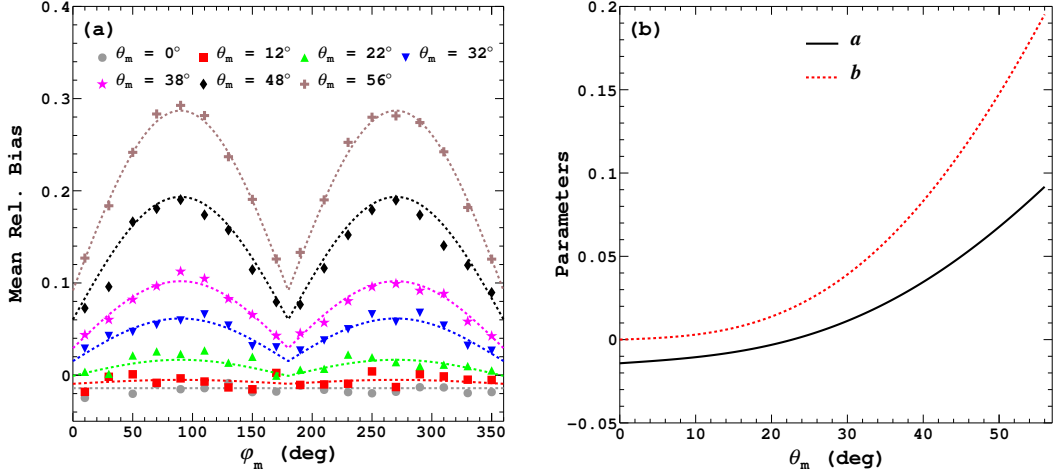


Figure 2: (a) Simulation results of the dependence of the bias on φ_m and θ_m , averaged over proton- and iron-induced showers of $10^{18.0}$ eV and $10^{18.5}$ eV, with φ_m grouped into 20° wide bins (symbols), and the corresponding curves obtained with the parametrization of Eq. (3.2) that best fits the data globally (lines). (b) Resulting coefficients $a(\theta)$ and $b(\theta)$ of the parametrization.

statistical correction

$$N_{s,\text{cor}} = -N_{\text{seg}} \ln(1 - N_s/N_{\text{seg}}), \quad (3.1)$$

where $N_{s,\text{cor}}$ is the number of corrected signals and $N_{\text{seg}} = 64$ is the segmentation of a module.

To address the problem that arises due to the bias of the corner-clipping effect, a geometrical correction based on simulations was developed. This reconstruction bias was determined on a module-by-module basis by examining the quantity $B = (N_{s,\text{cor}} - N_{\mu,\text{inj}})/N_{\mu,\text{inj}}$, i.e., the relative difference between the number of reconstructed signals in the 64 strips of the UMD module ($N_{s,\text{cor}}$) and the number of muons impinging on the module ($N_{\mu,\text{inj}}$). The simulation library employed to develop the geometrical correction was composed of proton- and iron-induced air showers of energies $E = 10^{18.0}$ and $10^{18.5}$ eV, zenith angles $\theta = 0^\circ, 12^\circ, 22^\circ, 32^\circ, 38^\circ, 48^\circ$ and 56° , azimuth angles uniformly distributed in the range 0° to 360° , and with QGSJET-II-04 as the high-energy hadronic interaction model [8]. The zenith and azimuth angles of the shower axis, θ and φ , respectively, were obtained by means of the SD reconstruction. Then, taking into account the azimuth rotation of each UMD module with respect to the SD coordinate system, φ_0 , the zenith and azimuth angles of the shower axis were referenced to the coordinate system of each module by using $\theta_m = \theta$, $\varphi_m = \varphi + \varphi_0$. Relative to the module coordinate system, the projection of the shower axis into the $x - y$ plane (in which the module itself is located) is parallel to the longitudinal direction of the strips when $\varphi_m = 0^\circ$ or 180° , and perpendicular to them when $\varphi_m = 90^\circ$ or 270° . Figure 2(a) shows the dependence of the relative bias correction on φ_m and θ_m , averaged over proton- and iron-induced showers of $10^{18.0}$ and $10^{18.5}$ eV, with φ_m grouped into 20° wide bins. Since for $\theta_m \neq 0$ the corner-clipping effect reaches minimum and maximum values at $\varphi_m = 0^\circ$ and 180° , and $\varphi_m = 90^\circ$ and 270° , respectively, the bias correction was parametrized as

$$C_{\text{bias}}(\theta_m, \varphi_m) = a(\theta_m) + b(\theta_m) |\sin(\varphi_m)|, \quad (3.2)$$

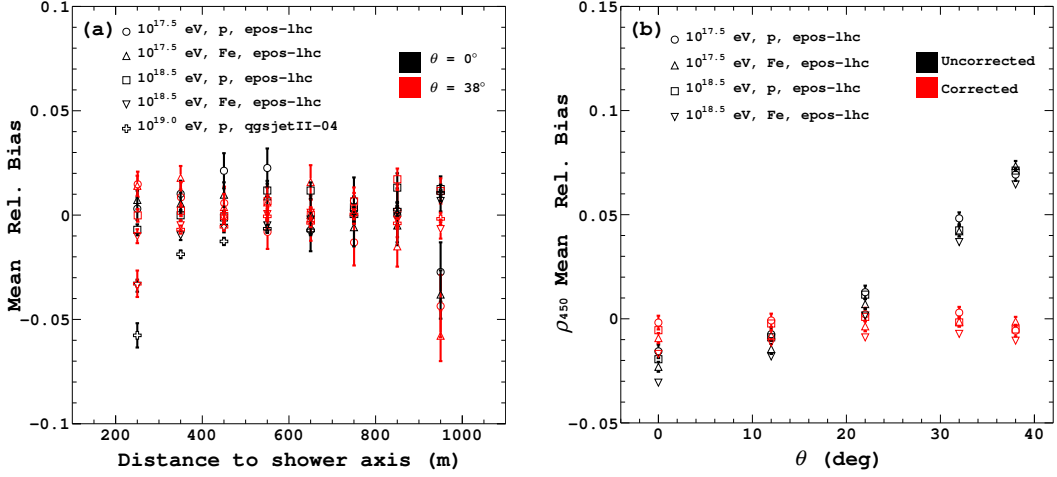


Figure 3: Simulation results of the counting biases obtained with the improved reconstruction that performs the correction due to the corner-clipping effect, for (a) the number of muons at station level vs. distance to the shower axis, and (b) the shower size (ρ_{450}) vs. zenith angle.

where $a(\theta_m) = x_0 + x_1(1 + x_2 \cos(\theta_m)) \sin(\theta_m)$, $b(\theta_m) = x_3(1 + x_4 \cos(\theta_m)) \sin(\theta_m)$ and x_i (for $0 \leq i \leq 4$) are free parameters. A global least-squares fitting was carried out by minimizing $R^2 = \sum_{k=1}^N (B_k - C_{\text{bias}}(\theta_{m,k}, \varphi_{m,k}, x_0, x_1, x_2, x_3, x_4))^2$, where the sum was performed over the total number of modules N available in the whole simulated data. As result, the best-fitting parameters are $x_0 = -0.014 \pm 0.002$, $x_1 = 0.27 \pm 0.02$, $x_2 = -0.94 \pm 0.04$, $x_3 = 0.52 \pm 0.03$, and $x_4 = -0.98 \pm 0.02$. The values taken by a and b as a function of θ_m are displayed in Fig. 2(b), and the good agreement between the parametrization and the simulated data can be seen in Fig. 2(a). The improved reconstruction obtained in this work consists of applying a correction factor given by $f(\theta, \varphi) = (1 + a(\theta) + b(\theta) |\sin(\varphi + \varphi_0)|)^{-1}$ on a module-by-module basis.

For testing this approach, independent sets of proton- and iron-induced showers were simulated by using the CORSIKA software package [9]. The energies and zenith angles were fixed to $E = 10^{17.5}$, $10^{18.5}$ and $10^{19.0}$ eV, and $\theta = 0^\circ$, 12° , 22° , 32° and 38° , while the azimuth angles were generated randomly in the range 0° to 360° for each air shower. QGSJET-II-04 and EPOS-LHC [10] were chosen as the high-energy hadronic interaction models for $E = 10^{19.0}$, and $10^{17.5}$ eV and $10^{18.5}$ eV, respectively. The simulation of the detector and the reconstruction method were carried out by using the Offline framework [11], and for each energy and zenith angle, 120 simulations/reconstructions were performed. Figures 3 (a) and (b) show the counting biases with the improved reconstruction. While with the former reconstruction method the biases are $\sim 5\%$ and $\sim 10\%$ for $\theta = 0^\circ$ and 38° , respectively, once the developed correction is applied, the large bias vanishes for $\theta = 38^\circ$ and remains negligible for $\theta = 0^\circ$, as can be seen in Fig. 3(a). The bias correction works well over the whole range of distances to the shower axis and for all considered zenith angles, primaries, models, and energies. The azimuthal dependence is also removed. Figure 3(b) shows the biases of the density of muons at 450 m from the shower axis (ρ_{450}) before and after applying the geometrical correction. The values of the muon content ρ_{450} are obtained by fitting a KASCADE-Grande-like function as expressed in Ref. [12] to the lateral distribution functions of muon densities. As can be seen, the biases from uncorrected muon numbers at the station

level obtained with the former reconstruction increase with θ , taking a value of $\sim 8\%$ for $\theta = 38^\circ$. On the other hand, corrected muon numbers at the station level yield biases in ρ_{450} values almost independent of θ and contained in a $\pm 2\%$ range.

4. Muon content at 450 m vs. primary energy

In this section the previously described improved reconstruction method is applied to data acquired with the UMD engineering array, and the energy dependence of the muon density at 450 m from the shower axis is presented. The data set comprises all cosmic-ray events collected from 21 October 2015 to 15 October 2016. In addition to the described bias correction, inefficiencies of the 5 m^2 and 10 m^2 modules due to light attenuation in the fibers were corrected for by dividing the reconstructed muon densities by 0.91 and 0.83, respectively, values obtained from laboratory measurements. The SD provided the energy and arrival direction of the primary cosmic rays from the timing and amplitudes of the signals produced by the air-shower particles in the stations [1]. The standard SD reconstruction algorithm and trigger condition were applied. The previously determined lateral trigger probability (LTP) of measuring 1 muon in 10 m^2 as a function of the radial distance and primary energy was used to select high-quality events. For each event, the radial distance for an $\text{LTP} \geq 0.7$ was calculated. Within this radial range the number of modules N_m and their maximal spacing d_{max} were determined. Then, to ensure a sufficiently spaced number of counters, the event was selected if: $N_m > 1$ and $d_{\text{max}} > 250\text{ m}$, or $N_m > 2$ and $d_{\text{max}} > 165\text{ m}$, or $N_m > 3$ and $d_{\text{max}} > 125\text{ m}$. Zenith angles up to 30° and energies higher than $10^{17.3}\text{ eV}$ were also required. Above this energy threshold, the trigger efficiency of the SD infill is $\geq 90\%$. After requiring those conditions, 535 events remained. UMD stations closer to the shower axis than 200 m were not taken into account.

ρ_{450} was used as an estimator of the muon content since its mean value is a robust composition estimator [13]. Because it is expected that the dependence of the muon content on the energy follows a power law [13], the experimental data shown in Fig. 4 was fitted by the expression

$$\rho_{450} = a(E/10^{17.7}\text{ eV})^b, \quad (4.1)$$

where the fitting parameters a and b represent the average muon content at $10^{17.7}\text{ eV}$ and the logarithmic gain of muons with growing energy, respectively. As can be seen, the fitted model is in good agreement with data. It was found that $a = (1.06 \pm 0.02)\text{ m}^{-2}$ and $b = 0.90 \pm 0.03$, the latter being in accord with the range $0.90 \leq b \leq 0.95$ obtained by Matthews [13] when a significant

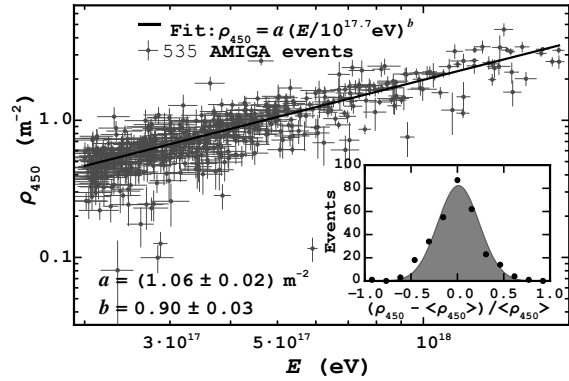


Figure 4: Dependence on the shower energy E of the muon content ρ_{450} for 535 selected events acquired by the AMIGA engineering array above $10^{17.3}\text{ eV}$ (gray dots) and a fit to the data by the power law given in Eq. (4.1) (line). The error bars display statistical detection uncertainties only. The inset shows the distribution of the deviations of the data points from the fitted curve.

inelasticity in pion interactions is included. Nevertheless, statements about composition cannot be made yet from these preliminary experimental results obtained with the UMD engineering array due to the still large statistical uncertainties and the ongoing study of systematic uncertainties.

5. Summary

An improved reconstruction method for the underground muon detector of AMIGA was developed with the aim of removing the overcount due to corner-clipping muons which, with the former reconstruction method, could be as high as $\sim 20\%$ for zenith angles of 45° . The new method, based on a parametrization of the bias obtained from shower and detector simulations, uses the SD reconstructed angles θ and φ and works well for all distances, primaries, models and energies. The improved method was applied to experimental data acquired by the UMD engineering array, and preliminary results of the muon content estimator ρ_{450} were presented as a function of energy. The logarithmic gain of muons with growing energy was found to be 0.90 ± 0.03 , which is in good agreement with models in which a significant inelasticity in pion interactions is included. Despite the fact that conclusions about composition cannot yet be drawn due to high statistical uncertainties and not yet accurately estimated systematics, the potentiality of the direct measurement of the muon component by the UMD of AMIGA is shown.

References

- [1] A. Aab et al., The Pierre Auger Collaboration, *Nucl. Instrum. Methods A* **798** (2015) 172.
- [2] A. Aab et al., The Pierre Auger Collaboration, *JINST* **11** (2016) P02012.
- [3] A. Aab et al., The Pierre Auger Collaboration, *JINST* **12** (2017) P03002.
- [4] I. C. Mariş, *The AMIGA infill detector of the Pierre Auger Observatory: Performance and first data*, in proceedings of *32nd International Cosmic Ray Conference, Beijing, China*, vol. 1, p. 9, 2011 [[arXiv:1107.4809](https://arxiv.org/abs/1107.4809)].
- [5] Hamamatsu, *Photomultiplier tube assembly H8804*, 2012. See http://www.hamamatsu.com/resources/pdf/etd/H8804_TPMH1333E.pdf.
- [6] B. Wundheiler, *The AMIGA muon counters of the Pierre Auger Observatory: Performance and first data*, in proceedings of *32nd International Cosmic Ray Conference, Beijing, China*, vol. 5, p. 9, 2011 [[arXiv:1107.4807](https://arxiv.org/abs/1107.4807)].
- [7] D. Ravnani et al., *Astropart. Phys.* **82** (2016) 108.
- [8] S. Ostapchenko, *Phys. Rev. D* **83** (2011) 014018.
- [9] D. Heck et al., *CORSIKA: A Monte Carlo code to simulate extensive air showers*, Forschungszentrum Karlsruhe Report FZKA 6019, 1998. See <http://bibliothek.fzk.de/zb/berichte/FZKA6019.pdf>.
- [10] T. Pierog and K. Werner, *Nucl. Phys. B* **196** (2009) 102.
- [11] S. Argirò et al., *Nucl. Instrum. Methods A* **580** (2007) 1485.
- [12] B. Wundheiler, *The AMIGA muon counters of the Pierre Auger Observatory: Performance and studies of the lateral distribution function*, in proceedings of *34th International Cosmic Ray Conference, The Hague, The Netherlands*, PoS (ICRC2015) 324 (2015).
- [13] J. Matthews, *Astropart. Phys.* **22** (2005) 387.



Recent Results of the Auger Engineering Radio Array (AERA)

Ewa M. Holt^{*ab} for the Pierre Auger Collaboration^c

^a*Karlsruhe Institute of Technology (KIT), Institut für Kernphysik, 76021 Karlsruhe, Germany*

^b*Instituto de Tecnologías en Detección y Astropartículas (CNEA, CONICET, UNSAM), Buenos Aires, Argentina*

^c*Observatorio Pierre Auger, Av. San Martín Norte 304, 5613 Malargüe, Argentina*

E-mail: auger_spokespersons@fnal.gov

Full author list: http://www.auger.org/archive/authors_icrc_2017.html

The Auger Engineering Radio Array (AERA) is located at the Pierre Auger Observatory in Mendoza Province, Argentina. More than 150 autonomous antenna stations, spread over 17 km², are used to measure the radio emission from extensive air showers initiated by cosmic rays with energies above 0.1 EeV in the frequency range of 30 – 80 MHz. AERA is operated in coincidence with the other detectors of the Observatory, which comprise an array of water-Cherenkov detectors, fluorescence telescopes and buried scintillators that are used to detect muons. This gives a unique opportunity of cross-calibration between the detector types and complementary analyses of shower parameters. From the radio measurements we reconstruct cosmic-ray properties like energy, arrival direction and estimators of the mass composition, in particular the atmospheric depth X_{\max} of maximum shower development. To determine X_{\max} , we follow a top-down approach with detailed simulations down to the individual particle level, also considering the refractive index. Two independent implementations are followed, both using an atmospheric model based on GDAS data. The results of the two analyses are consistent. We achieve a resolution of the radio detectors of ~ 39 g/cm². Since radio measurements are solely sensitive to the electromagnetic part of the shower, we can measure the electron-muon ratio in combination with the muon detector of AMIGA as an additional mass estimator. Recently AERA demonstrated that for inclined showers the area of the radio-emission footprint extends to several square kilometers. This shows great potential for future large-scale radio arrays, since the large footprints allow for a wide spacing of the antennas.

*35th International Cosmic Ray Conference — ICRC2017
10–20 July, 2017
Bexco, Busan, Korea*

**Speaker.*

1. Introduction

Over the last decade, the detection of air-shower radio emission has evolved from small-scale prototype setups to large-scale experiments performing measurements for cosmic-ray physics [1, 2]. Radio detectors are ideal to be used in combination with other cosmic-ray detection techniques like particle, fluorescence and air-Cherenkov detectors, which enable cross-calibration between the detectors. Since the radio emission is solely produced by the electromagnetic part of the shower, its detection delivers complementary information to the measurements of all-particle and muon detectors. The radio technique has an advantage over the fluorescence and air-Cherenkov technique, since it has an operational time of nearly 100 %. It is only disturbed from high atmospheric electric fields which occur in massive rain clouds and during thunderstorms [3, 4]. In addition, the radiation does not get attenuated since the atmosphere is transparent for radiation in the MHz range. The radio emission is sensitive to the shower development, i.e., to the depth of the shower maximum X_{\max} , which is statistically related to the mass of the primary particle. Furthermore, the emission contains information about the arrival direction and energy [5, 6] of the cosmic ray.

2. The Auger Engineering Radio Array (AERA)

The Auger Engineering Radio Array is located at the Pierre Auger Observatory in Mendoza Province, Argentina [7]. It is part of the low-energy enhancements of the Observatory together with AMIGA [8] and HEAT [9]. AMIGA is a combination of water-Cherenkov detectors spread on a grid of 750 m spacing and buried scintillators at 2.3 m depth to solely measure the muons of the showers. The half spacing compared to the Surface Detector (SD) array in the rest of the Observatory lowers the energy threshold. With HEAT, the Fluorescence Detector (FD) is extended by three high-elevation telescopes to observe low-energy air showers which evolve higher in the atmosphere. All four detector types are co-located in the same area of the Observatory and measure cosmic rays down to $\sim 10^{17}$ eV in coincidence. This allows for cross-calibration and complementary measurements. In addition, the SD and FD serve as a trigger for AERA.

AERA comprises 153 autonomous radio stations spread over an area of ~ 17 km². The array was completed in March 2015 after three deployment phases. As an engineering array, it combines different hardware, e.g., electronics and communication systems, different spacing between the antennas and different trigger concepts (internal and external). The dense center of AERA contains 24 logarithmic periodic dipole antennas (LPDA) on a 144 m grid. The rest of the array is built of butterfly antennas with 250 m, 375 m as well as 750 m spacing, the latter to measure inclined air showers. In figure 1, a map of AERA together with the other co-located detectors is shown and the different antenna types and trigger systems are indicated. The two antenna arms of each station are aligned in east-west and north-south directions, respectively, and are sensitive to the radio emission in the frequency range of 30 – 80 MHz. The antenna response pattern is calibrated using an emitting source attached to an octocopter, resulting in an overall uncertainty of 9.4 % on the amplitude [10]. For the time synchronization between the antennas, a beacon transmitter [11] at the FD site transmits well-defined sine waves. The nanosecond-level accuracy of this method was confirmed by independent measurements using radio pulses emitted by commercial airplanes [12].

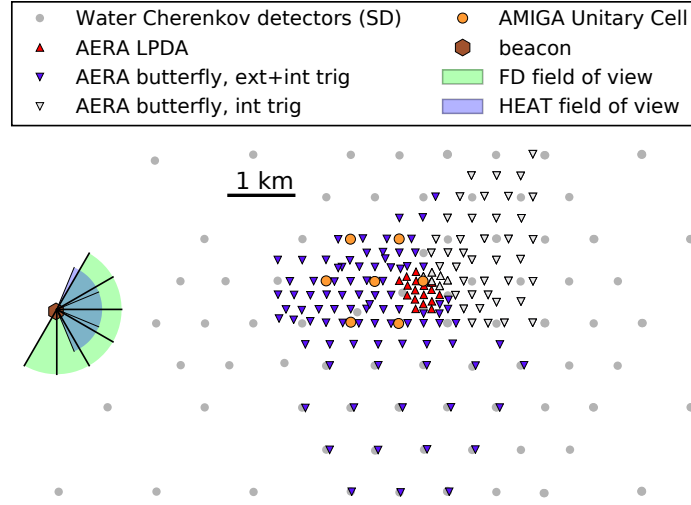


Figure 1: Map of the AERA array together with the other co-located detectors of the Pierre Auger Observatory and its enhancements.

3. Radio X_{\max} measurements

The atmospheric depth at which the number of secondary particles in the shower reaches its maximum is called X_{\max} . It is statistically correlated to the mass of the primary cosmic ray since heavier particles interact higher in the atmosphere. The radio emission is mainly produced around X_{\max} and emitted in a forward-directed cone around the direction of the propagation. Hence, the shape of the radio signal at the ground depends on the distance to the emission region and thus to X_{\max} . In AERA we follow several approaches to reconstruct X_{\max} from the measured radio signal. The width of the 2-dimensional lateral distribution [13, 14] as well as shape parameters of the hyperbolic wavefront [15, 16] vary with the distance to X_{\max} . In addition, the spectral slope of the radio signals measured in the antennas is sensitive to X_{\max} [17]. The best X_{\max} resolution is obtained by evaluating the agreement of measured radio signals to air-shower simulations of different X_{\max} , as explained in the following.

The fundamental approach of this method was developed in [18] and adapted to the AERA detector in two independent analyses. The basic principle is to produce a set of Monte Carlo simulations of air showers with different X_{\max} initiated by different primary particles, in particular protons and iron nuclei. The simulated radio signal is interpolated on a 2-dimensional map and fitted to the measured signals by a least χ^2 fit. The minimum of the distribution of these least χ^2 over their corresponding X_{\max} gives the best fit for X_{\max} .

In the analysis of [14] (analysis A), a simulation set was produced for each measured event using the CoREAS code [19], the US standard atmospheric model and the measured direction and primary energy from the SD array. The set contained more proton simulations than iron to account for the higher shower-by-shower fluctuations of X_{\max} for protons. The simulated electric field traces were transformed into energy fluences via the Poynting vector, which was then interpolated to a 2-dimensional lateral distribution. For each simulation the best fit for the shower core position in the AERA array was found with a least χ^2 fit. The fit included a scaling factor to account for uncertainties in the input energy, absolute antenna calibration and simulated amplitude. A parabolic

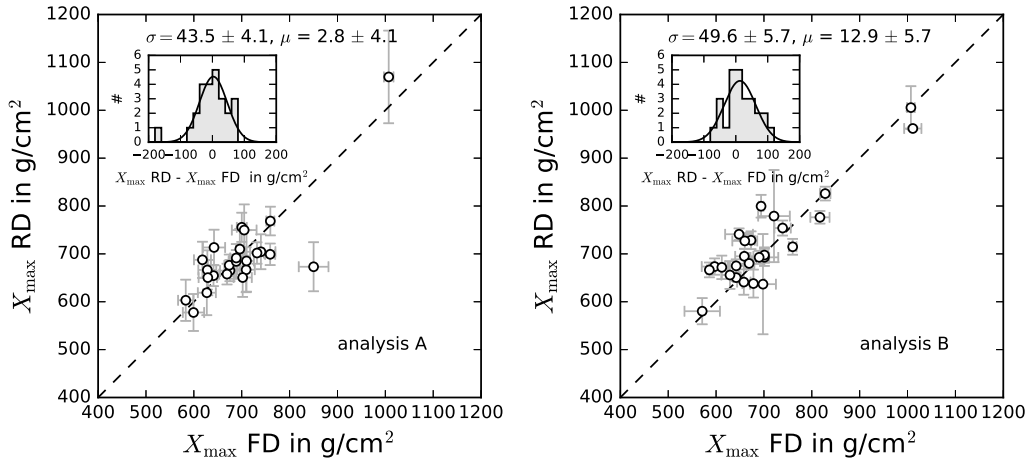


Figure 2: Reconstructed X_{\max} from radio measurements based on simulated energy fluence distributions [14] (left, analysis A) and simulated amplitude distributions [22] (right, analysis B), compared to the measured FD X_{\max} . The dashed lines indicate a one-to-one correlation. The insets in both figures show the distributions of the differences together with a Gaussian fit.

function of the simulated X_{\max} was fitted to the resulting distribution of least χ^2 to find the best fit for X_{\max} . To take into account effects of atmospheric conditions at the time of the measurements, a correction factor based on GDAS data (Global Data Assimilation System) [20, 21] was applied on the X_{\max} value at the end of the analysis chain. The method was applied to a high-quality data set of hybrid events measured from AERA (RD), SD and the fluorescence detector (FD) simultaneously. The results are compared to the reconstructed X_{\max} values from the FD in the left panel of figure 2.

A different, independent analysis with a similar approach was performed in [22] (analysis B). The simulations were calculated by the SELFAS code [23]. With GDAS data an air density and refractivity profile as a function of altitude were calculated for the time of the detected event and applied as atmospheric model in the simulations. The measured arrival direction of AERA and an arbitrarily chosen energy of 10^{18} eV were taken as input, which makes the analysis independent of SD measurements. The simulated amplitude was fitted to the measured data by shifting the shower core and scaling the absolute amplitude. The scaling factor was used to determine the primary energy, since to first order the amplitude is linearly proportional to the energy. The minimum of the χ^2 distribution determined the best fit value for X_{\max} . The analysis was applied to a high-quality set of hybrid events, using FD standard quality cuts and a minimum of 5 radio stations with signal. A comparison of the results to the FD X_{\max} values is shown in the right panel of figure 2.

The radio X_{\max} values of both analyses are compatible with the FD X_{\max} values with a resolution of 44 ± 4 g/cm² and 50 ± 6 g/cm², respectively, and a small offset compared to the resolution. This results in an overall radio X_{\max} resolution of about 39 g/cm² when subtracting the FD X_{\max} resolution of 26 g/cm² at an energy of $10^{17.8}$ eV [24]. The consistent results of the two independent AERA analyses confirm the validity of the method applied. Further investigations are needed to evaluate if the small differences in the results are caused by the different applications of the method or by the different simulation codes. A similar resolution of ~ 40 g/cm² was accomplished with the sparse radio array of Tunka-Rex that determined the X_{\max} resolution of the radio measurements by comparing to air-Cherenkov measurements [25]. With the dense core of LOFAR a resolution of

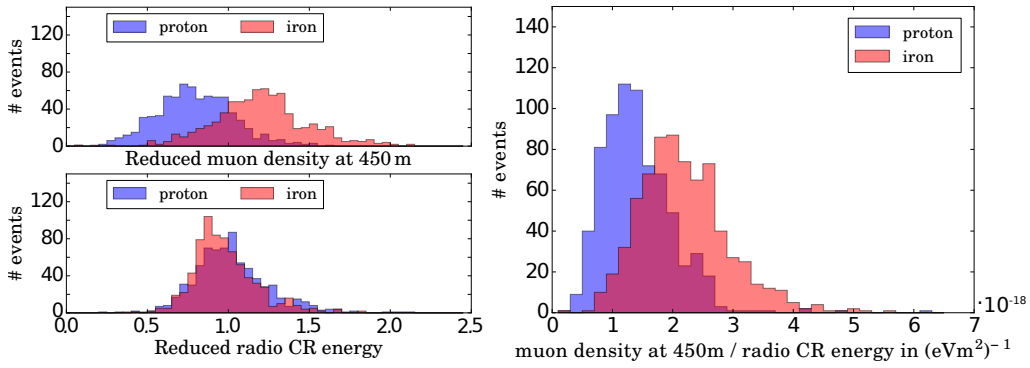


Figure 3: Simulations of hybrid measurements of radio emission and muons for proton- and iron-induced showers. Left upper panel: Muon density at a reference distance of 450 m from the shower axis relative to the mean muon density, reconstructed from the signal in the AMIGA scintillators. Left lower panel: Primary cosmic-ray energy reconstructed from the radio signal in the AERA antennas relative to the mean cosmic-ray energy. Right: Ratio of the muon density and primary cosmic-ray energy.

17 g/cm² was gained [26].

4. Hybrid measurements with muon detectors

The water-Cherenkov measurement technique features only limited sensitivity to the type of the secondary particles arriving in the detectors. Instead, for air showers up to $\theta \leq 55^\circ$ separate measurements of the electromagnetic and muonic components are realized with the combination of AERA and AMIGA measurements [27]. The radio emission measured by AERA is solely produced by the charged electromagnetic part of the shower. The scintillators of AMIGA are buried at 2.3 m depth (≈ 540 g/cm² of vertical mass) to shield the electromagnetic part and solely measure the high-energy muons ($E > 1$ GeV) of the showers at the ground. The relative magnitude of the electromagnetic and muonic components in the shower is a mass estimator complementary to X_{\max} . This concept has already been used, e.g., in the KASCADE-Grande experiment, where the ratio of the number of all charged particles to the number of muons at the ground was utilized to unfold the data in different elemental groups for a separate measurement of the cosmic-ray energy spectrum [28].

Contrary to particle measurements at the ground, the radio signal is produced along the shower development. To validate the mass sensitivity for the combination of the radio signal measured by AERA and the muon signal measured by AMIGA, air-shower simulations corresponding to measured AERA events for proton and iron primaries were studied. The amplitude and with it the total energy contained in the radio emission is correlated to the energy contained in the electromagnetic cascade, which induced this emission. A 2-dimensional double-Gaussian parametrization is used to fit the lateral distribution of the radio energy fluence (energy per unit area) at the ground [13, 5, 6]. The integral over this footprint yields the energy contained in the radio signal, the radiation energy. The primary cosmic-ray energy is reconstructed from the radiation energy for proton- and iron-induced air showers in the lower plot of the left panel of figure 3. It features on average 4% higher values for protons. The muon density at a reference distance of 450 m to the shower axis is

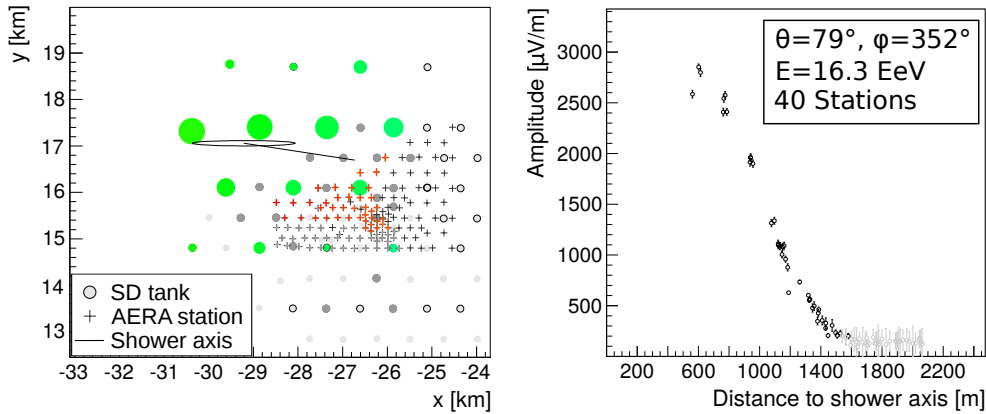


Figure 4: Example event of an inclined air shower with zenith angle of $\theta = 79^\circ$. Left: AERA antenna stations and SD particle detectors with a signal. The sizes of the '+' and circles depict the signal strength in the radio antennas and the particle detectors, respectively. Grey stations are not taken into account in the analysis. Right: The lateral distribution of the radio signal with respect to the shower axis distance. Black and grey circles mark stations above and below the signal threshold, respectively. Even though the shower core is not contained inside of the AERA array, the shower is detected with a high resolution on the lateral distribution of the signal.

correlated to the total number of muons at the ground and is reconstructed from the AMIGA scintillator data with a muon lateral-distribution function [8]. It is shown for proton- and iron-induced air showers in the upper plot of the left panel of figure 3, where the values are on average 40% higher for iron showers. The anti-correlated dependence on the primary mass maximizes the mass-separability for the ratio of the two observables, which is shown in the right panel of figure 3. Up to now, about 4 years of hybrid data of AERA and AMIGA are available to apply the findings in a combined analysis of this ratio.

The particle cascade of inclined air showers only contains muons when the shower arrives at the ground since the electromagnetic part is completely absorbed in the atmosphere. This leads to the opportunity of measuring the electromagnetic part with radio antennas and the muonic part with, e.g., water-Cherenkov detectors separately to determine the mass of the cosmic ray in future analyses.

5. Radio emission from inclined air showers

Since the radiation is beamed in the forward direction, the radio footprint on the ground has diameters of only a few hundred meters for near-vertical showers. This limits the maximum spacing between antennas for coincident measurements. The size of the footprint is almost independent of the primary energy, which is problematic for the detection of cosmic rays with the highest energies, where large detection areas are needed due to the low flux. However, simulations predict that the footprint grows to diameters of several kilometers for showers with zenith angles above $\sim 60^\circ$. This enables measurements of inclined air showers with sparse antenna arrays. For the first time, the lateral extent of such inclined air showers was measured with AERA [29, 30].

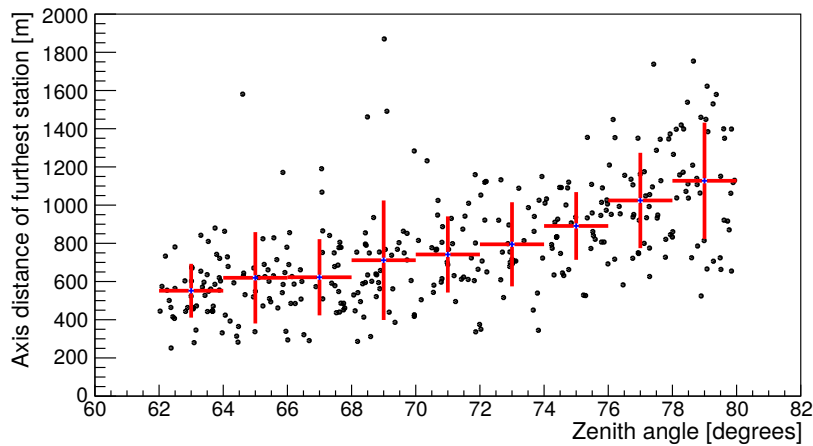


Figure 5: Distance of the furthest station with signal from the shower axis as a function of the zenith angle. The distances only depict a lower limit on the size of the radio footprints. Most footprints are not fully contained in AERA due to the limited size of the array.

Since the shower maximum is geometrically more distant to the detector for higher zenith angles, the forward beamed emission is spread over a larger area. In addition, the large angle between the shower plane and the ground plane causes an elliptic cross-section of the signal at the ground. Hence, the total emission of the shower is spread over a larger area. However, this leads to a weaker signal in a single antenna and a higher energy threshold for the detection of inclined air showers.

The large area of AERA of $\sim 17 \text{ km}^2$ and the co-location of water-Cherenkov detectors (SD) as a trigger, are ideal to measure such inclined air showers over the full extent of the footprint. A search for inclined air showers was performed with the 76 externally triggered antennas on the 144 m and 250 m grid (see figure 1). 344 events were measured in the zenith angle range between 62° and 80° . An example event with a zenith angle of 79° and 40 stations with a signal above background is shown in figure 4. The high number of signal stations illustrates the large radio footprint of such a shower. In figure 5 the distance to the shower axis of the furthest radio station with signal above background is shown as a function of zenith angle for all 344 events. The furthest axis distance where the shower is detected rises with the zenith angle, which shows that the footprint is extended over larger areas for more inclined showers. However, the measured axis distances only constitute lower limits to the size of the footprints due to the insufficient size of AERA. In the future investigations with the 25 additional stations on a grid with 750 m spacing are planned to test the feasibility of a sparse array for the detection of inclined air showers.

6. Conclusion

AERA is dedicated to measuring the radio emission of cosmic-ray air showers above 10^{17} eV . It measures in hybrid mode with the other Auger detectors to gain complementary information for the reconstruction of the cosmic-ray properties. We reconstruct the shower maximum from various observables of the radio signal such as the size of the footprint, wavefront shape parameters, the spectral slope or by evaluating the best agreement to simulations. By comparing our results

with the X_{max} measurements of the fluorescence telescopes we find a resolution of about 39 g/cm^2 with the latter method. We expect to improve the resolution with combining several methods in future analyses. Together with the buried scintillators we measure the electromagnetic and muonic components of the air shower separately. This allows us to measure the primary mass with the electron-muon ratio as a mass-sensitive parameter complementary to X_{max} . For the first time, we measured the lateral extent of inclined air showers with the large area of AERA. We measured events with more than 70 signal stations with a distance to the shower axis of up to 2 km.

References

- [1] T. Huege, *Phys. Rep.* **620**, 1 (2016).
- [2] F.G. Schröder, *Prog. Part. Nucl. Phys.* **93**, 1 (2017).
- [3] W.D. Apel *et al.* [LOPES Collaboration], *Adv. Space Res.* **48**, 1295 (2011).
- [4] J. Neuser, PhD thesis, Bergische Universität Wuppertal (2015), URN:468-20160205-112223-7
- [5] A. Aab *et al.* [Pierre Auger Collaboration], *Phys. Rev. D* **93**, 122005 (2016).
- [6] A. Aab *et al.* [Pierre Auger Collaboration], *Phys. Rev. Lett.* **116**, 241101 (2016).
- [7] A. Aab *et al.* [Pierre Auger Collaboration], *Nucl. Instrum. Meth. A* **798**, 172 (2015).
- [8] B. Wundheiler for the Pierre Auger Collaboration, *Proc. 34th Int. Cosmic Ray Conf.* (2015), [PoS\(ICRC2015\) 324](#).
- [9] H.-J. Mathes, for the Pierre Auger Collaboration, *Proc. 32nd Int. Cosmic Ray Conf.*, 3, 153 (2011).
- [10] A. Aab *et al.* [Pierre Auger Collaboration], Submitted to *JINST*; [arXiv:1702.01392].
- [11] F.G. Schröder *et al.*, *Nucl. Instrum. Meth. A* **615**, 277 (2010).
- [12] A. Aab *et al.* [Pierre Auger Collaboration], *JINST* **11**, P01018 (2016).
- [13] A. Nelles, S. Buitink, H. Falcke, J. Hörandel, T. Huege, and P. Schellart, *Astropart. Phys.* **60**, 13 (2015).
- [14] J. Schulz, [PhD thesis](#), Radboud Universiteit Nijmegen (2016).
- [15] Q.D. Hasankiadeh, for the Pierre Auger Collaboration, 6th ARENA (2014); [arXiv:1705.06230].
- [16] W.D. Apel *et al.*, *JCAP* **1409**, 025 (2014).
- [17] S. Grebe for the Pierre Auger Collaboration, 5th ARENA (2012); *AIP Conf. Proc.* **1535**, 73 (2013).
- [18] S. Buitink *et al.* *Phys. Rev. D* **90**, 082003 (2014).
- [19] T. Huege, M. Ludwig, and C.W. James, 5th ARENA (2012); *AIP Conf. Proc.* **1535**, 128 (2013).
- [20] NOAA Air Resources Laboratory (ARL), Global Data Assimilation System (GDAS1) Archive Information, Tech. rep. (2004). URL: <http://ready.arl.noaa.gov/gdas1.php>.
- [21] P. Abreu *et al.* [Pierre Auger Collaboration], *Astropart. Phys.* **35**, 591 (2012).
- [22] F. Gaté for the Pierre Auger Collaboration, *Proc. XXV ECRS* (2016); [arXiv:1702.02905].
- [23] V. Marin and B. Revenu, *Astropart. Phys.* **35**, 733 (2012).
- [24] A. Aab *et al.* [Pierre Auger Collaboration], *Phys. Rev. D* **90**, 122005 (2014).
- [25] P.A. Bezyazeev *et al.* [Tunka-Rex Collaboration], *JCAP* **1601**, 052 (2016)
- [26] S. Buitink *et al.*, 7th ARENA (2016); *EPJ Web Conf.* **135**, 01009 (2017).
- [27] E. M. Holt for the Pierre Auger Collaboration, TAUP (2015); *J. Phys. Conf. Ser.* **718**, 052019 (2016).
- [28] W.D. Apel *et al.*, *Astropart. Phys.* **47**, 54 (2013).
- [29] O. Kambeitz, [PhD thesis](#), Institut für Kernphysik, Karlsruhe Institute of Technology (2016).
- [30] O. Kambeitz for the Pierre Auger Collaboration, 7th ARENA (2016); *EPJ Web Conf.* **135**, 01015 (2017).



Studies of the microwave emission of extensive air showers with GIGAS and MIDAS at the Pierre Auger Observatory

Romain Gaïor^{*a} for the Pierre Auger Collaboration^b, and Matthew Richardson^c

^a*Laboratoire de Physique Nucléaire et de Hautes Energies (LPNHE), Universités Paris 6 et Paris 7, CNRS-IN2P3, Paris, France*

^b*Observatorio Pierre Auger, Av. San Martín Norte 304, 5613 Malargüe, Argentina*

^c*Vanderbilt University, USA*

E-mail: auger_spokespersons@fnal.gov

Full author list: http://www.auger.org/archive/authors_icrc_2017.html

In 2008, a radio signal interpreted as Molecular Bremsstrahlung Radiation (MBR) was detected at SLAC at microwave frequencies from electromagnetic showers produced in beam test experiments. Due to the isotropic nature of MBR and its insensitivity to atmospheric attenuation and light conditions, it would allow the measurement of the shower longitudinal profile with an almost 100% duty cycle compared to 15% at most with the fluorescence technique today. Several experiments either in the laboratory or in situ within cosmic-ray observatories have been set up aiming at the detection of the MBR flux. The Pierre Auger Observatory has been used as the base for two experiments pursuing the detection of the MBR at GHz frequencies. MIDAS is a radio telescope instrumented with a parabolic dish focusing the radio signal on an array of 53 horn antennas and has taken data for 2 years. GIGAS on the other hand is a single antenna detector embedded in a surface detector. It was implemented in three different versions with a gradually improved sensitivity to comply with the evolution in the expected MBR intensity. We review these two experimental efforts undertaken at the Pierre Auger Observatory attempting at MBR detection and present their latest results.

*35th International Cosmic Ray Conference — ICRC2017
10–20 July, 2017
Bexco, Busan, Korea*

**Speaker.*

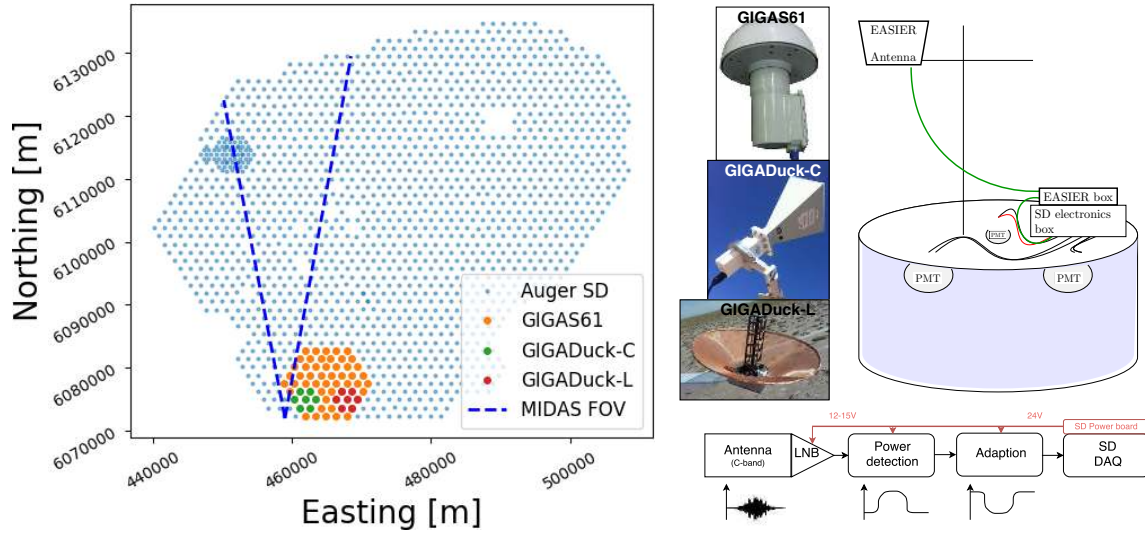


Figure 1: Left: The GIGAS arrays and MIDAS field of view overlaid with the surface detector of the Pierre Auger Observatory. Right: Scheme of GIGAS concept. The sensor placed on the tank is one the three antenna shown in the left side. The signal chain common for all the setups is represented on the bottom part.

1. Introduction

The measurement of the composition of Ultra High Energy Cosmic Rays (UHECR) is crucial to understand their origin. The Pierre Auger Observatory operates currently two main detectors to measure the properties of the Extensive Air Showers (EAS) induced by the UHECR. The Surface Detector (SD) is an array of over 1660 water-Cherenkov detectors (WCD), it measures the particle density at the ground. The Fluorescence Detector (FD) measures the fluorescence light emitted by EAS from 5 sites surrounding the SD. While the SD is limited in its sensitivity to the mass composition, the FD is sensitive to it via the measurement of the longitudinal profile but can be operated only with a duty cycle of 15%. The development of an additional particle detector complementing the existing one and improving its mass sensitivity is the focus of the current upgrade effort undertaken at the Pierre Auger Observatory [1].

New detection channels have also been considered. The observation of the EAS through the radio waves emitted along its development is one of them. In the VHF band (around 50 MHz) the radio signal from EAS is dominated by the coherent emission beamed around the shower axis within the Cherenkov cone [2], preventing the measurement of the longitudinal development.

A promising technique was proposed in 2008 [3] after the observation in a beam test of a signal in the microwave frequencies upon the passage of a particle shower in an anechoic chamber. This signal interpreted as Molecular Bremsstrahlung Radiation (MBR), is emitted isotropically and would allow one to measure the longitudinal profile of the EAS, like with the fluorescence technique but with a 100% duty cycle. Despite the efforts to measure this radiation in subsequent beam tests, or in *in situ* experiment, the intensity of the MBR was not confirmed [4, 5, 6]. In this contribution we present the development and the results of two radio experiments, GIGAS and MIDAS, installed within the Pierre Auger Observatory (see Figure 1 left). For each experiment we will describe the detector characteristics and then present a search for radio event in coincidence with the Auger SD.

2. GIGAS

2.1 Detectors

Concept GIGAS (GHz Identification of Giant Air Shower) is designed to observe the radio emission from EAS with an antenna looking up in the sky. Each radio detector is embedded in a WCD and thus takes advantage of the trigger but also of the solar power system and the data acquisition. The detector is composed of an antenna followed by an amplification and a filtering stage. The radio frequency (RF) signal is then transformed into its power envelope with a logarithmic amplifier which is in turn scaled to fit into the Auger SD front end where the GIGAS signal replaces a low gain channel of one of the three PMTs. The scheme of the GIGAS detector is shown in Figure 1 (right). This concept has been implemented in three different versions, two in the C-band (3.4 to 4.2 GHz) GIGAS61 and GIGADuck-C and one the L band (1 to 1.4 GHz), GIGADuck-L (see Figure 1 (right)).

GIGAS61 The GIGAS61 is the first array installed in the Pampa. A test bed of 7 antennas was installed in April 2011 and the completion to 61 detectors took place a year later. Each detector is composed of a C-band cylindrical horn antenna with a half power beam width (HPBW) of 90° . The antenna points toward the zenith. GIGAS61 has measured clear events in coincidence with the particle detector (see section 2.2). However, because of the short distance to the shower axis the origin of this signal can be attributed to coherent processes and cannot be evidence for the MBR.

GIGADuck-C GIGADuck is an array of seven detectors instrumented with a larger gain antenna to increase the sensitivity, and an optimized geometry to enhance the coincidence probability between radio detectors. Such a coincidence would favor the MBR origin of a signal against a coherent process. In this modified geometry, each antenna points in a different direction, the central one is pointed at the zenith while the other six are tilted by 20° and have their azimuth oriented in the direction of the central detector. In the C-band, the antenna is a pyramidal horn with 15 dB gain and a HPBW of 60° , followed by an LNB (Norsat 8115F).

GIGADuck-L The GIGADuck design has been also implemented in the L-band. The antenna is a helix antenna with a maximum gain at 1.4 GHz and a HPBW of 60° . Contrary to the two other setups, the amplification board was developed in laboratory. It integrates a band pass filter and an electric surge protection and two commercial LNA chips (Broadcom Limited MGA633P8 and MGA13116) in series. The gain and noise temperature of this board were characterized before the installation. The gain in the bandwidth is around 50 dB and the noise temperature ranges from 60 to 80 K among the 9 boards tested.

Detector calibration The sensitivity of a radio power detector like GIGAS can be estimated with the figure of merit that defines approximately the minimum flux one can detect, $F_{\min} = k_B T_{\text{sys}} / A_{\text{eff}} \sqrt{\Delta\nu \Delta t}$ where k_B is the Boltzmann constant, T_{sys} the system temperature, A_{eff} the effective area, $\Delta\nu$ and Δt the bandwidth and the time over which the signal can be integrated.

The comparison of the simulated A_{eff} of the three GIGAS detectors in the figure 2 (left) shows the direct increase in sensitivity from this parameter.

The system temperature is more difficult to estimate. For the three setups it was indeed measured

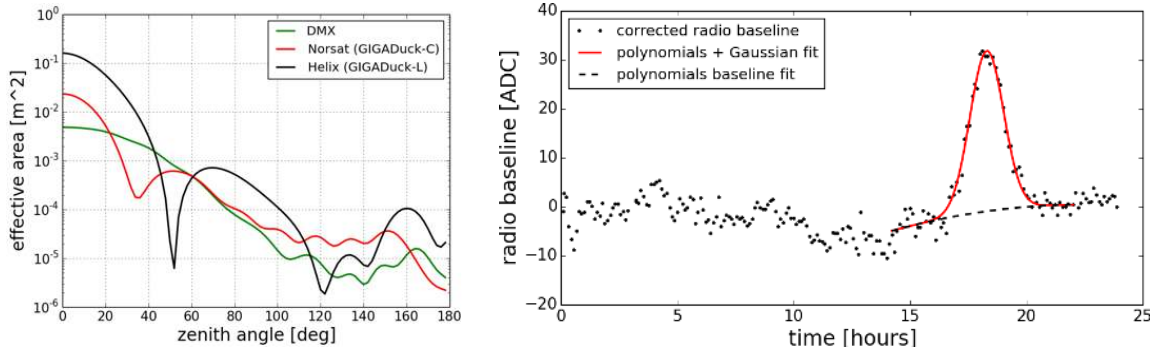


Figure 2: Left: Antenna effective area as a function of the zenith angle for the three setups. Right: Example of a daily baseline corrected from the outside temperature dependence.

with different methods. For GIGAS61 detectors it was estimated by applying the so called Y-factor method on a dedicated measurement on site. We simply measured the power output when the antenna was pointed towards the sky and then when it was oriented towards the ground, i.e. two different sources of microwaves emission. From the difference of power between these measurements, an intrinsic noise system temperature of 120 K was measured.

For the GIGADuck-C band, we have developed a method using the Sun as a calibration source. The emission from the Sun produces a bump in the radio baseline recorded in the monitoring system. After correcting the baseline from outside temperature dependence, we can fit this bump (see an example in Figure 2). We apply this method on a set of daily baselines selected on the quality of the radio data and the quality of the fit. The system temperature is deduced from the comparison with the expected amplitude of the Sun contribution estimated with the solar flux based on observations at the Nobeyama Radio Observatory (NRO)¹ at 3.75 GHz. By comparing the measured and simulated values of the amplitude of the bump but also the time of its maximum, the system noise temperature and the pointing direction of the antenna were measured simultaneously. We found system noise temperatures ranging from 54 to 61 K and an angular distance from the nominal pointing of a few degrees with a maximum of 12°.

The baseline of the GIGADuck-L detectors exhibits also a clear bump attributed to the Sun. However other contributions are noticed over the day and prevent us from isolating the Sun signal (a possible origin of these contributions are the positioning satellite like GPS which all emit in the L-band). Therefore the system temperature is directly measured from the baseline level in monitoring. This procedure is made possible thanks to the calibration carried out prior to the installation. Noise temperatures ranging from 95 to 145 K were found for the seven installed detector. This accounts also for the noise induced by the Sun and other sources, explaining the spread in the temperature.

2.2 Event search

We show in this section a search for radio events in coincidence with EAS recorded by the Auger SD. The radio data set is composed of the three setups and their operation time overlap from April 2011 to May 2017. We select high quality SD events, by applying regular selection criteria

¹The Nobeyama Radio Polarimeters is operated by Nobeyama Radio Observatory, a branch of National Astronomical Observatory of Japan.

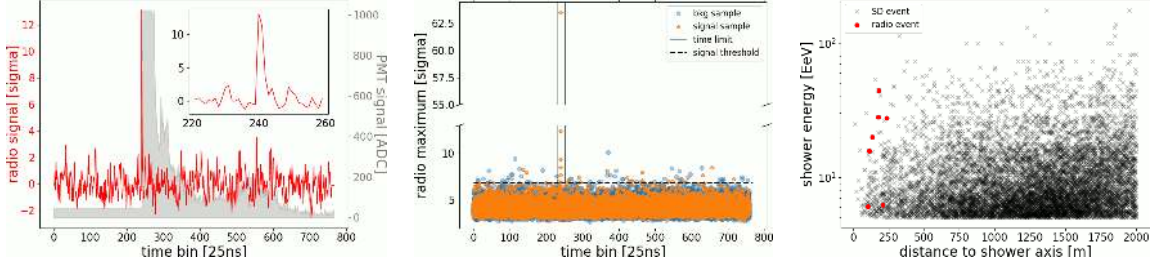


Figure 3: Left: radio waveform (normalized by the trace standard deviation). Middle: The radio maxima of the background and signal data sets. Right: event distribution in the energy / distance plane. The red dots are the event identified in radio.

Table 1: Characteristics of the radio events detected with GIGAS.

Event date	2011/06/30	2012/09/05	2013/01/03	2013/06/04	2013/07/16	2013/09/26	2015/02/03
Energy [EeV]	16	6	27	19.5	42	6.2	28
Distance [m]	112	103	237	133	181	208	176
(θ, ϕ)	(29.6, -17)	(48, 167)	(55, 34)	(53, -1.2)	(40, 155)	(59, -49)	(54, 1)
Radio maximum	13	7.7	12.3	6.9	63	8.5	9.4

on the shower reconstruction and by removing the events tagged as lightning. A second set of cuts is then applied on the radio traces: we remove traces with large RMS or with more than 10 bins saturated (out of 768). The data set is split in a *background set* composed of the WCD with a distance from the shower axis larger than 3 km and a *signal set* which selects, among the EAS event of energy larger than 5 EeV and zenith angle smaller than 60° , the WCD closer than 2 km from the shower axis. The former is not expected to contain any detectable radio event while the latter should be enriched in them. The radio waveform is linearized converted in unit of its standard deviation (see for instance Figure 3 (left)), the distribution of the radio maximum as a function of the time of this maximum is shown in Figure 3 (middle) for the GIGAS61 setup. One can see a clear accumulation of events with large signal to noise ratio at the time bin 240 which is only 50 ns before the SD trigger time (see Figure 3 (left)). To extract the radio events, we determine the value of the radio maximum that holds 99.7% of the events in the *background set* and we set this value as threshold for the *signal set*. The time of maximum is also required to be inside a 500 ns window around the particle trigger to absorb any possible time delay induced by the detector. Seven radio events were found, all detected with the GIGAS61 setup. A typical waveform is represented in Figure 3 (left), the radio signal (in red) is a high and short pulse of less than 50 ns long (see inset of Figure 3 (left)) coincident with the PMT signal start (in grey). The parameters of these events are listed in Table 1. A striking feature is the short distance to the shower axis of all the detected events. Indeed, among the high energy events recorded by the Auger SD, no signal at larger distances than 250 m induced a clear signal in GIGAS setups (Figure 3 (right)).



Figure 4: MIDAS detector installed in the Pampa at the Pierre Auger Observatory.

3. MIDAS

3.1 Detectors

The MIDAS detector, first commissioned at the University of Chicago in 2010 [7], was installed at the Pierre Auger Observatory in 2012, with its field of view covering a portion of the SD (Figure 1.) The telescope consists of a 5 m diameter parabolic antenna with a 53 pixel camera at its focus (Figure 4) covering a field of view of approximately $20^\circ \times 10^\circ$. Each pixel is composed of a feed horn, a low noise amplifier, and a frequency down converter. An RF power detector converts radio waves detected by a pixel to a voltage level which is digitized by a 14 bit analog-to-digital converter (ADC) at a sampling rate of 20 MHz (an ADC board serves 16 pixels.) Up to 2048 samples are stored in a circular buffer and processed by a first level trigger (FLT) algorithm implemented in the on-board field programmable gate array (FPGA). A second level trigger (SLT) decision is taken by a Master Trigger board by searching for 4-pixel patterns compatible with a track-like signal from an EAS. When an SLT is present, all 53 pixels are readout [7].

3.2 Event search and limits on MBR intensity

Event search A search for MBR signal from EAS based on time coincidence between MIDAS and SD events was performed with data collected from September 14, 2012 to September 26, 2014. Notice that the MIDAS telescope is self-triggered, contrary to GIGAS where the trigger is provided by the SD local station. Thus a first selection was performed to reject periods with high level of radio noise where the SLT rate can reach several kHz, to be compared with an expected SLT rate from white noise accidentals of less than a mHz. To remove these periods, the SLT rate was required to be less than 0.5 Hz. Also, periods when the FLT rate exceeded 2.4 kHz were removed. These criteria resulted in an active MIDAS observational time t_{obs} of about 359 days.

High quality SD events were selected by requiring the tank with the largest signal to be surrounded by active tanks and a reconstructed shower energy above 1 EeV. Also, the SD reconstructed shower core was required to be within the MIDAS field of view projected on the ground. Lastly, a search was performed for MIDAS and SD events occurring in a coincidence time window of $\pm 300 \mu\text{s}$, a

relatively large window to account for time delays due to microwave signal propagation. Only one event was found to fulfill all the selection criteria.

The expected rate r_c from random coincidences can be estimated by $r_c \simeq r_A r_M \tau$ where $r_A = 8.9 \times 10^{-4} \text{ Hz}$ and $r_M = 1.8 \times 10^{-2} \text{ Hz}$ are the measured Auger and MIDAS event rate medians, and $\tau = 600 \mu\text{s}$ is the coincidence time interval. The expected number of coincidence events is then given by $N_c = r_c t_{\text{obs}} \approx 0.3$. A similar estimate was obtained by repeating the analysis on mock samples where the SD event detection time was randomly shifted (see [8].) Thus, the single found candidate event is consistent with expectations from purely random coincidences. The waveforms of the SLT pixels associated with the candidate event are shown the Figure 5 (left), with the full pixel camera signals in the inset. The signal time characteristics and the multiple pixels patterns observed in the MIDAS camera are not compatible with an EAS event. In addition, the SD reconstructed shower has an energy of 2.5 EeV and a core located at 53 km distance from the MIDAS telescope. Since many more SD events of larger energy and smaller distance are present in the selected sample but not detected in coincidence with MIDAS, it is highly unlikely that the candidate event is real. Thus the candidate event was rejected and the search ended with a null result.

Limits on MBR properties Dedicated simulations were performed to establish limits on the properties of MBR from EAS. Following [3], we parameterize in the simulation the microwave flux of the EAS at the MIDAS detector, I_f , as

$$I_f = I_{f,\text{ref}} \frac{\rho}{\rho_0} \left(\frac{d}{R} \right)^2 \left(\frac{N}{N_{\text{ref}}} \right)^\alpha \quad (3.1)$$

where $I_{f,\text{ref}}$ is the power flux at a distance $d = 0.5 \text{ m}$ from a reference shower of $E_{\text{ref}} = 3.36 \times 10^{17} \text{ eV}$, R is the distance between the detector and the EAS segment, $\rho(\rho_0)$ is the atmospheric density at the altitude of the EAS segment (at sea level), and N is the number of shower particles in the EAS segment. N_{ref} is the average number of shower particles at the maximum of the EAS development for a proton primary of energy E_{ref} . N and N_{ref} are given by a Gaisser-Hillas [9] parameterization of their respective EAS. The exponent α accounts for the degree of coherence of the MBR emission, ranging from $\alpha = 1$ for incoherent to $\alpha = 2$ for fully coherent.

For a given pair of I_{ref} and α , events with the same energy and geometry of the selected SD events (Sect. 3.2) were simulated using Eq. 3.1 and a realistic detector response. A pair (I_{ref}, α) was excluded at 95% CL when the corresponding number of simulated events with SLT was less than 3 [10]. Limits on the MBR parameters are shown in Fig. 5, which improve significantly over previous MIDAS results [11] and unequivocally rule out the signal reported in [3] as MBR emission. Recent calculations [12] predict an incoherent MBR emission a factor 200 smaller than in [3], which would require a further improvement in the experimental sensitivity to be detected.

4. Discussion and conclusions

Two setups, GIGAS and MIDAS, aiming at the observation of the MBR in coincidence with event detected at the Pierre Auger Observatory were presented. While clear radio events were observed with GIGAS, no signal were found with MIDAS microwave telescope. These results are however compatible if one considers other emission origins. Indeed, the radio signal observed with

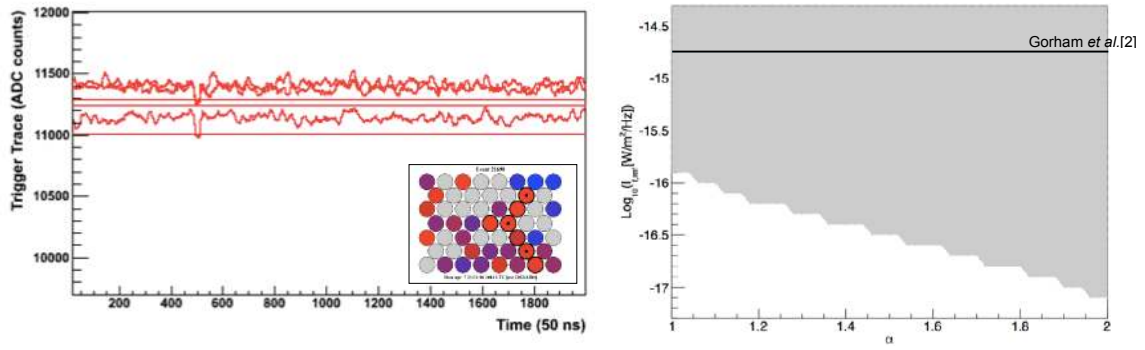


Figure 5: Left: MIDAS candidate event waveforms and pixel configuration. Right: 95 % CL limits in the plane of the reference intensity (I_{ref}) and the energy scaling (α) (see Eq. 3.1)

GIGAS are all from close shower axis and might be attributed to coherent emissions known to be dominant at lower frequencies [2]. This would also explain the absence of event observation in the MIDAS data since this detector views the shower from the side and is not optimized for the detection of short radio signals.

These results are in agreement with previous non detection of MBR in beam experiments [4, 5] and *in situ* experiment [6]. They ruled out for the first time all the parameters used for the interpretation in terms of MBR of the original beam test experiment. The intensity of the MBR found by subsequent calculations [12] is smaller by at least a factor 200 and is still uncertain. Going down to this level of sensitivity would require deeper developments such as a cryo-cooled system and is beyond the initial goal of a simple, inexpensive and mass sensitive system.

Acknowledgement

We acknowledge the support of the French Agence Nationale de la Recherche (ANR) under reference ANR-12- BS05-0005-01.

References

- [1] D. Martello, for the Pierre Auger Observatory, these proceedings.
- [2] F. Schröder, Prog. Part. Nucl. Phys. 93 (2017) 1–68.
- [3] P. Gorham *et al.*, Phys. Rev. D 78 (2008) 032007.
- [4] J. Alvarez-Muñiz *et al.*, RICAP2014, EPJ 121 (2016) 03010.
- [5] C. Williams *et al.*, EPJ 53 (2013) 08008.
- [6] R. Šmida *et al.*, Phys. Rev. Lett. 113 (2014) 221101.
- [7] J. Alvarez-Muñiz *et al.*, Nucl. Instrum. Meth. A 719 (2013) 70–80.
- [8] M. Richardson, Vanderbilt University, PhD thesis (2016).
- [9] T.K. Gaisser and A.M. Hillas, Proc. 15th Int. Cosmic Ray Conf., Plovdiv, Bulgaria, 8 (1977) 353.
- [10] G. Feldman and R. Cousins, Phys. Rev. D 57 (1998) 3873–3889.
- [11] J. Alvarez-Muñiz *et al.*, Phys. Rev. D 86 (2012) 051104.
- [12] I. Al Samarai *et al.*, Phys. Rev. D 93 (2016) 052004.

5

Cosmology and Geophysics





Probing Lorentz symmetry with the Pierre Auger Observatory

Denise Boncioli^{*a} for the Pierre Auger Collaboration^b

^a*DESY, Platanenallee 6, 15738 Zeuthen, Germany*

^b*Observatorio Pierre Auger, Av. San Martín Norte 304, 5613 Malargüe, Argentina*

E-mail: auger_spokespersons@fnal.gov

Full author list: http://www.auger.org/archive/authors_icrc_2017.html

Effects of Lorentz invariance violation (LIV) can be present at energies much lower than the quantum gravity scale. Here the possible LIV effects in ultra-high energy cosmic rays (UHECRs) are investigated. To this aim, modifications of the propagation of UHECR protons and nuclei in the extragalactic space due to LIV effects are taken into account. For the first time a fit of both flux and composition of UHECRs as measured by the Pierre Auger Observatory is used in order to evaluate the constraining power of current data on LIV parameters.

*35th International Cosmic Ray Conference — ICRC2017
10–20 July, 2017
Bexco, Busan, Korea*

^{*}Speaker.

1. Introduction

One of the fundamental symmetries of relativity is Lorentz Invariance (LI). In the last decades there has been progress in testing deviations from LI. A unified theory of Quantum Mechanics, that describes the universe at small scales, and General Relativity, that describes it at large scales, is still unknown. Lorentz Invariance Violations (LIV) are expected to be observable, if any, at energies near the Planck scale ($M_{\text{Pl}} \approx 1.2 \times 10^{28}$ eV). If compared with the current maximal energy attainable in accelerators, the observation of such phenomena requires particles to have 15 orders of magnitude larger than the LHC center-of-mass energy.

High energy astrophysics provides opportunities to probe energies much larger than the accelerator ones. In particular, in this work we study the interactions of Ultra-High-Energy Cosmic Rays (UHECRs), meaning with that particles that hit the Earth's atmosphere with energies above 10^{18} eV. Such particles are mainly expected to have extragalactic origin, since they arrive nearly isotropically to the Earth and the Galactic magnetic field would not be able to confine them. Moreover, extragalactic sources as Active Galactic Nuclei or Gamma-Ray Bursts are considered as good candidates to accelerate particles to such extreme energies. UHECRs are expected to travel from their sources through the extragalactic space and to interact with photon fields that fill it (Cosmic Microwave Background, CMB, and Extragalactic Background Light, EBL). These interactions, such as the photo-pion production and the photo-disintegration in the case of UHECR nuclei, would appear as low energy processes in the center of momentum. In contrast, in the laboratory frame very large Lorentz factors can be reached and the Special Relativity can be tested. The possibility of putting limits on LIV parameters with processes involving UHECRs was first discussed in [1]. Later on, the suppression of the flux at the highest energies was established and limits on LIV parameters were derived. As an example, parameter space studies were performed using the UHECR spectrum and a pure proton composition [2, 3]. Motivated by experimental indications of chemical composition of UHECRs heavier than protons, the modifications of LI in the propagation of nuclei were studied for example in [4]. A detailed summary can be found in [5].

In this work LIVs are taken into account during the extragalactic propagation of UHECRs. A fit of the UHECR spectrum [6] and composition data [7] is performed as done in [8] and the results including the propagation in presence of LIV are discussed.

2. LIV and UHECR propagation

LI modifications can be implemented in many ways, with different consequences on physical observables. A simple approach consists in proposing a modified dispersion relation for particles and keeping the usual conservation of energy and momentum. LIV will affect the dispersion relation as

$$E_i^2 - p_i^2 = m_i^2 \Rightarrow \mu_i^2(E, p, M_{\text{Pl}}) \approx m_i^2 + \sum_{n=0}^N \eta_i^{(n)} \frac{E_i^{2+n}}{M_{\text{Pl}}^n}, \quad (2.1)$$

where $p = |\vec{p}|$, μ is a function of momenta and energy, and η_i , which can be either positive or negative, parametrizes the strength of LIV for particle i . In the limit $\eta_i^{(n)} = 0$ the Lorentz invariant dispersion relation is recovered. From Eq. 2.1 one can see that the LI correction becomes larger than the mass of the particles if $p \geq (m_i^2 M_{\text{Pl}}^n / |\eta_i^{(n)}|)^{1/(2+n)}$.

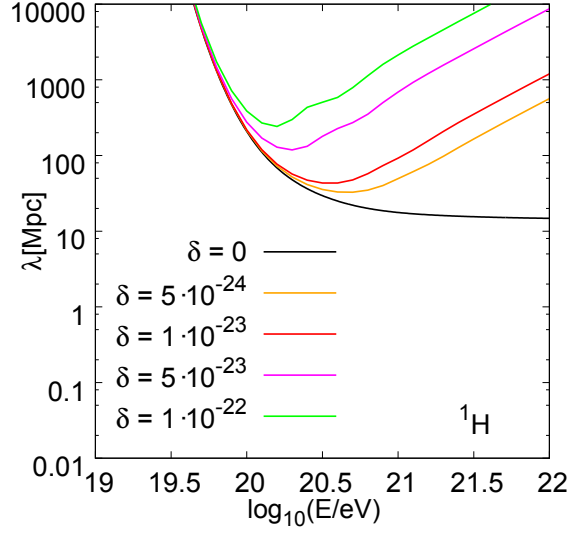


Figure 1: Attenuation length of protons interacting in the CMB at $z = 0$ as a function of the proton energy in the laboratory frame, for the LI case (black line) and for different choices of the LIV coefficient δ for $n = 0$ [9].

The LIV parameter can be defined as

$$\delta_i^{(n)} = \frac{\eta_i^{(n)}}{M_{\text{Pl}}^n} \quad (2.2)$$

Here we adopt the LIV framework of [10], where a first order perturbation is considered. Since we consider $n = 0$, the LIV parameter δ_i is dimensionless. It is interesting to notice that the LI violating term can be translated in a shift of the mass of the particle and a shift of the velocity from $c = 1$. Since different particles can have different maximum attainable velocities, these can be different from c as well as different from each other. The LIV parameter can be directly related to this difference [3].

We discuss first the photo-pion process. Soon after the discovery of the CMB it was realized that interactions of protons with CMB photons would deplete the CR flux at the highest energies (“GZK effect”) [11, 12]. A suppression of the flux at the highest energies was actually measured [13, 14]. However, its origin is still unknown, since this feature is sensitive to local deficit of sources and can also be mimicked by acceleration cutoffs at the source. The inelasticity of the process, meaning how much of the energy of the initial proton is carried away by the final pion, is modified introducing LIV. The LIV affecting the photo-pion production gives the most important contribution to the modification of the UHECR spectrum above the GZK energy. By considering modifications to the maximum attainable velocity of the pion, the phase space allowed for the interaction is reduced with respect to the LI case. This is due to the limits on the allowed range of the interaction angles coming out from kinematics study [10]. The effect of different δ parameters on the attenuation length of the protons in the CMB is shown in Fig. 1, where it is clear that changing the value of δ , the energy at which the LIV becomes significant is lower [9]. As a consequence, the UHECR spectrum is expected to exhibit a suppression near the GZK and to recover at higher energies.

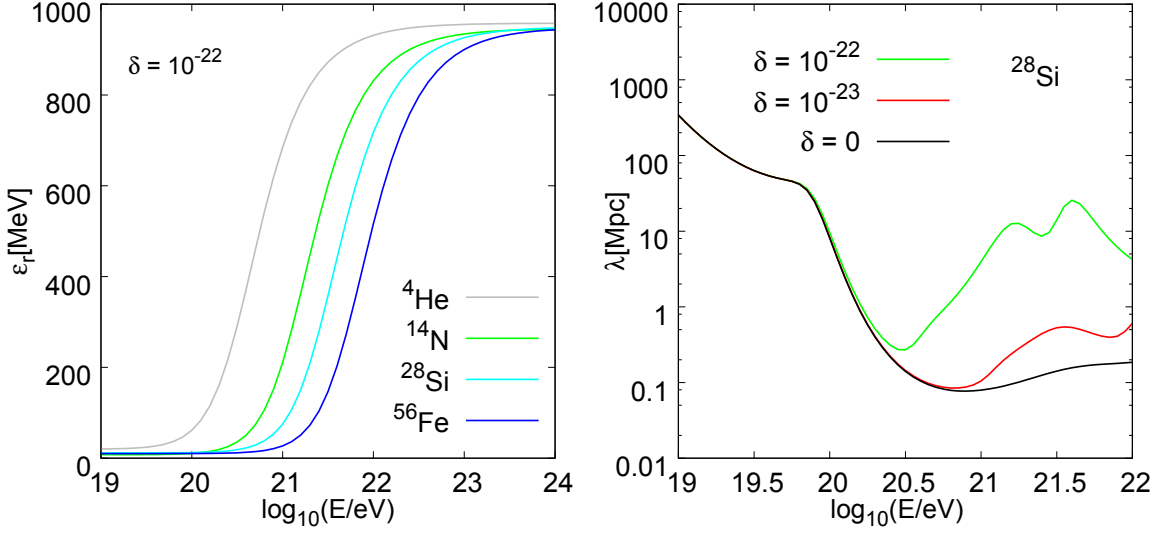


Figure 2: Left: Threshold energy in the nucleus rest frame for the photo-disintegration of nuclei as a function of the initial nucleus energy in the laboratory frame, for $\delta = 10^{-22}$ [9]. Right: Mean free path for the photo-disintegration of an silicon nucleus as a function of the energy in the laboratory frame, at $z = 0$. The LI scenario (black line) is compared to the LIV scenarios with $\delta = 10^{-22}$ and $\delta = 10^{-23}$ for $n = 0$ [9].

Concerning the propagation of nuclei in the Universe, the energy losses for photo-pion production are shifted at energies $\sim A$ times higher than the threshold for protons. However, the excitation of the giant dipole resonance (GDR) by photons of energy tens of MeV in the nucleus rest frame causes the disintegration of the nucleus ejecting one or more nucleons and is responsible for the steepening of the flux at the highest energies. The dispersion relation for nuclei can be written assuming a superposition model for nuclei, *i.e.* considering them as the combination of A nucleons of energy E/A . In this way, since we are dealing with the linear modifications $n = 0$, the LIV parameter can be assumed as equal to the one for protons. The threshold energy of the photon in the nucleus rest frame does not depend on the energy of the nucleus but only on its nuclear mass; including LIV effects makes the dependence on the energy of the nucleus appear, as shown in Fig. 2 (right panel). The effect in the spectrum is expected to be similar to what happens to the proton case in presence of LIV, since also in this case the mean free path departs from the LI case and increases with energy, as shown in the right panel of Fig. 2 for silicon nuclei.

The discussed modifications to LI were included [9] in *SimProp* [15], a simulation code for the propagation of UHECRs in the extragalactic space. The physical quantities used in the code to take into account the EBL model and the photo-disintegration cross sections for this study are the Gilmore EBL model [16] and the Puget-Stecker-Bredekamp (PSB) model [17, 18] respectively.

3. Fit results

A fit of the cosmic ray spectrum [6] and composition data [7] as measured by the Pierre Auger Observatory is performed following the method described in [8]. The UHECR sources are assumed to be identical and homogeneously distributed in a co-moving volume. The mass species at the injection are: ^1H , ^4He , ^{14}N and ^{28}Si , being the inclusion of heavier masses not relevant for

	γ	$\log_{10}(R_{\text{cut}}/\text{V})$	H(%)	He(%)	N(%)	Si(%)	$D(J)$	$D(X_{\text{max}})$	D
LI, $\delta = 0$	0.96	18.68	0.	67.3	28.1	4.6	13.3	161.1	174.4
LIV, $\delta = 5 \times 10^{-24}$	0.91	18.65	0.	71.8	23.9	4.3	15.1	163.5	178.5
LIV $\delta = 1 \times 10^{-23}$	0.91	18.65	0.	71.4	24.3	4.3	14.9	163.6	178.5
LIV $\delta = 1 \times 10^{-22}$	0.94	18.65	0.	72.8	22.7	4.6	18.2	163.6	181.8
max LIV	0.95	18.40	62.3	32.2	5.4	0.08	27.3	162.0	189.3

Table 1: Best-fit parameters for the LI reference model in [8] and for the LIV cases with different δ values. The maximal-LIV case is also reported. The fractions are defined at fixed energy ($E = 10^{18}$ eV).

improving the goodness of fit, as found in [8]. The injection spectrum is taken as

$$\frac{dN_A}{dE} = J_A(E) = f_A J_0 \left(\frac{E}{10^{18} \text{ eV}} \right)^{-\gamma} \times f_{\text{cut}}(E, Z_A R_{\text{cut}}), \quad (3.1)$$

where f_A is the fraction of the injected isotope over the total and is defined at fixed energy ($E = 10^{18}$ eV). The cutoff function is

$$f_{\text{cut}}(E, Z_A R_{\text{cut}}) = \begin{cases} 1 & (E < Z_A R_{\text{cut}}) \\ \exp\left(1 - \frac{E}{Z_A R_{\text{cut}}}\right) & (E > Z_A R_{\text{cut}}) \end{cases} \quad (3.2)$$

The parameters of the fit are the spectral index γ , the cutoff rigidity R_{cut} , the normalization of the spectrum J_0 and three of the fractions f_A , the fourth being fixed by $\sum_A f_A = 1$.

For the spectrum we fit the surface detector (SD) event distribution using a forward-folding procedure. For the composition we fit the X_{max} distribution adopting a Gumbel parametrization [19]. Both the spectrum and composition are fitted at energies $\log_{10}(E/\text{eV}) > 18.7$, *i.e.* above the ankle.

In the Auger data the energy spectrum and the X_{max} distributions are independent measurements and the model likelihood is therefore given by $L = L_J \cdot L_{X_{\text{max}}}$. The goodness-of-fit is assessed with a generalized χ^2 , (the deviance, D), defined as the negative log-likelihood ratio of a given model and the saturated model that perfectly describes the data,

$$D = D(J) + D(X_{\text{max}}) = -2 \ln \frac{L}{L^{\text{sat}}} = -2 \ln \frac{L_J}{L_J^{\text{sat}}} - 2 \ln \frac{L_{X_{\text{max}}}}{L_{X_{\text{max}}}^{\text{sat}}}. \quad (3.3)$$

To account for the LIV effects in the propagation of protons and nuclei we use the modified version [9] of *SimProp*, as earlier anticipated. The LIV parameter δ is considered to be the same in the photo-pion and photo-disintegration process. The simulations are performed for different δ values and the corresponding best-fit parameters are reported in Table 1, where the corresponding LI case and the maximal-LIV cases are compared. The best-fit parameters are found to be very similar to the LI case: the spectral index is hard and the rigidity cutoff is low, in order to reproduce the low level of mixture of masses at each energy.

Since the effect of enhancing the LIV parameter is to increase the interaction length of the particles, a way to investigate an extreme case is to switch off all the interactions with background

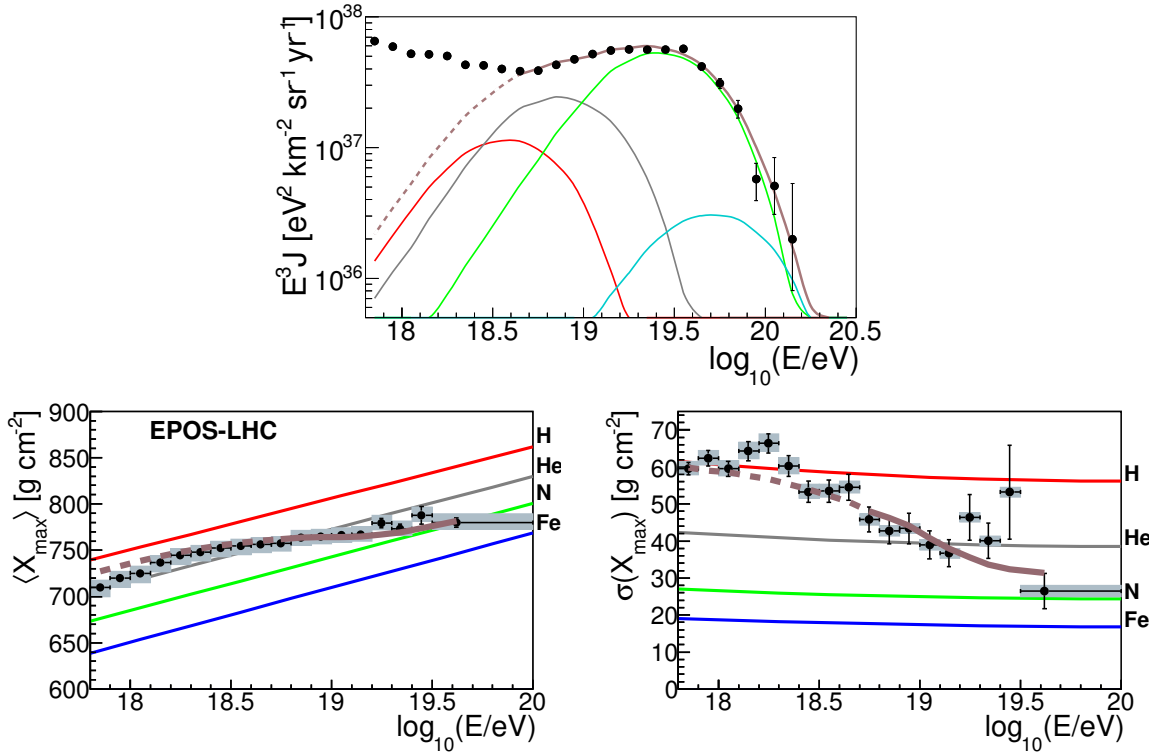


Figure 3: Top: simulated energy spectrum of UHECRs (multiplied by E^3) at the top of the Earth's atmosphere, obtained with the best-fit parameters for the case with maximal-LIV. Spectra at Earth are grouped according to the mass number as follows: $A = 1$ (red), $2 \leq A \leq 4$ (grey), $5 \leq A \leq 22$ (green), $23 \leq A \leq 28$ (cyan), total (brown), compared to data from [6]. Bottom: average and standard deviation of the X_{max} distribution as predicted (assuming EPOS-LHC [21] for UHECR-air interactions) for the model versus pure (^1H (red), ^4He (grey), ^{14}N (green) and ^{56}Fe (blue)) compositions, compared to data from [22]. Only the energy range where the brown lines are solid is included in the fit.

photons [20]. The maximal-LIV case is simulated with a simplified version of the propagation code, where only the adiabatical energy losses due to the expansion of the Universe are taken into account. The corresponding observables are shown in Fig. 3. The spectral index at the best fit is similar to the LI and partial LIV cases. A remarkable difference is visible in the rigidity at the best fit: in this case the rigidity has to be lower at the source with respect to the other case in order to compensate for the absence of interactions that would lower it during propagation. Another substantial difference is that in the LI or partial LIV cases the proton fraction at the source is almost negligible, while in the maximal-LIV case protons must be present already at the source in order to compensate for the absence of interactions.

4. Discussion and conclusions

In this work we use the interactions of UHECRs during their propagation from the sources to the Earth in order to investigate the possible violations of LI. A combined fit of the spectrum and composition data is used here for the first time for this purpose. In the LI case, it is shown that a scenario including a hard spectral index and a low rigidity cutoff can describe the data [8].

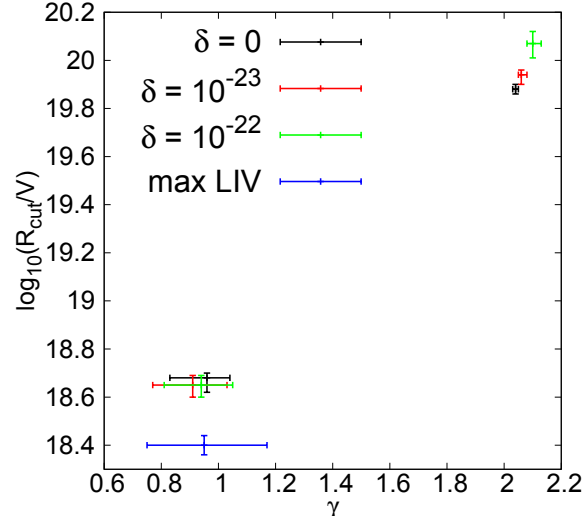


Figure 4: Position of the best-fit values as a function of the spectral index and rigidity cutoff, for the LI case and some of the LIV cases, are reported in the lower-left part of the figure. The error bars are computed from the interval $D \leq D_{\min} + 1$. The local minima are reported in the upper-right part of the plot: in this case the error bars are computed from the interval $D \leq D_{\min}^{\text{local}} + 1$.

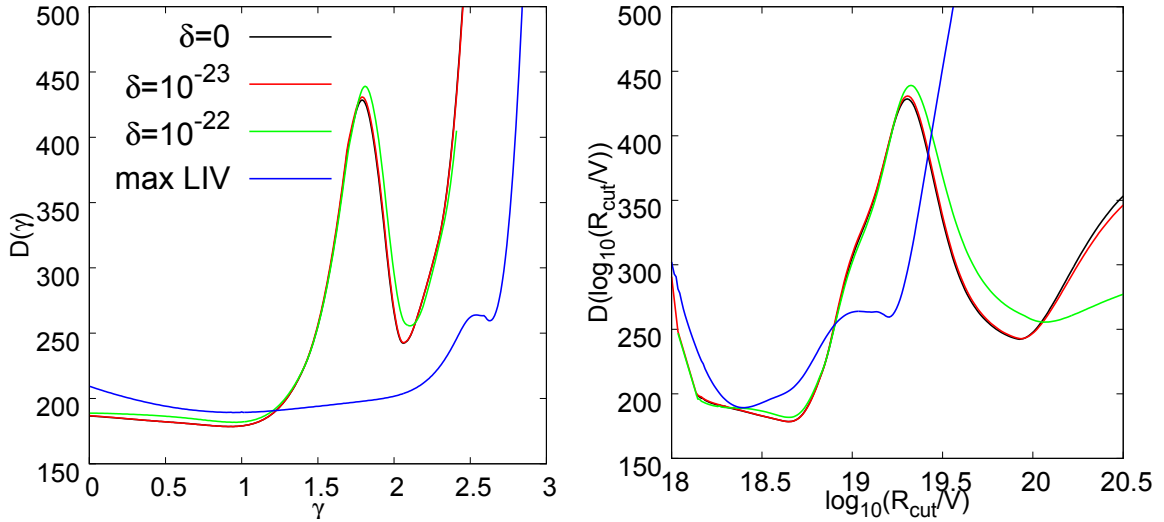


Figure 5: Deviance D versus γ (left) and R_{cut} (right) for the LI and LIV cases.

As a consequence, at the energies corresponding to the rigidity cutoff found from the fit, the LI corrections are not larger than the mass of the considered nuclei and the partial LIV cases are not distinguishable from the LI case. This can be also shown in Fig. 4, where the positions of the best-fit cases are found at very similar values (around $\gamma \sim 1$).

We also find a local minimum region around $\gamma \sim 2$ and $\log_{10}(R_{\text{cut}}/V) \sim 20$, as it is shown in Fig. 4. At the energies corresponding to these values of the rigidity, we start to be sensitive to the modifications to LI, mainly due to the survival of the light mass component up to the highest energies. A trend towards higher rigidities and softer spectral indices is visible while increasing the value of the LIV parameter. This is motivated by the fact that a larger δ implies that the interaction

length starts to increase at lower energies (see Fig. 2, right panel). As a result, the allowed rigidity cutoff at the source is larger. However, by looking at Fig. 5, where the deviance versus the spectral index and the rigidity cutoff is reported, it is clear that the significance of the local minimum is much smaller with respect to the main one, making this trend not useful for drawing a conclusion about the possibility of disfavoring a LIV parameter with the current measurements, which prefer a low-rigidity scenario.

We have also investigated an extreme case in which the interactions are switched off: this case can be reported to modifications of LI having $\eta < -2.5 \times 10^{-14}$ for $n = 1$ or $\eta < -4 \times 10^{-7}$ for $n = 2$, as studied in [20]. By comparing the values of the deviance at the minimum (see Table 1), the maximal-LIV case can be disfavored at more than the 3σ level. However, the absence of the interactions makes the maximal-LIV case more sensitive to the initial conditions, namely the number of injected species at the source and/or the choice for the functional shape of the cutoff at the sources.

References

- [1] R. Aloisio *et al.*, Phys. Rev. D **62**, 053010 (2000); [arXiv:astro-ph/0001258].
- [2] X. J. Bi *et al.*, Phys. Rev. D **79**, 083015 (2009); [arXiv:0812.0121].
- [3] S. T. Scully and F. W. Stecker, Astropart. Phys. **31**, 220 (2009); [arXiv:0811.2230].
- [4] A. Saveliev *et al.*, JCAP **1103**, 046 (2011); [arXiv:1101.2903].
- [5] S. Liberati, Class. Quant. Grav. **30**, 133001 (2013); [arXiv:1304.5795].
- [6] I. Valiño for the Pierre Auger Collaboration, PoS(ICRC2015)271; [arXiv:1509.03732].
- [7] A. Aab *et al.* [Pierre Auger Collaboration], Phys. Rev. D **90**, 122005 (2014); [arXiv:1409.4809].
- [8] A. Aab *et al.* [Pierre Auger Collaboration], JCAP **1704**, 038 (2017); [arXiv:1612.07155].
- [9] R. Guedes Lang, Master Thesis, University of São Paulo, Brazil (2017).
- [10] S.R. Coleman and S.L. Glashow, Phys. Rev. D **59**, 116008 (1999); [arXiv:hep-ph/9812418].
- [11] K. Greisen, Phys. Rev. Lett. **16**, 748 (1966).
- [12] G.T. Zatsepin and V.A. Kuzmin, JETP Lett. **4**, 78 (1966).
- [13] J. Abraham *et al.* [Pierre Auger Collaboration], Phys. Rev. Lett. **101**, 061101 (2008); [arXiv:0806.4302].
- [14] R.U. Abbasi *et al.* [HiRes Collaboration], Phys. Rev. Lett. **100**, 101101 (2008); [arXiv:astro-ph/0703099].
- [15] R. Aloisio *et al.*, JCAP **1210**, 007 (2012); [arXiv:1204.2970].
- [16] R.C. Gilmore *et al.*, Mon. Not. Roy. Astron. Soc. **422**, 3189 (2012); [arXiv:1104.0671].
- [17] J.L. Puget *et al.*, Astrophys. J. **205**, 638 (1976).
- [18] F.W. Stecker and M.H. Salamon, Astrophys. J. **512**, 521 (1999); [arXiv:astro-ph/9808110].
- [19] M. De Domenico *et al.*, JCAP **1307**, 050 (2013); [arXiv:1305.2331].
- [20] D. Boncioli *et al.*, PoS(ICRC2015)521; [arXiv:1509.01046].
- [21] T. Pierog *et al.*, Phys. Rev. C **92**, no. 3, 034906 (2015); [arXiv:1306.0121].
- [22] A. Porcelli for the Pierre Auger Collaboration, PoS(ICRC2015)420; [arXiv:1509.03732].



Reconstructed properties of the sources of UHECR and their dependence on the extragalactic magnetic field

David Wittkowski^{*a} for the Pierre Auger Collaboration^b

^a*Department of Physics, Bergische Universität Wuppertal, Gaußstraße 20, D-42097 Wuppertal, Germany*

^b*Pierre Auger Observatory, Av. San Martín Norte 304, 5613 Malargüe, Argentina*

E-mail: auger_spokespersons@fnal.gov

Full author list: http://www.auger.org/archive/authors_icrc_2017.html

We present simulations of the propagation of ultra-high energy cosmic rays (UHECR) in three-dimensional space, including realistic assumptions about the extragalactic magnetic field (EGMF) and taking into account interactions of the UHECR with the cosmic microwave background and extragalactic background light as well as the cosmological evolution of the universe. On this basis, we study which energy spectrum and chemical composition of the UHECR must be assumed at their sources to obtain an energy spectrum and a chemical composition of the UHECR arriving at Earth that are in best agreement with the measurements by the Pierre Auger Observatory. We find that the best-fitting energy spectrum and chemical composition parameters depend strongly on the properties of the EGMF, showing that the EGMF must be carefully taken into account. Furthermore, we address the dependence of these parameters on the source evolution.

*35th International Cosmic Ray Conference — ICRC2017
10–20 July, 2017
Bexco, Busan, Korea*

^{*}Speaker.

1. Introduction

Two of the main unresolved questions in high energy astrophysics concern the origin of ultra-high-energy cosmic rays (UHECR, particles with energies $\geq 1 \text{ EeV}$) and the properties of their sources [1, 2]. To address these fundamental questions, the propagation of UHECR from their sources to Earth is simulated under assumptions regarding the sources as well as interaction effects in the propagation of UHECR through the universe. The energy spectrum and chemical composition of the simulated UHECR events arriving at Earth are then compared to those of actual UHECR measured at Earth. Recently, such a comparison has been made between simulation results based on a one-dimensional (1D) astrophysical model and measurements from the Pierre Auger Observatory [3]. By fitting the model to the experimental data, information on the energy spectrum and chemical composition of the UHECR at the sources have been obtained.

The most important assumptions that affect the simulation results concern the positions of the sources, the energy spectrum and chemical composition of the UHECR at the sources, the cosmic microwave background (CMB) and extragalactic background light (EBL) with which the UHECR can interact, and the extragalactic magnetic field (EGMF) that bends the trajectories of charged particles. While the CMB is known with high accuracy and the influence of the EBL on the simulation results was recently addressed alongside other influences in [3], the dependence of the simulation results on the other assumptions still needs to be studied in detail. Common simplifications in previous simulation studies are assuming a homogeneous distribution of the UHECR sources, although we can expect that the real sources are discrete objects that follow the mass distribution of the universe, and 1D simulations, which consider only one spatial degree of freedom and are therefore not able to take, e.g., the structured spatially anisotropic EGMF appropriately into account.

Going beyond these previous studies, here we investigate the propagation of UHECR by elaborate four-dimensional (4D) simulations, which take into account all three spatial degrees of freedom as well as the cosmological time-evolution of the universe, and consider discrete sources whose distribution follows the local mass distribution of the universe. On this basis we study for which energy spectrum and chemical composition at the sources the simulated energy spectrum and chemical composition at Earth are in the best possible agreement with the latest data from the Pierre Auger Observatory, and how this depends on the EGMF.

2. Methods

2.1 Simulation of the UHECR propagation

To simulate the propagation of UHECR from their sources to Earth, we used the 4D mode of the Monte Carlo code CRPropa 3 [4]. The sources were assumed to be discrete objects and their positions were chosen randomly following the large-scale structure of Dolag et al. [5], which is a common model for the local mass distribution of the universe. To avoid effects of near-Earth sources, which are influenced only marginally by the EGMF, we considered sources with a minimal distance $d_{\text{min}} = 10 \text{ Mpc}$ from the observer. For the maximal redshift of the sources we chose $z \approx 1.3$, which is equivalent to a maximal comoving distance $d_{\text{max}} \approx 4 \text{ Gpc}$. Considering known bounds on the source density ρ [6], we chose $\rho \approx 10^{-4} \text{ Mpc}^{-3}$. Furthermore, we assumed that all sources are similar and that they isotropically emit particles consisting of the five representative elements ^1H ,

${}^4\text{He}$, ${}^{14}\text{N}$, ${}^{28}\text{Si}$, and ${}^{56}\text{Fe}$ with a power-law energy spectrum $J_0(E_0) = dN/dE_0$ with an exponential cut-off for rigidities $E_0/Z_\alpha \geq R_{\text{cut}}$:

$$J_0(E_0) \propto \sum_{\alpha} f_{\alpha} E_0^{-\gamma} \begin{cases} 1, & \text{if } \frac{E_0}{Z_{\alpha}} < R_{\text{cut}}, \\ \exp\left(1 - \frac{E_0}{Z_{\alpha} R_{\text{cut}}}\right), & \text{if } \frac{E_0}{Z_{\alpha}} \geq R_{\text{cut}}. \end{cases} \quad (2.1)$$

Here, $N(E_0)$ is the number of particles emitted with energy E_0 , Z_{α} is the atomic number of element $\alpha \in \{\text{H, He, N, Si, Fe}\}$, R_{cut} is the cut-off rigidity, f_{α} are the element fractions with $\sum_{\alpha} f_{\alpha} = 1$, and γ is the spectral index. We ran our simulations until more than $5 \cdot 10^6$ particles had reached the observer. Since experiments showed that UHECR mainly consist of charged nuclei [7–9], we simulated only the propagation of such nuclei and neglected, among others, photons and neutrinos.

For the EBL we applied the model of Gilmore et al. [10] (the so-called ‘‘fiducial’’ model) as well as the photodisintegration cross sections from the TALYS code [11, 12] with parameters adjusted as described in [13], which is the default in CRPropa 3. Moreover, we used the EGMF model proposed in [4], which describes a relatively strong EGMF, together with reflective boundary conditions. This EGMF model is based on the Dolag model [5] for the mass distribution and the Miniati model [14] for the magnetic field in the universe. To obtain good statistics, the radius of the observer was chosen as 1 Mpc and we took particles arriving with redshifts $-0.025 < z < 0.025$ into account, ensuring that no simulated particle hit the observer more than once. We carried out simulations with (model I) and without (model II) EGMF. In both cases we allowed for different values of the source parameters f_{α} , γ , and R_{cut} and applied a fit procedure similar to that described in [3] to determine the particular parameter values for which the energy spectrum and chemical composition of the simulated UHECR arriving at the observer are in the best possible agreement with the corresponding Pierre Auger Observatory data.

2.2 Fit procedure

Differently from [3], where the simulated energy spectrum is folded with a function that models detector effects and afterwards compared with the raw data from the Pierre Auger Observatory, our fit procedure for convenience fits the simulated energy spectrum to the published Pierre Auger Observatory data for the energy spectrum [15] that have been adjusted for detector effects. When fitting the energy spectrum, we took only experimental data above 5 EeV, i.e., above the so-called ‘‘ankle’’ of the experimental energy spectrum [15], into account, since the data for lower energies can have a considerable galactic contribution.

The Pierre Auger Observatory does not directly measure the chemical composition of the UHECR arriving at Earth, but instead observes the longitudinal profile of extensive air showers and measures the position of the maximum of energy deposition per atmospheric slant depth, commonly called ‘‘depth of the shower maximum’’ X_{max} [16]. Measuring the composition-sensitive quantity X_{max} is currently the most reliable technique to achieve information about the mass composition of UHECR. Therefore, we translated our simulation results for the chemical composition of the arriving UHECR into a distribution of the quantity X_{max} to allow for a direct comparison with the experimental data. For this purpose, we used the common parametrization of the X_{max} distribution for particles arriving with energy E and mass number A by generalized Gumbel functions [17], which are based on air-shower simulations with the CONEX code [18] and the EPOS-LHC model

Model	γ	$\log_{10}(\frac{R_{\text{cut}}}{\text{eV}})$	$f_{\text{H}}/\%$	$f_{\text{He}}/\%$	$f_{\text{N}}/\%$	$f_{\text{Si}}/\%$	$f_{\text{Fe}}/\%$	$D_{\text{min}} = D_{\text{min}}^J + D_{\text{min}}^{X_{\text{max}}}$
I	$1.61^{+0.08}_{-0.07}$	$18.88^{+0.03}_{-0.07}$	3.0	2.1	73.5	21.0	0.4	$191.9 = 37.3 + 154.6$
II	$0.61^{+0.05}_{-0.06}$	$18.48^{+0.01}_{-0.02}$	11.0	13.8	67.9	7.2	0.1	$221.3 = 48.7 + 172.6$
see [3]	$0.87^{+0.08}_{-0.06}$	$18.62^{+0.02}_{-0.02}$	0	0	88	12	0	$191.9 = 29.2 + 162.7$

Table 1: Best-fit parameter values of γ , R_{cut} , and f_{α} with $\alpha \in \{\text{H, He, N, Si, Fe}\}$ obtained by minimizing the deviance D as well as the minimal deviance D_{min} and the contributions D_{min}^J and $D_{\text{min}}^{X_{\text{max}}}$ for our models I (with EGMF) and II (without EGMF). For comparison, the results of the 1D simulations from [3] are also shown.

for hadronic interactions [19]. In order to take detector effects into account, we multiplied the resulting Gumbel distribution with the energy-dependent detector acceptance and convolved this product with the energy-dependent detector resolution [16].

To determine the source properties (i.e., the values of f_{α} , γ , and R_{cut}) that describe the data from the Pierre Auger Observatory best, we minimized the deviance $D = D_J + D_{X_{\text{max}}}$ with $D_J = -2\ln(\mathcal{L}_J/\mathcal{L}_J^{\text{sat}})$ and $D_{X_{\text{max}}} = -2\ln(\mathcal{L}_{X_{\text{max}}}/\mathcal{L}_{X_{\text{max}}}^{\text{sat}})$ with respect to f_{α} , γ , and R_{cut} . Here, \mathcal{L}_J and $\mathcal{L}_{X_{\text{max}}}$ are the likelihood values of the simulated energy spectrum and X_{max} distribution, respectively, for certain values of f_{α} , γ , and R_{cut} . Furthermore, $\mathcal{L}_J^{\text{sat}}$ and $\mathcal{L}_{X_{\text{max}}}^{\text{sat}}$ are the likelihood values corresponding to \mathcal{L}_J and $\mathcal{L}_{X_{\text{max}}}$ for the saturated model that perfectly describes the experimental data (see [3] for details). The minimal deviance $D_{\text{min}} = D_{\text{min}}^J + D_{\text{min}}^{X_{\text{max}}}$ with the contributions D_{min}^J and $D_{\text{min}}^{X_{\text{max}}}$ from the energy spectrum and X_{max} distribution, respectively, quantifies the goodness of fit. To estimate the uncertainties in the best-fit values of the parameters γ , and R_{cut} that originate from uncertainties in the data from the Pierre Auger Observatory, we applied the same method as has been used to obtain the uncertainties given in Tab. 8 in [3].

3. Results

When considering models I and II with and without an EGMF, respectively, and fitting the element fractions f_{α} with $\alpha \in \{\text{H, He, N, Si, Fe}\}$, the spectral index γ , and the cut-off rigidity R_{cut} to the Pierre Auger Observatory data by minimizing the deviance D , we obtain the best-fit parameter values and the corresponding minimal deviances shown in Tab. 1.

Obviously, the best-fit parameter values of f_{α} , γ , and R_{cut} depend strongly on the chosen EGMF. The minimal deviance D_{min} in Tab. 1 is smaller for model I than for model II, showing that our model with an EGMF is in better agreement with the Pierre Auger Observatory data than our model without an EGMF. For comparison, also the results of the previous global fit to the experimental data [3], which is based on 1D simulations of the UHECR propagation using a homogeneous source distribution and considering no EGMF, are shown in Tab. 1.¹ Interestingly, when extending to the 4D simulations with discrete sources following the local mass distribution of the universe and without EGMF (model II), γ and R_{cut} remain similar, whereas the deviance increases. In contrast, when including the EGMF in the 4D simulations (model I), γ and R_{cut} strongly increase and the deviance is found to be at the same level as for the 1D simulations. This shows that the

¹The fit procedure used in [3] is slightly different from the one used in the current work, but we expect that this has only a negligible effect on the results.

Model	γ	$\log_{10}(\frac{R_{\text{cut}}}{\text{eV}})$	$f_{\text{H}}/\%$	$f_{\text{He}}/\%$	$f_{\text{N}}/\%$	$f_{\text{Si}}/\%$	$f_{\text{Fe}}/\%$	$D = D_J + D_{X_{\text{max}}}$
I	$2.30^{+0.02}_{-0.02}$	$20.00^{+0.14}_{-0.08}$	12.7	5.2	38.3	42.5	1.3	$243.0 = 45.8 + 197.2$
II	$2.01^{+0.03}_{-0.03}$	$19.90^{+0.10}_{-0.09}$	1.0	35.5	17.2	44.9	1.4	$286.9 = 24.2 + 262.7$

Table 2: The same as in Tab. 1, but now for the local (second) minimum instead of the global minimum of the deviance D corresponding to our models I and II.

EGMF has a stronger effect on the simulation results than the source distribution. In particular, neglecting the EGMF leads to hard spectral indices ($\gamma < 1$), whereas including the EGMF leads to softer spectral indices ($\gamma > 1$). This is an important finding, since most UHECR acceleration models predict $\gamma > 1$. Following [20] this result could be interpreted as an effect of magnetic horizons and magnetic suppression. Furthermore, all models in Tab. 1 show a high nitrogen fraction f_{N} and a low iron fraction f_{Fe} , suggesting that the chemical composition of the UHECR at their sources is nitrogen-dominated.

If we use our best-fit parameter values from Tab. 1 and simulate the propagation of UHECR from their sources to Earth, we obtain results that can directly be compared to the Pierre Auger Observatory data. Figure 1 shows the simulated energy spectrum and the first and second moments of the simulated X_{max} distribution for the best-fit parameter values of model I as well as the corresponding data from the Pierre Auger Observatory.

It is apparent that these simulation results and the Pierre Auger Observatory data are in good agreement. Note that in Fig. 1(a) the additional curves show the contributions to the energy spectrum that stem from observed nuclei of different mass numbers A .

Besides the global minimum of the deviance D , which is strongly pronounced, there is only one distinct local (second) minimum of D at $\gamma \approx 2$, which was previously reported in [3] and thus seems to be a common feature independent of the particular model. The agreement of the simulation results and experimental data is less good when the parameter values of f_{α} , γ , and R_{cut} for the local (second) minimum of D are used. Table 2 shows these values together with the corresponding values of the deviance D , which are larger than in Tab. 1. The simulation results corresponding to the second minimum of D are still in good agreement with the Pierre Auger Observatory data for the energy spectrum (see the values of D_J), but the agreement is worsened when comparing the results for the X_{max} distribution (see the values of $D_{X_{\text{max}}}$).

When investigating the effect of the evolution of the sources, the EGMF was usually neglected in the past (see, e.g., [21]). To close this gap, we parameterized similar as in [3] the emissivity of the sources with $\propto (1+z)^m$, where z is the redshift of the sources and m is a source evolution parameter. The results for the best-fit parameter values of γ and R_{cut} of model I for different source evolutions are shown in Tab. 3.

From the considered source evolution parameters the value $m = 3$ shows the best agreement with the experimental data. When m becomes smaller, the agreement decreases and the spectral index γ increases. Assuming a negative source evolution with $m \approx -6$ results in compatibility of the data with first-order Fermi acceleration of UHECR or other acceleration mechanisms leading to emission spectra with a spectral index of about 2. When neglecting the EGMF, even more negative source evolutions would be required for compatibility of the data with first-order Fermi acceleration [3, 21].

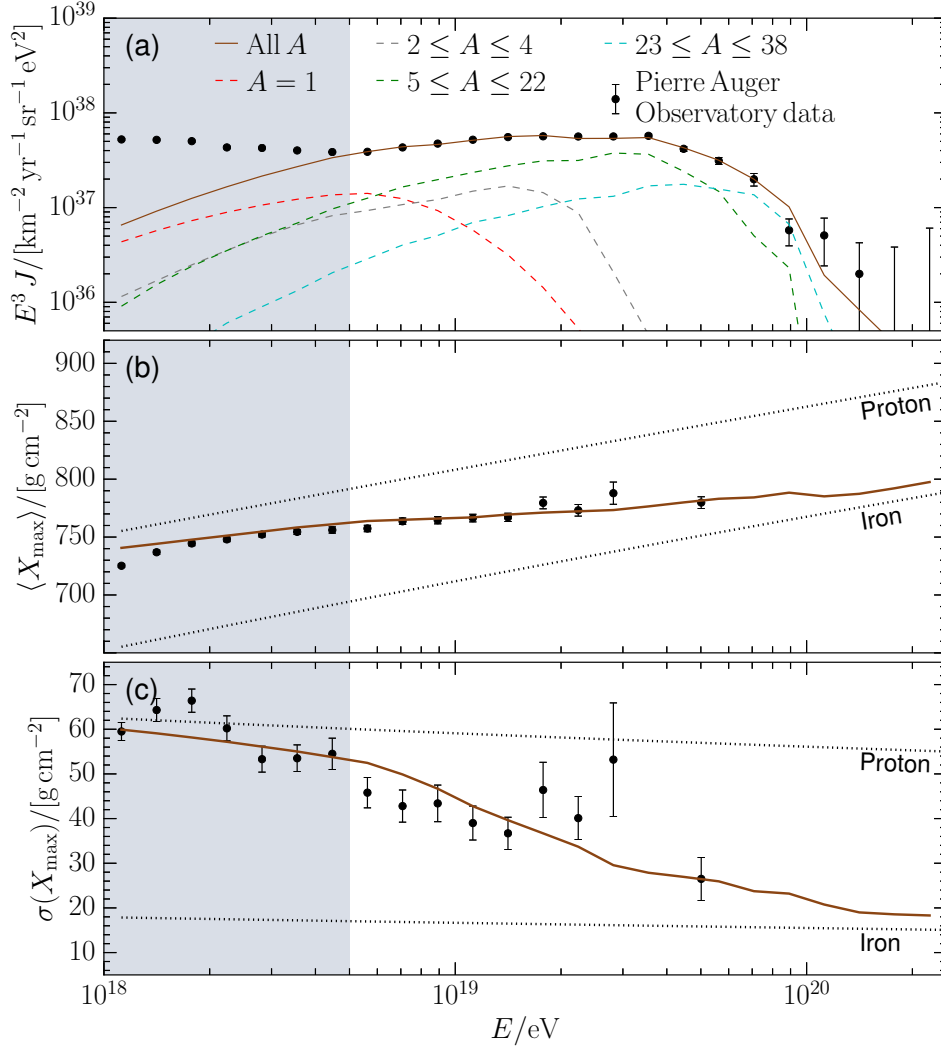


Figure 1: (a) Energy spectrum $J(E)$ [15] as well as (b) mean $\langle X_{\max} \rangle$ and (c) standard deviation $\sigma(X_{\max})$ of the X_{\max} distribution [16] for the Pierre Auger Observatory data (data points with error bars) and for our simulation results (brown solid curves). The simulation results shown here correspond to the best-fit parameter values of f_α , γ , and R_{cut} for model I (see Tab. 1) and are in good agreement with the experimental data. In (a) the additional curves show the contributions to the energy spectrum that stem from detected nuclei of different mass numbers A . The black dotted lines in (b) and (c) indicate the simulation results that one would obtain if the sources were emitting only protons (upper lines) or iron nuclei (lower lines). The Pierre Auger Observatory data with energies below the “ankle” at ≈ 5 EeV (gray regions) were not taken into account in the fit procedure described in Sec. 2.2, since they can have a considerable galactic contribution.

4. Conclusions

Based on elaborate 4D simulations of the propagation of UHECR we have studied i) for which energy spectrum and chemical composition of the UHECR at their sources the simulated energy spectrum and chemical composition at Earth are in the best possible agreement with the latest data from the Pierre Auger Observatory and ii) how the source parameters describing the reconstructed initial energy spectrum and chemical composition are affected by the EGMF. Our simulations take

m	γ	$\log_{10}(\frac{R_{\text{cut}}}{\text{eV}})$	$f_{\text{H}}/\%$	$f_{\text{He}}/\%$	$f_{\text{N}}/\%$	$f_{\text{Si}}/\%$	$f_{\text{Fe}}/\%$	$D_{\text{min}} = D_{\text{min}}^J + D_{\text{min}}^{X_{\text{max}}}$
3	$1.20^{+0.06}_{-0.07}$	$18.70^{+0.02}_{-0.02}$	2.3	4.0	78.4	15.0	0.3	$184.0 = 28.2 + 155.8$
0	$1.61^{+0.08}_{-0.07}$	$18.88^{+0.03}_{-0.07}$	3.0	2.1	73.5	21.0	0.4	$191.9 = 37.3 + 154.6$
-3	$1.78^{+0.07}_{-0.08}$	$18.77^{+0.03}_{-0.05}$	27.6	5.7	50.8	15.4	0.5	$199.0 = 41.2 + 157.8$
-6	$1.95^{+0.06}_{-0.10}$	$18.77^{+0.03}_{-0.04}$	29.3	5.8	47.2	17.0	0.7	$202.0 = 40.5 + 161.5$
-9	$2.05^{+0.08}_{-0.09}$	$18.78^{+0.02}_{-0.02}$	29.0	6.5	46.3	17.4	0.8	$203.4 = 42.2 + 161.2$

Table 3: Best-fit parameter values of γ , R_{cut} , and f_{α} with $\alpha \in \{\text{H, He, N, Si, Fe}\}$ obtained by minimizing the deviance D as well as the minimal deviance D_{min} and the contributions D_{min}^J and $D_{\text{min}}^{X_{\text{max}}}$ for model I and different values of the source evolution parameter m .

account of all three spatial degrees of freedom, the cosmological time-evolution of the universe, a discrete source distribution that follows the local mass distribution of the universe, and a structured EGMF.

The results of our simulations show that the source parameters reconstructed from the Pierre Auger Observatory data depend strongly on the EGMF. Assuming an EGMF leads to soft spectral indices (> 1), whereas neglecting the EGMF leads to harder spectral indices. This behavior is qualitatively consistent with predictions of [20]. Moreover, for both situations the Pierre Auger Observatory data suggest that the chemical composition of the UHECR at their sources is dominated by intermediate-mass nuclei, which is in accordance with previous 1D simulations [3]. The source parameters deduced from the local (second) minimum of the deviance are well in line with a spectral index of about 2, but are disfavored, since they miss to reproduce the change of the mass composition observed in the Pierre Auger Observatory data.

We also found that the assumed source evolution affects the reconstructed source parameters. In the presence of an EGMF a positive source evolution parameter shows the best agreement with the experimental data. For decreasing values of the source evolution parameter the agreement becomes worse while the spectral index becomes larger. In case of a negative source evolution parameter of ≈ -6 the spectral index is ≈ 2 and thus similar to what is predicted for first-order Fermi acceleration of UHECR. In the absence of an EGMF, even more negative source evolutions would be required to see compatibility of the data with first-order Fermi acceleration [3, 21].

For the future, it would be interesting to extend our work by comparing not only the energy spectrum and chemical composition of the simulated UHECR arriving at Earth but also the anisotropy in their arrival directions with the corresponding data collected by the Pierre Auger Observatory [22, 23].

References

- [1] G. Sigl, *Science* **291**, 73 (2001).
- [2] K. Kotera and A.V. Olinto, *Annual Review of Astronomy and Astrophysics* **49**, 119 (2011).
- [3] A. Aab *et al.* [Pierre Auger Collaboration], *JCAP* **2017**, 038 (2017).
- [4] R. Alves Batista *et al.*, *JCAP* **2016**, 038 (2016).
- [5] K. Dolag, D. Grasso, V. Springel, and I. Tkachev, *JCAP* **1**, 9 (2005).

- [6] P. Abreu *et al.* [Pierre Auger Collaboration], *JCAP* **2013**, 009 (2013).
- [7] J. Abraham *et al.* [Pierre Auger Collaboration], *Astropart. Phys.* **31**, 399 (2009).
- [8] P. Abreu *et al.* [Pierre Auger Collaboration], *Adv. High Energy Phys.* **2013**, 18 (2013).
- [9] R. Aloisio, D. Boncioli, A. di Matteo, A.F. Grillo, S. Petrera, and F. Salamida, *JCAP* **2015**, 006 (2015).
- [10] R.C. Gilmore, R.S. Somerville, J.R. Primack, and A. Domínguez, *Mon. Not. R. Astron. Soc.* **422**, 3189-3207 (2012).
- [11] A.J. Koning, S. Hilaire, and M.C. Duijvestijn, *AIP Conf. Proc.* **769**, 1154 (2005).
- [12] A.J. Koning and D. Rochman, *Nucl. Data Sheets* **113**, 2841 (2012).
- [13] R. Alves Batista, D. Boncioli, A. di Matteo, A. van Vliet, and D. Walz, *JCAP* **2015**, 063 (2015).
- [14] G. Sigl, F. Miniati, and T.A. Ensslin, *Phys. Rev. D* **68**, 043002 (2003).
- [15] I. Valiño for the Pierre Auger Collaboration, *Proc. 34th Int. Cosmic Ray Conf., The Hague, The Netherlands*, [PoS\(ICRC2015\)271](#)
- [16] A. Aab *et al.* [Pierre Auger Collaboration], *Phys. Rev. D* **90**, 122005 (2014).
- [17] M. De Domenico, M. Settimo, S. Riggi, and E. Bertin, *JCAP* **2013**, 050 (2013).
- [18] T. Pierog *et al.*, *Nucl. Phys. B Proc. Suppl.* **151**, 159 (2006).
- [19] T. Pierog, I. Karpenko, J. Katzy, E. Yatsenko, and K. Werner, *Phys. Rev. C* **92**, 034906 (2015).
- [20] S. Mollerach and E. Roulet, *JCAP* **2013**, 013 (2013).
- [21] A.M. Taylor, M. Ahlers, and D. Hooper, *Phys. Rev. D* **92**, 063011 (2015).
- [22] A. Aab *et al.* [Pierre Auger Collaboration], *Astrophys. J.* **802**, 111 (2015).
- [23] A. Aab *et al.* [Pierre Auger Collaboration], *Astrophys. J.* **804**, 15 (2015).



Peculiar lightning-related events observed by the surface detector of the Pierre Auger Observatory

Roberta Colalillo^{*a} for the Pierre Auger Collaboration^b

^a*Università Federico II di Napoli and INFN, Sezione di Napoli, Italy*

^b*Observatorio Pierre Auger, Av. San Martín Norte 304, 5613 Malargüe, Argentina*

E-mail: auger_spokespersons@fnal.gov

Full author list: http://www.auger.org/archive/authors_icrc_2017.html

The surface detector (SD) of the Pierre Auger Observatory has collected some very peculiar events. The signals produced by these events in the SD stations are very long-lasting compared to those produced by cosmic rays. For many events, the number of stations with long signal is big, and they are arranged in a circular shape with a radius of about 6 km. Moreover, a correlation with lightning was observed.

Many checks were performed to exclude the possibility that electronics problems could simulate the observed signals, but these revealed that the peculiar events are indeed produced by particles and/or photons that cross the Auger Cherenkov detectors. A search algorithm was implemented based on the duration of the signal. These events are very sporadic. Using a small sample of “golden” events, studies are currently under way to characterize these events, and to understand their origin. The main features of these events will be described and a preliminary reconstruction will be shown.

*35th International Cosmic Ray Conference — ICRC2017
10–20 July, 2017
Bexco, Busan, Korea*

^{*}Speaker.

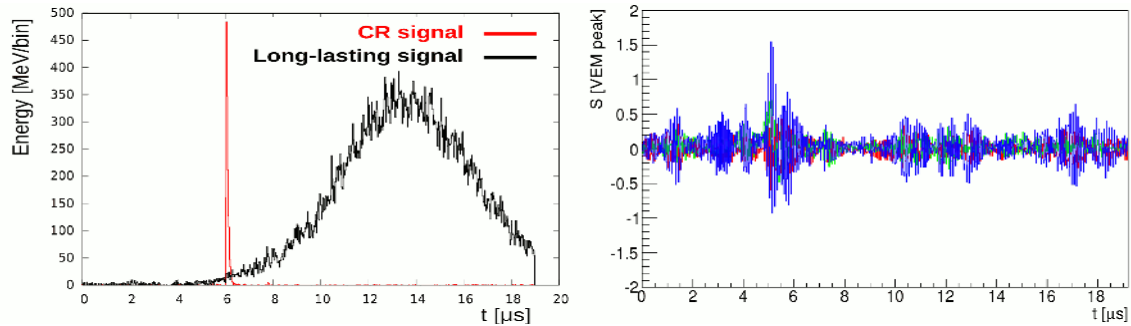


Figure 1: *Left:* differences between a cosmic-ray trace and the long-lasting signal detected by several triggered stations of the observed events. *Right:* signal collected by a so-called lightning station. Each color corresponds to the signal from one of the three PMTs.

1. Introduction

Peculiar events have been collected by the surface detector of the Pierre Auger Observatory. They are characterized by stations with a long-lasting signal compared to the standard Auger signal produced by extensive air showers, and by stations collecting a signal dominated by high frequency noise. Moreover, for the events with a high number of stations, the long-signal stations are arranged in a circular shape with a radius of about 6 km. The reality of these events was checked, an algorithm for their search was developed, and several studies are in progress to understand their main characteristics and their origin.

The Pierre Auger Observatory is located in the Argentinian Pampa at about 1400 m a.s.l. It is a hybrid detector composed of a fluorescence detector (FD), which studies the longitudinal profile of the cosmic-ray showers, and of a surface detector array (SD) which maps the distribution of shower particles at the ground [1]. The SD is made up of 1600 water-Cherenkov detectors (WCDs) placed on a triangular grid of 1500 m spacing which covers an area of 3000 km². Each WCD consists of a 3.6 m polyethylene tank containing a liner with a reflective inner surface and filled with 12,000 litres of ultra-pure water. Cherenkov light produced by the passage of relativistic charged particles through the water is collected by three PMTs. The two output signals from PMTs, one directly from the anode (HG channel) and the other one from the last dynode (LG channel) with an amplification factor of 32 to increase the dynamic range, are processed by six FADCs with a sampling rate of 40 MHz.

2. Main Features

The first event was recorded on 4 May 2005 at about 4am. It triggered 65 stations and differs from cosmic-ray events in the time-scale and the spatial distributions of the detector involved. Among the event stations, there are 24 stations with signals that last for a long time (long-signal stations). In Fig. 1-left, this signal, that occurs over $\sim 10 \mu\text{s}$, is compared to a cosmic-ray signal lasting $\sim 0.1 \mu\text{s}$. Another important characteristic is the presence of at least one active station with high frequency noise, called a lightning station, shown in Fig. 1-right. Also stations with a standard cosmic-ray trace are present in some of these events, but they are not correlated in time with the long stations. The footprint of three events at the ground is shown in Fig. 2. The long-signal stations,

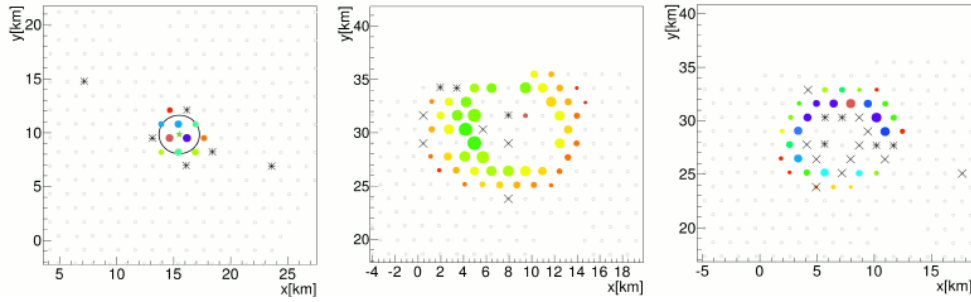


Figure 2: Footprint of three events at the ground. The size of the colored markers (long-signal stations) is proportional to the signal in the stations, the color is related to the arrival time. The blue stations arrive first, finally the red ones. The stars are the lightning stations, while the crosses are the standard cosmic-ray stations. Only the last two events, which have a bigger number of stations, present a hole in the center, but the main characteristics of the three events are the same.

represented by the coloured markers, are organized in a circular shape, the stars symbolize the lightning stations, while the crosses the stations with cosmic-ray traces. The footprint of the first event on the left has a radius of ~ 2 km, the other two events have a bigger number of long stations, a radius of ~ 6 km, and present a hole in the center. The signal and timing characteristics of these three events are the same.

3. Checks for the Reality of the Observed Events

These events are very peculiar. Therefore, it is very important to test that the detected signals are really compatible with Cherenkov light produced inside the stations, and are not artificially induced by electromagnetic noise. We checked the consistency among the signals recorded by the three PMTs and that, for each of them, the HG and LG signal are in a consistent ratio. The three PMT signals are shown in Fig. 3-left in three different colors, red, blue, and green, together with the ratios between two PMTs at a time calculated bin-by-bin, and the distributions of the mean of these ratios from all stations, that are peaked at 1 as we expected.

The HG and LG signals are shown in red and blue respectively in Fig. 3-right. When the high gain channel is not saturated and on the low gain channel there is a signal with an amplitude not too low, the ratio between the high gain and the low gain signal multiplied by the amplification factor (D/A constant) is expected to be 1. To verify this, the ratio was computed for each station with a LG signal with an amplitude not too low (at least 5 bins that are above 7 FADC counts are requested on the LG channel), excluding the saturated part of the high gain channel. The distributions obtained for each PMT following these cuts are also shown in figure 3, and they are peaked at 1. The cut on the LG signal is very strict, but we still found six events with a bigger number of long stations. These events are physical: they are not due to electromagnetic noise. In the following, these cuts will be released, and the HG signal will be used except in the cases where the HG channel is saturated.

Another important characteristic that has to be checked is the hole in the center of large events. We do not know if it is physical. The SD trigger, optimized for cosmic rays may not be adequate to handle the complex timing of these events. Work is being done at the station trigger level to

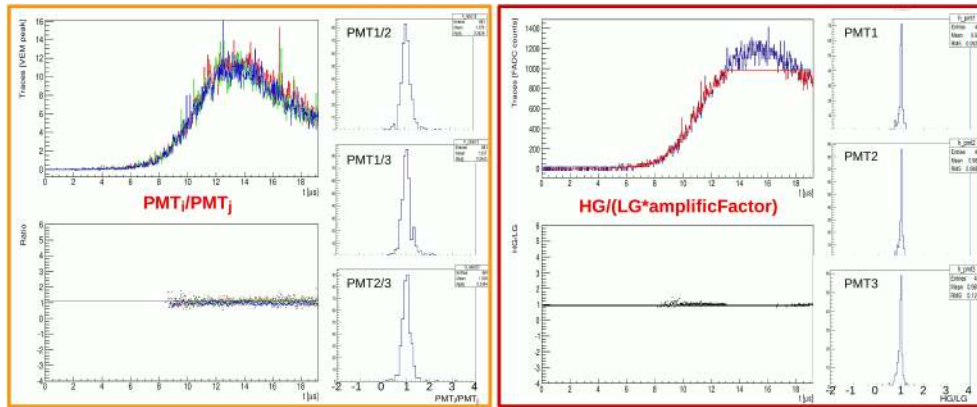


Figure 3: *Left:* HG signal collected by the three PMTs of an active station of one of the detected events (left-top). Ratios between two PMTs at a time calculated bin-by-bin (left-bottom). Distributions of the mean of the ratios that are peaked at 1 as expected (right). *Right:* HG and LG signal collected by one PMT in red and blue respectively (right-top). HG signal divided by LG signal multiplied by the amplification factor (right-bottom). Distributions of the mean of the ratio obtained using all stations which pass the cuts described in the text.

explore if the central data of events with many stations may be lost due to the high frequency signal detected in the central stations before our events.

4. Search Algorithm

The data sample analyzed in this work consists of all events collected by the SD since January 2004 up to 15 May 2017, which pass the first standard Auger trigger levels. This cut is looser than the one asked for the standard SD analyses [2]. A first cut is applied on data to select events with at least one lightning station. It was fixed after the observation, on a large sample of data, that all events have both long-signal stations and lightning stations. On selected events, about 200000, a “moving mean” on 9 bins of the high gain trace is performed to reduce fluctuations. On this smeared trace, at least 80 consecutive bins above 1 baseline error are requested (long-signal condition); if there are at least ten stations with at least two PMTs with a long signal, the event is accepted. Thanks to this algorithm, 105 events have been selected. Among them, there is a large number of events with noisy stations or several consecutive muon peaks confused with long stations, but a visual scanning selected 28 events with real long stations. Moreover, 16 of these events have a large number of long stations, arranged in a ring shape with a big radius. Most of the selected events were collected between the end of 2007 and the beginning of 2008. They were detected both during the day and the night. Most of our events are concentrated in few days. In particular, four events were collected in 15 minutes: three of them happened in 1.5 ms and in the same zone of the array. They are shown in figure 4. Unfortunately, in 2007, the array was not completed, but long signal and lightning stations are dominant in these events.

The high frequency noise observed in several stations could be associated with lightning-caused signal, which suggests that these events happened during thunderstorms. To verify this, we checked the correlation between our events and lightning strikes of the WWLLN (World Wide Lightning Location Network) catalogue. We compared 22 events and we found a correlation for nine events, $\sim 41\%$ of our sample. The time difference between our events and WWLLN data

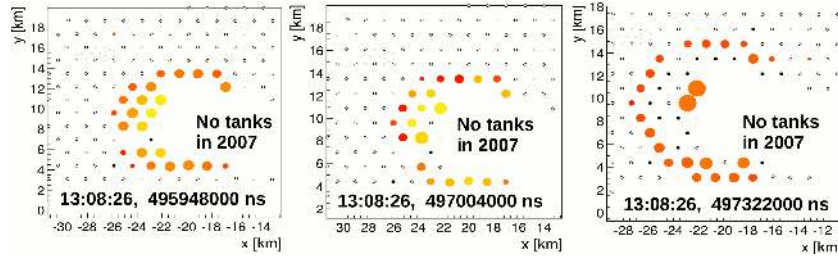


Figure 4: Three events collected in 1.5 ms in the same zone of the array.

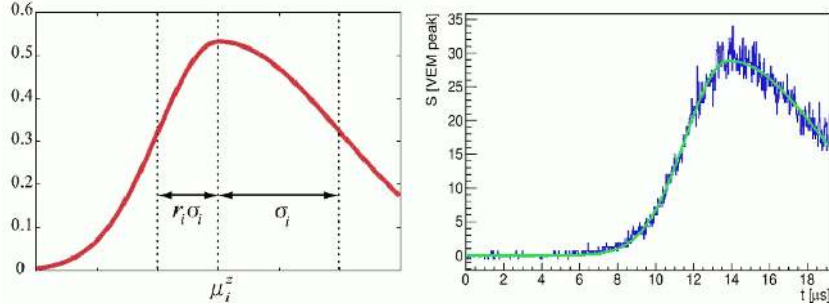


Figure 5: The asymmetric Gaussian is the function which best describes our signal shape (left). Fit obtained from an unweighted chi-square minimization using the asymmetric function. In this case, the low gain signal (blue) is used because the high gain channel is saturated (right).

spands from $10 \mu\text{s}$ to 100ms . The spatial correlation is very good considering that the global location accuracy for WWLLN network assuming 5-station involvement ranges over 1.9 to 19 km [3]. In the last years, five lightning stations were installed at the Observatory by the AERA group [4]. A more detailed correlation study can be performed in future. Several experiments, on satellite [5] and at ground [6][7], have claimed the observation of radiation bursts in coincidence with lightning activity. The relationship between the observed γ emission and lightning is under investigation. Further studies on our events are necessary to understand if we are observing the same radiation bursts or new phenomena.

5. Long-lasting Signal Characteristics

In many cases, the long-lasting signals of the events are not fully contained in our acquisition time window. To recover the part of the signal we cannot detect directly and the saturated part when also the low gain channel is saturated, we need to characterize in the best way the shape of the signal as follows. We used the small sample of stations where the signal is completely visible to choose the fit function. The asymmetric Gaussian distribution best describes the leading and falling edge of the signal. It is shown in Fig. 5 together with an example of fit. A chi-square minimization is performed to fit the signal. To define the common weight to assign to each bin of the trace, we performed the Fourier transform of the long-lasting signal and separated the signal frequencies from the fluctuations. The inverse transform of the signal in the frequency domain with frequencies bigger than 2 MHz is shown in Fig. 6-left. The RMS of this signal, consistent with the Poissonian fluctuations, is used as weight. To fit all the parameters of the asymmetric Gaussian, we need to see

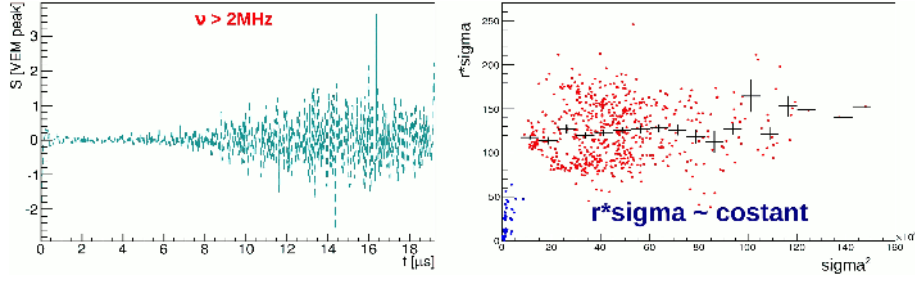


Figure 6: *Left:* Inverse transform of the long-lasting signal Fourier transform after cutting the frequencies less than 2 MHz corresponding to the signal. The RMS of the Inverse transform is used as weight for the signal fit. *Right:* Correlation between $r_i \sigma_i$ and σ_i^2 obtained from the fit of “good” stations. $r_i \sigma_i$ is constant as a function of σ_i^2 .

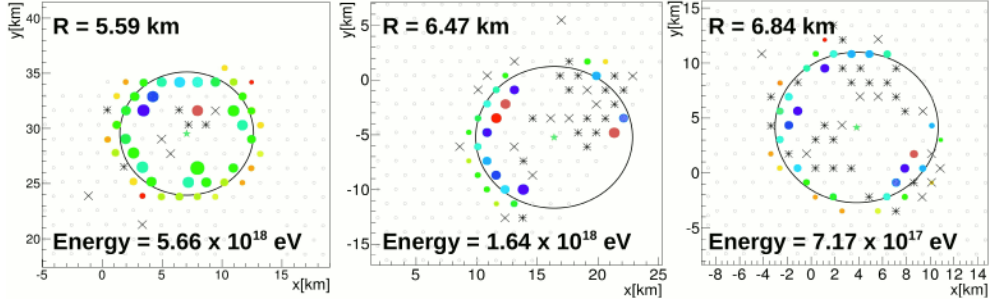


Figure 7: First reconstruction steps for some events.

at least a small part of the falling edge of the signal. For this reason, we require that the peak of the Gaussian is in the DAQ window. We select good fits asking that the percentage difference between the sum of the content of the trace bins and the integral of the fitting function in our time window is less than 5% and that the duration of the total fitting function is less than 100 μ s. Stations where at least two of the three PMT signals meet these conditions will be called “good” stations. From the distributions and correlations among the fit parameters of “good” stations, we observed that the rise time of the signal ($r_i \sigma_i$) is smaller than the fall time (σ_i), σ_i is bigger than 2.5 μ s, and $r_i \sigma_i$ is constant as a function of σ_i^2 (see Fig. 6-right).

The signal detected by each PMT is given by the total integral of the fitting function. The signal per station is the mean of the PMT signals. The reconstruction will be performed only for those events with at least eight “good” stations. Ten events pass this cut, and the $\sim 80\%$ of this sample shows a correlation with WWLLN lightning.

6. Event Characterization: Reconstruction and Global Features

The first step to study the global characteristics of our events is to reconstruct the center of their circular footprint. An unweighted chi square minimization allows us to find the center (green star) and the radius of the circle shown in Fig. 7 for some events.

The total energy deposited at ground is calculated starting from the energy collected in each long-signal stations, which spans from $\sim 10^4$ MeV to $\sim 10^6$ MeV. We can calculate the energy per m^2 and multiply this value for the area really covered by the active stations. The obtained energies oscillate between 10^{17} and 10^{18} eV. The energy deposited at ground by a vertical cosmic-ray

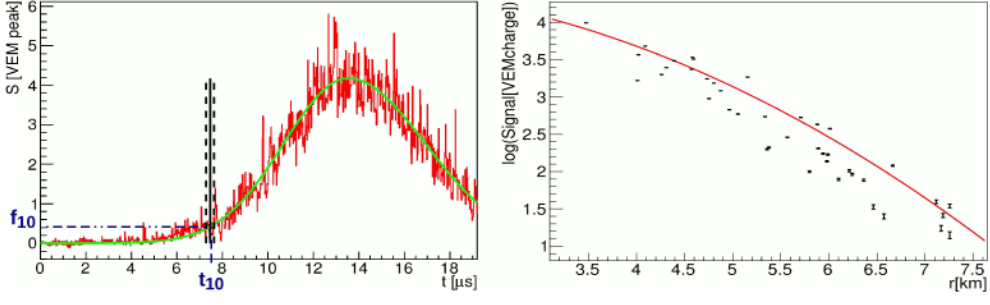


Figure 8: *Left:* Start time of long-lasting signal: 10% of the value of the asymmetric Gaussian in its peak. *Right:* Log(long signal) as a function of the distance from the center. It is larger in the inner stations and decreases as the distance from the center increases.

shower initiated by a proton with energy 10^{19} eV is about two order of magnitude lower. Moreover, comparing our energy per m^2 with the deposited energy at ground measured at 100 m from the source by NaI scintillators of the experiments which detected radiation bursts [6], we observed that our energy is of the same order of magnitude or bigger close to the center of the circle (at least 0.5 km from the center), lower at the outer region. The energy measured by the plastic scintillator of the TA experiment [7], instead, is $\sim 10^2$ MeV per m^2 , two orders of magnitude lower of our smallest energy, but it is important to remember that they have a small efficiency for photon detection.

The start time of our long-lasting signals is defined as the time corresponding to the 10% of the value of the asymmetric Gaussian in its peak, t_{10} . It is depicted (black line) with its uncertainty (black dashed lines) in Fig. 8-left. The time of each long station is given by the GPS time of the station plus t_{10} . The station time as a function of the distance from the center is shown in Fig. 9. The signal arrives first in the inner stations and then reaches the external ones. The log(long signal) as a function of the distance from the center, instead, is shown in Fig. 8-right and is well fit by a parabola. The signal is larger in the inner stations and decreases as the distance from the center increases.

The arrival times of the long-signal stations are fit considering a spherical propagation model. Four parameters are obtained: x_0 , y_0 , and ct_0 , that are the coordinates of the origin point of the event, and t_{off} which takes into account the offset between the event time and t_0 . The altitudes of the origin point obtained from the spherical fit are very low, do not exceed 1 km. To compare the evolution of the front with expectations, a simple MC assuming a spherical front was performed. The origin point of the event was fixed at different altitudes, for each impact point at ground, the distance from the origin point was calculated, and assuming relativistic particles, the arrival time was obtained. The simulated arrival times are represented by the colored lines shown in Fig. 9. Each line corresponds to a different altitude of the origin point of the event, from 0 to 10 km. Subtracting t_{off} at the real arrival times, they superimpose to the simulated line corresponding to an origin point at 0 as we can see in Fig. 9 for two events. The event without hole shown on the left of Fig. 2 do not pass the quality cuts asked for the reconstruction because the peak of the long-lasting signals is never visible in our time window. Anyway, performing a raw reconstruction of this event, we observe also in this case that the signal arrives first in the inner stations, where it is bigger than in the outer stations, and that the propagation of this event is compatible with a spherical front with the source very close to ground and a radial expansion at the speed of light.

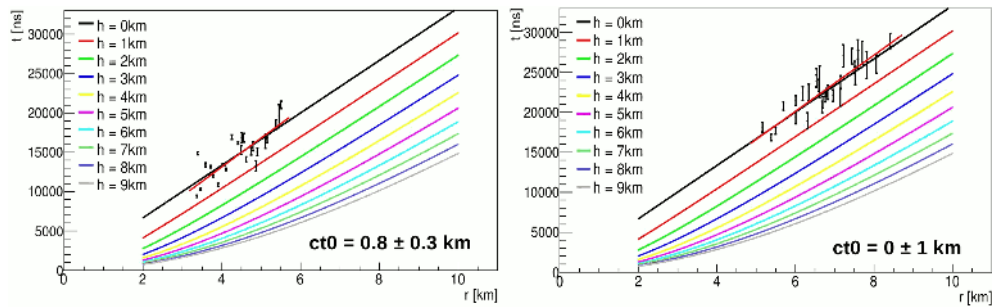


Figure 9: Arrival times as a function of the distance from the center. The black points are the real arrival times of the long stations with their uncertainty. The colored lines represent the simulated times obtained by a simple MC. Each line corresponds to a different altitude of the origin point of the event, from 0 to 10 km. Data are compatible with an origin point of the event very close to ground.

7. Conclusions

Very peculiar events, characterized by the presence of stations with very long-lasting signals have been detected by the Pierre Auger Observatory. Some of them have many active detectors arranged in a ring shape, with no detected signal at the center. Events with many stations have been characterized. Their signals are well described by an asymmetric Gaussian shape with the rising edge steeper than the trailing one. A correlation between the two widths has been observed. The amplitude of the signal is bigger in the inner part of the ring and decreases with the increasing of the distance from the center. The event moves from the center of the circle to the external part, the observed timing is consistent with a spherical front expanding at the speed of light with an origin point very close to ground or to a cylindrical front. For many events, a correlation with lightning was observed. Many experiments have collected radiation bursts in coincidence with lightning activity. Studies are in progress to understand if we are also observing radiation bursts or other phenomena and if the hole observed in some big events is physical or not.

Acknowledgments

The authors wish to thank the World Wide Lightning Location Network (wwlln.net), a collaboration among over 50 universities and institutions, for providing the lightning location data used in this paper.

References

- [1] Pierre Auger Collaboration, Nucl. Instrum. Meth. A 798 (2015) 172–213.
- [2] Pierre Auger Collaboration, Nucl. Instrum. Meth. A 613 (2010) 29–39.
- [3] C.J. Rodger, J.B. Brundell, and R.L. Dowden, Ann. Geophys. 23 (2005) 277–290.
- [4] J. Rautenberg, for the Pierre Auger Collaboration, 34th Int. Cosmic Ray Conf., The Hague (2015).
- [5] G.J. Fishman *et al.*, Science 264 (1994) 1313–1316.
- [6] J.R. Dwyer *et al.*, Geophys. Res. Lett. 31 (2004) L05119.
- [7] Telescope Array Collaboration, arXiv:1705.06258.

6

Detectors and AugerPrime Upgrade





The Pierre Auger Observatory Upgrade

Daniele Martello^{*a} for the Pierre Auger Collaboration^b

^aUniversity of Salento and INFN Lecce, via per Arnesano, 73100 Lecce, Italy

^bObservatorio Pierre Auger, Av. San Martín Norte 304, 5613 Malargüe, Argentina

E-mail: auger_spokespersons@fnal.gov

Full author list: http://www.auger.org/archive/authors_icrc_2017.html

Over the past decade the Pierre Auger Observatory has accumulated the largest exposure to ultra-high energy cosmic rays, and provided a data set of unprecedented quality. The analysis of these data has led to major breakthroughs in the understanding of the origin and properties of the highest-energy cosmic rays, but a coherent interpretation has not yet been achieved. New questions have emerged, including that of the mass composition of cosmic rays in the energy region of the flux suppression, which is of key importance for making progress.

To answer these open questions, the Observatory has started a major upgrade, called AugerPrime. The upgrade program will include new plastic scintillator detectors on top of the water-Cherenkov detectors of the surface array (SD), more powerful SD electronics and an extension of the dynamic range with an additional PMT installed in the water-Cherenkov detectors. The main goal of AugerPrime is to improve the mass composition sensitivity of the surface detectors. At the end of 2016 an Engineering Array of the upgraded detectors was installed and it has taken data since then.

After reviewing the physics motivation of AugerPrime, an overview of the different parts of the upgrade will be given. The expected performance and the improved physics sensitivity of the upgraded Observatory will be discussed together with the first data collected with the Engineering Array.

*35th International Cosmic Ray Conference — ICRC2017
10–20 July, 2017
Bexco, Busan, Korea*

*Speaker.

1. Introduction

The nature of ultra-high energy cosmic rays (UHECRs) above 10^{17} eV is still unknown, even if data collected in the last decade have partially answered these puzzling questions. Understanding the sources and the propagation properties of UHECRs is one of the key questions in astroparticle physics. The data collected with the Pierre Auger Observatory [1] have contributed to a number of steps forward in this field. The measurements confirmed with high precision the suppression of the primary cosmic ray energy spectrum, the differential flux falls to one-half of the value of the power-law extrapolation at energies above 4×10^{19} eV [2]. This suppression is compatible with the Greisen-Zatsepin-Kuzmin (GZK) effect, but the level of its contribution to the cut-off remains unclear. The measured limits on the flux of photons [3, 4, 5] and neutrinos [6, 7] at ultrahigh energy indicate that top-down mechanisms such as the decay of super-heavy particles cannot be the main producer of the observed particle flux. The distributions of the depth of shower maximum (X_{\max}) have been used to determine the UHECR composition on Earth, indicating the presence of a large fraction of protons in the energy range of the spectral ankle. At the same time, according to the Auger data [8], the anisotropy of the arrival directions of these protons cannot be larger than a few percent. Moreover the proton component disappears at 10^{19} eV [9, 10] where heavier components appear.

The isotropy in the flux of the more energetic cosmic rays observed in numerous tests of the small-scale angular distribution is remarkable [11], challenging the original expectations that assumed only a few cosmic ray sources with a light composition at the highest energies. On the other hand, an evident dipole behavior is observed for energies above 8 EeV [12].

The all particle spectrum by itself and the knowledge of the composition below the suppression region cannot provide sufficient discrimination between the different astrophysical hypotheses, therefore the determination of the primary composition at energies higher than a few times 10^{19} eV is mandatory to reach any reliable conclusion. To explore these energies the Auger fluorescence detector is not adequate due to its limited duty cycle (presently 15%).

2. The motivation for AugerPrime

In order to extend the composition sensitivity of the Auger Observatory into the flux suppression region, an upgrade of the Auger Observatory (named AugerPrime[13, 14]) has been planned. The main aim of AugerPrime is to provide, on a shower-by-shower basis, additional measurements of mass composition sensitive observables, allowing an estimation of the primary mass of the highest energy cosmic rays. The study of the origin of the flux suppression will provide fundamental constraints on the astrophysical sources and will allow us to determine more precise estimates of gamma-ray and neutrino fluxes at ultra-high energy. The measurement of the flux contribution of the light elements will elucidate the physics potential of existing and future cosmic ray, neutrino, and gamma-ray detectors. Therefore, the aim of AugerPrime is to reach a sensitivity as small as 10% in the flux contribution of protons in the suppression region on a shower-by-shower basis.

The determination of the primary mass composition of ultra-high energy cosmic rays is deeply related to our understanding of extensive air showers and hadronic interactions. In the Auger data,

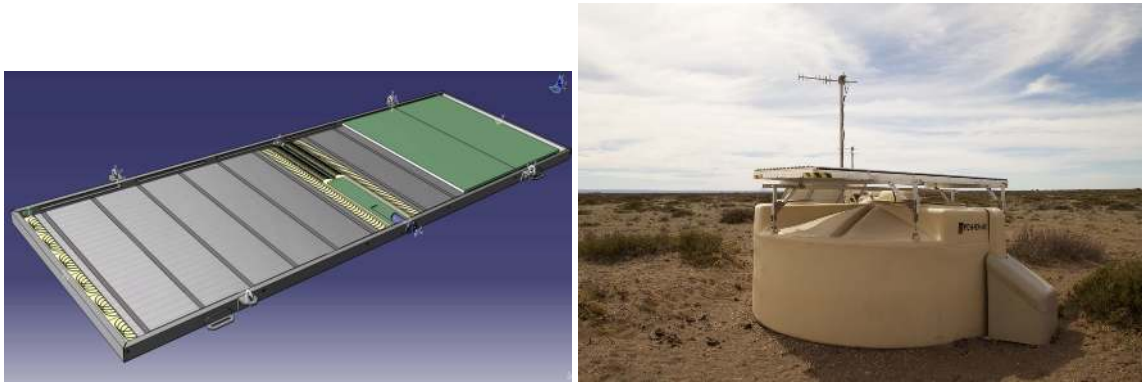


Figure 1: Left: the layout of the Surface Scintillator Detector (SSD); Right: One station of the AugerPrime Engineering Array.

there is a disagreement between the observed and expected muon numbers [15, 16], therefore it is of fundamental importance to study the hadronic multiparticle production in extensive air showers.

3. Description of AugerPrime

The AugerPrime upgrade consists of many improvements of the Pierre Auger Observatory. The most important is the installation of a new detector above each of the existing water-Cherenkov detectors (WCD). This new detector, named the Surface Scintillator Detector (SSD), consists of a plane of plastic scintillator that will be triggered by the larger WCD below it.

An SSD unit is a box of area $3.8 \text{ m} \times 1.3 \text{ m}$, containing two scintillator sub-modules, each composed of 24 bars of extruded scintillator produced at the Fermi National Accelerator Laboratory of about 1.6 m length, 5 cm width and 1 cm thickness [17]. The 3.8 m^2 scintillator planes are protected by light-tight, weatherproof enclosures, and mounted on top of the existing WCD with a strong support frame (see figure 1). The scintillator light will be collected with wavelength-shifting fibers inserted into straight extruded holes in the scintillator planes. The fibers (Kuraray Y11(300)M S-type) are bundled and connected from both sides to one 1.5" photomultiplier tube (PMT). The PMT selected in the baseline design is the model Hamamatsu R9420. It has a bi-alkali photo-cathode and a quantum efficiency of about 18% at the wavelength of 500 nm. This PMT has been chosen for its excellent linear response.

The other important improvement included in the AugerPrime program is the upgrade of the electronics of the SD and the extension of the dynamic range of the WCD. The new electronics will process both WCD and SSD signals [18]. It will increase the data quality thanks to better timing accuracy and a faster ADC sampling. The signals of the SSD and WCD will be sampled synchronously at a rate of 120 MHz (three times the current rate). The new GPS receiver will allow a timing accuracy of 5 nanoseconds, about a factor two better than the current value. Faster data processing and more sophisticated local triggers are enabled by the use of a more powerful processor and FPGA, and improved calibration and monitoring capabilities are foreseen. The dynamic range of the WCD will be enhanced by a factor 32 with an additional small (1") PMT that will be inserted in the WCD [19].

To verify and fine-tune the methods used to extract shower muon content using the SSD and WCD stations, an underground muon detector (AMIGA) will be installed to provide a direct measurement of the muon content of a sample of showers observed by the upgraded Auger SD [20]. The AMIGA detector consists of 61 units deployed on a 750 m grid, instrumenting a total area of 23.5 km². Each unit consists of a plane of plastic scintillator of about 30 m² that will be buried about 2.3 meters underground.

The Auger Fluorescence Detector (FD) [1] provides information about extensive air showers such as a model-independent energy reconstruction and longitudinal development profiles of the extensive air showers. The main limitation of the FD is its duty cycle, currently at the level of 15%. A significant increase of the duty cycle is possible by the extension of the FD operation to times at which a large fraction of the moon in the sky is illuminated. During such operating conditions the PMT gains must be reduced by lowering the supplied high voltage to avoid high anode current and, therefore, a deterioration of the PMTs. The HV power supplies used for the FD allows switching between two high voltage levels and the PMTs can be operated at the nominal gain (standard operation mode) and a lower gain (new operation mode for periods of high night sky background).

4. Expected Performance

A thin scintillation detector, which is mounted above the larger WCD, provides a robust and well-understood scheme for particle detection that is sufficiently complementary to the water-Cherenkov technique and permits a good measurement of the density of muons. This can be understood by comparing the signal contributions for different shower components as shown in figure 2. Over a wide range in lateral distance, the ratio between the integrated signal of electromagnetic particles (photons and electrons) and that of muons is more than a factor two higher in an unshielded scintillation detector compared with a water-Cherenkov detector [13].

One of the key aims of the Pierre Auger upgrade is to discriminate between different compositions and physics scenarios in the energy range of the flux suppression. This is very difficult to demonstrate without knowing what composition to expect. For this reason two benchmark descriptions have been chosen as representations of a maximum-rigidity scenario (scenario 1 corresponding to the best fit solution in [22]) and of a photo-disintegration scenario (scenario 2 corresponding to the second minimum in [22]). While the two scenarios approximately reproduce the spectrum and the X_{\max} and $\sigma(X_{\max})$ so far measured by the Pierre Auger Observatory, they are generated by very different compositions and spectra at the sources.

Figure 3 shows the mean X_{\max} and the corresponding $\sigma(X_{\max})$ for these scenarios, using the SD data of the upgraded observatory. The $\sigma(X_{\max})$ contains the intrinsic air-shower fluctuations and the detector resolution. The same quantities expected for pure proton and pure iron compositions are illustrated. While the mean X_{\max} and $\sigma(X_{\max})$ are very similar up to 10^{19.2} eV, which corresponds to the energy range presently covered by data of the fluorescence telescopes, the models predict significantly different extrapolations into the suppression region and the two scenarios can be distinguished with high significance and statistics. In addition to these studies, the availability of muon information on an event-by-event basis allows studies of the features of hadronic interactions. Moreover, the information on an event-by-event basis will permit the selection of a

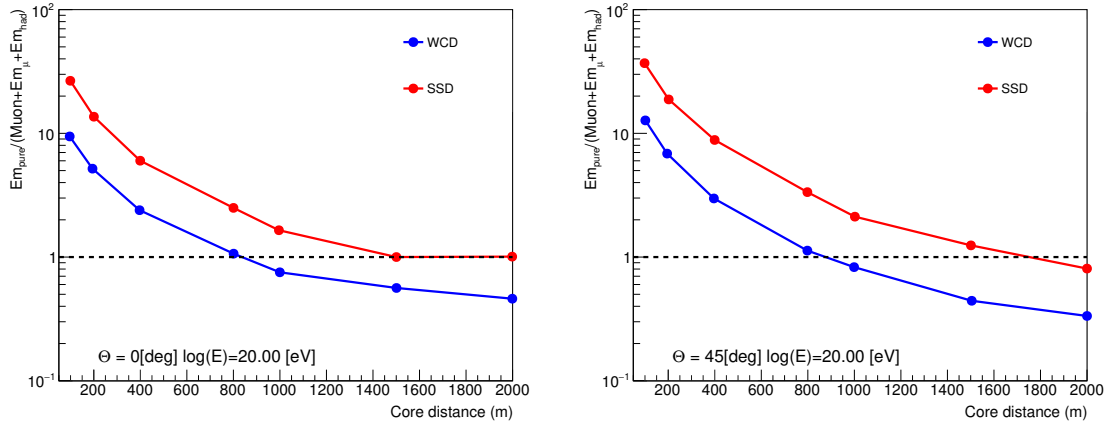


Figure 2: Ratios of different contributions to the integrated signal detected for air showers of 10^{20} eV at two zenith angles. Shown is the ratio between the electromagnetic component and the muonic component. The curve labeled “WCD” corresponds to the water-Cherenkov detectors of the Auger array, while the red one “SSD” corresponds to the scintillator detectors.

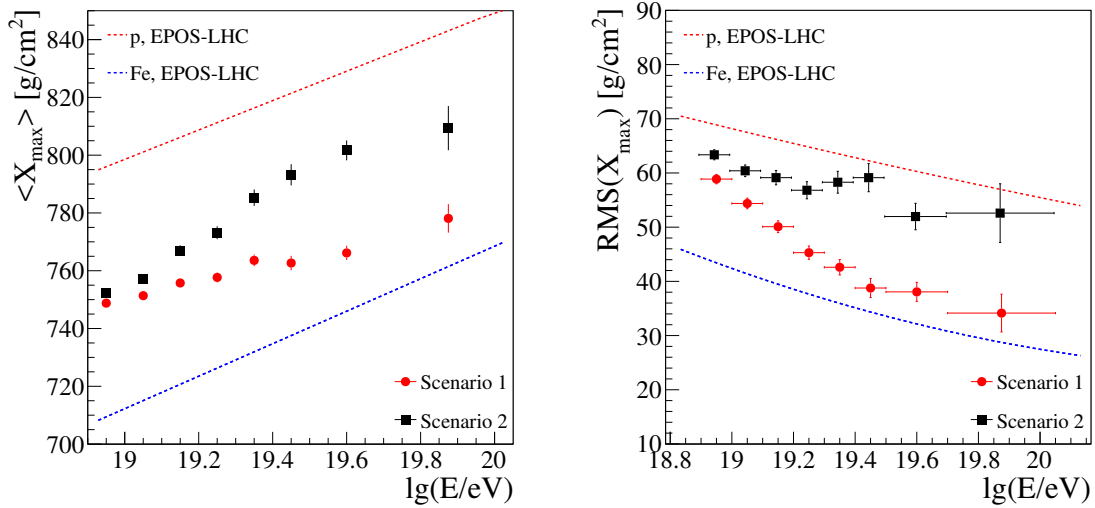


Figure 3: Predicted X_{\max} and $\sigma(X_{\max})$ for the two benchmark scenarios ([22]). Scenario 1: maximum-rigidity; Scenario 2: photo-disintegration

sub-sample of events in the cutoff region enriched with light elements, increasing the capacity of the Observatory to identify the potential sources of UHECRs.

5. Status of AugerPrime and its Engineering Array

The first twelve stations of AugerPrime, forming the Engineering Array of the upgrade, were assembled in Europe and deployed at the Pierre Auger Observatory in September 2016. The stations of the Engineering Array are partially located inside the standard 1500 m spaced array (9 detectors) and partially in the more dense area where the separation of the stations is 750 m (3

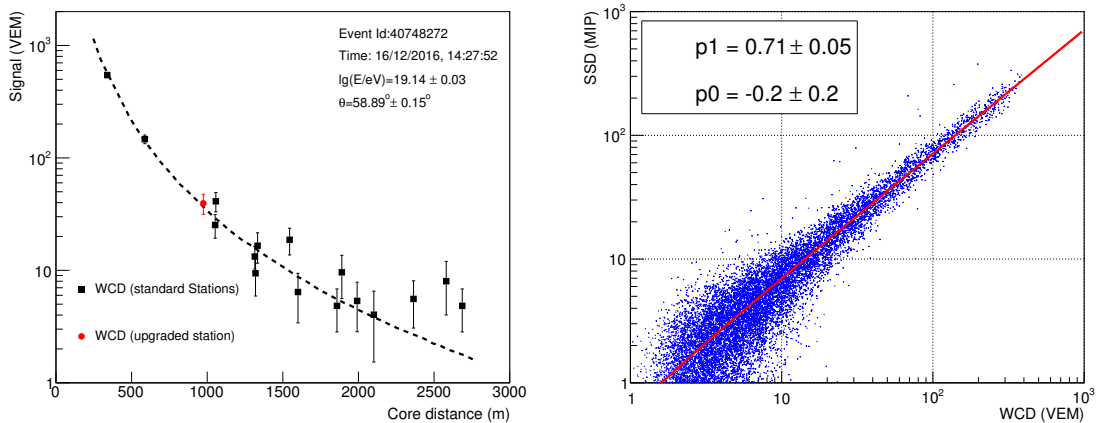


Figure 4: Left: one event reconstructed with the regular 1500 m array in close proximity to the EA. The reconstructed signals in the EA are compared with the LDF of the event; Right: correlation of the signals of the SSD and the WCD. Both signals have been calibrated;

detectors) [21]. The Engineering Array has been in continuous data taking mode since begin of October 2016 and has collected more than 30000 local triggers. Standard stations in the EA area have been used to reconstruct more than 3000 events, the larger fraction of them in the 750 m array [21].

The performance of the upgraded stations has been monitored with the data collected by the EA. In figure 4 (left) is shown one event collected and reconstructed with the 1500 m spaced array in the region of the EA. The reconstructed number of Vertical Equivalent Muons (VEMs) detected with an upgraded WCD is shown with a different color. The upgraded stations produce signals that are in good agreement with expectations. Figure 4 (right) shows the good correlation between the calibrated signals of the SSD and the calibrated signals in the WCD. The correlation between the two signals verifies the independent calibration procedures developed for the new detectors (see [21] for a description of the calibration procedures). The ratio of 0.7 between the signals in the two detectors is expected and is due to a combination of the geometry of the WCD and the SSD and of the response of the two detectors.

Important for the determination of the primary mass with the upgrade stations are the detectors viewing a large number of particles. To avoid saturated stations close to the shower core a strong effort in the upgrade has been dedicated to the extension of the dynamic range of the WCD and in providing a sufficient dynamic range for the new SSD [19]. In figure 5 (left) is shown the measured dynamic range of one of the SSD stations in the EA. The figure shows that the SSDs are linear within 5% up to a signal of 20000 particles. As expected, the SSDs are more sensitive to the electromagnetic component of the extensive air showers. The lateral density function (LDF) of SSD signals is higher than the corresponding LDF of the WCD in the region close to the shower axis (see figure 5 (right)). Far from the shower core the showers are dominated by the muons and the signal density in the two detectors becomes comparable. The different response of the two detectors to the two main components of the EAS is the tool for the identification of the mass of the primary cosmic rays on a event-by-event basis [13].

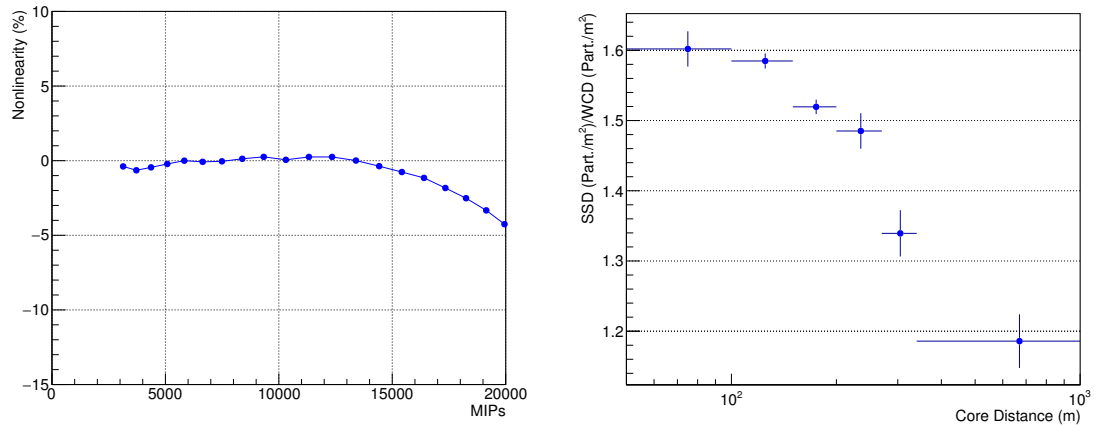


Figure 5: Left: Measured dynamic range of one SSD detector, the detector is linear within 5% up to 16000 particles. Right: ratio between the SSD and the WCD particle density versus the distance from the shower core (detectors without signals have been excluded)

6. Conclusions

AugerPrime will collect high-quality data from 2018 until 2024. In this period, the number of events collected will be comparable with the statistics collected up to now by the existing Pierre Auger Observatory, with the advantage that every future event will have mass information and will allow us to better address some of the most pressing questions in UHECR physics. Obtaining additional composition-sensitive information will help to better reconstruct the properties of the primary particles at the highest energies. Moreover, it will improve the measurements in the important energy range just above the spectral ankle. Measurements with AugerPrime will help to reduce systematic uncertainties related to the hadronic interaction models and to the reconstruction algorithms. This improved knowledge of air-shower physics will allow a reanalysis of existing data for improved energy evaluation and for improved mass composition studies. A new agreement has been signed between the funding agencies in November 2015 extending the acquisition period of the Pierre Auger Observatory until 2024 and supporting the AugerPrime upgrade. The start of the deployment of the upgraded stations is expected in January 2018.

References

- [1] The Pierre Auger Collaboration, Nucl. Instrum. Meth. A 798 (2015) 172.
- [2] F. Fenu, for the Pierre Auger Collaboration, these proceedings.
- [3] The Pierre Auger Collaboration, JCAP 04 (2017) 009.
- [4] The Pierre Auger Collaboration, Astropart. Phys. 31 (2009) 399.
- [5] M. Niechciol, for the Pierre Auger Collaboration, these proceedings.
- [6] E. Zas, for the Pierre Auger Collaboration, these proceedings.
- [7] The Pierre Auger Collaboration, Phys. Rev. D 91 (2015) 092008.

- [8] The Pierre Auger Collaboration, Phys. Lett. B 762 (2016) 288.
- [9] J. Bellido, for the Pierre Auger Collaboration, these proceedings.
- [10] The Pierre Auger Collaboration, Phys. Rev. D 90 (2014) 122006.
- [11] U. Giaccari, for the Pierre Auger Collaboration, these proceedings.
- [12] O. Taborda, for the Pierre Auger Collaboration, these proceedings.
- [13] Pierre Auger Collaboration, *The Pierre Auger Observatory Upgrade AugerPrime: Preliminary Design Report*, arXiv:1604.03637. (2016).
- [14] R. Engel, for the Pierre Auger Collaboration, Proc. 34th Int. Cosmic Ray Conf. 2015, The Hague, Netherlands, PoS(ICRC2015)686.
- [15] The Pierre Auger Collaboration, Phys. Rev. Lett. 117 (2016) 192001.
- [16] The Pierre Auger Collaboration, Phys. Rev. D 91 (2015) 032003.
- [17] R. Smida, for the Pierre Auger Collaboration, these proceedings.
- [18] T. Suomijärvi, for the Pierre Auger Collaboration, these proceedings.
- [19] A. Castellina, for the Pierre Auger Collaboration, these proceedings.
- [20] The Pierre Auger Collaboration, JINST 11 (2016) P02012.
- [21] Z. Zong, for the Pierre Auger Collaboration, these proceedings.
- [22] The Pierre Auger Collaboration, JCAP 04 (2017) 038.



New electronics for the surface detectors of the Pierre Auger Observatory

Tiina Suomijärvi^{*a} for the Pierre Auger Collaboration^b

^a*Institut de Physique Nucleaire, Université Paris-Sud, Université Paris-Saclay, IN2P3-CNRS, Orsay, France*

^b*Observatorio Pierre Auger, Av. San Martín Norte 304, 5613 Malargüe, Argentina*

E-mail: auger_spokespersons@fnal.gov

Full author list: http://www.auger.org/archive/authors_icrc_2017.html

The surface detector array of the Pierre Auger Observatory consists of 1660 water-Cherenkov detectors that sample at the ground the charged particles and photons of air showers initiated by energetic cosmic rays. Each detector records data locally with timing obtained from Global Positioning System (GPS) units and power from solar panels and batteries. In the framework of the upgrade of the Auger Observatory, AugerPrime, new electronics has been designed for the surface detectors. The electronics upgrade includes better timing with up-to-date GPS receivers, higher sampling frequency, increased dynamic range, increased processing capability, and better calibration and monitoring systems. It will also process the data of the AugerPrime scintillator detectors. In this paper, the design of the new electronics will be presented and its performance will be discussed in light of results from test measurements and from the engineering array data analysis.

*35th International Cosmic Ray Conference — ICRC2017
10–20 July, 2017
Bexco, Busan, Korea*

^{*}Speaker.

1. Introduction and design objectives

The surface detector (SD) of the Pierre Auger Observatory, located near Malargüe, Mendoza Province, Argentina, consists of an array of 1660 water-Cherenkov detectors (WCD) read out by three large XP1805 photomultipliers (PMT). The Collaboration is planning an upgrade of the detector that includes the addition of a scintillator-based surface detector (SSD) atop each WCD, together with an upgrade of the surface detector electronics (SDE) to both improve the performance of the existing detector and to provide an interface to allow the scintillator detectors co-located with the SD stations to make use of the data processing and communication infrastructure of the stations. The SDE records the PMT signals, makes local triggering decisions, sends timestamps to the central data acquisition system for the global triggers, and stores event data for retrieval when a global trigger condition is satisfied. These functions are implemented in a single board, called the upgraded unified board (UUB). Because of the small bandwidth (1200 bits/s) available to each tank, the station must operate semi-autonomously, performing calibrations and taking action in response to alarm conditions at the station level. The current SDE was designed 15 years ago using the technology available at that time. Evolution in processors, power consumption of electronics components, and timing systems make it possible today to design and implement a higher performance electronics system for the surface-detector array. The design of the current detector and its electronics is discussed in [1].

The design objectives of the new electronics globally aim to increase the data quality by faster sampling for ADC (analog-to-digital converter) traces, by better timing accuracy, and by increased dynamic range; to enhance the local trigger and processing capabilities by using more powerful local-station processor and FPGA (field-programmable gate array); and to improve calibration and monitoring capabilities of the SD stations. Backwards-compatibility with the current dataset will be maintained by retaining the current timespan of the PMT traces and providing for digital filtering and downsampling of the traces to emulate the current triggers in addition to any new triggers. The design objectives also aim for higher reliability and easy maintenance. A detailed description of the AugerPrime design can be found in [2].

An engineering array (EA) with 12 AugerPrime prototype detector stations was deployed on the Observatory site in October 2016 and has allowed us to verify the performance of the new electronics. In the following, the main features of the AugerPrime electronics are described. The performances based on the first EA data are discussed in [3].

2. Front-end and timing

The anode channel of the large XP1805 PMTs is split and amplified to have a gain ratio of 32. The signals are filtered and digitized by commercial 12 bit 120 MHz flash ADC (FADC). The pulse response of the XP1805, when expressed in terms of bandwidth, is ~ 70 MHz. This is well matched to a 120 MHz FADC and associated 60 MHz Nyquist filter. We have chosen to use commercial 12 bit 120 MHz AD9628 FADCs, which achieve this performance with minimal power consumption, an important consideration due to the 10 W station-power budget.

A design goal of AugerPrime is to measure shower properties at energies above 6×10^{19} eV as close as 250 m from the shower core. For this purpose the WCD is equipped with an additional

small photomultiplier tube (SPMT), a 1 inch Hamamatsu R8619 PMT, dedicated for the unsaturated measurement of large signals. The SPMT signal is also digitized with 12 bits at 120 MHz in a separate channel. The SPMT gain and the amplification are set such that the dynamic range is extended by a factor of at least 30 to about 20,000 VEM (vertical equivalent muon).

The anode channel of the SSD PMT is split; one is amplified to have a gain ratio of 32 and the other one is attenuated by a factor of 4. This yields a total gain ratio of 128. The signals are filtered and digitized similarly to the WCD PMT signals. The expected dynamic range for the SSD is 20,000 MIP (minimum-ionizing particle).

The calibration of the large PMT signals is performed by using background muons. The cross-calibration between the large PMTs and the small PMT is performed either by using small shower events or the existing LED flasher system that is adapted for brighter light pulses. A more detailed discussion on the dynamic range can be found in Ref. [4]. All the front-end functions as well as the LED (light-emitting diode) controller are directly implemented on the UUB to avoid connectors.

Synchronization of the detectors is provided by disciplining a local clock using the global positioning system (GPS). For the upgraded electronics we have selected the I-Lotus M12M timing GPS receiver manufactured by I-Lotus, LLC (Singapore). The M12M timing receiver is designed to be functionally compatible with the Motorola Oncore UT+ GPS receiver that is used with the current electronics. Choosing a compatible unit requires fewer and simpler modifications to the basic time-tagging system design. Specifically, the M12M provides the same 1 PPS (pulse per second) timing output with serial control and data. The specified intrinsic device accuracy after the applied granularity correction (the so-called negative sawtooth) is about 2 nanoseconds. This accuracy is very good relative to the UUB specification to achieve better than 5.0 ns RMS accuracy. The fundamental architecture of the time-tagging firmware module parallels the time-tagging design concept used in the current electronics and is implemented in the UUB board FPGA. The on-board software for initialization of the time-tagging modules, GPS hardware control, and timing data is similar to the current one, with minor modifications needed for the new UUB hardware.

3. Slow control and calibration

The UUB is equipped with a micro-controller (MSP430) for the control and monitoring of the PMT's high voltage, the supervision of the various supply voltages and reset functionality. For that purpose it controls 16 logic I/O lines, steers a DAC (digital-to-analog converter) with eight analog outputs and senses through multiplexers up to 64 analog signals with its internal ADC. The MSP430 also provides a USB (universal serial bus) interface and is tied via an I²C-bus to an EEPROM (electrically-erasable programmable read-only memory) and a pressure sensor. More than 90 monitoring variables - including currents and voltages of the power supply and the PMTs - are managed by the slow-control software.

The VEM signal is the reference unit of the WCD high-gain calibrations, and was determined on a test tank with an external trigger hodoscope to give on average 95 photoelectrons at the cathode of the XP1805 PMTs, corresponding roughly to 150 integrated ADC counts above pedestal after signal digitization. The calibration of the low-gain channel compared to the high-gain channel is purely electronic and has an accuracy of better than about 2%.

The SSD calibration is based on the signal of a minimum-ionizing particle going through the detector. Since this is a thin detector, the MIP will not necessarily be well separated from the low-energy background but, being installed on top of the WCD, a cross-trigger can be used to remove all of the background. About 40% of the calibration triggers of the WCD produce a MIP in the SSD. Similarly to the WCD, the cross-calibration between high-gain and low-gain channels is defined by the electronics.

In addition to routine calibrations with physics events, each WCD is equipped with two LEDs. While these are not stable sources of calibrated light, they are very useful for monitoring and for linearity tests. These LEDs can also be used for the SSD.

4. Main electronics board

The various functions (front-end, calibration, time tagging, trigger, monitoring) are implemented on a single board, the UUB. An architecture with an FPGA containing an embedded ARM processor is used. The general architecture of the UUB is shown in Fig. 1.

The heart of the UUB is a Xilinx Zynq FPGA with two embedded ARM Cortex A9 333 MHz microprocessors. It is connected to a 4 Gbit LP-DDR2 memory and 2 Gbit flash memory. The FPGA implements all basic digital functions like the readout of the ADCs, the generation of triggers, the interface to the LED flasher, GPS receiver, clock generator and memories. High-level functions like the data handling and the communications with the radio transmitter are implemented under LINUX.

The speed of the upgraded CPU will be >10 times faster than that of the current one, with a similar increase in memory. This will allow much more sophisticated processing in the local station. The addition of accessible trigger IN/OUT and GPS 1 PPS signals will simplify time synchronization with other possible additional detectors. Furthermore, the high-speed USB will facilitate interfacing them. The current local-station software has been ported to LINUX. The data acquisition will be simplified by extending the use of FPGA firmware.

The trigger and time-tagging functionalities are implemented in the FPGA. The current local triggers (threshold trigger, time-over-threshold trigger (ToT), multiplicity of positive steps (MoPS) trigger, etc) will be adapted to the 120 MHz sampling rate. The increased local processing capabilities will allow new triggers to be implemented such as asymmetry-based triggers, and combined SSD and WCD triggers. The current muon memories and scalers will be retained. The trigger scheme includes the ability to down-sample and filter the data to the current 40 MHz rate which will allow the detectors to be operated with the new electronics emulating the current system. This will allow deployment of new electronics during the maintenance of the current system without disturbance to the data taking.

The UUB will be installed in the current enclosure with a new front panel. Two digital connectors are provided for possible additional detectors. These connectors provide 8 differential lines, each of which can be individually defined as input or output in the FPGA. An example of such allocation could be: trigger out, clock out, PPS out, busy in, data in, sync in, data out, sync out, etc. Moreover, this connector will provide unregulated +24 V, switched and limited, with a current monitor.

5. Current status and performance

An engineering array with 12 AugerPrime prototype detector stations was deployed on the Observatory site in October 2016. The data show generally good performance of the new electronics and satisfy most of the requirements. The noise levels are slightly higher than the requirements. However, the VEM and MIP calibration can be easily performed and the dynamic range is close to the requirements. The power consumption is currently 12 W which is higher than the 10 W requirement. The detectors have been continuously taking data since October without any problems due to the power system. The performances based on the first EA data are discussed in [3].

In order to further reduce noise, to lower the power consumption, and to implement some other minor changes, a new main electronics board has been designed. This board will be tested in laboratories and in the engineering array before the pre-production and production that are planned for early 2018.

6. Conclusions

The AugerPrime upgrade will complement the existing WCD with an additional SSD for better identification of air-shower particles. An extra small PMT will extend the dynamic range of the WCD. The upgraded Auger electronics will support the PMTs of the WCD and SSD detectors. It provides much higher performance in computing power, memory size, timing, and sampling frequency than the current electronics. Furthermore, the new electronics can be easily interfaced with any other additional detectors through the digital connectors.

Since October 2016, an AugerPrime engineering array has been in operation at the Auger Observatory site. The first results show generally good performance of the new electronics. To implement some minor design changes, a new main board is being fabricated and tested before the pre-production and production that are planned to start early 2018.

References

- [1] A. Aab *et al.* (The Pierre Auger Collaboration), *The Pierre Auger Cosmic Ray Observatory*, Nucl. Instrum. Meth. A 798 (2015) 172; arXiv:1502.01323.
- [2] The Pierre Auger Collaboration, *The AugerPrime Design Report*, arXiv:1604.03637.
- [3] Z. Zong, for the Pierre Auger Collaboration, *The first results from the AugerPrime Engineering Array*, these proceedings.
- [4] A. Castellina, for the Pierre Auger Collaboration, *The dynamic range of the AugerPrime Surface Detector: technical solution and physics reach*, these proceedings.



The dynamic range of the AugerPrime Surface Detector: technical solution and physics reach

Antonella Castellina^{*a} for the Pierre Auger Collaboration^b

^a*Osservatorio Astrofisico di Torino (INAF) and INFN, Sezione di Torino, Italy*

^b*Observatorio Pierre Auger, Av. San Martín Norte 304, 5613 Malargüe, Argentina*

E-mail: auger_spokespersons@fnal.gov

Full author list: http://www.auger.org/archive/authors_icrc_2017.html

Ground arrays for ultra-high energy cosmic ray detection based on water-Cherenkov stations or scintillator modules are unavoidably limited by the saturation suffered by the counters closest to the shower axis. Reducing to a negligible level the amount of events with saturated detectors is mandatory to unambiguously record the highest energy events and to decrease the systematic uncertainties affecting the measurements. The Surface Detector Array of the upgraded Pierre Auger Observatory includes 1660 water-Cherenkov stations covered by a 3.8 m² plastic scintillator plane. The impact point of the extensive air shower, its arrival direction and the lateral distribution of particles at the ground can be reconstructed exploiting the recorded signals and their timing. The stations will use new electronics that will process signals from both the tanks and the scintillators with increased quality. The addition of an extra small photomultiplier in each surface station and suitable photomultipliers with very large linearity in the scintillator detectors will allow us to extend the dynamic range to more than 32 times the largest signals currently measured. We describe the chosen technical solutions and discuss the expected performance of the detectors, which will be able to measure non-saturated traces as close as a couple of hundred meters to the shower core.

*35th International Cosmic Ray Conference — ICRC2017
10–20 July, 2017
Bexco, Busan, Korea*

*Speaker.

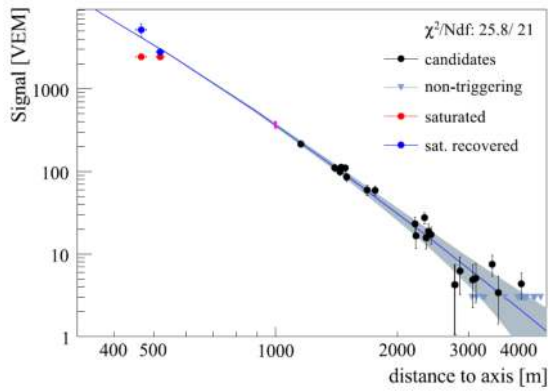


Figure 1: Lateral distribution of the signal sizes recorded in the WCD. Red circles: saturated stations. Blue circles: recovered signals.

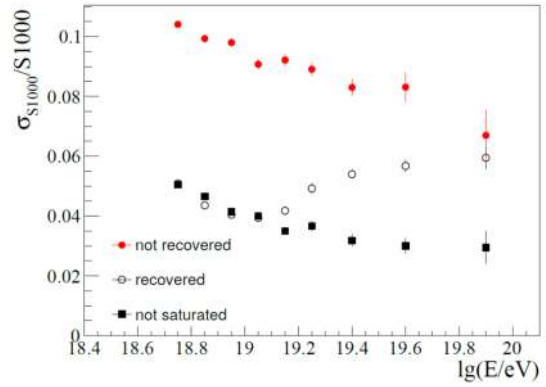


Figure 2: $S(1000)$ resolution for events without (black) or with at least one saturated station (red) and using the recovery procedure (empty).

1. Introduction

Extensive air showers with energies above 3 EeV are measured in the Pierre Auger Observatory Surface Detectors (SD) by recording the signals and arrival times of the secondary particles reaching the ground, which spread over a large area of more than 15 km².

The Cherenkov light produced by the secondary particles in each water-Cherenkov detector (WCD) is collected by three large 9 inch photomultipliers (Photonis XP1805), from now on LPMTs, which are individually sampled and digitized by FADC in two overlapping ranges with different resolutions. The dynamic range of the measurement varies from few photoelectrons in the stations very far from the shower core and from the low energy muon signals used to calibrate the detectors, to hundreds of thousands in the station closer to the core. When the impact point of the shower at the ground is close to a detector, the dynamic range of the recording electronics is smaller than required to record the Cherenkov signal produced by the particles. The largest particle density measurable before signal saturation is not only constrained by the acquisition electronics (e.g. anode FADC overflow) but, more substantially, by the limited extension of the LPMTs linear range, which deviates from linearity for peak currents in excess of ~ 50 mA. Conservatively assuming a maximum current of 40 mA, this value is well matched via standard 50 Ω termination resistors by the 2 V input range of the front-end digitizers. A recovery procedure is currently implemented to estimate the signal in case of saturation [1], thus allowing to include the saturated stations in the lateral distribution function fits with consequent improvements in energy estimation.

An example of the lateral distribution of an event produced by a vertical 100 EeV proton is illustrated in Fig. 1 where the signal size is expressed in VEM (Vertical Equivalent Muon, i.e. the average signal from a vertical muon crossing the WCD).

Both the saturated signals and the recovered ones are shown for the stations closest to the shower core. Due to the current limited information, the accuracy of the recovered signals larger than 10⁴ VEM can be worse than 70%. An accuracy as good as 15% in the measured signals can only be obtained with a detailed knowledge of the individual PMT responses in the non-linear region (a non feasible solution, which needs a measurement of the deep saturation curve of each

of the 5000 PMTs and the monitoring of their properties in time). It is important to note that the expectation value of the SD energy estimator $S(1000)$ is not affected by having a station with a saturated signal in the event, only the reconstruction resolution is worsened to some extent. The resolution in the reconstructed $S(1000)$ is related to the uncertainty in the knowledge of the lateral distribution function. Due to the choice of a specific lateral distribution function, a systematic uncertainty of less 4% is induced on $S(1000)$, at $10^{19.5}$ eV, for events without saturated stations. On the contrary, as shown in Fig. 2, this value increases to 8% if one of the signals is saturated and only a limited correction to $\sim 6\%$ can be obtained by applying the recovery procedure.

2. The AugerPrime extended dynamic range

A substantial upgrade of the Pierre Auger Observatory (AugerPrime) [2] is underway with the main goal of improving the mass determination of primary cosmic rays in the suppression region, above $10^{19.5}$ eV. For this purpose, all the water-Cherenkov detectors of the existing surface array are equipped by a 3.8 m^2 , 1 cm thick scintillator plane. Owing to their different response to the muonic and electromagnetic components of the extensive air showers, these new detectors will provide a complementary measurement of the shower particles at the ground.

The surface detector electronics has been redesigned with faster sampling ADC channels, powerful FPGA, and better timing accuracy [3] to enhance the local trigger and processing capabilities and to allow the acquisition of both water-Cherenkov and scintillator detector signals.

In particular, the SD data quality will be improved by extending the acquisition dynamic range in both detectors, thus allowing to measure non-saturated signals at distances as close as 250 m from the shower core. In order to benefit the most from the combined information of the SSD and the WCD signals, the dynamic range of both detectors should be similar. Significant signals are expected close to the shower core and also at intermediate distances, where the simultaneous measurements will be most important for the separation of the different components of the shower, furthermore allowing a direct cross-check of the two detectors.

An engineering array of 12 stations, fully equipped with scintillators and new electronics has been deployed in the field and has been taking data since October 2016.

2.1 Extended dynamic range of the water-Cherenkov detectors

When exposed to the same photon density, photomultipliers with photocathode of different size (operated at the same gain) will produce output signals proportional to their sensitive surfaces. Similarly, the introduction of an additional photomultiplier with small diameter in each surface detector can largely reduce the occurrence of saturated signal in the stations closest to the shower axis. This solution increases the linear operative range of the water-Cherenkov Detectors with limited changes to the station mechanics and electronics and without interfering with their standard operation. The small photomultiplier (hereafter SPMT) can be easily installed in the station by exploiting an unused and easily accessible 30 mm diameter window on the Tyvec bag containing the hyper-pure water of the surface detectors, avoiding any changes on the tank mechanical structure.

Different photomultipliers from various companies have been considered and tested. The final choice of the Hamamatsu-R8619 photomultiplier was the best compromise between performance

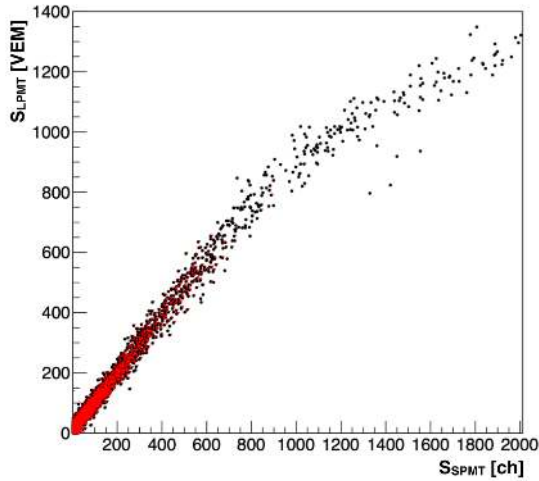


Figure 3: Average integrated signal from the 3 LPMTs (VEM) versus the SPMT signal (ADC ch). In red, the region with non-saturated LPMTs.

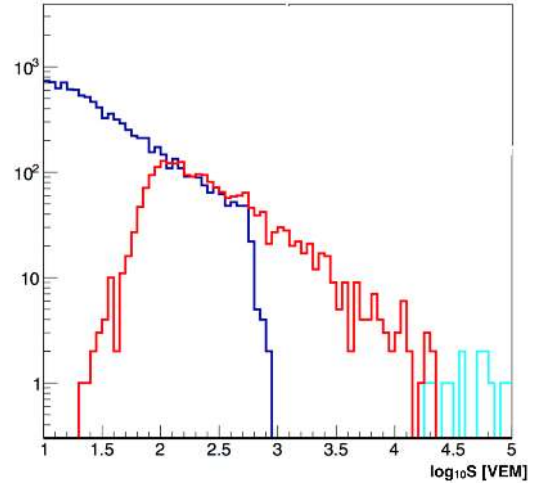


Figure 4: Logarithm of the charge for a single station, as measured by the LPMTs (blue) and by the SPMT (red and cyan).

and price. Its active area is only 1/100 of the XP1850 (LPMT), potentially allowing for an equivalent dynamic range extension. Adjusting the gain, the ratio $R = \langle S_{\text{LPMT}} \rangle / S_{\text{SPMT}}$ can be limited to a value of 32, enough to allow for a linear range extension of the dynamic range up to 2×10^4 VEM. The optimal R value is initially setup for each SPMT by a preliminary and fast procedure exploiting intense light pulses by the LED onboard each station. This setting almost completely eliminates the occurrence of saturated signals also at the highest energy.

The SPMT anode signal is read and digitised by the new AugerPrime electronics with a dedicated input, analogous to those for the LPMTs at lower resolution. Being the single muon signal (1 VEM) too small to be detectable by the SPMT, the absolute scale in physical units is obtained by cross-calibrating the SPMT and LPMT signals in the overlapping region, as shown in Fig. 3 (red dots) for one of the AugerPrime engineering array stations. A dedicated trigger selecting small local showers is set up to this aim, furthermore imposing a minimum threshold of ~ 80 VEM on the LPMTs to guarantee a reasonably large signal on the SPMT, not affected too much by statistical fluctuations. The distribution of Fig. 3 is then fitted in the region of superposition of the two PMTs (excluding the LPMT saturation) to obtain the slope, i.e. the calibration value to convert to VEM the integrated charge of the SPMT.

The SPMT gain is tuned by this automated procedure only during the first 24 hours following the installation; successively the value of the slope is continuously monitored and its value updated in the offline data analysis. Indeed a variation of the slope with the temperature is expected, as the temperature dependence of the gain is accounted for in the calibration of the LPMTs only.

The charge spectrum for a single station of AugerPrime is shown in Fig. 4, as measured by the standard LPMTs (blue histogram for the anode channel) and by the SPMT (red histogram for the unsaturated SPMT; in cyan, the few values where the SPMT is saturated too). The dynamic range is extended from $\sim 10^3$ VEM to few $\sim 10^4$ VEM obeying the power law behaviour expected for the distribution of the signal from individual stations.

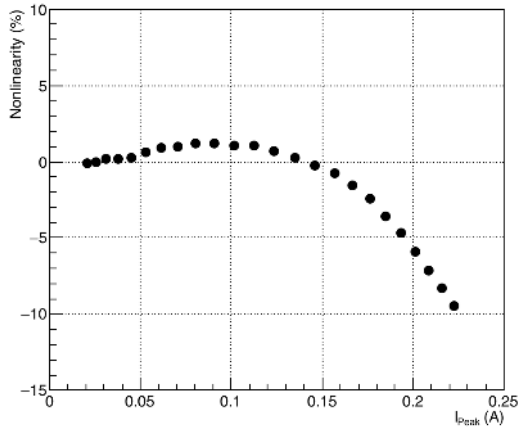


Figure 5: Linearity behaviour of one of the R9420 employed in the AugerPrime scintillators. The photomultiplier is linear within 5% up to ~ 160 mA as required.

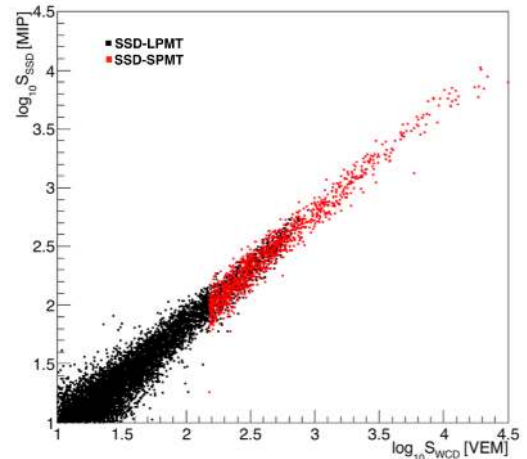


Figure 6: Relation between the water-Cherenkov station and the scintillator signals as measured by one detector of AugerPrime.

2.2 Extended dynamic range of the scintillator detectors

Each surface scintillator detector (SSD) consists of two identical modules made of extruded plastic scintillator bars, read by U-shaped 1.0 mm wavelength-shifting (WLS) fibers. A single photomultiplier is optically coupled to a bundle collecting the 48 fibers from both the modules and integrating the total signal of all bars. This configuration combines extreme simplicity with excellent performance/cost balance, giving both a satisfactory light yield of ~ 30 phe/MIP (photoelectrons per minimum ionizing particle) and an acceptable spatial non uniformity ($\pm 10\%$).

Care is required in the choice of the best photomultiplier for this application, because of the requirement on the dynamic range. For consistency with the associated water-Cherenkov detector, it must in fact span from the signal of a single particle, as needed for calibration, to large signals, up to $\sim 2 \times 10^4$ MIP. The Hamamatsu R9420 photomultiplier (8 stage, 1.5 inch bialkali photocathode) has been chosen in the baseline design based on its excellent linear response also when operated at low gain. The tube is in fact linear within 5% for peak currents up to 160 mA (for a gain of 8×10^4), as shown in Fig. 5. In the electronics front-end, the R9420 anode signal is filtered and split in two in a similar way as the signals from the standard LPMTs of the surface stations. To reach the required dynamic range after the splitting, one of the two signals is attenuated by a factor of 4, while the other is amplified by a factor of 32 [3]. The SSD calibration is based on the signal deposited by a minimum ionising particle (MIP) crossing the detector. About 40% of the calibration triggers of the water-Cherenkov stations produces a corresponding MIP in the scintillator. The statistics of calibration events recorded in a minute, corresponding to the standard calibration interval for the water-Cherenkov detectors, is therefore enough to obtain a precise measurement of the MIP.

An example of the relation between the signals in one of the water-Cherenkov stations and in the corresponding scintillator is shown in Fig. 6, exploiting the recordings of 4 months of data taken by the engineering array of AugerPrime. Both scales are expressed in physical units: the SPMT response is calibrated in VEM and the scintillator photomultiplier in MIP as discussed before. The dynamic range in the surface detector is nicely covered by the LPMTs up to the saturation (black

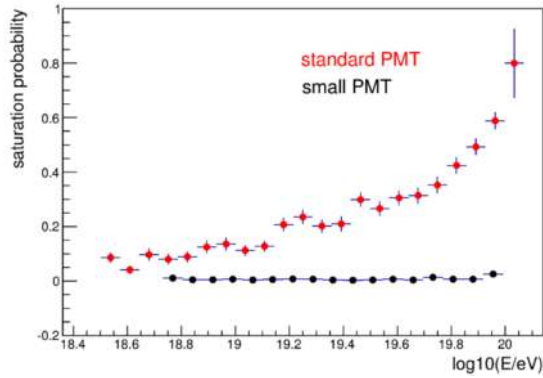


Figure 7: Probability of at least one saturated station/event as a function of energy.

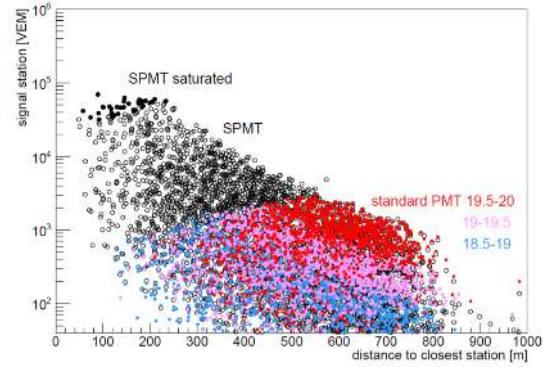


Figure 8: Simulated signals as a function of distance to shower core for different energies.

dots) and then extended to the highest particle densities by the SPMT (red dots) up to the highest particle densities measured by one detector of AugerPrime.

3. Expected physics performance

A large set of simulations of air showers induced by primary protons with energy between 3 and 100 EeV (based on the CORSIKA code [4]) has been generated to demonstrate the benefits of the extended dynamic range.

The broadening of the dynamic range by more than a decade is highly expected to record an event above 10^{20} eV unambiguously, with full signals in all stations. Due to the limited dynamic range of the LPMTs and old electronics, the probability of having at least one saturated station (the closest to the shower core) per event was steadily increasing with energy, reaching $\sim 30\%$ at $10^{19.5}$ eV, as shown in Fig. 7 (red dots). In AugerPrime, thanks to the SPMT installation, this probability is basically zero in the whole range (black dots).

As demonstrated above in Fig. 6, the dynamic range is increased by more than one decade in both the water-Cherenkov and the scintillator detectors, thus helping in unambiguously separating the shower components in all stations and to cross check the two measurements, which are affected by different systematic uncertainties.

A comparison of the signals measured at different distances to the shower core is shown in Fig. 8 for different energies in the case of the LPMTs (coloured circles) and of the SPMT (black circles) for the same air showers. Complete signals could be measured at the highest energies (above $10^{19.5}$ eV) only above ~ 500 to 600 m from the shower core. With the increased dynamic range, we will be able to measure the lateral distribution function of the showers down to distances as close as 250 to 300 m from the shower core; below this distance, the uncertainty in the core position would anyway limit the usefulness of the measurements. We will thus be able to test the modelling of the lateral distribution function in a range of distances never before explored at these ultra high energies and to study the shower components in the region where most of the energy is deposited.

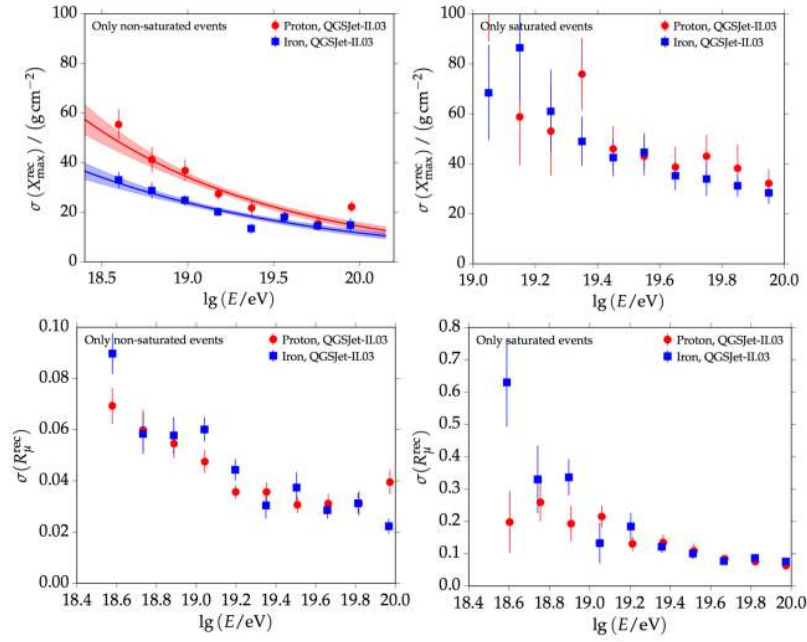


Figure 9: Resolution of the X_{\max} (top panel) and of the relative number of muons R_{μ} (bottom panel) as obtained from universality, derived using non saturated (left) or saturated-only (right) events.

The signal variance in the extended dynamic range interval will be reduced significantly, being dominated by the calibration uncertainties (see Fig. 2). Event selection based on cuts in energy will be more accurate and flux corrections of the energy spectrum due to resolution-dependent migrations will be smaller.

The complementarity of the techniques employed in AugerPrime will allow us to efficiently separate the two main components of the air showers at the ground, namely the electromagnetic and the muonic ones. Exploiting the fact that the ratio between the two components is more than a factor two higher in the unshielded scintillator slab than in the water-Cherenkov detector, the muonic signal can be derived on a station-by-station basis. On the other hand, an analysis based on shower universality ([5] and references therein) allows us to correlate the detector signals at different lateral distances, taking also advantage of the temporal structure of the signal measured in the detectors. In the latter, a parametrization of the signals is expressed as a function of the air shower macro parameters, e.g. the depth of shower maximum X_{\max} or the muon content relative to a reference model R_{μ} .

As shown in Fig. 9, the universality method allows us to reconstruct an unbiased X_{\max} with an energy dependent resolution of $\sim 50 \text{ g/cm}^2$ to $\sim 20 \text{ g/cm}^2$, with a spread smaller for iron induced showers as compared to proton induced ones, when using only non saturated events. The same conclusion can be drawn for R_{μ} : the resolution in the relative number of muons stays below 10% at all energies if saturation is cured.

An engineering array of 12 stations has been deployed in the field and has been taking data since few months [6]. In Fig. 10 we show the lateral distribution of one of the measured events, reconstructed with $E = 1.59 \times 10^{19} \text{ eV}$ and arrival direction $\theta = 16^\circ$. For the station closest to the shower core (here at 153 m) both the saturated signal from the LPMTs and the full signal from the

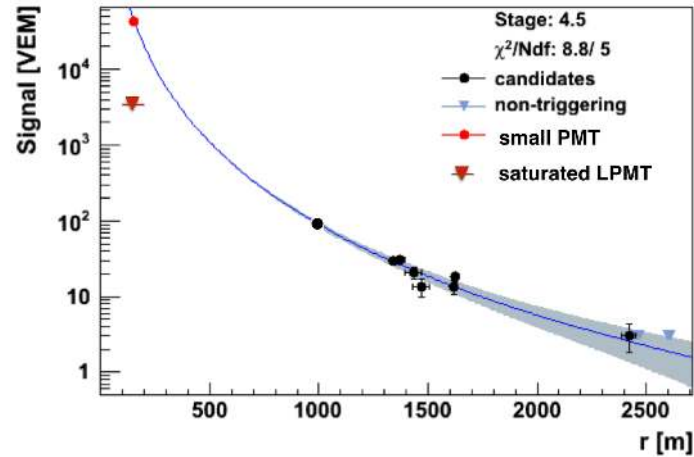


Figure 10: Lateral distribution for one event measured in the engineering array of AugerPrime. The signal in the station closest to the shower core (153 m) is recorded by the SPMT (red point); the signal in the LPMTs is saturated (red triangle).

SPMT are shown.

4. Summary

The dynamic range of the AugerPrime upgrade of the Pierre Auger Observatory has been extended to particle densities as high as few thousand per m^2 , thus allowing us to measure full signals from all the stations of the air shower footprints at the ground down to a distance of about 250 m from the shower core.

A small diameter PMT has been added to this aim in the water-Cherenkov detectors, while a PMT with suitable range has been chosen for the scintillators. They have been deployed in the engineering array of AugerPrime and their data are now under scrutiny. The first results confirm the effectiveness of the choice and the expected behaviour of the measurements.

References

- [1] D. Veberič (Pierre Auger Coll.), *Estimation of Signal in Saturated Stations of Pierre Auger Surface Detector*, Proc. 33rd Int. Cosmic Ray Conf., Rio de Janeiro, Brasil, arXiv:1307.5059.
- [2] The Pierre Auger Collaboration, *The AugerPrime Design Report*, arXiv:1604.03637.
- [3] T. Suomijarvi, for the Pierre Auger Collaboration, *The AugerPrime electronics*, these Proceedings.
- [4] D. Heck, J. Knapp, J.N. Capdevielle *et al.*, *CORSIKA: a Monte Carlo code to simulate extensive air showers*, FZKA 6019 (Forschungszentrum, Karlsruhe, 1998).
- [5] M. Ave, M. Roth, and A. Schulz, *A universal description of temporal and lateral distributions of ground particles in extensive air showers*, Proc. 34th Int. Cosmic Ray Conf., The Hague, Netherlands, PoS (2015) 378.
- [6] Z. Zong, for the Pierre Auger Collaboration, *The first results from the AugerPrime Engineering Array*, these Proceedings.



Scintillator detectors of AugerPrime

Radomír Šmída^{*a} for the Pierre Auger Collaboration^b

^aKarlsruhe Institute of Technology (KIT), Karlsruhe, Germany

^bObservatorio Pierre Auger, Av. San Martín Norte 304, 5613 Malargüe, Argentina

E-mail: auger_spokespersons@fnal.gov

Full author list: http://www.auger.org/archive/authors_icrc_2017.html

As part of the upgrade of the Pierre Auger Observatory, called AugerPrime, scintillator detectors will be mounted on top of all water-Cherenkov detectors (WCDs) of the surface array. By combining the data from WCDs with those of scintillator surface detectors (SSDs), we can derive information needed to reconstruct the energy and composition of cosmic rays at energies higher than those reached by the Auger fluorescence telescopes. In this contribution, the mechanical structure of the SSDs and their optical properties are discussed. We also present novel techniques used in the construction of the prototype detectors deployed in the Engineering Array. The efficiency and light output of these detectors were measured using cosmic-ray muon tomography, providing an absolute calibration of the detectors at the same time. We have achieved $\pm 10\%$ uniformity in the signal for particles impinging on any given detector at various impact points.

*35th International Cosmic Ray Conference — ICRC2017
10–20 July, 2017
Bexco, Busan, Korea*

*Speaker.

1. Introduction

Information on the composition of cosmic rays, particularly at the highest energies, is of primary interest. Further studies of the origin and properties of the most energetic subatomic particles in the universe are substantially limited by the lack of composition information. Furthermore, the measurement of the fraction of protons is important for estimating the physics potential of existing and future cosmic-ray, neutrino, and gamma-ray detectors [1]. The composition has been studied up to the flux suppression region, i.e. $\sim 4 \times 10^{19}$ eV, with the fluorescence detector (FD) [2] of the Pierre Auger Observatory [3]. To provide statistically significant composition information about primary particles in the flux suppression region, the Observatory is being upgraded with scintillator surface detectors (SSDs) and new electronics in water-Cherenkov detectors (WCDs) [1].

The SSD will provide a complementary measurement of extensive air shower particles to the data collected with the existing surface detector (SD). The sampling of secondary particles with two detectors having different responses to muons and electromagnetic particles is required to achieve accuracy on the composition comparable to the FD data. The design chosen for the SSD consists of a flat plastic scintillator positioned on top of every WCD. This design was selected because such a detector is reliable, low maintenance and cost effective. The area of the scintillator inside the SSD is 3.8 m^2 in order for the statistical uncertainty to be comparable to that of the WCD.

The technical requirements on the SSD are manifold. The detector must be lightweight to avoid excessive stress on the plastic tanks installed in the Argentine Pampa for more than a decade. The total weight of one complete SSD is about 120 kg, which satisfies this requirement. The detector must be durable to withstand the harsh environment for at least seven years and of negligible maintenance. No complex production steps are desired and the same holds for the transportation and deployment.

Aluminum alloys have been selected as the most optimal material for the enclosure box, sun-roof and support frame of the SSD, because they satisfy the criteria described above and they have good corrosion resistance and strength. In addition, a custom profile can be easily extruded from aluminum alloy.

A drawing and a picture of the SSD on top of a WCD are shown in Fig. 1. The position of the SSD allows easy access to the dome housing the SD electronics and also to the SD photomultiplier tubes (PMTs).

2. Enclosure box

As can be seen in Fig. 2 the enclosure box is composed of a frame profile, an aluminum composite panel and a top sheet. These components, made primarily from aluminum, make a water-tight housing for plastic scintillator bars, fibers and a PMT with electronics.

The frame profile is custom extruded and its double wall structure provides additional strength for the module and the place for installing closed-end blind rivets. Each wall is 83 mm high and 2 mm thick and the space between two walls is 26 mm. The thickness of the top part of the rectangular profile is 2 mm and 3 mm at the bottom. The bottom part of the extruded profile frame protrudes inward 30 mm and supports the aluminum composite panel. Four beams, two 3800 mm

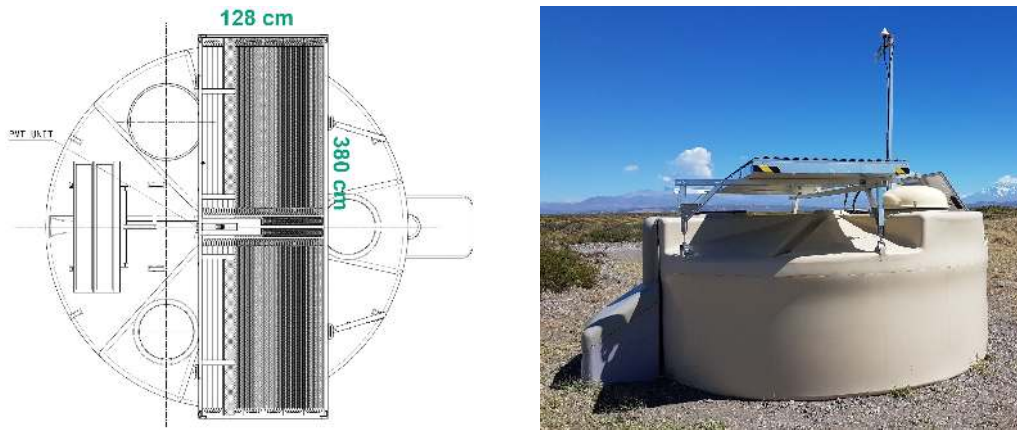


Figure 1: Drawing of an open SSD on top of a WCD (*left*) and a photo of one installed SSD (*right*).

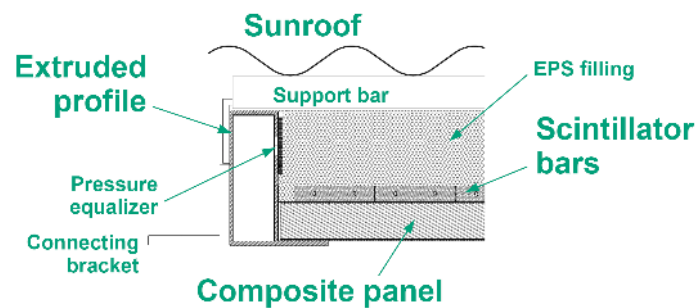


Figure 2: Side-view cut in the drawing of the SSD. Main parts are marked.

and the other two 1280 mm long, are connected in two ways depending on the assembly site: corner inserts and nails are used in the first case and corners are welded in the second case.

The composite panel has two 1 mm thick aluminum sheets glued to a 22 mm thick block of extruded polystyrene (XPS). The panel is glued to the frame with Ottocoll S610, which acts also as a sealant. The panel not only increases the structural integrity, but its flat area is convenient for placing components inside the box during assembling. Four aluminum U-beams fix the scintillator bars from above and lightweight blocks of expanded polystyrene (EPS) are used to fill the space.

The air volume inside the detector is reduced to less than 10 liters this way and a top sheet is supported from below. The exchange of air between the outside and the inside of the detector is achieved via a couple of holes at the bottom of the profile frame and one hole in the inner wall of the profile. The latter hole has a diameter of 12 mm and is covered with a round piece of sintered metal. This system acts as a pressure equalizer.

The top of the box is closed with a 1 mm thick aluminum sheet. This top sheet is glued to the frame profile with the same glue as the panel and in addition, the connection is reinforced with closed-end blind rivets. Even though the first shipment of SSDs had experienced acceleration up to 15 g during transportation, these acceleration shocks had caused no damage.

3. Sunroof

The main purpose of the sunroof is to deflect sunlight and keep excursions of the temperature inside the detector below 50°C as can be seen in the top graph in Fig. 7. The sunroof is made from corrugated sheets and the air flow under it provides passive cooling, keeping the SSD at around the temperature of the ambient air.

The roof is riveted to six support bars fixed on top of the enclosure box. These six rectangular beams are connected to the frame with angles riveted to the outer wall and they are also glued to the top sheet. The beams support the sunroof and in addition they hold and reduce any vibration of the almost 5 m² large top sheet.

4. Support frame

The support frame holds the SSD in the horizontal position on top of the SD. It must be adjustable enough to compensate for deformations of the plastic tanks standing on the sandy ground for more than a decade. It is made from aluminum beams and can be easily assembled. Two shorter beams are fixed to the main beam and this structure is supported by four legs connected to lifting lugs molded into the plastic tank.

The enclosure box is placed on top of the already mounted support frame with a jib crane installed on a pickup truck. The box has two brackets riveted to its two long sides and it is going to be fixed with screws to the support frame in these four positions. The installation procedure takes only about ten minutes. An SSD installed on WCD is shown in the right picture in Fig. 1

5. Scintillators and fibers

The active area of the detector is made from extruded scintillator bars produced at the Fermi National Accelerator Laboratory, USA [4]. Each bar is 1600 mm long, 50 mm wide and 10 mm thick. There are 48 pieces in an SSD distributed equally between two wings. Two bean-shape holes are inside each bar at the distance of 25 mm from each other. A TiO₂ layer with a typical thickness of 0.25 mm is co-extruded on the bar. This outer layer protects bars from damage during handling, prevents cross talk between bars and due to its high diffuse reflectivity increases the collected signal. The total area of the scintillators is 3.8 m². The emission lines of the scintillator material lie between 330 and 480 nm, but all light emitted below 400 nm is attenuated within a 10 mm path length of the scintillator.

Plastic wavelength shifting (WLS) fibers are used to collect sufficient light signal. The total length of each fiber is about 5.8 m. The fiber Kuraray Y11(300)M, S type of 1 mm diameter is used in the SSD [5]. The absorption spectrum of this WLS fiber matches the emission spectrum of the scintillator material. The light emitted by the fiber has wavelengths above 450 nm.

The fiber is pushed through one of the holes in a scintillator bar and guided in a router to a hole in another scintillator bar. The second hole is at a distance of 100 mm from the first hole to comply with the recommended minimum bending diameter for low light loss due to bending and long term reliability. This U-turn is shown in Fig. 3. In the center of the SSD all the fibers are guided in routers and collected in a bundle in a cookie, a housing made from PMMA, where

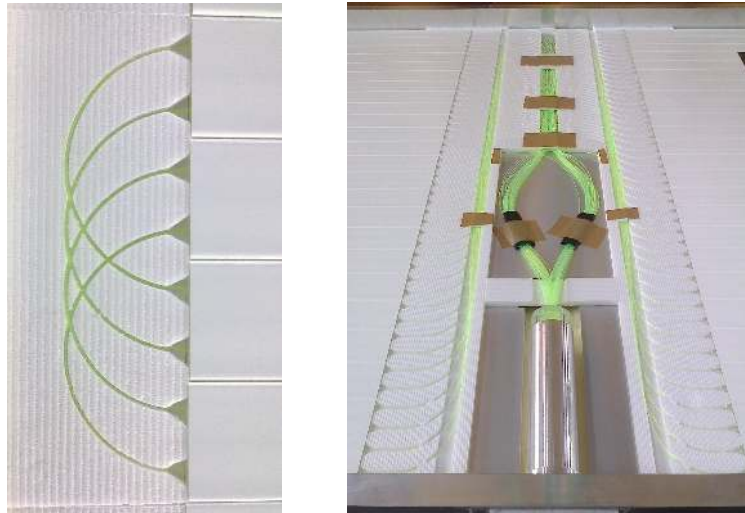


Figure 3: Routers for guiding and protecting fibers on the side (*left*) and in the center (*right*).

both ends of each fiber end. The length of the fiber between the scintillator bar and the cookie is about 1.1 m, see the right picture in Fig. 3. Therefore, only photons with the wavelength above ~ 500 nm survive the whole path, because of their sufficiently long attenuation length. Owing to the guiding in routers, no significant light loss due to bending happens in any part of the fiber over its whole length. The routers also keep fibers in their position and reduce the risk of damage during subsequent procedures.

Almost one half of light is lost, if a fiber's end surface is not finished after cutting. A novel method has been developed for finishing the 96 ends of plastic WLS fibers already installed in the SSD. This procedure is based on melting each end of a fiber on a borosilicate glass plate warmed to $150 \pm 30^\circ\text{C}$. The end of the fiber, held by hand, is touched for about one second to the glass plate. Its surface slightly melts and flattens. The advantages of this procedure are as follows: easy and simple, the required time for melting can be checked visually¹ and any defect (e.g. a bubble due to a too long contact with the plate) can be repaired by cutting a small piece of the fiber and repeating the procedure. In Fig. 4 the end of a fiber before and after melting is shown. We have verified that the fiber finished with the melting method provides within 10% the same amount of light as a carefully polished fiber. This new procedure is less labor intensive than polishing all 96 ends of the fibers glued in the cookie at once.

The ends of all fibers are bundled in the cookie, which has a body and front window made of PMMA. The hole for fibers in the center of the PMMA body has a diameter of 13 mm and two smaller holes along it for filling optical cement and allowing air to escape. The fiber ends are aligned 1 – 2 mm in front of the window which is pushed into the main body. This front window has a diameter of 22 mm and a thickness of 6 mm, and it will protect the ends of the fibers and act as a diffuser. At the end, the optical cement (we use Eljen EJ-500) is poured inside – slowly, to avoid air bubbles forming in front of the fibers.

¹A clear decrease in the amount of side-scattered light can be observed during the melting of a fiber. Side-scattering is caused by surface roughness after cutting a fiber.

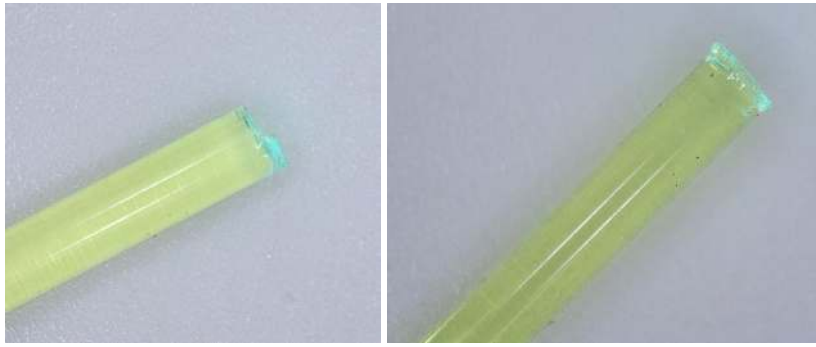


Figure 4: A fiber's end after cutting (*left*) and after finishing with the melting procedure (*right*).

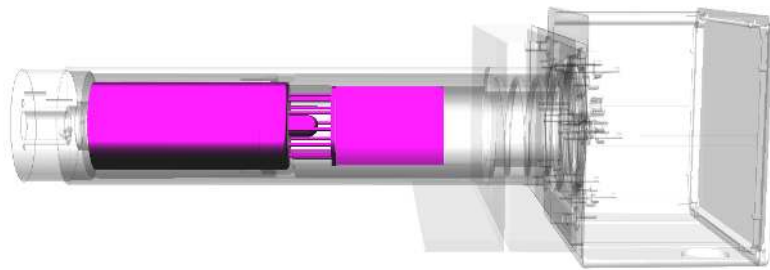


Figure 5: The housing of a PMT. The PMMA cookie in the front of the aluminum tube and the PMT with the integrated HVPS are highlighted, visible are also the spring and flange with connectors and the protection box on the right side. Cables are not included here.

6. Photomultiplier tube

A photomultiplier tube (PMT) measures the signal delivered from the scintillators with fibers. The main candidate for the PMT is the model Hamamatsu R9420. It is a 1.5" PMT with a standard bialkali photocathode and a quantum efficiency of about 18% at the wavelength of 500 nm. The dynode chain has eight stages. The PMT provides the required linearity range at the operating PMT gain $\sim 7 \times 10^5$ [1, 6, 7]. The high voltage power supply (HVPS) is based on a custom-made design manufactured by the ISEG company. As a backup, the PMT ET Enterprises 9902B is considered. The PMT signal will be read out with the upgraded SD electronics presented in [1, 8].

An important design criterion on a PMT module was the ability to remove the PMT from the SSD. This has been accomplished by housing the PMT, the HVPS and accompanying electronics in a PVC tube. The PVC tube can be easily installed and removed from the aluminum tube, which is permanently fixed in the profile frame, see Fig. 5 and the bottom of the right picture in Fig. 3. The PMT is pressed with a spring to the cookie, where a silicone pad makes an optical connection which also distributes any pressure over the entrance glass window of the PMT. The inner volume of the aluminum tube is closed with a flange equipped with an SMA and multipole connector for an analog signal and a slow control cable, respectively. The weather protection of the connectors is guaranteed by an aluminum cover box.

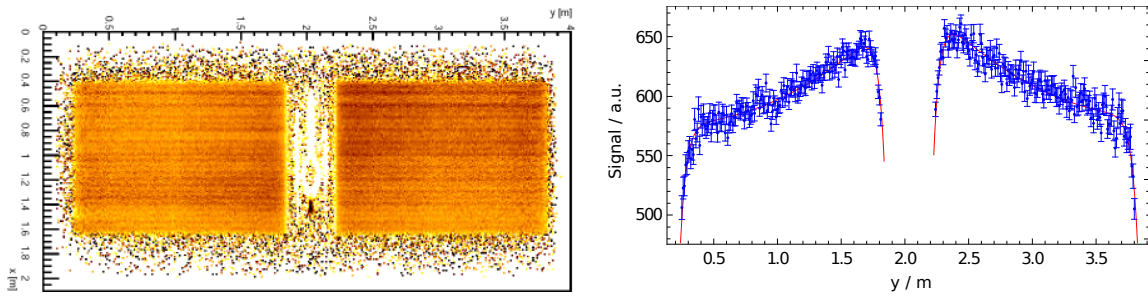


Figure 6: *Left:* Logarithm of the signal charge measured in the muon telescope. Individual scintillator bars and bundles of fibers in the center can be recognized. Compare with the right picture in Fig. 3. *Right:* The signal measured for MIPs along the long axis of scintillator bars for two halves of the SSD. The PMT is located at $y = 2$ m.

7. Testing

Tomography with cosmic-background muons has been used to test all assembled SSDs, see Fig. 6. The spatially sensitive muon telescope used for this purpose came from the KASCADE experiment [9]. It consists of three $2\text{ m} \times 4\text{ m}$ plates vertically separated by 1 m. A spatial resolution of ~ 10 mm can be achieved for a particle measured in all three layers. Some detectors were studied in multi-day runs and these data allow a detailed study of the signal from individual fibers.

The charge of a single photoelectron and a minimum ionizing particle (MIP) have been measured in the same configuration for all SSDs. From these two charges, the number of photoelectrons (p.e.) has been calculated for each MIP and converted to a vertical-equivalent MIP (VMIP). The fit of measured signals with the Gaussian function gives 30 ± 2 p.e./VMIP, while the mean signal is 37 p.e./VMIP.

Due to the U-turns of the fibers and their sufficient length outside of the scintillator bars, the uniformity of the measured signal is $\pm 5\%$ along bars and $\pm 10\%$ between bars for MIPs depositing signal at any position of the detector, see the right picture in Fig. 6. We can conclude that the response of the detector will be uniform for all measured particles of an extensive air shower.

The length and shape of pulses have also been studied. The signal is wider and narrower at the close and far end of the detector, respectively. The attenuation length of the light in a fiber is $\lambda = 312 \pm 3$ cm and the effective index of refraction is $n \simeq 1.76$.

Results of the measurements have been fully implemented in our Offline framework [10].

8. Performance and Conclusions

Twelve scintillator detectors were deployed in the Engineering Array in the middle of September 2016 and have been taking air shower data since October of the same year. Due to the deployment in an easily accessible part of the Observatory, six detectors were installed during one day. No issue with either mechanics or performance has been noticed after almost half a year and all SSDs fulfill our requirements. The SSDs have provided first results, which have been presented in [11].

Each SSD is equipped inside with two temperature sensors and a humidity sensor. As can be seen in the top graph in Fig. 7, the temperature inside the enclosure box closely follows the air

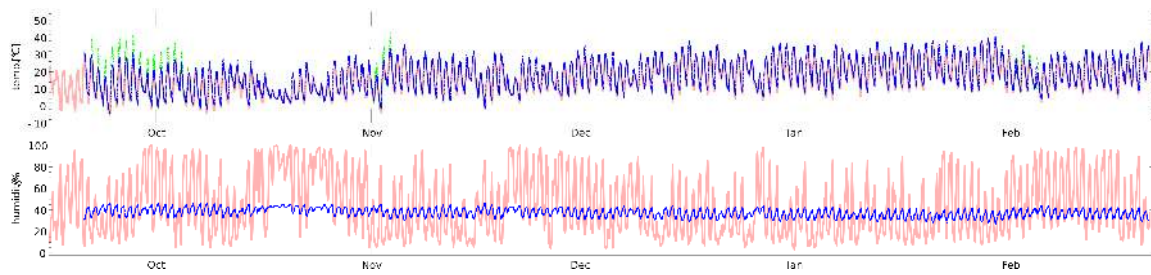


Figure 7: *Top:* Temperatures inside and outside an SSD (measured in the shade) are shown in blue and red color, respectively. Green points correspond to temperatures in direct sunlight. *Bottom:* Humidities inside and outside an SSD are shown in blue and red color, respectively.

temperature measured in the shade and only rarely exceeded 40°C . The evolution of the humidity can be seen in the same figure. The humidity has been slowly decreasing from the original value of $\sim 40\%$, see the bottom graph in Fig. 7.

The SSDs for the AugerPrime will be produced in different facilities around the globe. On average, about one SSD can be produced at each facility per day, which is sufficient to produce all detectors for AugerPrime within the next two years.

References

- [1] Pierre Auger Collab., Preliminary Design Report, arXiv:1604.03637.
- [2] Pierre Auger Collab., Phys. Rev. D 90 (2014) 122005.
- [3] Pierre Auger Collab., Nucl. Instrum. Meth. A 798 (2015) 172.
- [4] A. Pla-Dalmau *et al.*, FERMILAB-Conf-03-318-E.
- [5] <http://kuraraypsf.jp/psf/ws.html>
- [6] D. Martello, for the Pierre Auger Collaboration, PoS (ICRC2017) 383.
- [7] A. Castellina, for the Pierre Auger Collaboration, PoS (ICRC2017) 397.
- [8] T. Suomijarvi, for the Pierre Auger Collaboration, PoS (ICRC2017) 450.
- [9] P. Doll *et al.*, Nucl. Instrum. Meth. A 488 (2002) 517.
- [10] D. Schmidt, for the Pierre Auger Collaboration, PoS (ICRC2017) 353.
- [11] Z. Zong, for the Pierre Auger Collaboration, PoS (ICRC2017) 449.



First results from the AugerPrime engineering array

Zizhao Zong^{*a} for the Pierre Auger Collaboration^b

^a*Institut de Physique Nucléaire d'Orsay, IN2P3-CNRS, Université Paris-Sud, Université Paris-Saclay, 91406 Orsay Cedex, France*

^b*Observatorio Pierre Auger, Av. San Martín Norte 304, 5613 Malargüe, Argentina*

E-mail: auger_spokespersons@fnal.gov

Full author list: http://www.auger.org/archive/authors_icrc_2017.html

The surface detector array of the Pierre Auger Observatory consists of 1660 water-Cherenkov detectors (WCDs) which sample the charged particles and photons of air showers initiated by cosmic rays of very high energy. With the AugerPrime upgrade, the collaboration aims to increase the particle identification capability of the surface detectors. Scintillator surface detectors (SSDs) will be added above the water-Cherenkov detectors and the stations will be equipped with new electronics having better timing accuracy, higher sampling frequency, and increased processing capability. Furthermore, small photomultipliers will be added to the WCDs to allow for an increase of the dynamic range of the signal readout. In October 2016, an engineering array consisting of 12 AugerPrime detector stations was installed within the existing array of the Observatory.

In this contribution, we will discuss the first results from the AugerPrime engineering array. In particular, the detector calibration in units of vertical equivalent muon (VEM) for WCD and minimum ionizing particle (MIP) for SSD. Furthermore, we will discuss the temperature dependence of the detector parameters, show the lateral distribution function of showers measured with both detector types, and present the preliminary results of the study on signals from doublet stations.

*35th International Cosmic Ray Conference — ICRC2017
12–20 July, 2017
Bexco, Busan, Korea*

*Speaker.

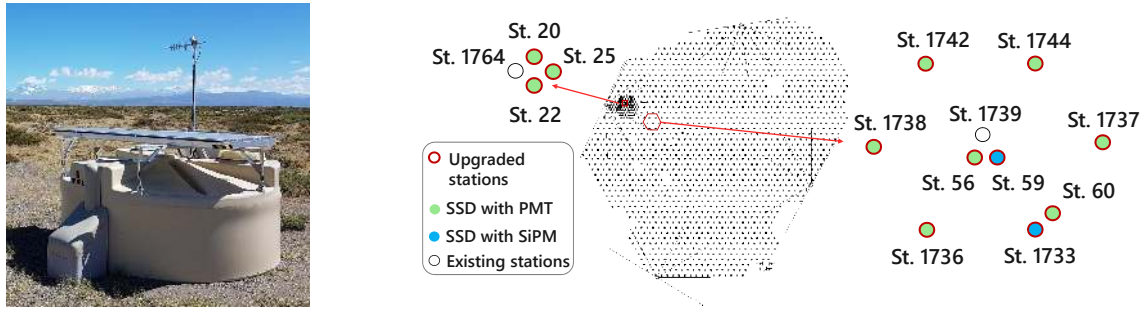


Figure 1: *Left:* Photograph of an AugerPrime surface detector (St. 56) in operation. *Right:* Layout of the AugerPrime engineering array. Several groups of multiplet stations are deployed in the EA: stations (1739,56, 59), (1733, 60), and (1764, 20, 22, 25).

1. Introduction

The Pierre Auger Observatory [1], located in western Argentina, near the city of Malargüe in Mendoza province, at a high altitude of 1400 m a.s.l., aims to probe the origin and characteristics of ultra-high-energy cosmic rays (UHECR). The Observatory combines four fluorescence detector (FD) sites consisting of 27 fluorescence telescopes and a surface detector (SD) array consisting of 1660 water-Cherenkov detectors (WCD), each of which has three 9" photomultiplier tubes (PMT), covering 3000 km² to achieve a hybrid detection of the Extensive Air Showers (EAS) produced by UHECRs in the atmosphere. In the last decade, several important results have been obtained by the Observatory [2].

By proposing the AugerPrime project [3, 4], the Auger collaboration aims to upgrade the Observatory for shower-by-shower measurements of the mass composition of cosmic rays at the highest energies. The AugerPrime implementation for the SD detectors includes three main elements:

- 1 Scintillator surface detectors (SSD) of ~ 3.8 m² will be mounted above the existing WCDs (see Fig.1 left). Each SSD is composed of 48 extruded plastic scintillator bars, which are read out by wavelength-shifting (WLS) fibers coupled to a single photo-detector [5].
- 2 Upgraded electronics with better timing accuracy (~ 5 ns), higher sampling frequency (120 MHz), and increased processing capability will be employed for upgraded surface detector stations (WCD + SSD) [6].
- 3 A small PMT (SPMT) will be added to each WCD. It will work together with the three large PMTs to extend the dynamic range of the WCDs [7].

The AugerPrime engineering array (EA) of 12 upgraded detectors was deployed in October 2016 and has been since then continuously taking data. Fig. 1-right shows the layout of AugerPrime EA. Nine upgraded stations are located in a hexagon shape surrounding the existing SD station 1739 in the regular SD array (1500 m spacing). Three upgraded stations are deployed in the so-called AERAlet area near the station 1764 (433 m spacing). Some stations are deployed close to each other (with 11 m spacing) as doublet or multiplet stations for signal accuracy and other studies (see Fig. 1 right).

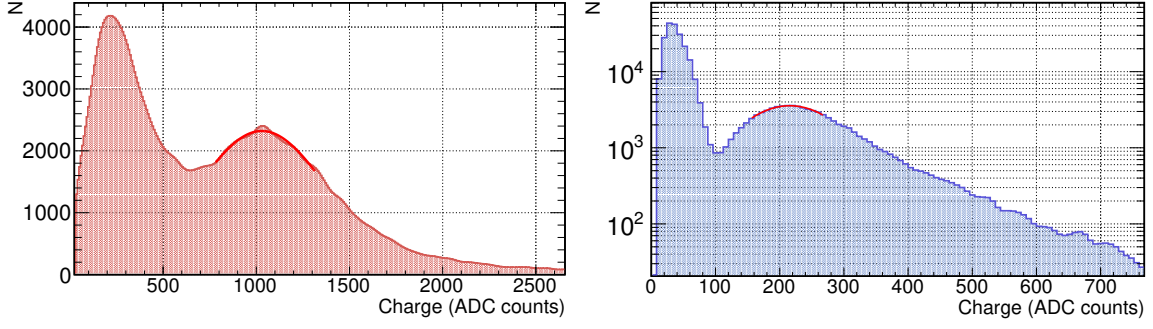


Figure 2: *Left:* The VEM charge spectrum measured by one of the WCD PMTs. The second peak corresponds to the charge deposited by single muons traversing the detector station. *Right:* The MIP charge spectrum from the SSD PMT.

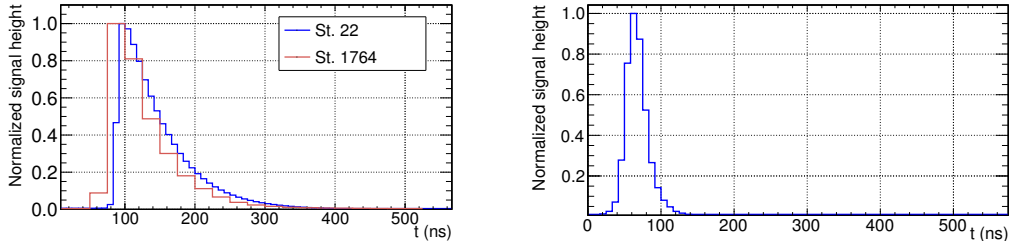


Figure 3: *Left:* Comparison of muon signal shapes from the existing station 1764 and the upgraded station 22. The signals are normalized by their signal heights. *Right:* The muon signal shape from a SSD PMT.

In this paper, we present the first results from the AugerPrime engineering array. In particular, we will discuss the calibration and the operation status of WCD and SSD detectors, the shower signals from both detector types, and the signal accuracy obtained with the doublet stations.

2. Calibration and operation status of the detectors

In the WCD calibration, the main measured parameter is the average charge deposited by an incident vertical, central muon passing through the WCD [8]. This parameter can be obtained from the charge spectrum of background muons measured by each PMT in the WCD (see Fig. 2-left). In the muon charge spectrum, the second peak is induced by the muons crossing the WCD from all directions. By fitting the peak position, the approximate charge value of a vertical equivalent muon (VEM) can be determined. Based on simulations and measurements with test-detectors, the final VEM charge used in the detector calibration is determined with $Q_{\text{VEM}} = Q_{\text{VEM}}^{\text{raw}}/1.01$, where 1.01 is the factor of the conversion from omni-directional to vertical muons.

For the SSDs, the charge deposited with a minimum ionizing particle (MIP) is used for the calibration (see Fig. 2-right). The *raw MIP charge* is obtained by fitting the second peak position in the muon spectrum from SSD and the final MIP charge is determined with $Q_{\text{MIP}} = 0.87 Q_{\text{MIP}}^{\text{raw}}$, where 0.87 is determined based on related measurements and simulations [5, 9].

The muon charge spectra from both WCDs and SSDs are stored in the muon buffer of each

local station and sent to the central data acquisition system (CDAS) every 6 minutes. The signals of shower events from the detectors are calibrated based on the real-time muon spectra.

The average signal shapes of background muons from WCDs and SSDs are also recorded and sent to CDAS (see Fig. 3). Various quantities to evaluate the detector performance can be parameterized from the digitized average signal shapes. The PMTs have a fast response to a single muon, dominated by the Cherenkov light reflected only once at the tank liner. After reaching the peak, the signal exponentially decays due to the losses in consecutive multiple reflections and absorption in water, since the decay time of the muon signals in WCDs is related to the reflection coefficient of the liner and to the transparency of the water in each WCD.

Among the 1660 SD stations, the average value of muon decay time is around 60 ns (distributed between 50 to 70 ns). The area-over-peak (AoP) ratio of the muon signal, proportional to the signal width, is introduced to describe the detector performance and is available from the detector in real-time. Previous studies by the Auger collaboration have shown the long-term evolution of AoP and its importance for detector monitoring [10]. For the current SD stations, the average value of AoP is around 3.5, or in time units, around 88 ns. In the upgraded stations with new faster electronics (120 MHz) we see essentially the same AoP ratios of around 10.5 which corresponds to 88 ns in time units.

The muon signal shape in SSD is narrow since the plastic scintillator bars with a thickness of 1 cm have a fast time response and a good time resolution for the measurement of background muons. In this work, the width (FWHM) of the SSD muon signal is used to monitor the detector performance. From the experimental data, the average value of muon signal width is ~ 35 ns for all SSDs.

In the observatory area, the day-night temperature variation is around 20°C . Fig. 4 shows the related parameters introduced above from the station 20 together with the temperature measured in the CLF (central laser facility) as a function of time over the first week of May 2017. From the plots, we can see that the day-to-night fluctuations of these detector parameters affected by the temperature are: $<3\%$ for VEM charge, $<5\%$ for MIP charge, $\sim 1\%$ for area-over-peak from WCD and ~ 3 ns for the FWHM of SSD muon signals. Concerning the WCD, similar variation

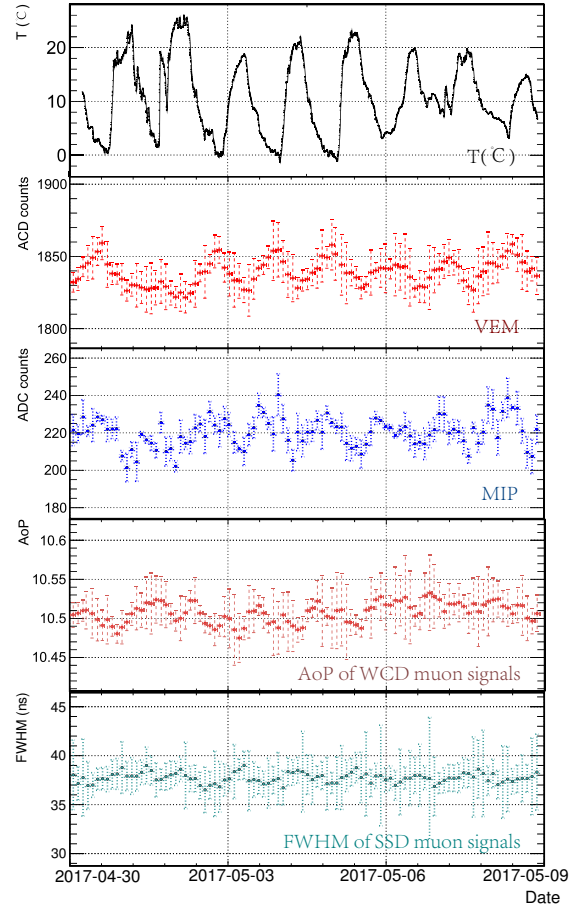


Figure 4: The operation quantities of the detector are affected by the temperature in the field. With the day-to-night temperature fluctuation of $\geq 20^\circ\text{C}$, the detector operates in the good stability with an acceptable variation of calibration and signal properties.

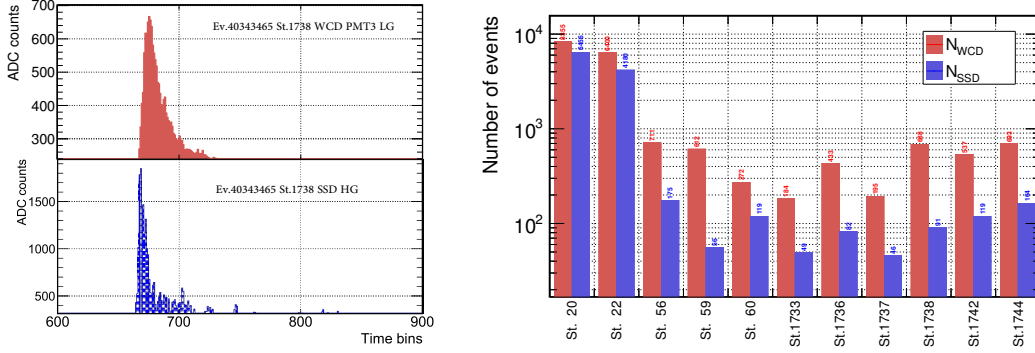


Figure 5: *Left:* The WCD and SSD signals of station 1738 for the same event. *Right:* The summary of the event numbers in all EA stations.

was reported for the existing detectors [10]. Since for both detectors, the calibration is performed nearly continuously, the temperature dependence does not affect the data.

3. Shower signals from AugerPrime stations

The two detector types have different responses to the electromagnetic (EM) and muonic components of the EAS. Their signals in VEM or MIP units are highly related to the EM energy flux and the muonic flux at ground level. Therefore, signal densities sampled in the same position with WCD and SSD are essential for the determination of the muonic shower component, which is crucial for primary particle identification.

3.1 Signals from WCD and SSD for detected showers

Currently, for the detection of shower events in each station the SSD is triggered by the WCD. Fig. 5 shows the signals of WCD and SSD from station 1738 for the same event. The main signal in WCD spreads relatively longer than the one in SSD due to the multiple reflections of the Cherenkov light in the water tank. With the SSD signals, we can clearly see the particles which arrived later than the main flow of secondary particles produced in the EAS development.

During the operation of EA, more than 8000 shower events were recorded. Fig. 5 shows the number of WCD and SSD events in each station. We can see that in the station 20 and 22, which are in the AERAlet area (433 m spacing), have much higher trigger rate than the others, which are deployed in the regular SD array area. As we have been maintaining and optimizing the detectors in the last few months, some of the stations were not working with a full duty cycle. The number of events recorded by EA stations have slight differences but are comparable with the event numbers from stations near by. As the active SSD area is much less than the WCD area (about two fifths), the trigger rate of the shower events for SSDs is relatively less than it is for WCDs. The area of detectors also affects the signal amplitudes of each shower event. For most events, the signal ratio of S_{SSD}/S_{WCD} is less than 1 (average ratio around 0.65). However, for a given shower, the correlation of S_{SSD} and S_{WCD} depends on the distance from the station to the shower axis. The related results are shown in the next section.

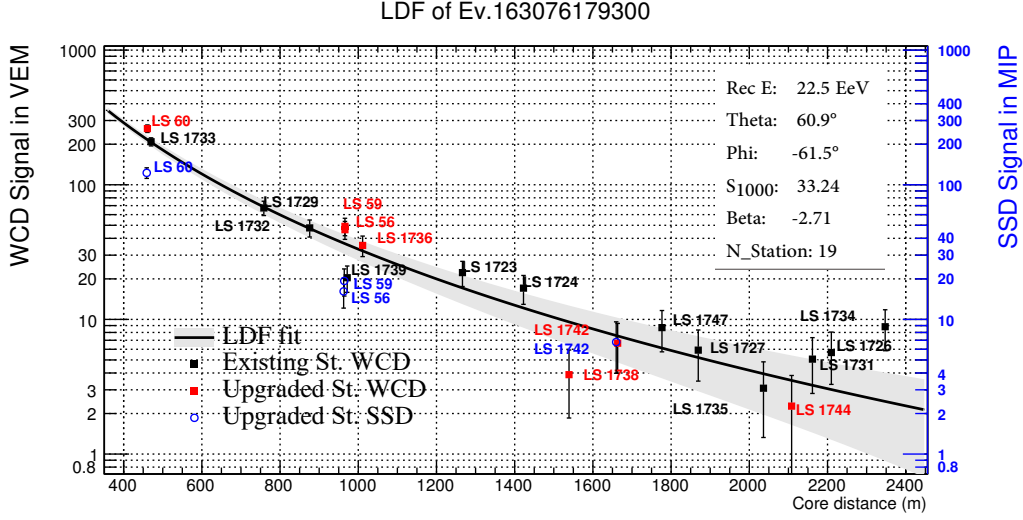


Figure 6: Signals from upgraded local stations (LS) compared to the LDF reconstructed from the existing local stations.

3.2 Signals from EA stations compared to the lateral distribution function

The events triggered by the SD array are first selected with the T4 and T5 triggers [11]. The arrival direction is obtained by fitting the start time of each SD signal to a spherical front. The shower core on the ground can be obtained from the fits of the SD signals. The lateral distribution function (LDF) of the air shower can then be described as a modified NKG function

$$S(r) = S(r_{\text{opt}}) \left(\frac{r}{r_{\text{opt}}} \right)^{\beta} \left(\frac{r + r_1}{r_{\text{opt}} + r_1} \right)^{\beta + \gamma} \quad (3.1)$$

where r_{opt} is the reference distance, $r_1 = 700$ m and the $S(r_{\text{opt}})$ is an estimation of the shower size. As the spacing of stations is 1500 m for the SD array, the r_{opt} is chosen to be 1000 m. For the in-fill array with the 750 m spacing, the r_{opt} is 450 m. Note that the parameters β and γ have some residual dependence on the zenith angle and the shower size.

Fig. 6 shows an example event with a primary energy of 22.5 EeV. For this event, 12 existing stations and 7 upgraded stations were triggered. The LDF in the plot is fitted with signals from the existing stations. As can be seen in Fig. 6, WCD signals from upgraded stations are in good agreement with this LDF curve, and SSD signals are relatively lower than WCD signals, as expected.

The global LDF corresponding to the signals from upgraded stations is shown in Fig. 7. Signals from WCDs and SSDs normalized by the shower size are plotted as a function of distance from the station to the shower axis. The LDF of S_{WCD} from upgraded stations agrees well with the LDF of $S_{\text{WCD-old}}$ from the existing stations. As expected, the LDF of S_{SSD} is higher than the LDF of S_{WCD} in the region close to the shower axis and then gets lower in the region further away. Correspondingly, the ratio of $S_{\text{SSD}}/S_{\text{WCD}}$ is observed to be larger than 1 for the region near the shower axis and then tends to be ~ 0.4 at large distances (>700 m). This can be understood as the effect of the SSD sensitivity to the EM components of the EAS and the relatively smaller area of SSDs.

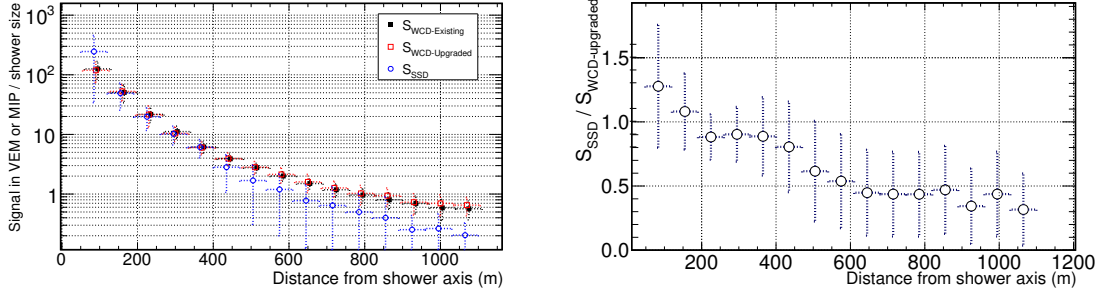


Figure 7: *Left:* The global LDF of signals from upgraded stations and existing stations. 3084 events reconstructed with the Auger 750 m array are selected for this analysis (Event selection: T4 events, ≥ 4 existing stations triggered, no saturation in the stations.) *Right:* The ratio of $S_{SSD}/S_{WCD-upgraded}$ as a function of distance from the shower axis.

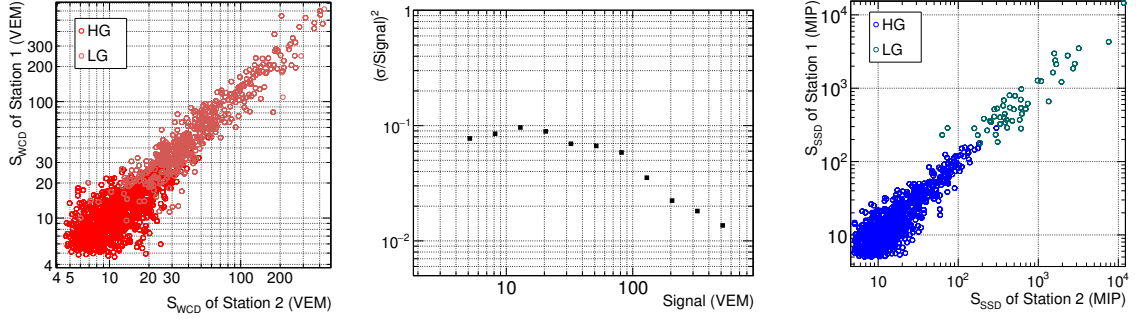


Figure 8: *Left and right:* The correlations of doublet WCD and SSD signals, respectively. *Center:* The measured WCD signal accuracy of upgraded stations with respect to the signal amplitude in VEM.

3.3 Signals from doublet stations

Some detectors in the EA area are deployed close to each other (spacing ~ 11 m) as doublet or multiplet stations. Since the footprint of a typical EAS extends over several km^2 , the signals from these multiplet stations can be regarded as measurements in the same point of the shower. The signal correlations of doublets for WCDs and SSDs are shown in Fig. 8. The S_{WCD} from each station in the doublet is corrected by the LDF to the mean distance of the doublet. This correction can reduce the bias due to the difference of a steep LDF over the 11 m distance. Good correlation can be seen for S_{WCD} from both high-gain (HG) and low-gain (LG) channels. For S_{SSD} , therefore, the doublet signals of small amplitudes (< 100 MIP) are in good agreement. Currently, there is no LDF fitted to S_{SSD} available for the doublet signal correction, the signal difference for the large signals (from LG channels) measured near the shower axis is relatively larger than that for the small signals.

A preliminary result from the study of signal accuracy is shown in Fig. 8-center. For the WCD signal of the upgraded stations, the signal accuracy is around 10%, which is comparable to the signal accuracy of the existing stations [12]. Further studies on signal accuracy will be performed with better statistics.

4. Summary

The AugerPrime engineering array has been taking data since October 2016. Detectors are calibrated with the charge of single VEM for S_{WCD} and single MIP for S_{SSD} . The upgraded stations with WCDs and newly deployed SSDs operate with good stability at the Auger site under a harsh environment with a day-to-night temperature fluctuation of $>20^{\circ}\text{C}$. Signals from EA stations are in a good agreement with the LDF curve fitted with signals from the existing stations. The global LDF for S_{WCD} from the upgrade stations, normalized by the shower size, agrees well with the results of the LDF fitted to the existing stations. Furthermore, the global LDF of S_{SSD} shows the SSD sensitivity to the EM components of the EAS as expected. The signals from doublet stations are well correlated and the measured signal accuracy for the WCDs of the upgraded stations is around 10%. Further studies with better statistics are currently under way.

References

- [1] Pierre Auger Collaboration, *The Pierre Auger cosmic ray observatory*, Nucl. Instrum. Meth. A 798 (2015) 172–213.
- [2] M. Unger, for the Pierre Auger Collaboration, *Highlights from the Pierre Auger Observatory*, these proceedings.
- [3] Pierre Auger Collaboration, *The Pierre Auger Observatory Upgrade-Preliminary Design Report*, (2016) arXiv:1604.03637.
- [4] D. Martello, for the Pierre Auger Collaboration, *The Pierre Auger Observatory Upgrade*, these proceedings.
- [5] R. Šmída, for the Pierre Auger Collaboration, *Scintillator detectors of AugerPrime*, these proceedings.
- [6] T. Suomijärvi, for the Pierre Auger Collaboration, *Upgraded electronics for AugerPrime*, these proceedings.
- [7] A. Castellina, for the Pierre Auger Collaboration, *The dynamic range of the AugerPrime Surface Detector: technical solution and physics reach*, these proceedings.
- [8] X. Bertou, for the Pierre Auger Collaboration, *Calibration of the surface array of the Pierre Auger Observatory*, Nucl. Instrum. Meth. A 568 (2006) 839–846.
- [9] D. Schmidt, for the Pierre Auger Collaboration, *AugerPrime implementation in the Offline simulation and reconstruction framework*, these proceedings.
- [10] R. Sato, for the Pierre Auger Collaboration, *Long Term Performance of the Surface Detectors of the Pierre Auger Observatory*, Proc. Int. Cosmic Ray Conf., Beijing, China, 3 (2011) 204–207.
- [11] Pierre Auger Collaboration, *Trigger and aperture of the surface detector array of the Pierre Auger Observatory*, Nucl. Instrum. Meth. A 613 (2010) 29–39.
- [12] P. Bauleo, for the Pierre Auger Collaboration, *The accuracy of signal measurement with the water Cherenkov detectors of the Pierre Auger Observatory*, Nucl. Instrum. Meth. A 578 (2007) 180–184.



AugerPrime implementation in the Offline simulation and reconstruction framework

David Schmidt^{*ab} for the Pierre Auger Collaboration^c

^aKarlsruhe Institute of Technology (KIT), Institut für Kernphysik, Karlsruhe, Germany

^bInstituto de Tecnologías en Detección y Astropartículas, Buenos Aires, Argentina

^cObservatorio Pierre Auger, Av. San Martín Norte 304, 5613 Malargüe, Argentina

E-mail: auger_spokespersons@fnal.gov

Full author list: http://www.auger.org/archive/authors_icrc_2017.html

The Pierre Auger Observatory is in the process of upgrading its surface detector array by placing a 3.84 m² scintillator atop each of the existing 1660 water-Cherenkov detectors. The differing responses of the two detectors allow for the disentanglement of the muonic and electromagnetic components of air showers, which ultimately facilitates reconstruction of the mass composition of ultrahigh-energy cosmic rays on an event-by-event basis. Simulations of the scintillator surface detector enable both an assessment of proposed reconstruction algorithms and the interpretation of real shower measurements. The design and implementation of these simulations within a Geant4-based module inside Auger's software framework (Offline) are discussed in addition to the tuning of these simulations to prototype-detector measurements performed using a muon telescope. Augmentations of the Offline framework in order to accommodate a large-scale detector upgrade are also summarized.

35th International Cosmic Ray Conference — ICRC2017
10–20 July, 2017
Bexco, Busan, Korea

*Speaker.

1. Introduction

The primary objective of the AugerPrime upgrade [1] is to install the additional detector hardware necessary to estimate the composition of ultrahigh-energy cosmic rays on an event-by-event basis. The aim is to provide measurements allowing for the separation of signal contributions from the muonic and electromagnetic shower components at Earth's surface. A better handle on the magnitude of the electromagnetic signal will enhance the precision and accuracy in reconstructing primary energies, whereas the more directly measurable observable of the number of muons reaching the ground will allow for an estimation of the primary mass. The auxiliary detector technology chosen to provide the necessary measurements is the scintillator, of which one will be placed on top of each water-Cherenkov detector in the 3000 km² array. Multiple reconstruction algorithms capitalizing on the differing responses of the two types of detectors have demonstrated their joint capacity to disentangle shower components. Detector simulations are necessary in assessing and providing the parameterizations for such algorithms in addition to interpreting the real measurements. Such simulations have been implemented in the *Offline* simulation and reconstruction framework [2], which has also been adapted and outfitted with new machinery necessary in accommodating a large-scale detector upgrade.

A surface scintillator detector (SSD) consists of 48 plastic scintillator bars distributed between two symmetric modules covering a combined area of 3.84 m². The two modules are housed within a common polystyrene casing, which in turn is encapsulated within an aluminum box. Wavelength-shifting optical fibers route photons from the scintillator bars to a 1.5 inch Hamamatsu R9420 PMT situated between the two modules. For a schematic representation of the SSD design, see Figure 1a.

2. Simulations

At the core of the SSD simulations lies the use of real detector measurements and parameterizations obtained therefrom where possible. Where measurements of a desired quantity are not possible or can not be obtained, for instance the energy deposit of crossing particles during simulation, the latest version of the field-standard simulation software, Geant4 [3] has been employed.

2.1 Detector construction and particle injection

Auger's *Offline* development team has upgraded the software to incorporate the latest release from the Geant4 collaboration, version 4.10. The volumes for the SSD are constructed according to the latest geometry and material properties of the engineering array detector design [4]. The scintillator bars are constructed of polystyrene volumes, which are situated within a larger polystyrene casing housed inside an aluminum box. Precise specification of non-sensitive volumes, which act as shielding, is important as they can influence the signal by, for example, changing the rate of electron absorption and gamma conversion above and below the scintillator bars. The scintillator position relative to the water-Cherenkov detector is also of vital importance as many of the same particles traverse and deposit energy in both detectors, which manifests in correlations in signal, the strength of which must be well reproduced. A visualization of the SSD volumes above the water-Cherenkov detector volumes may be observed in Figure 1b.

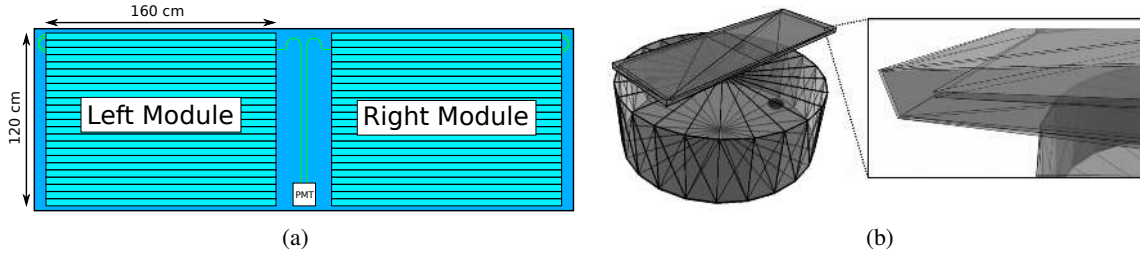


Figure 1: (a) Schematic of a surface scintillator detector, which is comprised of two symmetric modules consisting of 24 plastic scintillator bars each for a combined area of 3.84 m^2 . (b) Visualization of scintillator and water-Cherenkov detector volumes as implemented in Geant4 within the Offline framework.

Particles resampled [5] from CORSIKA [6] ground particle files are injected onto a virtual cylinder that houses both the water-Cherenkov and scintillator detectors that comprise a surface detector station. In the injection procedure, the momenta of resampled particles are preserved and the entry position of each particle is randomized in such a way that reflects the true probability distribution of intersecting the virtual cylinder at different points on its surface.

2.2 Photoelectrons

Whenever a particle track crosses the scintillator bar volumes in Geant4, the amount of energy deposited in the scintillator is extracted. The expected number of photoelectrons $\bar{N}(\mathbf{x})$ produced at the PMT's photocathode is then calculated via

$$\bar{N}(\mathbf{x}) = N_{\text{ref}} \frac{E_{\text{dep}}}{E_{\text{ref}}} f_{\text{att}}(\mathbf{x}) \quad (2.1)$$

in which E_{dep} is the energy deposit, E_{ref} and N_{ref} are the respective reference energy and photoelectron numbers for the simulations, $f_{\text{att}}(\mathbf{x})$ is a function which describes position-dependent signal attenuation, and \mathbf{x} is the position of the crossing particle. E_{ref} was obtained by simulating a sample of one hundred thousand 10 GeV vertical muons with randomized positions across the surface of the scintillator bars. The distribution of deposited energy, as shown in Figure 2a, has a peak at 1.72 MeV. This peak energy deposit corresponds to the peak in the distribution of vertical-equivalent photoelectron numbers as determined by an analysis of measurements of scintillator modules performed using a muon telescope taken from the former KASCADE experiment [7]. $f_{\text{att}}(\mathbf{x})$ was obtained from an analysis of the same muon telescope measurement setup, which provided a resolution on the positions of particles crossing the scintillator to the order of a couple of centimeters. The dependence of measured charge on the the position of the crossing particle may be described by

$$\tilde{f}_{\text{att}}(\mathbf{x}) = A(\mathbf{x})L(\mathbf{x}) , \quad (2.2)$$

where $A(\mathbf{x})$ corresponds to the attenuation of photons along the fiber and is defined as

$$A(\mathbf{x}) = e^{-\ell_c(\mathbf{x})/\lambda_f} + e^{-\ell_r(\mathbf{x})/\lambda_f} , \quad (2.3)$$

which includes two summed exponential terms corresponding to the fact that photons may travel in either direction and still reach the PMT given the looped fiber layout schematically depicted in

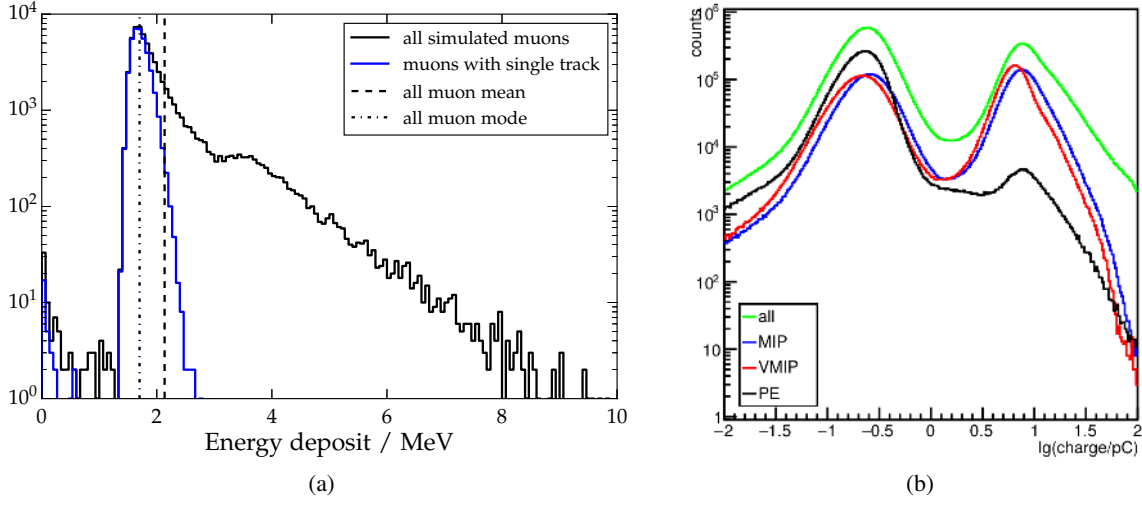


Figure 2: (a) Distribution of energy deposited by one hundred thousand simulated, vertical 10 GeV muons. The peak of the distribution is $E_{\text{ref}} = 1.72$ MeV. (b) Distribution of charge measured by a surface scintillator detector triggered using a muon telescope from the KASCADE experiment [7]. Peaks corresponding to single photoelectrons and minimum ionizing particles are visible.

Figure 3. $\ell_c(\mathbf{x})$ and $\ell_f(\mathbf{x})$ correspond to the two possible distances photons must travel along the fibers from the point of particle intersection to the PMT. λ_f corresponds to the attenuation length of the fiber. The term $L(\mathbf{x})$ in Equation (2.2) is a factor accounting for the decreased yield for particle tracks very close to the edge of the scintillator bars, namely

$$L(\mathbf{x}) = (1 - \alpha e^{-d_c(\mathbf{x})/\lambda_b})(1 - \alpha e^{-d_f(\mathbf{x})/\lambda_b}), \quad (2.4)$$

where α corresponds to the maximum loss, λ_b corresponds to the effective attenuation length of this boundary effect, and $d_c(\mathbf{x})$ and $d_f(\mathbf{x})$ respectively correspond to the distance between the particle crossing point and the close and far ends of the scintillator bars.

The reference number of photoelectrons N_{ref} from Equation (2.1) is acquired by mandating that the peak in the distribution of the number of photoelectrons produced by vertical minimum ionizing particles across the surface of the scintillator equals the estimate of 30 (denoted as $N_{\text{PE}}/\text{VMIP}$ in Equation (2.6)) obtained from an independent analysis of muon telescope data [4]. This mandate is fulfilled by integrating f_{att} only along the portion of the fiber between the ends of the scintillator bars, namely

$$\bar{f}_{\text{att}} = \frac{1}{p_f - p_c} \int_{p_c}^{p_f} f_{\text{att}}(\ell) d\ell, \quad (2.5)$$

where p_c and p_f respectively correspond to ends of the bars with shorter and longer travel distances along the fiber to the PMT. The quoted photoelectron count is then divided by the result to obtain N_{ref} ,

$$N_{\text{ref}} = \frac{N_{\text{PE}}/\text{VMIP}}{\bar{f}_{\text{att}}}. \quad (2.6)$$

In the actual simulation code, the expected number of photoelectrons is calculated for each individual leg of the signal using an equivalent formulation of Equation (2.2). A Poisson randomization

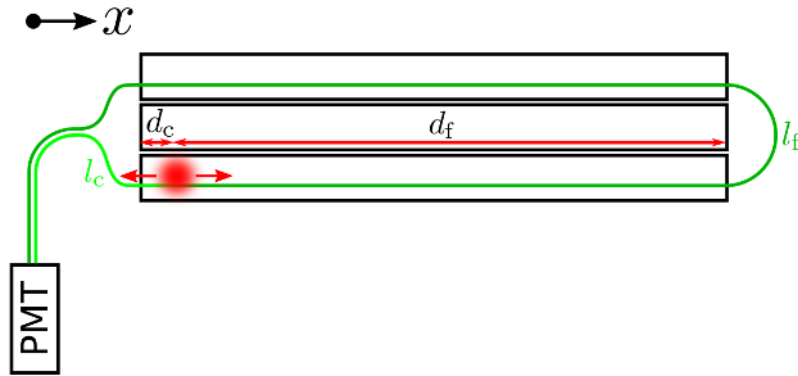


Figure 3: Schematic depiction of single particle scenario. Photons produced within a scintillator bar may travel to the PMT in either direction along the fiber. Depending on the direction, photons are attenuated to different degrees. Additional losses are observed for particles crossing near the edges of the scintillator bars.

is then performed on each expectation to obtain the true number of photoelectrons arriving from each leg at the PMT. The results of a set simulations may be observed in Figure 4a alongside the fit of $f_{\text{att}}(\mathbf{x})$ to muon telescope measurements. The mean number of photoelectrons observed here is greater than the peak value used for tuning due to the asymmetry in the distribution of energy deposit depicted in Figure 2a, which may also be observed in the charge distribution from muon telescope measurements shown in Figure 2b.

Once the number of photoelectrons has been determined, their production times at the photocathode must be simulated. The distribution of arrival times for photons having traveled nearly the same length of fiber before reaching the PMT was examined using muon telescope measurements. Although the true decay schema is likely considerably more complex, a model of two sequential exponential decays was found to provide a reasonable description of the data as shown in Figure 4b.

The decay constants from the fit are used to define two decay time distributions, which are randomly sampled for each photoelectron. Each photoelectron's arrival time is then determined by summing the time at which the particle crossed the scintillator bar, the time photons needed to travel from the crossing point to the fiber, and the two decay times. The time delay due to travel along the fiber is calculated using an effective index of refraction also obtained from muon telescope measurements.

2.3 PMT

Once a time trace of photoelectrons is obtained, the PMT is simulated as follows. For each photoelectron, the measured single photoelectron pulse shape is scaled by a random draw from the measured charge distribution (see Fig. 5a). The resulting scaled pulses are linearly added to a base current time distribution. This procedure makes two assumptions. The first is that the shape of the pulse at the base of the PMT does not depend on charge. The second is that the response of the PMT is linear. Post-PMT signal amplification in the upgraded electronics [8] has been set such that the limit of the dynamic range is reached prior to PMT departure from non-linearity.

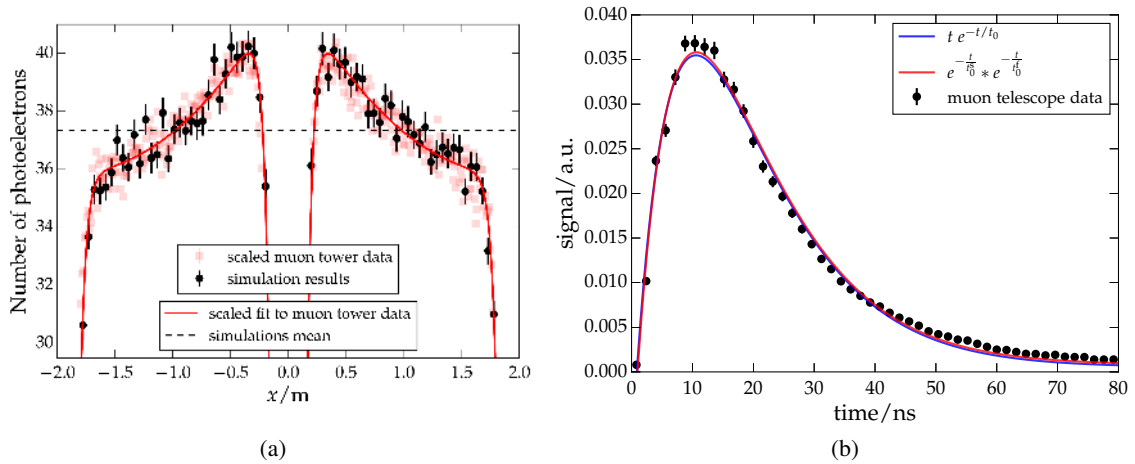


Figure 4: (a) Simulated number of photoelectrons alongside scaled muon telescope measurements and fit of the attenuation model f_{att} . (b) Fit to photoelectron production time distribution.

2.4 Electronics

The procedure for simulating the post-PMT electronics is as follows. The current at the base of the PMT is convolved with the transfer function measured for the 40 MHz unified board [9] scaled to accommodate for the higher frequency of the 120 MHz upgraded unified board (see Figure 5b). Given the similar designs of the standard and upgraded front ends, it is assumed that this scaling yields a reasonable estimate for the transfer function, the form of which should fall well within the variance expected between boards. Nonetheless, a direct measurement of the transfer function will be considered once the exact production design of the upgraded unified board is confirmed. The result of the convolution is then scaled with a parameter analogous to gain and sampled at 120 MHz to obtain ADC traces. The parameter analogous to gain is tuned such that the mean charge (in ADC) of a vertical muon passing through any point of the scintillator surface equals the charge measured by deployed engineering array prototypes as determined via a vertical equivalent muon calibration detailed in [10].

3. Offline upgrade

Auger's Offline software framework has served as a simulation and reconstruction backbone for the Collaboration for over a decade, and has been adopted or used in some manner by a handful of other collaborations. In order to house the scintillator simulations described in this proceeding as well as the related storage, access, and processing needs of all the AugerPrime hardware, a number of upgrades to and augmentations of the software's framework have been performed. Greater flexibility in the detector description (see Figure 7) including the ability to group different types of hardware unique to individual stations at different points in time has been implemented. The corresponding machinery in updating the detector between events has also been upgraded. In this process, heavy focus has been maintained on keeping interfaces with users and module developers simple in order to keep the entry level skill necessary for programming the physics modules relatively low and reduce errors as a result.

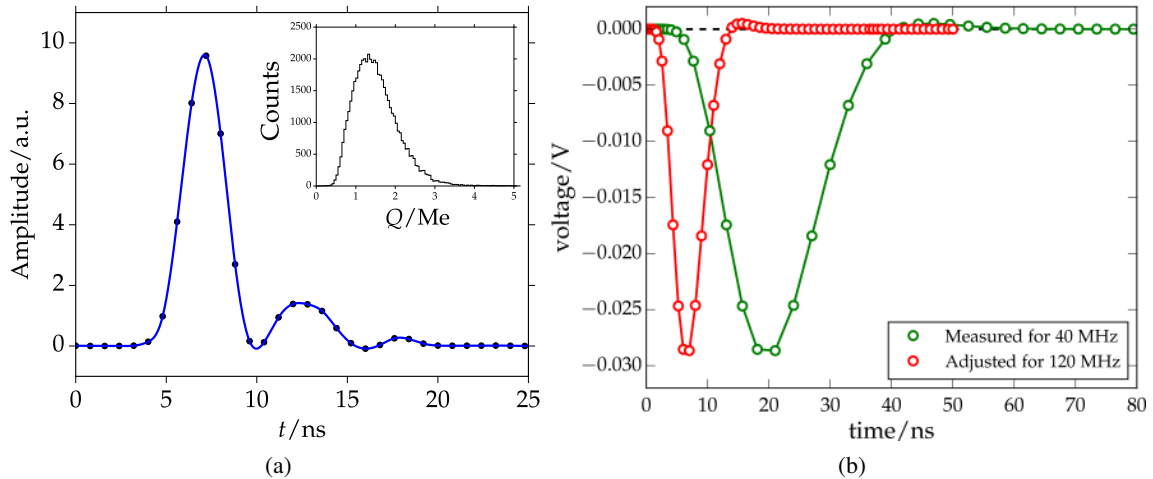


Figure 5: (a) Pulse shape and charge distribution (inset) for properly amplified photoelectrons as measured using the the muon telescope setup. (b) Transfer function measured for Auger’s 40 MHz electronics along with scaled version used for the 120 MHz simulations up to the present.

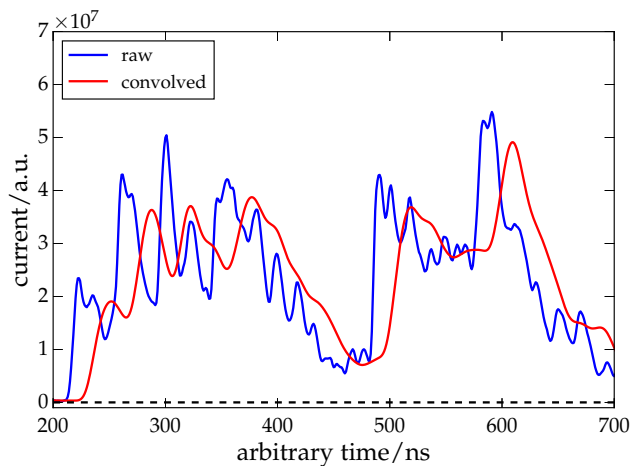


Figure 6: Sample simulated current at the base of the PMT and convolution with electronics transfer function.

4. Conclusions

Simulations of the AugerPrime surface scintillator detector have been implemented within Auger’s Offline software framework. At the core of these simulations lies the use of models and parameterizations derived from real prototype detector measurements where possible and the use of the latest field-standard software, Geant 4.10, where measurements are impossible or unavailable. The simulations have been tuned to the latest data from the AugerPrime engineering array, and promise to aid in both a detailed understanding of the upgraded surface detector as well as interpretation of future measurements of the observatory as the upgrade moves into the deployment phase. The Offline software has also been modified and augmented with the classes and machinery necessary to accommodate the data of the new hardware with the enhanced flexibility required by

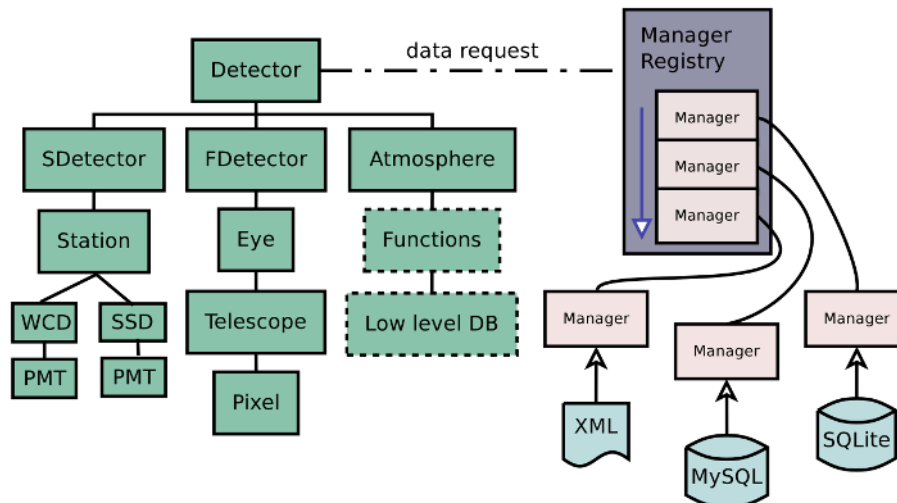


Figure 7: Schematic depiction of detector description machinery in *Offline* (taken from [1]) including both logically motivated classes with user interfaces (left) and the manager structure (right). This machinery has been updated for greater flexibility in the grouping of hardware components and the time evolution of the hardware on the individual station level.

a detector description for which both the existence and properties of hardware components vary between stations and in time.

References

- [1] Pierre Auger Collaboration, Preliminary Design Report, arXiv:1604.03637.
- [2] S. Argiro, *et al.*, Nucl. Instrum. Meth. A 580 (2007) 1485; arXiv:0707.1652.
- [3] S. Agostinelli *et al.*, Nucl. Instrum. Meth. A 506 (2003) 250.
- [4] R. Smida, for the Pierre Auger Collaboration, PoS (ICRC2017) 390.
- [5] P. Billoir, Astropart. Phys. 30 (2008) 270.
- [6] D. Heck, G. Schatz, T. Thouw, J. Knapp, and J. Capdevielle, Forschungszentrum Karlsruhe – Wissenschaftliche Berichte (1998).
- [7] P. Doll *et al.*, Nucl. Instrum. Meth. A, 488 (2002) 517.
- [8] T. Suomijärvi, for the Pierre Auger Collaboration, PoS (ICRC2017) 450.
- [9] The Pierre Auger Collaboration, Nucl. Instrum. Meth. A, 798 (2015) 172; arXiv:1502.01323.
- [10] X. Bertou *et al.*, for the Pierre Auger Collaboration, Nucl. Instrum. Meth. A 568 (2006) 839.



Improvements to aerosol attenuation measurements at the Pierre Auger Observatory

Max Malacari^{*a} for the Pierre Auger Collaboration^b

^a*Kavli Institute for Cosmological Physics, University of Chicago, Chicago, IL, USA*

^b*Observatorio Pierre Auger, Av. San Martín Norte 304, 5613 Malargüe, Argentina*

E-mail: auger_spokespersons@fnal.gov

Full author list: http://www.auger.org/archive/authors_icrc_2017.html

Sound knowledge of the aerosol loading in the atmosphere above the Pierre Auger Observatory is essential for the accurate reconstruction of shower energy deposit profiles using the atmospheric fluorescence technique. The vertical aerosol optical depth is inferred from hourly measurements of the vertically-fired UV laser beams of the Observatory's central laser facilities via two complementary techniques. We report on recent refinements made to these aerosol analysis techniques, and on verification of the resulting aerosol measurements through internal consistency checks using reconstructed air shower data. These analysis improvements include accounting for the shape of the aerosol scattering phase function, and the treatment of multiple scattered light from the laser beam. The cumulative effect of these improvements is a modest increase in the measured vertical aerosol optical depth above the Observatory. We will discuss the impact of this increase on the reconstruction of showers measured with the Observatory's fluorescence detector.

*35th International Cosmic Ray Conference — ICRC2017
10–20 July, 2017
Bexco, Busan, Korea*

^{*}Speaker.

1. Introduction

The Pierre Auger Observatory is a hybrid observatory for the detection of ultra-high energy cosmic rays ($E > 10^{18}$ eV) via the extensive air showers they produce when they interact with the earth's atmosphere [1]. It consists of a 3000 km² surface detector (SD) array which records the lateral distribution of shower particles reaching ground level, as well as a fluorescence detector (FD) which observes the longitudinal development of showers in the atmosphere through the faint isotropic fluorescence light emitted between 300 and 420 nm by excited N₂ molecules. The ground array is made up of 1660 water-Cherenkov detectors arranged on a triangular grid with a spacing of 1.5 km. It is overlooked from its periphery by 27 fluorescence telescopes located at 4 sites.

While the SD records the footprints of extensive air showers with a duty cycle of almost 100%, the energy scale of the Observatory is determined using coincident observations of a subset of these showers with the fluorescence detector (having a duty cycle of $\sim 15\%$ [1]), which provides a near-calorimetric measurement of the shower energy. As this fluorescence light can travel tens of kilometres between its point of emission and a fluorescence detector, it is essential that the transmission properties of the atmosphere are well understood [2]. In the lowest 15 km of the atmosphere where air shower measurements occur, aerosols play an important role in modifying the light transmission. While the UV extinction due to aerosols is several times less than the extinction due to molecules, the aerosol atmosphere is highly variable over short time-scales and, on hazy nights, the light flux from distant showers can be reduced by a factor of 3 or more due to aerosol attenuation.

2. Measurement of the vertical aerosol optical depth

Measurements of vertical laser tracks from the Observatory's Central and eXtreme Laser Facilities (CLF and XLF) are used to infer the vertical distribution of aerosols above the array with a time resolution of one hour via two independent and complementary techniques [3, 4]. Sets of 50 vertical depolarized 355 nm laser pulses are measured every 15 minutes at each of the 4 FD sites during each night of observation. To minimize the statistical uncertainty in the measured laser signal, each set of measurements within an hour block is averaged before being used to calculate the Vertical Aerosol Optical Depth (VAOD), the integral of the aerosol attenuation coefficient α_A from the ground to height h , within the field of view of each of the FD sites. In the Data Normalized (DN) method, the hourly averaged laser traces are compared to averages collected under nominally aerosol-free conditions (called reference nights¹), and in the Laser Simulation (LS) method, the average traces are compared to simulations generated under different aerosol attenuation conditions. Hourly VAOD profiles for each FD site are written to an aerosol database which is queried during air shower reconstruction to determine the aerosol attenuation between any two points in the atmosphere above the array.

The DN method is the primary technique used to retrieve the VAOD, and aerosol profiles calculated in this way comprise $\sim 90\%$ of the database. The fundamental equation for the calculation of the VAOD using this method, which can be analytically derived under the assumptions that the

¹Typically a new reference night is chosen each year.

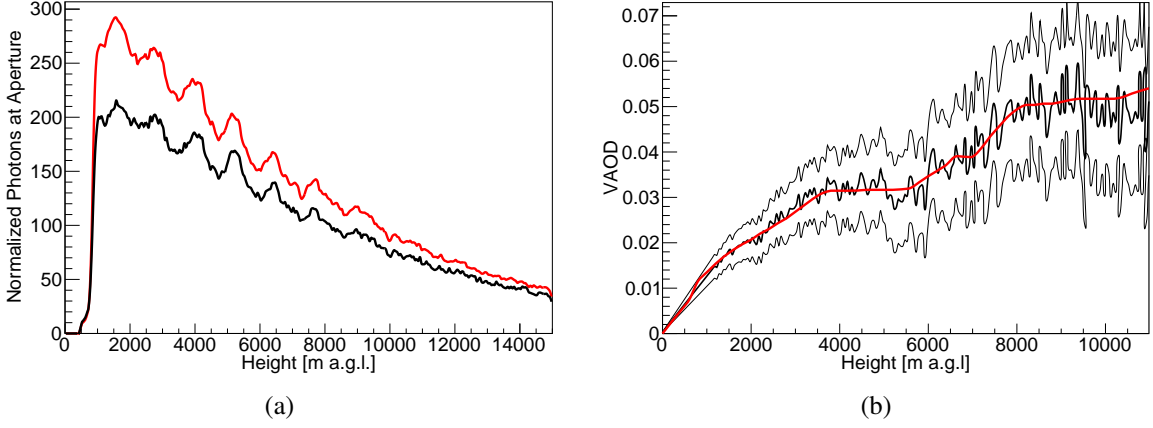


Figure 1: (a) Example of a measured laser trace (black). In red is the associated nominally clear reference trace. (b) The VAOD as derived from this measurement. The central black profile is the raw VAOD, and in red is a smoothed version. The upper and lower black profiles denote the raw upper and lower uncertainty bounds on the VAOD.

aerosol atmosphere is horizontally uniform, and that multiple scattered light from the laser does not contribute to the light flux measured at the FD, is

$$\text{VAOD}(h) = \underbrace{\frac{-1}{1 + 1/\sin \phi_2} \ln \left(\frac{N_{\text{aer}}}{N_{\text{ref}}} \right)}_{(1)} + \underbrace{\frac{1}{1 + 1/\sin \phi_2} \ln(1 + S_A/S_M)}_{(2)}. \quad (2.1)$$

Here N_{aer} and N_{ref} are the photon fluxes originating from height h (on the night of measurement and the reference night respectively), ϕ_2 is the elevation of the laser track segment with respect to the detector, and S_A and S_M describe the fraction of the laser beam scattered towards the detector from that height by aerosols and molecules respectively. Terms (1) and (2) of Eq. 2.1 both encode separate pieces of information about the aerosol attenuation properties of the atmosphere, with the first part representing the transmission of laser light along the laser beam to height h , and from that point to the aperture of a fluorescence detector, and the second representing the scattering of laser light out of the beam and towards the detector. Traditionally the analysis operates under an additional assumption; that the density of molecular scattering centres in the atmosphere is much greater than that of aerosols. This, coupled with the fact that the aerosol scattering phase function is strongly forward peaked and the vertical laser beam is always viewed nearly side on, means that the S_A term is much smaller than the S_M term. In this case, term (2) $\rightarrow 0$ and the VAOD at a given height depends only on the ratio of the measured light flux originating from that height relative to that measured on the reference night. An example of a measured averaged laser trace, along with a reference trace, is shown in Fig. 1a. In Fig. 1b is the corresponding reconstructed VAOD determined using the DN technique. The average VAOD at 3 km above ground level (above the planetary boundary layer) measured at the Observatory site is approximately 0.04 [2].

3. Improvements to the analyses

The two aerosol analyses have been updated to remove their reliance on a number of simpli-

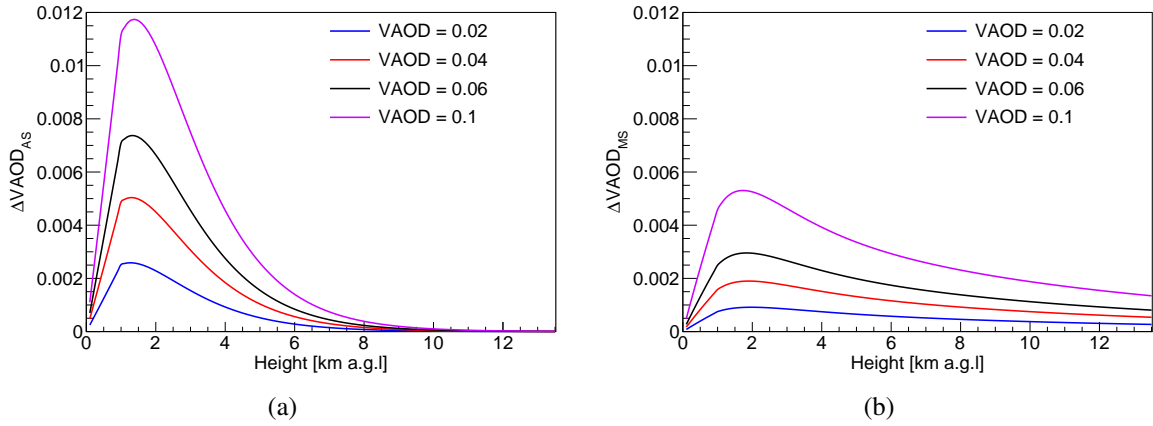


Figure 2: (a) Correction for aerosol scattering out of the laser beam in the DN analysis. (b) Correction for the small multiple scattered component of the received laser light flux at the detector.

fying assumptions which are described here.

3.1 Correction for aerosol scattering

The DN analysis previously operated under the assumption that scattering out of the laser beam towards the fluorescence detector is due to the molecular component of the atmosphere only.

Term (2) in Eq. 2.1 can be considered as the correction term taking into account aerosol scattering of photons out of the laser beam. Since S_A and S_M are always ≥ 0 , this term is always positive and hence serves to increase the VAOD. Physically speaking, increasing S_A is akin to increasing the *expected* photon flux at the detector (as we now expect to measure both molecular and aerosol scattered light), and as the measured light flux is fixed, this will have the effect of decreasing the apparent aerosol transmission.

An analytical approximation to the magnitude of this correction as a function of height is shown in Fig. 2a. In this model the aerosol atmosphere is approximated using a simple 3-parameter exponential with a planetary boundary layer of uniform aerosol density. The thickness of the mixing layer and the scale height are fixed, while the aerosol horizontal attenuation length at ground level is varied to emulate a range of typical VAODs at the top of the atmosphere. The correction has the largest effect low in the atmosphere where the aerosol concentration is highest. The scale height of the molecular atmosphere is typically several times larger than the scale height of the aerosol atmosphere, so the ratio of the number of aerosol to molecular scattering centres decreases rapidly with height. This, coupled with the very small aerosol phase function component at scattering angles $> 90^\circ$ means that the correction drops off quickly above its height of maximum amplitude.

In practice the quantity S_A is not known *a priori* as it relies on knowledge of the aerosol scattering coefficient at each height. The correction is therefore applied iteratively by assuming that $S_A \ll S_M$, calculating the aerosol scattering coefficient from the resultant VAOD profile, and then recalculating the VAOD profile using Eq. 2.1.

3.2 Correction for multiple scattering

In both VAOD reconstruction techniques it was previously assumed that any light that is not

initially scattered out of the laser beam and towards the detector is lost. This assumption ignored the possibility that some photons will reach the detector after one or more additional scatterings. As multiple scattering serves to make the laser appear slightly brighter than it would under the assumption of single scattering only, both of these VAOD reconstruction methods compensated for this effect by reconstructing an aerosol atmosphere that was marginally cleaner than reality.

The DN and LS aerosol analyses can be corrected for multiple scattering by effectively subtracting the estimated multiple scattered contribution from the total light flux in each height bin. For the DN analysis this has the form

$$\frac{N_{\text{aer}}}{N_{\text{ref}}} \rightarrow \frac{N_{\text{aer}}}{N_{\text{ref}}} \frac{1 - f_{\text{aer}}}{1 - f_{\text{ref}}}, \quad (3.1)$$

where f_{aer} and f_{ref} denote the fraction of multiple scattered light received in a given signal time bin relative to the total (on the night of measurement and the reference night respectively). By substituting this expression into term (1) of Eq. 2.1 the VAOD can be corrected for multiple scattering of the laser beam.

The quantity f is parametrized using Monte Carlo raytracing simulations of a vertical 355 nm laser beam and has the form

$$f_{\zeta}(\alpha, \tau) = k \alpha^A \tau, \quad (3.2)$$

where α denotes the total volume scattering coefficient at the laser track (aerosol and molecular, in m^{-1}) in a given time bin, and τ is the total optical depth between the fluorescence detector and the laser track segment [5]. The parameter ζ denotes the angular size (in degrees) of the region on the focal surface of the detector (centred on the laser's track across the camera) over which light is integrated in each signal time bin. For analyses of vertical laser shots ζ is fixed to 1.5° , and the parameters k and A are 12.98 and 0.57 respectively. Fig. 3a shows the flux of photons at the detector's focal surface as a function of direction taken from the raytracing simulation, and Fig. 3b shows the fitted parametrization for an integration angle of 1.5° .

The expected magnitude of the VAOD increase as a function of height above ground level based on simulations is shown in Fig. 2b. In practice the correction must be applied iteratively to the DN analysis, as the aerosol scattering coefficient at the laser track and the aerosol optical depth between the laser track and the detector, necessary for the calculation of f_{ζ} , are unknown *a priori*. In the case of the LS analysis, the multiple scattered fraction can simply be added to the simulated light flux at the detector before comparison with a measured laser trace.

3.3 Measurement of the aerosol scattering phase function

Both of the improvements made to the aerosol analysis which are described here have a dependence on the shape of both the molecular and aerosol scattering phase functions. The shape of the aerosol scattering phase function can not be calculated analytically, and depends on the size and shape distributions of the aerosols present in the atmosphere, which can vary over short time-scales. The shape of the aerosol phase function at a wavelength of 350 nm (close to the CLF and XLF wavelength) is measured hourly at the Observatory during FD data taking, using observations of a xenon flasher fired horizontally across the field of view of two of the fluorescence detectors [6].

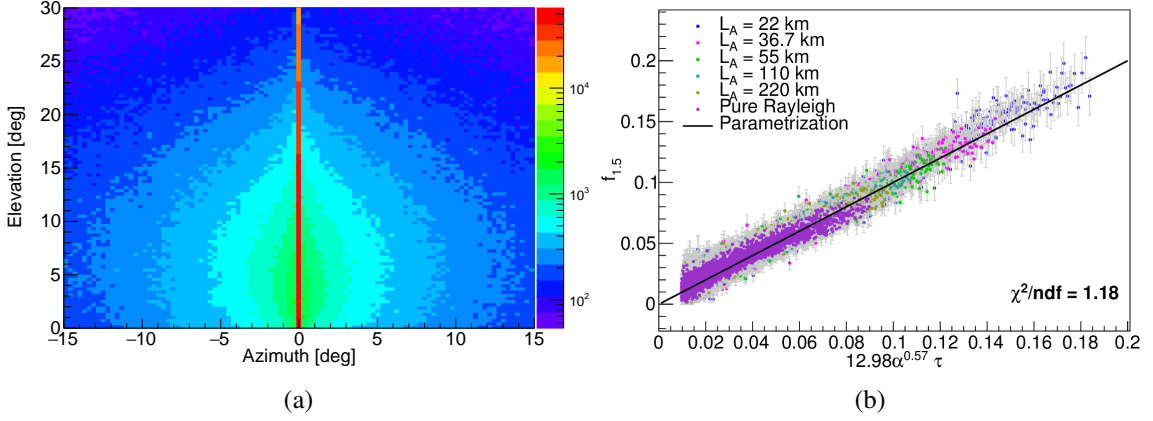


Figure 3: (a) Simulated distribution of light at the focal surface of the FD (photons at the aperture) from a vertical laser beam (integrated over time). The intense red stripe at an azimuth of 0° corresponds to single scattered photons from the laser beam. All other photons are multiple scattered. (b) Simulated multiple scattered fraction within $\zeta = 1.5^\circ$ for a range of aerosol attenuation conditions overlaid with the parametrization $f_\zeta(\alpha, \tau)$.

The form of the aerosol scattering phase function used for calculations at the Pierre Auger Observatory is the modified Henyey-Greenstein phase function

$$\left(\frac{1}{\sigma} \frac{d\sigma}{d\Omega} \right)_A = \frac{1-g^2}{4\pi} \left(\frac{1}{(1+g^2-2g\cos\theta)^{3/2}} + f \frac{3\cos^2\theta-1}{2(1+g^2)^{3/2}} \right), \quad (3.3)$$

which describes the fraction of light per unit solid angle that is scattered in a particular direction by aerosols. The Henyey-Greenstein phase function includes two parameters, f and g , known as the backscattering and asymmetry parameters, which describe its shape. For a backscattering parameter of $f = 0$ the asymmetry parameter is simply equal to the mean cosine of the scattering angle. The nominal values for these parameters at the Auger site are $g = 0.6 \pm 0.1$ and $f = 0.4$ [2].

The improvements to the aerosol analysis described in this contribution both have a dependence on the aerosol phase function shape, in particular the asymmetry parameter g . The shape of the aerosol scattering phase function is expected to have some seasonal variation, as the size and shape distributions of aerosol particles above the array change throughout the year [7]. Approximately 2100 hours of xenon flasher measurements taken at the Coihueco FD site between 2011 and 2015 were analyzed to search for significant departures of the asymmetry parameter from its average value throughout the year. Fig. 4a shows the mean value of g measured over this 5-year dataset, which is in agreement with the previously published value of this parameter [2]. Fig. 4b shows the average asymmetry parameter as a function of the time of year. A small seasonal dependence is evident, however the drift in the parameter throughout the year is less than the root-mean-square spread within any single month. Therefore g is set to its nominal value of 0.6 for both of the aerosol analysis improvements described here.

4. Effect on reconstructed air showers

The height-dependence of these aerosol analysis improvements results in the alteration of re-

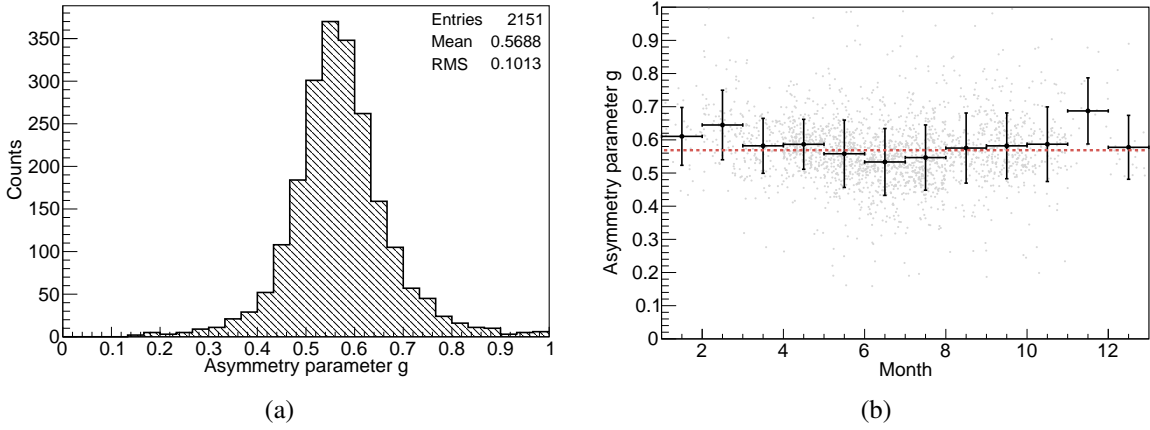


Figure 4: (a) Distribution of the fitted asymmetry parameter over the 5-year dataset. (b) Drift in the asymmetry parameter throughout the year. Vertical error bars indicate the root-mean-square of the fitted asymmetry parameter distribution in each month of data. The horizontal line indicates the average value over the whole dataset.

constructed shower profiles in both shape and normalization. Reconstructed shower energies are increased on average by 1.5% at $10^{17.5}$ eV, up to 3% at an energy of $10^{19.5}$ eV. Showers of higher energy tend to be detected at larger distances, meaning the aerosol transmission is lower, and hence the relative decrease in the aerosol transmission under these aerosol analysis improvements is larger. Changes in the average depth of shower maximum are driven by the elongation of the decaying tail of shower profiles and range from 2 g/cm^2 at $10^{17.5}$ eV, up to 5 g/cm^2 at an energy of $10^{19.5}$ eV. The larger VAOD increases close to the ground (shown in Fig. 2) lead to a modest elongation of the trailing edge of reconstructed energy deposit profiles, shifting their depth of maximum development slightly deeper in the atmosphere. Both the energy and X_{max} increases are small on average, and are within current aerosol transmission related systematic uncertainties in the energy and X_{max} scales published in [8, 9].

A useful metric for verifying the validity of the aerosol attenuation measurements used in shower reconstruction is the ratio $E_{\text{SD}}/E_{\text{FD}}$, the ratio of reconstructed SD to FD energy. If the aerosol loading above the array is characterized correctly we should see internal consistency within our reconstructed air shower data, and there should be no dependence of this ratio on the aerosol transmission to the depth of maximum shower development, which functions as a proxy for the distance of the shower from the FD (the reconstructed SD energy is independent of the distance of the shower from the fluorescence detector). If the relationship exhibits a negative slope it indicates that showers observed at larger distances to the FD are being reconstructed with lower energies on average, suggesting that the aerosol content in the atmosphere has been underestimated (Fig. 5a). Conversely, a positive slope to the relationship would indicate an overcorrection for aerosol attenuation. Following the improvements to our aerosol analysis techniques, we see a slope in this ratio of -0.006 ± 0.036 (Fig. 5b), fully consistent with zero, and a strong indication that our VAOD measurements accurately describe the status of the aerosol atmosphere above the array. The sensitivity of the slope to uncertainties in the aerosol concentration is currently being assessed.

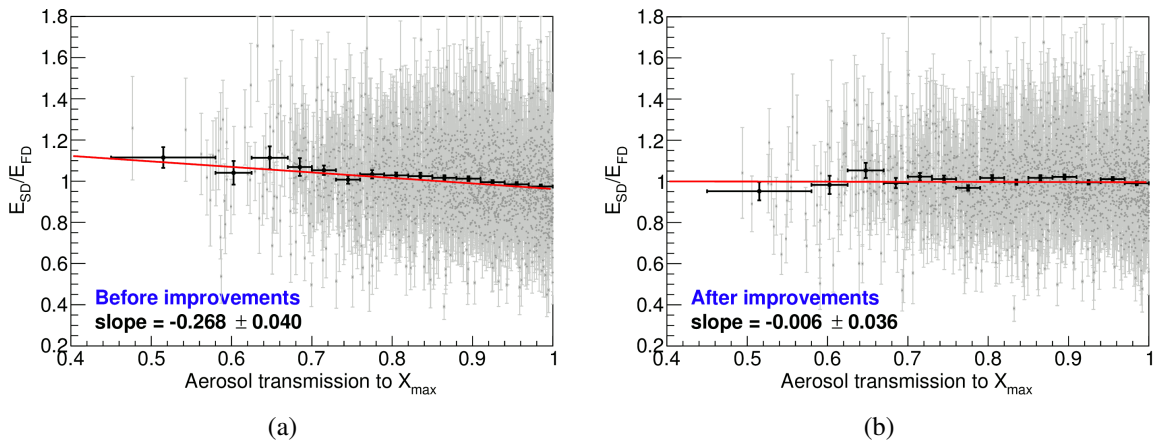


Figure 5: Ratio of the reconstructed SD to FD energy as a function of the aerosol transmission to the depth of shower maximum. (a) Before the improvements made to aerosol extinction measurements. The negative slope indicates that the aerosol content of the atmosphere has been underestimated. (b) Following the improvements made to aerosol extinction measurements. The slope is fully compatible with zero, demonstrating internal consistency within the data.

5. Conclusion

Two simplifying assumptions used in the calculation of the aerosol transmission properties of the atmosphere above the Pierre Auger Observatory have been removed. These refinements include properly accounting for the aerosol side-scattering and multiple scattering of light from the Observatory's two laser facilities, which are used to make hourly measurements of the vertical aerosol loading above the array.

These analysis improvements increase the reconstructed aerosol concentration close to the ground on average, resulting in modest energy-dependent increases in the reconstructed energy and depth of maximum of air showers measured with the Observatory's fluorescence detector, which are within our current aerosol related systematic uncertainties. In addition, we see internal consistency between shower energies reconstructed with both the surface and fluorescence detector, indicating a sound knowledge of the aerosol loading in the atmosphere above the Observatory.

References

- [1] The Pierre Auger Collaboration, *Nucl. Instr. Meth. A* **798** (2015) 172–213.
- [2] The Pierre Auger Collaboration, *Astropart. Phys.* **33** (2010) 108–129.
- [3] B. Fick et al., *JINST* **1** (2006) P11003.
- [4] The Pierre Auger Collaboration, *JINST* **8** (2013) P04009.
- [5] M. Malacari and B.R. Dawson, *Astropart. Phys.* **93** (2017) 38–45.
- [6] S.Y. BenZvi et al., *Astropart. Phys.* **28** (2007) 312–320.
- [7] The Pierre Auger Collaboration, *Atmos. Res.* **149** (2014) 120–135.
- [8] V. Verzi for The Pierre Auger Collaboration, *Proc. 33rd Int. Cosmic Ray Conf.* (2013).
- [9] The Pierre Auger Collaboration, *Phys. Rev. D* **90** (2014) 122005.



The FRAM Telescope at the Pierre Auger Observatory

Jiri Blazek^{*a} for the Pierre Auger Collaboration^b

^a*Institute of Physics, Prague, Czech Republic*

^b*Observatorio Pierre Auger, Av. San Martín Norte 304, 5613 Malargüe, Argentina*

E-mail: auger_spokespersons@fnal.gov

Full author list: http://www.auger.org/archive/authors_icrc_2017.html

The knowledge of both the long-term characteristics of the atmosphere and of its immediate state is of vital importance for the study of extensive air showers. The F/Photometric Robotic Atmospheric Monitor (FRAM), installed at the Pierre Auger Observatory, is an autonomously operating instrument which measures the integral light extinction in a given direction using stellar photometry. Its primary purpose is the rapid observation of atmospheric conditions soon after the fluorescence detectors of the Observatory have recorded a particularly interesting shower. This information is crucial for the study of showers with anomalous longitudinal profiles, which are predicted by hadronic interaction models but whose observation can also arise as a consequence of the presence of clouds or aerosol layers. The current status of the analysis is presented. In addition to the primary function of the FRAM, the integral aerosol content can be obtained by utilizing the large number of stars identified in the wide-field images of the instrument. The method for this is also briefly described.

*35th International Cosmic Ray Conference
10–20 July, 2017
Bexco, Busan, Korea*

^{*}Speaker.

1. The Pierre Auger Observatory

The Pierre Auger Observatory utilizes a hybrid design for the simultaneous detection of cosmic rays of ultrahigh energy, making use of both the surface and the fluorescence detectors [1]. The surface detector (SD) array comprised of water-Cherenkov stations observes a portion of the incoming shower hitting the ground. It functions with a full uptime of 24 hours per day and covers an area of 3000 km² in a triangular grid with a spacing of 1.5 km. The arrival direction and the energy of the primary particle can be inferred from the particle densities recorded by the SD stations. The fluorescence detector (FD) concurrently views the fluorescence light emitted during the development of the shower in the atmosphere. Its telescopes are concentrated at four sites, with a combined field of view of 180° per site, overlooking the SD array. The FD is capable of measurement only during nights with a low moon fraction and sufficiently clear weather, resulting in a duty cycle of approximately 15%. By observing the longitudinal profile of the shower the detector is able to perform an almost calorimetric measurement, where the energy corresponding mostly to the electromagnetic part of the shower cascade is obtained by integrating the fitted fluorescence profile.

The collected fluorescence light is attenuated by molecular scattering and by scattering on aerosols present between the detector position and the shower. The estimation of the energy of the shower thus depends strongly on the state of the atmosphere. The presence of absorbing or scattering layers can further cause the observation of additional features in the profile which have an origin outside of hadronic interactions.

Precise knowledge of the atmospheric conditions is thus of major importance. The Pierre Auger Observatory employs an extensive atmospheric monitoring program; see [1] for the description of the various instruments. The respective installations record the atmospheric observables at regular, periodic intervals. However, in order to study particularly interesting and rare showers, a greater spatial and temporal resolution is crucial. In the following we will describe the Shoot-the-Shower (StS) program and in particular the F/photometric Rapid Atmospheric Monitor (the FRAM telescope), which were designed to rapidly perform a measurement after a shower was recorded by the fluorescence detector.

2. Shoot-the-Shower: the FRAM Telescope

The instrument consists of a wide-field camera, optical focuser and a set of rotating filters, jointly attached to a remotely controlled mount. This system is encased in a dome with dimensions of approximately 2.5 m × 2.5 m. The data acquisition and the operation of the hydraulics of the enclosure are handled by a control computer. The remotely operated camera features a field of view of 7° × 7°. Using a 30 second exposure, thousands of stars are typically seen in a single image, depending on the particular area in the sky. The instrument is located at the Los Leones site, very near the fluorescence detectors. Fig. 1 shows the telescope with the enclosure in an open state.

The Shoot-the-Shower analysis chain functions as follows. The raw data recorded by the surface and fluorescence detectors are being passed to a centrally located computer. A hybrid reconstruction is performed and the retrieved parameters of the shower are passed further to a

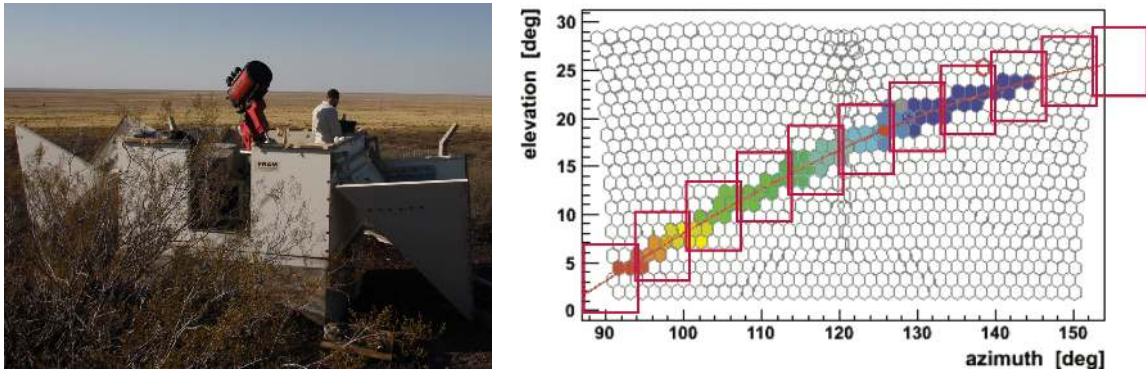


Figure 1: *Left:* A photo of the FRAM telescope, with an open enclosure. *Right:* An illustrative sketch of the area covered by FRAM for a single event, in this case recorded by two neighboring fluorescence telescopes at a single site.

control computer of the FRAM telescope. A set of predefined triggers is applied: currently, these look for showers with an anomalous profile, highly energetic showers and candidates for a shower caused by a highly energetic gamma primary. If the cuts are passed, the telescope records images along the reconstructed axis of the shower. The retrieval of the data from the SD and FD and the subsequent reconstruction takes approximately 3 to 5 minutes, after which the telescope is ready to shoot the first picture. The median number of recorded images per trigger is 5, but the number of recorded images could also be significantly higher in case of inclined shower geometries coming parallel to the focal plane of the FD, spanning a wide range in azimuth angle (Fig. 1). Events with fewer than 4 images are discarded, as in many cases they don't cover a sufficient portion of the development of a shower as recorded by the FD.

During analysis, stars are extracted from the images and then matched with sources in the Tycho2 [2] star catalog. Comparing the light fluxes obtained using star photometry on the images recorded by FRAM with the values listed in Tycho2, an extinction for each source can be retrieved. A global fit can then be performed based on the predicted dependence of the extinction on the airmass. Any significant variations from the fit then point to the presence of attenuating inhomogeneities. The most frequently triggered type of event is the double-bump candidate, described in the following section.

3. Double-Bumps

The showers with an anomalous longitudinal profile, or the so-called double-bump showers, differ markedly from a universal profile described, e.g., by the empirical Gaisser-Hillas function [3]. An example of such a shower simulated in a Monte Carlo generator is shown in the left part of Fig. 2. To be classified as anomalous, the profile should feature a prominent second maximum or a clearly distinguishable set of two additional inflexion points. Such a property can be explained by a particle originating in the first several generations of a shower development which receives a sufficiently high fraction of the energy of the primary particle. If it then propagates deeply into the atmosphere without losing a significant portion of its energy, it creates a secondary sub-shower which can be clearly distinguished from the products of the primary cascade. Such a

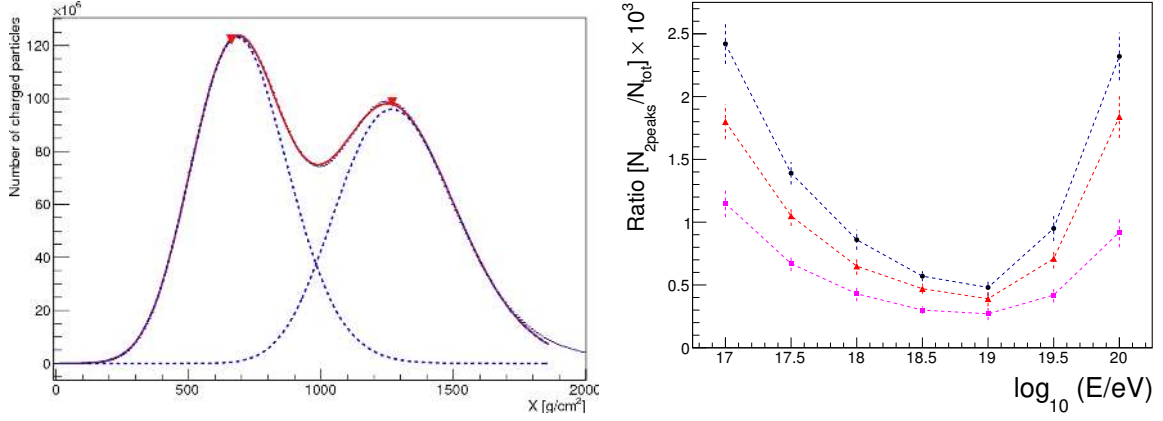


Figure 2: *Left*: a sample example of an anomalous longitudinal profile, generated by the CONEX software for a proton primary with energy 10^{20} eV. *Right*: dependence of the ratio of double bumps on energy for a proton primary. The hadronic interaction model EPOS-LHC was used. The three lines represent three reasonable choices for a parameter defining an anomalous profile. Taken from [5].

process however requires a light nucleus as the primary particle, since the nucleons in heavy nuclei do not possess sufficient energies and the resulting sub-shower would be too insignificant for detection and would get smeared out among the sub-showers originating from the rest of the nucleons. Observing an anomalous shower profile at a given energy would then represent direct evidence of the presence of a light fraction in the mass composition of the primary cosmic rays. Furthermore, given that a sufficient dataset is acquired, the distribution of the profile maxima of the secondary sub-showers can be used to inspect the particle-air cross section.

Several studies [4], [5] were performed on very large samples of Monte Carlo generated events, using various definitions of anomalous profiles for the purposes of their identification. The concrete quantitative predictions of the rate of double bumps depend on the particular definition used, on the energy of the primary particle, on the hadronic interaction model employed in the Monte Carlo simulations and on the type of the primary particle. For a proton primary, the ratio of anomalous profiles N_{anom} to the total number of events N_{tot} is of the order of 10^{-3} , see the right part of Fig. 2. A very reliable rejection of false positives is thus of crucial importance. Studying data from the fluorescence detector of the Pierre Auger Observatory, it is clear that the overwhelming majority of profiles displaying anomalous features is the result of atmospheric conditions in the vicinity of the shower axis. There are two mechanisms through which a shower with a regular longitudinal profile could masquerade as anomalous. Either there is a cloud in between the axis and the detector, obfuscating part of the fluorescence light and creating an artificial minimum, or the cone of Cherenkov light, narrowly collimated along the shower axis, hits a cloud or an aerosol layer and scatters a portion of the light towards the fluorescence detector, creating an artificial maximum in the profile. The FRAM telescope is sensitive to clouds between the telescope and the edge of the atmosphere and is able to identify both types of events. The exception is the case where the perpetrator is a uniformly distributed, thin homogeneous layer. Such an extended layer can however be recognized by the other atmospheric monitoring devices.

4. Image Processing

Each telescope of the fluorescence detector has a field of view of $30^\circ \times 30^\circ$ in azimuth and altitude, with a minimal angle of approximately 1.5° above the horizon. Accordingly, the FRAM telescope is configured to cover a range in altitude from roughly 35° all the way to the horizon, depending on the geometry of the particular shower. This range is more than sufficient, since the angular span of the FD profile is usually significantly smaller than 30° . Moreover, by scanning a larger portion of the sky than that covered by an air shower we can also make sure that a portion of the FD profile is not missing due to a presence of a cloud.

During analysis, the processed images have to be first calibrated by applying a correction with regards to “flat” and “dark” images. The process is described in detail in [6]. After removing a large part of the background, stars are then identified, their coordinates are extracted and their light flux is calculated by means of aperture photometry. Pairs of stars closer than twice the aperture are removed to avoid any light cross-contamination. Finally, the obtained fluxes are compared to values provided by the Tycho2 catalog [2] for stars that should be present in that particular spot in the night sky. The difference in magnitudes then gives the extinction for the respective star. By analyzing several wide-field images, hundreds to thousands of stars spanning a wide range in altitude (and the airmass, respectively) can be identified on a single scan and a fit can be performed to obtain the extinction coefficient. The predicted dependence on the airmass A is simple,

$$m_{\text{inst}} = m_{\text{cat}} + Z + kA + \text{correction terms} \quad (4.1)$$

where m_{inst} is the apparent light flux in magnitudes, m_{cat} is the flux of a matched star in the Tycho2 catalog, Z is the value of the zeropoint, which fixes the otherwise arbitrary scale and is the primary calibration constant and k is the extinction coefficient. The last part of the equation refers to terms correcting various properties of the optical system and of the star catalog itself. The correction terms are fitted once for a large sample of scans featuring no cloud contamination and then kept fixed.

Finally, one obtains a plot of the extinction profile for a given scan, such as shown in the middle column of Fig. 3. The left column shows the associated FD profile, which triggered the scanning. The right column shows deviations from the fit plotted against slant depth, to be directly comparable to the FD profile. Fig. 3-top is an example of a very clear event, with the stars clustered along the predicted extinction curve and no signs of any clouds. The consequences of their presence could be seen in Fig. 3-bottom – many stars are attenuated by several magnitudes and their location differs from the extinction curve by many sigma. In this case the fitted curve is not reliable anymore, since the regions with attenuated stars are causing an artificial flattening of the slope. Note that, apart from a region near 8° in altitude, the stars are still visible through the clouds. In many other cases whole portions of the profile are missing.

The presence of clouds is ascertained by a strict visual inspection. However some types of densely populated profiles could prove misleading and hide a slightly deviating population of stars. To get a better quantitative handle we inspect the difference between the measured and fitted extinction for each star and plot it against the slant depth (Fig. 3), so it can be directly compared to the FD profile (this step requires knowledge about the geometry of the shower). Negative values represent stars with missing light and point to the presence of a thin cloud. Positive values indicate

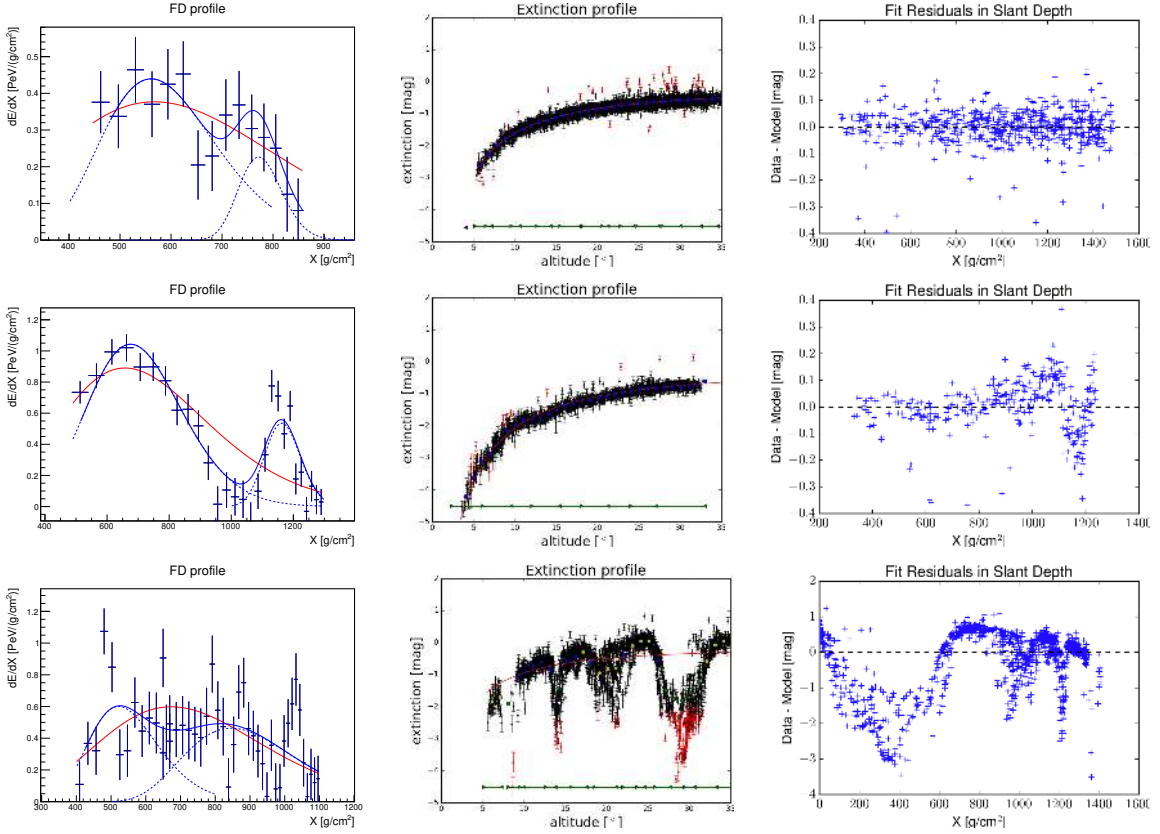


Figure 3: Every row represents a single shower and the associated FRAM scan. *Left column:* a fluorescence profile recorded by the FD which passed the double-bump trigger. The red line represents a fit of a regular Gaisser-Hillas function, blue line a combination of two G.-H. functions. *Middle column:* an extinction profile recorded by FRAM. The red line shows the fitted function 4.1. The green lines near the x axis plot the range in altitude for every image in the scan. Each point represents a single star, large outliers being plotted in red. *Right column:* the differences between the measured and the fitted extinction value for every star, recast in terms of the slant depth.

an abundant light. This is caused mainly by the aforementioned flattening of the extinction curve, but simple statistical fluctuations and effects like possible inhomogeneities of the star catalog could also play a role.

The event in the middle row in Fig. 3 is a curious case: the FD profile features a clear secondary peak, whose width is nonphysically narrow in the sense that it differs vastly from a universal shape of a shower created by a proton primary. The extinction profile in Fig. 3-middle does not exhibit significant deviations from the fit. However, Fig. 3-middle shows a clearly attenuated population in the vicinity of 1200 g/cm^2 , which also exactly corresponds to the location of the maximum in Fig. 3-middle. Thus in this case the anomalous profile was a result of scattering of the Cherenkov light off a thin cloud.

The presence of such inhomogeneities also generally leads to larger fluctuations in fit residuals of individual stars in the profile. Consequently, a new cut on the Root Mean Square (RMS) was introduced in order to eliminate events of this type. Its value was set to 0.1 mag and its application

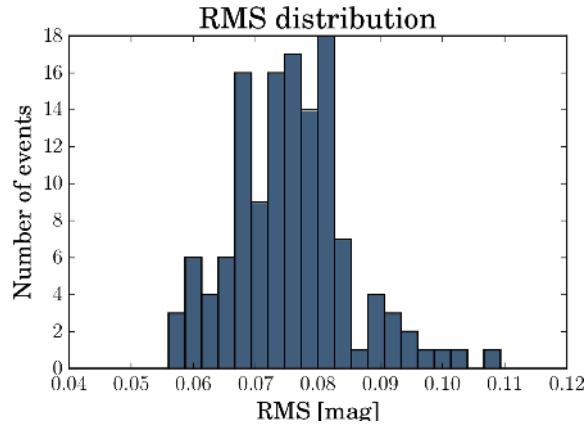


Figure 4: Average fluctuations from a predicted profile.

resulted in a loss of approximately 5% of events. An illustrative graph presenting the distribution of the RMS is shown in Fig. 4. Several large outliers were already excluded in order to make the graph clearer. The shown data sample consists of scans previously classified as clear from several months in 2016.

5. Measuring the Aerosol Content of the Atmosphere

As already mentioned in section 1, the attenuation of incoming fluorescence light attributable to aerosols plays an important role in the shower reconstruction and has a direct impact on the estimated energy of the primary particle. The FRAM telescope incidentally produces scans over a wide range of airmass while looking for clouds during the StS program. This can be utilized for the precise determination of the attenuation coefficient k , obtained by fitting the simple functional form 4.1 while carefully handling the contributions of the various correction terms. Moreover, the StS scans are recorded in the B filter (with effective midpoint wavelength of approximately 440 nm), where the attenuation due to aerosols is much smaller than the contribution by molecular scattering. Because the optical system has a finite passband and Rayleigh scattering is also wavelength dependent, the two need to be attentively combined, corrected for the temporal fluctuations in air density using data from the GDAS network and then finally subtracted from k to obtain the aerosol contribution. This process is described in detail in [6].

The method works well during cloudless nights with a low moon fraction, where no additional or missing light is distorting the quality of the fit. The RMS of the fit residuals is $\langle \text{RMS} \rangle = 0.075$ mag. Their dependence on various parameters of the fit is shown in Fig. 5. The residuals are reasonably small, with no identifiable major data populations which systematically and significantly deviate. The statistical errors connected to the determination of the coefficient k itself are of the order of 0.01.

6. Summary

We have introduced the FRAM telescope and its role within the context of the Pierre Auger Observatory, in particular in the Shoot-the-Shower program. The described cloud identification

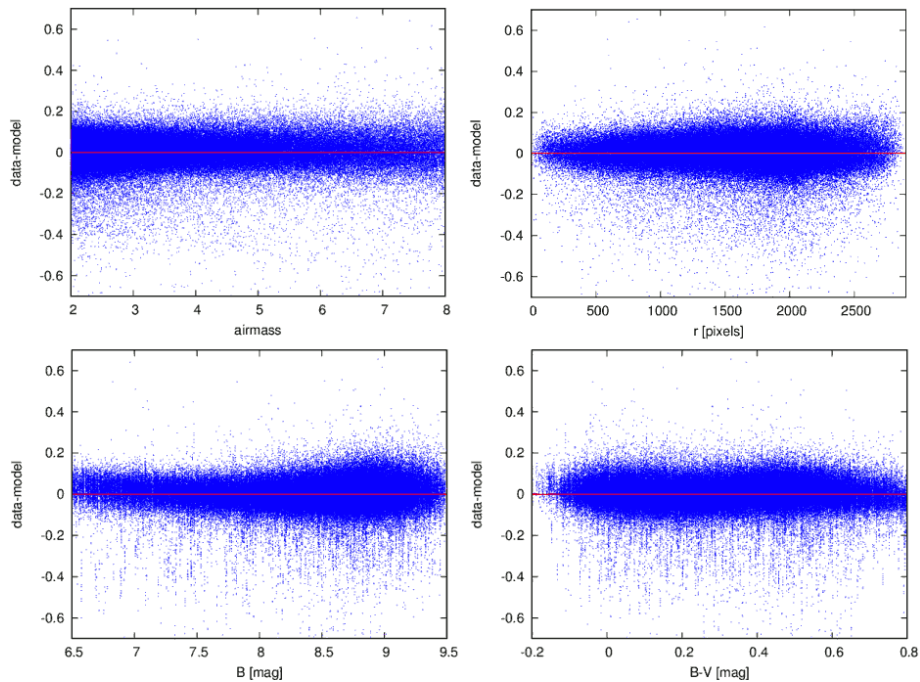


Figure 5: Residuals of the global fit as a function of the airmass, the distance from the center of the image, the magnitude measured in the B filter and the color dependence of the measurement in the B and V filters.

method based on stellar photometry performed on a set of wide-field images serves as a basis for the selection of showers featuring longitudinal profiles undistorted by atmospheric effects. The question of whether the obtained sample of candidate events is indeed showing anomalous bumpy features originating in hadronic interactions is still open and the work on the interpretation of the dataset is ongoing. We have also very briefly described a novel method for the measurement of attenuation due to aerosols using scans across a wide range of airmass. The statistical uncertainties of the obtained extinction coefficients are of the order of 0.01 and thus sufficiently low for the purposes of atmospheric monitoring, but the estimation of the various connected systematic errors is difficult and is still work in progress.

References

- [1] A. Aab *et al.* [Pierre Auger Collaboration], *Nucl. Instrum. Meth. A* **798**, 172 (2015), [arXiv:1502.01323].
- [2] E. Hog *et al.*, *Astron. Astrophys.* **355**, L27 (2000).
- [3] T.K. Gaisser and A.M. Hillas, *Proc. 15th ICRC 1977*, Plovdiv, Bulgaria, **8**, 353 (1977).
- [4] C. Baus, R. Engel, T. Pierog, R. Ulrich, and M. Unger, *Proc. 32nd ICRC 2011*, Beijing, China, **2**, 206 (2011) [arXiv:1111.0504].
- [5] J. Blazek [Pierre Auger Collaboration], *EPJ Web Conf.* **144**, 01009 (2017).
- [6] J. Ebr *et al.* [Pierre Auger Collaboration], *EPJ Web Conf.* **144**, 01011 (2017).

7

Outreach



PIERRE
AUGER
OBSERVATORY



Education and public outreach of the Pierre Auger Observatory

Charles Timmermans^{*a} for the Pierre Auger Collaboration^b

^a*Nikhef and Radboud University, Nijmegen, the Netherlands*

^b*Observatorio Pierre Auger, Av. San Martín Norte 304, 5613 Malargüe, Argentina*

E-mail: auger_spokespersons@fnal.gov

Full author list: : http://www.auger.org/archive/authors_icrc_2017.html

The scale and scope of the physics studied at the Pierre Auger Observatory continue to offer significant opportunities for original outreach work. Education, outreach and public relations of the Auger Collaboration are coordinated in a separate task whose goals are to encourage and support a wide range of education and outreach efforts that link schools and the public with the Auger scientists and the science of cosmic rays, particle physics, and associated technologies. This paper focuses on the impact of the Collaboration in Mendoza Province, Argentina. The Auger Visitor Center in Malargüe has hosted over 110,000 visitors since 2001, and a sixth Collaboration-sponsored science fair was held on the Observatory campus in November 2016. Numerous online resources, video documentaries, and animations of extensive air showers have been created for wide public release. Increasingly, collaborators draw on these resources to develop Auger-related displays and outreach events at their institutions and in public settings to disseminate the science and successes of the Observatory worldwide. The presentation will also highlight the impact of the recently renovated Visitor Center, configured now to allow self-guided tours, which has increased the visitor count over the last year and provided a boost to local outreach.

*35th International Cosmic Ray Conference — ICRC217
10–20 July, 2017
Bexco, Busan, Korea*

^{*}Speaker.



Figure 1: Auger collaborators participating in the November 2016 Malargüe Day parade.

1. Introduction

Education and public outreach (EPO) have been an integral part of the Pierre Auger Observatory since its inception. The collaboration's EPO activities are organized in a separate Education and Outreach Task that was established in 1997. With the Observatory headquarters located in the remote city of Malargüe, population 28,000, early outreach activities, which included public talks, visits to schools, and courses for science teachers and students, were aimed at familiarizing the local population with the science of the Observatory and the presence of the large Collaboration of international scientists in the isolated communities and countryside of Mendoza Province. As an example of the Observatory's integration into local traditions, the Collaboration has participated in the annual Malargüe Day parade since 2001 with collaborators marching behind a large Auger banner (see Fig. 1). Close contact with the community fosters a sense of ownership and being a part of our scientific mission. The Observatory's EPO efforts have been documented in previous ICRC contributions [1, 2, 3]. Fifteen years after opening to the public, the Auger Visitor Center has been modernized, and, in parallel, web-based outreach efforts are intensified.

2. The Auger Visitor Center in Malargüe

The Auger Visitor Center (VC), located in the central office complex in Malargüe, continues to be a popular attraction. The VC is managed by a small staff led by an Observatory employee; they share the task of giving presentations and tours to visitors and school groups. Through May, 2017,

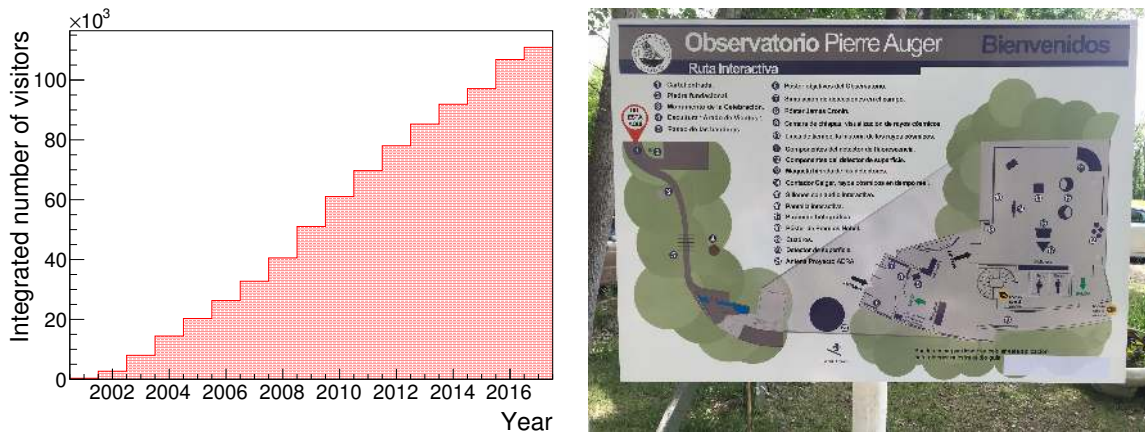


Figure 2: Left: The integrated number of visitors logged at the Auger Visitor Center since 2001. Right: The self guided tour starts outside in the garden of the Observatory.

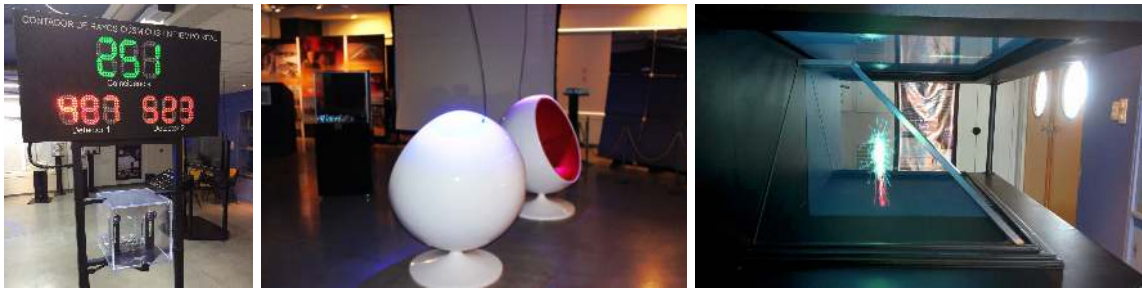


Figure 3: Different elements of the upgraded Auger Visitor Center in Malargüe. From left to right: Geiger Müller counters provide live information on the number of muons, pods describe different features of the Observatory, a 'holographic' display of an air shower shows the development of air showers to the public.

the VC has hosted 110,920 visitors. Fig. 2 shows the integrated number of visitors since Nov. 2001. The noticeable increase of visitors since 2008 occurred after the opening of a nearby planetarium [4], which is operated independently of the Observatory, in August of that year. A recent increase in the number of visitors occurred in 2016 after the opening of the modernized Visitor Center.

An upgrade of the Observatory's detector systems, currently in progress, provided an incentive to modernize the VC, and thereby re-inviting people who have seen the Observatory in the past to relive this experience through a self-guided tour. As shown in Fig. 2, this self-guided tour starts in the beautiful gardens of the Observatory where several monuments commemorate the inauguration of the Observatory and highlight the international character thereof. Furthermore, actual detectors are on display. In the VC, located inside the James Cronin office building, the tour continues.

Audio and video displays explain the effect of cosmic rays in the atmosphere, methods to measure cosmic rays, and the workings of the Observatory. Several objects and 3D models help to understand the different topics, as shown in Fig. 3. These updates to the VC demonstrate a genuine interest of the Collaboration to communicate with the people from Mendoza Province and beyond about the science and tools of the Observatory. In addition, the VC still allows for lectures to school audiences, as shown in Fig. 4.



Figure 4: High school students listening to a presentation on the working of the Observatory inside the modernized VC.

3. The 2016 Auger Science Fair

The Observatory hosted its sixth biannual Science Fair in the Assembly Building on November 17-19, 2016, as shown in Fig. 5. Twenty-four student teams from all over Mendoza Province, with ages ranging from primary school through high school, presented research projects in the areas of natural science, exact science, and technology. More than 20 Auger collaborators, from different nationalities, and a few invitees served as judges for the student projects. Prizes were awarded to the top teams in several categories in the closing ceremony on November 19. The November 2016 Science Fair owes its success to the Observatory staff, the collaborators who served as judges, the Municipality of Malargüe, the participating teachers and students, and special mention goes to the lead local organizers: Miguel Herrera, Fabian Amaya, and Alicia Piastrellini.

4. The Online Observatory

The Auger public event display allows the general public to see what information is recorded from an incoming air shower, and to grasp the steps involved in obtaining information on the incoming cosmic ray creating this air shower. The Collaboration has committed to providing 10% of its data to the general public. The target group for outreach purposes includes even university



Figure 5: Left: An impression of the 2016 Science Fair. Right: The participants of the Fair.

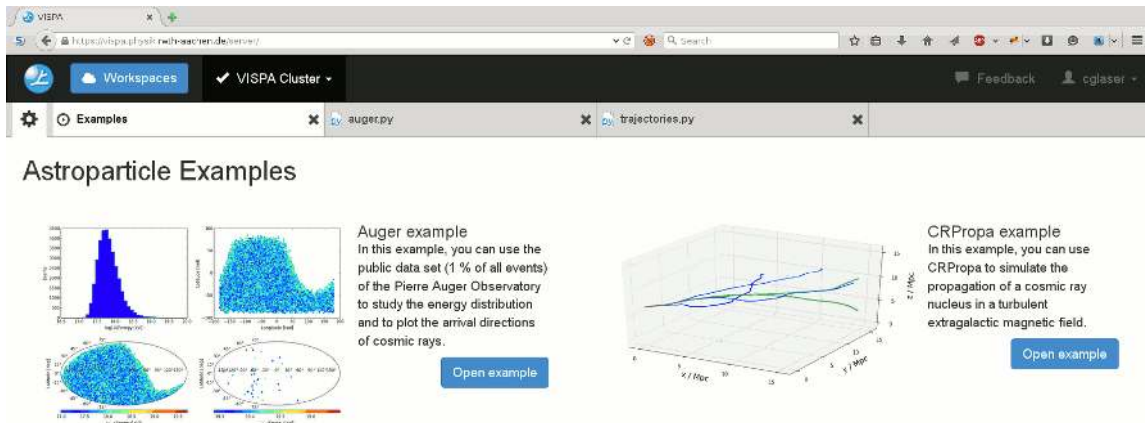


Figure 6: Example of the web-based VISPA public data analysis package. Left: Examples using the Auger public data set. Right: Simulations using the CRPropa package [10].

students for whom statistical tools and analysis packages such as VISPA [6, 7, 8, 9] (see Fig. 6) are available to handle substantial amounts of data.

At the same time, high-school students are able to make online selections on the events they would like to see or use for their own purposes thereby reducing the data volume while increasing the number of interesting events substantially with respect to when using the more basic tools they are used to.

The self-guided tour described above triggered a presence of the Observatory on the *izi.travel* website, thus providing the option of a virtual tour of the Observatory [11]. In addition, the Collaboration communicates with the general public through its Facebook page [12], that is used by science fair participants as well as the general public. In addition to providing information about the status of the Observatory, the Collaboration also writes summaries of recent scientific achievements on its main homepage [13] (see Fig. 7). All information and tools combined provide a good overview about the detectors and achievements of the Collaboration, as well as an invitation to the



Figure 7: Left: The home page of the Pierre Auger Collaboration. Right: The Facebook page of the Pierre Auger Collaboration.

general public to use the data provided by the Collaboration for their own inquiry.

5. Conclusions

The Pierre Auger Observatory continues to provide unique education and outreach opportunities which expose people of all ages to the excitement of astroparticle physics. Its Visitor Center and Science Fairs have great local impact near Malargüe, while collaborators from around the world ensure that the Observatory's science and successes have international reach. The upgrade of the Observatory has provided an excellent opportunity to modernize the Visitor Center and strengthen the relations between the Collaboration and the local community.

The improved presence of the Collaboration on the internet allows people across the globe to visit the Observatory, interact with scientists and learn about the exciting new knowledge that scientists have extracted from the data obtained by the Observatory.

References

- [1] C. Timmermans, for the Pierre Auger Collaboration, *Education, Outreach and Public Relations of the Pierre Auger Observatory*, Proc. 34th ICRC 2015, The Hague, The Netherlands, PoS(ICRC2015)587.
- [2] G. Snow, for the Pierre Auger Collaboration, *Education and Outreach Activities of the Pierre Auger Observatory*, Proc. 33rd ICRC, Rio de Janeiro, Brazil, **2** (2013) 116; [arXiv:1307.5059].
- [3] G. Snow, for the Pierre Auger Collaboration, *Education and Public Outreach of the Pierre Auger Observatory*, Proc. 32nd ICRC, Beijing, China, **2** (2011) 190; [arXiv:1107.4806].
- [4] See <http://www.planetariomalargue.com.ar>.
- [5] See <https://www.auger.org/index.php/edu-outreach/event-display>.
- [6] See <http://vispa.physik.rwth-aachen.de>.
- [7] H.P. Bretz *et al.*, *A Development Environment for Visual Physics Analysis*, JINST **7** (2012) T08005; [arXiv:1205.4912].

-
- [8] M. Erdmann *et al.*, *A field study of data analysis exercises in a bachelor physics course using the internet platform VISPA*, Eur. J. Phys. 35 (2014) 035018; [arXiv:1402.2836].
- [9] D. van Asseldonk *et al.*, *The VISPA internet platform for outreach, education and scientific research in various experiments*, to appear in 21st International Conference on Computing in High Energy and Nuclear Physics (CHEP2015), Okinawa, Japan, (2015).
- [10] K.H. Kampert *et al.*, *CRPropa 2.0 – a Public Framework for Propagating High Energy Nuclei, Secondary Gamma Rays and Neutrinos*, (2012) [arXiv:1206.3132].
- [11] See <https://izi.travel/en/6095-pierre-auger-observatory/en#db48-pierre-auger-observatory/en>.
- [12] See <https://www.facebook.com/ObservatorioPierreAuger.VisitorCentre/>.
- [13] See <https://www.auger.org>.